Numerical Modeling of Fluvial Urban Floods: Implications for Flood Mitigation Strategies

Qingcheng Yu

Thesis submitted to the University of Ottawa

in partial Fulfillment of the requirements for

the PhD degree in Civil Engineering (Water Resources)

Department of Civil Engineering

Faculty of Engineering

University of Ottawa

Abstract

Fluvial urban floods, also known as riverine urban floods, occur when water levels in urban streams or rivers rise rapidly due to heavy rainfall, snowmelt, or dam releases. Climate change significantly affects the severity, frequency, and predictability of floods, presenting new challenges to the relevant studies. In this thesis, numerical modeling is used to investigate the morphodynamic and inundation processes of fluvial urban floods and to explore engineering solutions to the associated problems.

The first study employed Delft-3D to develop a numerical model for examining the morphodynamic processes of the 2013 Bow River flood in Calgary, Canada. The model was calibrated using velocimetry data and validated with post-flood bathymetry data. The temporal and spatial distributions of the modeled flow and morphodynamic data were presented and analyzed. Results indicate that the timing of morphological changes during the flood varies among different morphodynamic units (MUs) but remains consistent within similar MUs. It was demonstrated that, given the same flood peak and duration, a regulated flood event with a brief rising period, as opposed to a prolonged rising period, might result in reduced bank erosion and bar growth. Additionally, bedload transport rates were found to be more sensitive to flow velocities than to bed sediment sizes in the Bow River case, due to the greater spatial and temporal variation of velocities during the flood.

Another issue arising from the 2013 Bow River flood was the flood-induced bar growth, which constricted the river channel and increased future flood risk. The second study focused on exploring the optimal bar management solution for the Bow River. Using the developed morphodynamic model, we compared the effectiveness of a traditional bar removal plan with a novel bar realignment plan. Results indicate that while appropriate bar realignment can protect aquatic habitats and provide river recreation opportunities, bar removal is more effective in reducing future flood peak levels. The findings also suggest that manipulating instream bars has minimal morphological impact on downstream reaches. This study also highlights that creating a less obstructed channel is a fundamental strategy for flood mitigation.

The third study emerged from surface image velocimetry analysis of the flow field in a large-scale physical model of flood mitigation strategies for the Bow River. We developed a new post-processing algorithm called Time Frequency Analysis (TiFA) to address challenges in Large Scale Particle Image Velocimetry (LSPIV) under unfavorable tracer conditions. TiFA involves three steps: (1) plotting the temporal

frequency distribution of PIV-recognized velocities at a specific location; (2) fitting a bimodal Gaussian distribution model to the plot to identify the "most likely" velocity at that location; and (3) repeating these steps at all locations to generate a spatially distributed velocity map. We evaluated the performance of TiFA, the traditional temporal-averaging method, and the ensemble correlation method using the scaled physical model surface imagery. Results showed that TiFA produced lower errors compared to the temporal-averaging method and was at least 40% faster than the ensemble correlation method, demonstrating the great potential of TiFA in LSPIV post-processing.

While the flow characteristics of open channel confluences have been extensively studied, the inundation dynamics of urban confluence floods remain unexplored. The fourth study aims to fill this research gap by investigating a 100-year flood event at the Ottawa-Gatineau (OG) confluence in Canada, utilizing in-situ measurements, remote sensing, and a two-dimensional (2D) hydrodynamic model. A flow rating curve was first developed at the confluence outlet, showing that the total discharge and water level follow a power-law function, with minimal influence from confluence discharge ratio. The developed rating curve also showed a distinct segmentation behavior, where water level increases faster with total flow discharge in the overbank flow stage than that in the in-channel flow stage, probably due to the combined effects of the change of roughness and friction slope. Then, we employed MIKE+ to develop a two dimensional (2D) unsteady hydrodynamic model to study the confluence flood dynamics. The developed 2D model reproduced well the measured inland floodwater velocity and urban flood inundation extent, demonstrating its reliability in simulating large-scale urban confluence floods. Model results show that confluence flood inundation extent is mainly a function of total flow discharge, with minimal impact from discharge ratio or flow unsteadiness. Therefore, using steady-state models may be appropriate in future modeling of urban confluence floods.

To Xi Chen,

who taught me the meaning of love…

Acknowledgments

I am deeply grateful to my supervisor, Dr. Colin Rennie, for his invaluable support throughout my studies. He is immensely knowledgeable and remarkably humble. He is rigorous towards research and approachable in demeanor. As the saying goes: "A true master is an eternal student." My supervisor embodies this spirit. Another saying goes: "An excellent supervisor is someone you aspire to be when you take on the role of a supervisor". My supervisor is such a role model to me. I am more than fortunate to have his unwavering encouragement and guidance during my study.

I would also like to extend my heartfelt thanks to my parents, Wei jiao and Haiying Yu, whose dedication has paved the way for me to reach today's point. Their selflessness and support have been the backbone of my achievements, and I am profoundly grateful for their constant presence in my life.

Very special and deep thanks go to my wife, Xi Chen, whose love, support and encouragement have been the foundation for everything I have achieved today. From the moment we first met, she has been by my side and supporting me throughout every challenge and milestone. The greatest happiness I have known is having her in my life. She is my soul, my heaven, my inspiration, my anchor, and my teacher, and I am endlessly grateful for her presence in my life.

I would like to thank all the members of my thesis examiners: Dr. Majid Mohammadian, Dr. Ioan Nistor, Dr. Ousmane Seidou, and Dr. Elli Papangelakis. I am grateful for the time they spent reviewing my work and for their insightful feedback which greatly enriched the quality of my thesis.

I would like to thank all the colleagues who have helped me along the way. I would like to express my gratitude to Dr. Ruihua Nie and Dr. Lu Wang for their precious guidance, and to Dr. Saiyu Yuan, who provided foundational support during my Master's studies. My gratitude also goes to Parna Parsapour-Moghaddam for her hands-on teaching on Delft-3D. Thank you to Jonathan Slaney from the City of Calgary, Sean Ferguson and Mitchel Provan from the National Research Council of Canada, Kate Neigel and Xiatong Cai from the University of Ottawa for their assistance in my experiments. Their support has been indispensable.

Lastly, I would like to express deep gratitude to my motherland, China, and wish for her continued peace, strength and prosperity.

Contents

List of Tables

List of Figures

Nomenclatures

A	Cross-sectional flow area	[m^2]
A_c	Number of model cells correctly predict the measured flood extent	[-]
$A^{(m',n')}$	Area of the computational cell (m', n')	[m^2]
$ADCP$	Acoustic Doppler Current Profiler	Abbr.
ADV	Acoustic Doppler Velocimetry	Abbr.
AOI	Area of Interest	Abbr.
a	Edge limiter	[-, integer]
a_1	Coefficient in the power law flow rating curve function	[m^2/s]
B_e	Ensemble baseline bed elevation predictions	[m]
B_c	Number of model cells overestimate the measured flood extent (i.e. false alarms)	[-]
B_w	Width of the rectangular channel	[m]
BSS	Brier Skill Score	[-]
b	Total bin number of the joint distribution histogram	[-, integer]
b_1	Coefficient in the power law flow rating curve function	[m]
C	Chézy coefficient	[$m^{0.5}$/s]
C_c	number of model cells underestimate the measured flood extent (i.e. misses)	[-]

CDE	Cumulative deposition height (or erosion depth)	[m]
CFL	The Courant-Friedrichs-Lewy number	[-]
CSI	Critical Success Index	Abbr. [-]
CVC	Cumulative volumetric changes	[m^3]
c	Coefficient in the power law flow rating curve function	[-]
D	Flow depth	[m]
D_{50}	Grain size at which 50% of the sediment by weight are smaller	[m]
D_{90}	Grain size at which 90% of the sediment by weight are smaller	[m]
D_*	Non-dimensional particle diameter	[-]
DEM	Digital Elevation Model	Abbr.
$Diff$	Water surface elevation difference between different time stamps	[m]
DN_R	Digital numbers of the red band in a panchromatic imagery	[-]
DN_B	Digital numbers of the blue band in a panchromatic imagery	[-]
DN_G	Digital numbers of the green band in a panchromatic imagery	[-]
DOF_n	Degree of freedom of the numerator in F-test	
DOF_d	Degree of freedom of the denominator in F-test	
D_T	Empirical spatial clustering level of tracers	[-]

EC	Ensemble Correlation	Abbr.
F	F-statistic	[-]
F_{α}	Threshold F-statistic under the confidence level of (1-α)	[-]
FFT	Fast Fourier Transformation	Abbr.
$FMGT$	FMGeocoder Toolbox	Abbr.
FWI	Floodwater index	[-]
f_{Cor}	Coriolis coefficient	[rad/s]
f_c	Total friction factor	[-]
f_c'	Grain-related friction factor	[-]
f_{MorFac}	User-defined morphological time scale factor	[-]
GNSS/INS	Global Navigation Satellite System/Inertial Navigation System	Abbr.
g	Gravitational acceleration	[m/s^2]
H	Water surface elevation	[m]
h	Flow depth	[m]
IA	Interrogation Area	Abbr.
JF_m	Joint distribution matrix at a certain velocity site "m" ($1 \leq m \leq N_v$)	[-]
K	Von Kármán constant	[-]

$KLT - IV$	Kanade Lucas Tomasi Image Velocimetry	Abbr.
K_S	Strickler flow resistance coefficient	[$m^{1/3}$/s]
k	Activation flow stage in a segmented flow rating curve	[m]
k_s	Roughness height	[m]
$LiDAR$	Light Detection and Ranging	Abbr.
$LSPIV$	Large-scale Particle Image Velocimetry	Abbr.
$LSPTV$	Large-scale Particle Tracking Velocimetry	Abbr.
MAE	Mean Absolute Error	Abbr.
$MBES$	Multi-beam Echo-Sounder	Abbr.
$MorFac$	Morphological time scale factor	Abbr.
M_{sum}	Ensemble correlation matrix	[-]
M_t	Instantaneous correlation matrix	[-]
MU	Morphological Units	Abbr.
M_x	Instantaneous velocity matrix in the "x" direction at all velocity sites	[px/frame]
M_y	Instantaneous velocity matrix in the "y" direction at all velocity sites	[px/frame]
m	Velocity site sequence in a PIV-processed frame ($1 \leq m \leq N_v$)	[-]
m'	The first coordinate of a computational cell	[-]

N	Sample volume	[-]
NaN	Not a Value	Abbr.
NSE	Nash-Sutcliffe model efficiency coefficient	[-]
N_T	Number of tracers	[-]
N_v	Total number of velocity sites in one frame	[-]
n	Manning roughness	[s/m$^{1/3}$]
n_c	Number of surface velocity candidates	[-]
n'	The first coordinate of a computational cell	[-]
$\bar{O}$	Means of the observed data	TBD
O_e	Ensemble observed data series	TBD
O_i	Observed data sequenced at "i"	TBD
OG	Ottawa-Gatineau	Abbr.
OTV	Optical Tracking Velocimetry	Abbr.
$\bar{P}$	Means of the predicted data	TBD
P_e	Ensemble predicted data series	TBD
P_i	Predicted data sequenced at "i"	TBD
$PBIAS$	Percent Bias	Abbr.

PIV	Particle Image Velocimetry	Abbr.
PTV	Particle Tracking Velocimetry	Abbr.
p	Number of unknown parameters in F-test	[-]
ppp	Particles Per Pixel	Abbr. [-]
px	Pixel	Abbr.
Q	Flow discharge	[m^3/s]
$Q_u^{(m',n')}$	Computed bedload sediment transport rate in the u direction at the computational cell (m',n')	[kg/s]
R	Correlation R	[-]
R^2	Coefficient of determination	[-]
$RIVeR$	Rectification of Image Velocity Results	Abbr.
RSS	Residual Sum of Squares	Abbr.
RTK	Real-Time Kinematic	Abbr.
S_0	Bed slope	[-]
S_1	Bin candidate matrix in the TiFA algorithm	[-]
S_2	Final results matrix in the TiFA algorithm	[-]
SA	Search Area	Abbr.
S_b	Magnitude of bedload transport rate per unit width	[kg/m/s]

SDI	Seeding Density Index	[-]
S_f	Friction slope	[-]
S_{QH}	Average rate of WSE increase with flow discharge	[cm/(m^3/s)]
$SSIV$	Surface Structure Image Velocimetry	Abbr.
$STIV$	Space-Time Image Velocimetry	Abbr.
s	Relative density of sediment particle to water	[-]
T	Total number of video frames	[-]
T_b	Dimensionless excess bed shear ratio	[-]
$TiFA$	Time Frequency analysis	Abbr.
t	Time	[s]
U	Longitudinal flow velocity in 1D modeling	[m/s]
u	Depth-averaged velocity components in the x directions	[m/s]
u_c	Efficiency factor	[-]
u'_*	Effective bed shear velocity	[m/s]
$\bar{V}$	Depth-averaged velocity magnitude	[m/s]
$Vel_{m,x}$	Temporal velocity matrix in the "x" direction at a certain velocity site "m" ($1 \leq m \leq N_v$)	[px/frame]
$Vel_{m,y}$	Temporal velocity matrix in the "y" direction at a certain velocity site "m" ($1 \leq m \leq N_v$)	[px/frame]

V_{noise}	Noise threshold	[px/frame]
$\overline{V_s}$	Overall average surface flow velocity	[px/frame]
V_t	Instantaneous velocity vector	[m/s]
V_x	Surface flow velocity matrix in the "x" direction	[px/frame]
V_y	Surface flow velocity matrix in the "y" direction	[px/frame]
v	Depth-averaged velocity components in the y directions	[m/s]
WSE	Water Surface Elevation	Abbr.
Z_b	Water bottom surface elevation (or bed level)	[m]
α	Discharge ratio	[-]
ε	Residual error	TBD
$\Delta_{SED}^{(m',n')}$	Change of bed sediment mass at the computational cell (m', n')	[kg/m^2]
Δt	Computational time step	[s]
η	Morphological development index	[-]
θ_{cr}	Threshold parameter calculated from the classical Shields curve	[-]
ν	Kinematic viscosity of water	[m^2/s]
ρ_c	Seeding density	[ppp]
ρ_{cv1}	Converging seeding density at the Poisson case	[ppp]

ρ_s	Bulk density of sediment	[kg/m^3]
ρ_T	Overall average tracer density	[ppp]
ρ_w	Water density	[kg/m^3]
τ_b'	Effective bed shear stress	[N/m^2]
$\tau_{b,cr}$	Critical bed shear stress	[N/m^2]
τ_{bx}	Shear stress on the bed surface in the x direction (Unit: pa)	[N/m^2]
τ_{by}	Shear stress on the bed surface in the y direction (Unit: pa)	[N/m^2]
τ_{xx}	Depth-averaged Reynolds normal stress in the x direction from the boundary parallel to the x-axis	[N/m^2]
τ_{xy}	Depth-averaged Reynolds shear stress in the y direction from the boundary parallel to the x-axis	[N/m^2]
τ_{yx}	Depth-averaged Reynolds shear stress in the x direction from the boundary parallel to the y-axis	[N/m^2]
τ_{yy}	Depth-averaged Reynolds normal stress in the y direction from the boundary parallel to the y-axis	[N/m^2]

Chapter 1. Background

1.1 Definition

Throughout human history, cities have been situated near rivers, lakes and sea for greater water resources availability and transportation flexibility. However, great water resources come with high risks for flooding. Flooding is defined as a large amount of water covering an area that is usually dry. Floods can take place at a relatively short time due to rapid snowmelt, heavy rainfall, tsunami, dam or levee failure, or a sudden release of water, which are usually hard to predict and can cause severe damages (Zhang et al., 2024).

Floods that take place at urban areas are named urban floods. According to the fundamental causes, urban floods can be further classified as three major types (Zhang & Crawford, 2020): fluvial (or "riverine") urban floods, and pluvial urban floods, coastal urban floods:

- **Fluvial urban floods** are also named as "riverine urban floods", which result from river flow overtopping the banks. River flow overtopping could be due to many reasons such as snow melting, ice jamming, upstream rainfall, an upstream dam breach and landslides.

- **Pluvial urban floods** are caused by local heavy rainfall (e.g. a hurricane passing by). Different from the fluvial flood which is related to a river, a pluvial flood could occur in any city, especially low-lying cities with poor drainage ability. The fundamental reason of a pluvial flood is usually not only the rainfall event itself, but the large paved areas that lower the infiltration ability and the poor drainage system that is unable to handle the excessive surficial floodwater during the rainfall.

- **Coastal urban floods** are often related to coastal extreme events such as tsunami and storm surge. The range of a coastal flood is controlled not only by the flood intensity but also the topography of the coastal land exposed to flooding. Wave-induced coastal floodwater could have a very high kinetic energy, which may have destructive impacts to urban infrastructure and thus human lives.

This thesis will focus on fluvial urban floods, which will be short-noted as "urban floods".

1.2 Significance

As one of the most devastating natural disasters in human history, urban floods pose a range of significant hazards and engineering problems to human society. The potential hazards of urban floods are not only the floodwater itself that may cause loss of livelihood and properties in the urban areas, but also the hurtling debris and sediment carried with the flow, exposure to electricity and potential failure of infrastructure such as buildings and bridges during floods. A recent study shows that urban floods could result in not only a noticeable damage to urban infrastructure due to overland inundation, but also the disturbance of social order (Vestby et al., 2024). In addition, the flood-induced morphological impacts such as bank-erosion (Lawal & Omosanya, 2023; Kumar et al., 2024), in-channel bar formation (Yu et al., 2022), and river diversion (Brooke et al., 2022) are also important issues for river engineers.

There have been many notable examples of urban flood events recently. For example, in 2012, an extreme rainfall in Beijing caused a pluvial urban flood event with return period of 60 years, resulting in 79 deaths and economic loss of 11.64 billion RMB (Wang et al., 2018). The catastrophic 2013 Alberta fluvial flood that inundated the downtown area of the City of Calgary, resulted in 5 deaths, evacuation of 100,000 people, and 6 billion CAD economic loss (Parsapour-Moghaddam et al., 2019). The magnitude of this flood event is classified as a return period of 80-100 years. Also in 2013, an extreme flood event took place in Europe, which caused losses of over €8 billion nationwide in Germany. Similar to the case in Calgary flood, this flood event was classified as the most severe flood event in Germany for the last 60 years (Thieken et al., 2016). The Pacific Northwest floods that took place in November 2021 resulted from a hydro-meteorological phenomenon called "atmospheric river". The flooding comprised a series of floods that affected British Columbia (B.C.), Canada, and parts of Washington State in the U.S. This flooding in B.C. was considered as a 500-year flood event and could be one of the costliest flood events in Canada’s history. Blöschl et al. (2019) and Gudmundsson et al. (2021) investigated the historical flood events in regional and global scales in the last 50 years and found that the flood changes are broadly consistent with climate model projections, suggesting that climate driven changes are already happening.

Future urban floods could have even higher risks compared to the abovementioned urban flood events. It is also reported that the urban population will increase from 3.6 billion in 2011, to 6.3 billion in 2050, which represents a growth from 51% to 68% of the global population (UN, 2011). As more and more people live in densely populated urban areas, which are often situated on flood plains and low-lying coastal areas, their exposure to flood hazards is also increased (Hammond et al., 2013). Further, as a city expands, the development of its urban sewer system could be slower than the city's development. There also could be more and more impervious ground areas (i.e. change of land use). On the other hand, climate change has significantly altered both global and local hydrological processes in recent years (Qian et al., 2022; Taherkhani et al., 2020), which brings additional uncertainties to urban floods. Hirabayashi et al., (2013) demonstrates a large increase in the frequency of future pluvial floods in Southeast Asia, Peninsular India, eastern Africa and the northern half of the Andes (Figure 1.1).

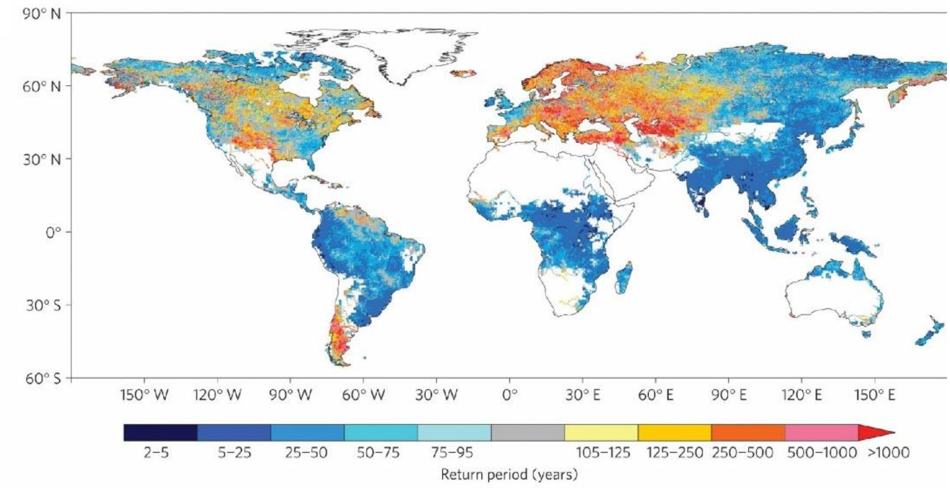

Figure 1.1. Multi-model median return period (years) in 21st century for discharge corresponding to the 20th century 100-year flood (Hirabayashi et al., 2013).

Chapter 2. Literature review

2.1 Data collection

The first step to understand the urban floods is to collect urban flood data, which could help to determine the reason of flooding, calculate the flood damage and losses, determine the evacuation plan, and more importantly, provide essential materials to build and validate an urban flood model. Essential data of fluvial urban floods include:

- Flood hydrograph: discharge & water level;
- River bathymetry and when necessary, river sediment;
- Flood inundation extent and depth;
- Flow velocity;

Nowadays, with the development of micro-electronics and image recognition technology, the data collection tool is quickly evolving: from "big" to "small", from "manned" to "unmanned", from "connective" to "remote-control", from "unsafe" to "safe". In the next few sections, the collection methods and usage of those above-mentioned data will be reviewed and elaborated.

2.1.1 Flood hydrograph data

2.1.1.1 Hydrometric gauges

Flood hydrograph data (discharge and water level data) could be used as the boundary conditions of a numerical model or a scaled physical model. In most situations, the downstream boundary of a model is usually selected at the location where there is a known river gauge, which can provide reliable water level data during fluvial urban floods. However, due to the lack of river monitoring at some flood-prone urban areas (i.e. ungauged reaches), the nearest river gauge could be far away from the study area. This distancing may not bring too much difference to the discharge value between the study area and the river gauge, as long as there is no noticeable inflow between them. However, the water level difference between the study area and the river gauge could be large. This problem could be solved by developing a simple hydrodynamic model (e.g. a one-dimensional (1D) model or a coarse-meshed 2D model) from the nearest upstream river gauge to the nearest downstream river gauge. By doing so, the time series of water level data any site within the simple model domain can be exported and used in other more complex numerical models (e.g. Parsapour-Moghaddam et al., 2019b; Yu et al., 2022). However, in order to make sure the modeled water level data are valid, field measurements of water level and velocity data are often required to validate the numerical model.

2.1.1.2 Remote sensing

Remote sensing technology could also be used to generate the water level data, and sometimes water surface slope data and discharge data at ungauged river reaches. During a flood event, water surfaces are usually considered as rough and wavy due to sub-surface turbulence and possibly surface wind shear, which could produce signal backscattering at large look angles (30° to 58°), meaning that active remote sensing (ARS) satellite such as the Shuttle Radar Topography Mission (STRM), which can directly yield water surface elevation (WSE) and water surface slope (WSS) during a flood event (Yan et al., 2015). However, this approach is built on the rough water surfaces assumption, which may limit its usage during low-flow conditions where water surfaces are more calm. An alternative approach is to use satellite altimetry, which measures the WSE and WSS using laser ranging technology. Such an application has been widely demonstrated recently for the Water and Ocean Topography (SWOT) mission (Biancamaria et al., 2016) and the ICESat-2 mission (Scherer et al., 2022; Christoffersen et al., 2023; Liu et al., 2023). An example of remote-sensed WSS is shown in Figure 2.1. Another advantage of remote sensing is that it can measure the flow width, which can further yield discharge data from the Manning's equation. In the study done by LeFavour & Alsdorf (2005), the remote-sensed water slope and discharge data in Amazon River only had 6.2% difference compared with the in-situ measurement data. Moreover, the WSE and WSS data quality may vary with the satellite sensor quality, weather conditions such as cloud coverage, flow turbidity, etc. Another approach is to combine remote sensing technology with the digital elevation model (DEM) of dryland: when floods inundate dryland, the WSE at the edge of floodwater is equal to the elevation value of the dryland site where floodwater touches with the dryland. This approach was also widely used to detect WSE during flood events and showed reliable performance (e.g. Tarpanelli et al., 2013; Pavelsky, 2014; Gleason & Wang, 2015). The advantage of this method lies in its lower reliance on high-quality satellite sensors compared to the previous approach, which results in improved cost-effectiveness and accessibility. Due to the unpredictability of extreme flood events, no matter which above-mentioned approach is used, a common limitation of remote-sensing-based methodology is that there might not be remote-sensing satellites passing by the study area during the flood event.

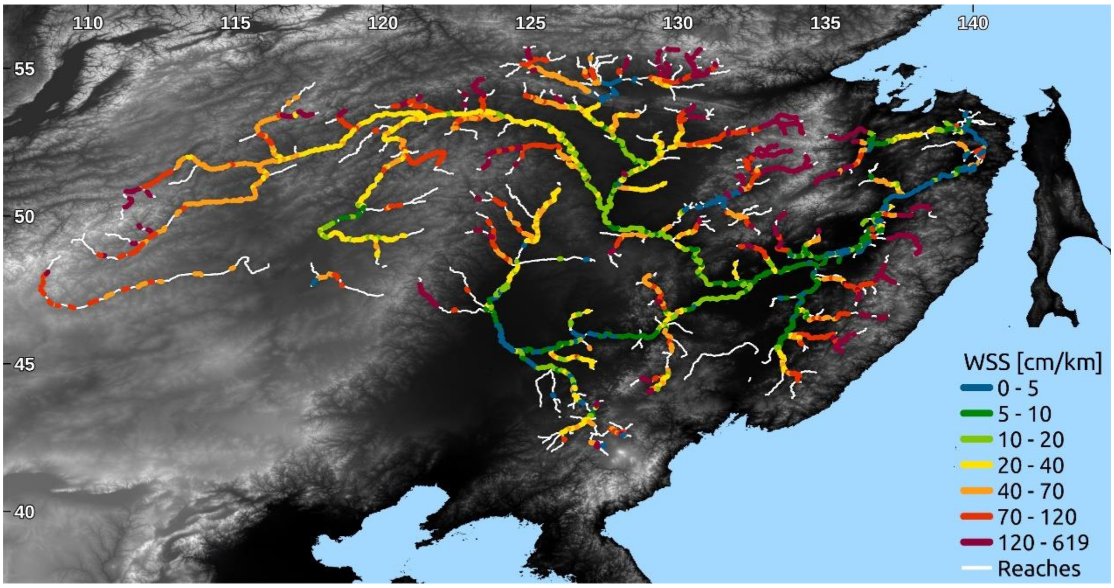

Figure 2.1. Median Water Surface Slope (WSS) assigned to SWORD reaches in the Amur Basin based on ICESat-2 data from October 2018 to October 2022 (Christoffersen et al., 2023).

2.1.1.3 Flow rating curves

Using hydrometric gauges or remote sensing to obtain WSE during urban floods shares a common limitation: it is only applicable for known flood events. It may not be suitable for determining water level data for a design flood event. In the latter situation, flow rating curve (or "Q-H relationship") could be an appropriate option: based on the Chezy's formula, under a certain channel control or a section control, flow discharge and WSE may follow a power law function (Chow, 1959), which allows to estimate WSE from the discharge of a design flood event. However, it may not be suitable in some complex flow situations where discharge and WSE do not follow a consistent relationship. For example, in open channel confluences, a defining feature is the confluence hydrodynamic zone (CHZ; see Best, 1987), where flow characteristics can change with variations in discharge ratio (Yuan et al., 2016). The research done by Hidayat et al. (2011) and Liu et al. (2023) has shown that the unique one-to-one power law Q-H relationship was found invalid upstream of river confluences due to the backwater effect. However, the Q-H relationship at the confluence outlet during fluvial flood events remains uncertain. It is unclear to what extent the WSE at confluence outlet might be influenced by variations in discharge ratio and flow unsteadiness within the confluence. The presence of a flow recovery zone may stabilize the energy slope at the outlet, potentially supporting the power-law application. Conversely, the combined effects of momentum exchange and secondary flows create complex spatial variations in water levels across the CHZ (Biron et al., 2002; Zhang et al., 2020; Shen et al., 2023), which could challenge the validity of a power-law relationship. To avoid this uncertainty, some researchers have extended downstream model boundaries far beyond the confluence to known gauge stations (e.g., Ding & Wang, 2012; Shi et al., 2022), although this adds computational cost. Therefore, field measurements are necessary to clarify the Q-H relationship at the confluence outlet, especially during fluvial flood events

2.1.2 River bathymetry and sediment data

All fluvial urban floods start from a river. Thus, the river-related data such as river bathymetry and sediment data play a crucial role in studying and modeling fluvial urban floods.

River bathymetry is the fundamental data to build a fluvial flood numerical or physical model. It is also one of the most significant sources of uncertainty in hydraulic modeling (Jung & Merwade, 2012). The river bathymetry data collected before a flood event could be used as the model boundary for the flood model to start with. Furthermore, for those rivers that have significant morphological changes during the flood, the river bathymetry survey is usually done two times: one pre-flood survey, one post-flood survey, in order to identify the flood-induced morphological changes. Those two sets of data have also been widely used to calibrate or validate a morphodynamic numerical model (i.e. Parsapour-Moghaddam et al., 2019b; Williams et al., 2016; Yu et al., 2022). So far, the widely-used approach to obtain the river bathymetry data is through field survey, by means of acoustic Doppler current profiler (ADCP) (e.g. Golder Associates, 2015; Parsapour-Moghaddam & Rennie, 2018) or multi-beam echo-sounder (MBES) (e.g. Huizinga & Heimann, 2018; Hasan et al., 2023).

Sediment data include bed sediment grain size distribution data and bedload/suspended load transport data. During an urban flood event, both flow velocity and flow depth are extremely high and unpredictable. It is both dangerous and difficult to take any measurements within the channel. Thus, sediment data have usually been obtained from a channel survey during low-flow conditions (e.g. Klohn Crippen Berger, 2016). Those data could be used to determine the river bottom roughness and the bed stratigraphy (i.e. the vertical distribution of sediment, which is important for rivers with surface armouring), which are both important in development of a numerical model (e.g. Guan et al., 2016; Parsapour-Moghaddam et al., 2019). Bedload/suspended load transport data can be obtained at river gauge stations (e.g. Water Survey of Canada, 2024) or measured from ADCP (Rennie & Millar, 2004; Williams et al., 2015) during medium flow or freshet situations. An example of ADCP-measured bedload data is shown in Figure 2.2. Sediment transport data could be used as the boundary conditions or validation dataset for a morphodynamic model (e.g. Li et al., 2008).

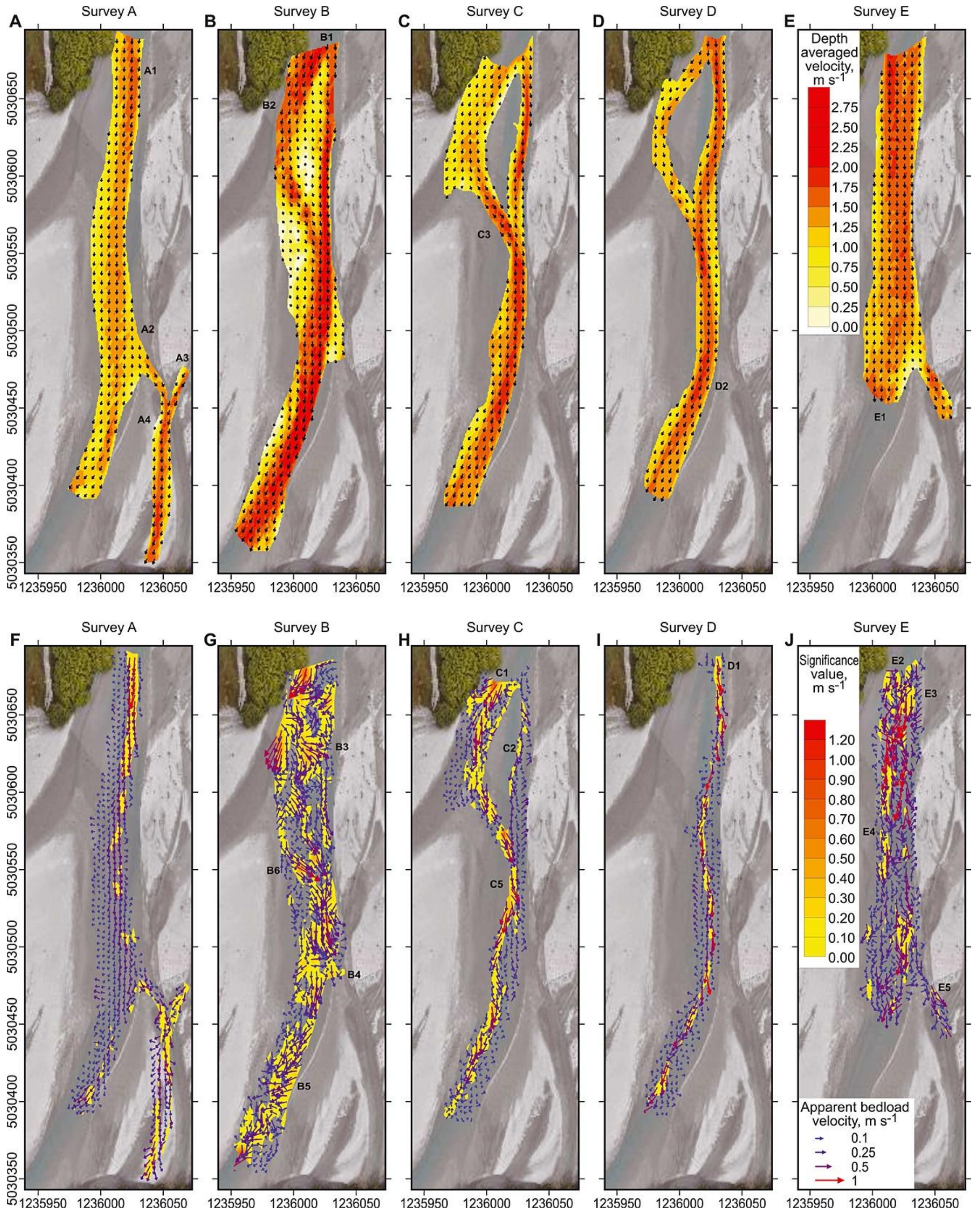

Figure 2.2. (A–E) Interpolated depth-averaged velocity data and (F–J) apparent bed load velocity collected from ADCP survey on the Rees River, New Zealand (Williams et al., 2015).

2.1.3 Flood inundation data

2.1.3.1 Field survey

Given that urban floods are fairly unpredictable and can be highly destructive, it is challenging to take direct measurements during an urban flood event. Nonetheless, city planners recognized the importance of flood inundation data for flood recording, estimation of flood losses and development of future mitigation strategies. Thus, in earlier days, urban flood inundation extent and depth were passively recorded with post-event wracks or flood marks on building (e.g. Neal et al., 2009; Pekárová et al., 2013, see Figure 2.3). Although this fully-passive technique is incapable of mapping the overall inundation extent, the inundation depth data obtained from this technique can be quite accurate. Thus, this passive recording technique is in part useful in urban flood observation and still works as a reliable subsidiary tool to calibrate urban flood numerical models (e.g. Neal et al., 2009) and assess flood hazards (e.g. Luu et al., 2017).

Figure 2.3. Historical flood marks at Passau (Germany), Ybbs (Austria), and Melk (Austria). (Pekárová et al., 2013)

2.1.3.2 Remote sensing

With the development of aerospace engineering and optical technology, remote sensing techniques have become the key tools for flood extent monitoring in recent years. The use of remote sensing data can supplement in-situ observations over vast ungauged regions, delineate the flood extent, and identify areas vulnerable to future flooding

(Klemas, 2015). Moreover, quantification of flooding extent through remote sensors can help to calibrate and evaluate hydrologic models and, therefore, improve hydrologic prediction and flood management strategies, especially in poorly gauged catchments (Khan et al., 2011).

One of the most commonly used remote sensing approach in flood inundation extent observation is to use Synthetic Aperture Radar (SAR) (e.g. Schlaffer et al., 2015; Dasgupta et al., 2021; Xu & Gao, 2024; Jiao et al., 2024). Apart from its all-weather and day-night imaging capability, the most important advantage of using SAR imagery lies in its ability to sharply distinguish between land and water (Sanyal & Lu, 2004). However, due to the side-looking configuration, SAR-based techniques suffer from the problems of shadowing, layovering and backscatter from buildings (Kiage et al., 2005), which limits the application of SAR in terms of flood extent modeling in densely built-up urban areas. For example, Schlaffer et al. (2015) utilized the alternating polarization SAR to map the urban flood inundation. They found that accuracies at the urban areas are below 50%. In addition, those high-resolution SAR images (e.g., TerraSAR-X, COSMO-SkyMed SAR images) are only acquired occasionally, which lead to difficulties in timely detection of urban flooding (Zhang et al., 2021). Another major problem is associated with the water surface properties. During a flood event, wind frequently causes ripples in the water surface, which could change the roughness of water surface and thus induce confusion of floodwaters with specular reflection of smooth land surfaces such as pavement (Zhang & Crawford, 2020). Thus, delineating fluvial urban flood extent using SAR is still challenging.

In comparison, fully RGB-based aerial photography and panchromatic (PAN, single-band grayscale image that combines the information from the visible R, G, and B bands) satellites such as WorldView, GeoEye, and Pleiades are capable of providing very high-resolution imagery. However, the applications of those high resolution RGB-based imageries in terms of flood extent delineation are very scarce. This may be because RGB bands alone have very limited capability of discriminating surface features, compared to those with additional bands of near-infrared and mid-infrared. In order to overcome this limitation, Zhang & Crawford (2020) recently introduced a spectral differential index, floodwater index (FWI), to automatically separate the turbid floodwater from the urban land surfaces classes:

$$FWI = \frac{(DN_R - DN_B) - (DN_R - DN_G)}{100} \tag{2.1}$$

Where DN_R, DN_G, and DN_B are the digital numbers in red, blue, and green bands, respectively. The factor of 100 is included as a reduction factor. The overall accuracies for visible floodwater extraction using FWI were above 96.68% (see Figure 2.4). However, the FWI relies on turbid floodwater, which is not always present in fluvial urban floods.

Figure 2.4. Aerial photos (upper images) and derived floodwater extent using FWI (lower images) during the 2013 flood in Calgary, Canada. (Zhang & Crawford, 2020)

2.1.4 Flow velocity

2.1.4.1 Field survey

In numerical modeling of urban floods, model validation against spatially distributed flow velocity is a critical step in evaluating the model performance and understanding the floodwater dynamics, especially for simplified 2D models. However, insufficient and/or unsatisfactory validation against measured flow velocity is a shared imperfection among most numerical studies on fluvial floods (e.g. Li et al., 2016; Aureli et al., 2021; Kim et al., 2021; Nguyen et al., 2021; Yang et al., 2022). Moreover, Bates & De Roo (2000) reported that 2D models may not be suitable for urban inundation modeling as flow at the transition region between river channel and floodplain has strong 3D features due to intense shear. Despite the findings of Bates & De Roo (2000), it is not necessary to completely discard 2D models in overland flood modeling, yet it is essential to validate the model against inland floodwater velocity to prove its accuracy and reliability when using 2D models to simulate urban pluvial floods. Taking measurements of the floodwater velocity also helps to understand better the inland floodwater dynamics and propagation process.

In order to collect inland floodwater velocity, one option is to use the passive approach, which refers to the installation of stationary data collection equipment at the place-of-interest during a flood event. For example, Brown & Chanson (2013) installed several ADV probes (see Figure 2.5) at riverine city streets during the 2011 Brisbane River flood to record floodwater velocity. They also manually recorded the free surface elevations using a measuring tape with reference to landmarks that were surveyed after the flood. This study found that the floodwater elevations and velocities fluctuated with distinctive periods linked with some local topographic effects. Although it is relatively safe to take velocity measurements in a passive way, the disadvantage of the passive floodwater measurement techniques is that they can only take local, stationary measurements.

The method of installing experimental equipment on-site is not only time-consuming and labor-intensive, but it may also not be applicable to all flood scenarios. Alternatively, velocity measurements could be done actively by operating a survey boat in the inland floodwater with the measurement equipment mounted to it or towed behind (e.g. ADCP). The primary advantage of such a method is its ability to facilitate rapid preparation and execution of measurements during flood events, while being applicable in various topographical scenarios. However, this type of data was not found in the literature.

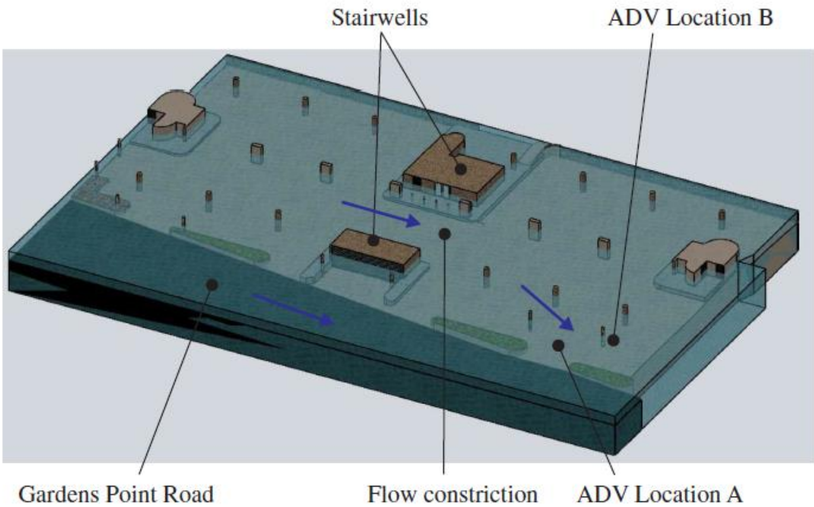

Figure 2.5. ADV installation near a riverine city street, Garden Point Road, during a fluvial urban flood event. Arrows indicate primary inland floodwater flow directions. (Brown & Chanson, 2013)

2.1.4.2 Remote sensing

Whether using passive or active measurement techniques, conducting field survey during floods poses significant potential risks to both personnel and equipment. In this context, remote sensing techniques, such as Large Scale Particle Image Velocimetry (LSPIV), can be an ideal solution.

The reliability and performance of LSPIV have been thoroughly evaluated across a wide range of scenarios. For instance, Muste et al. (2004) demonstrated that under optimal conditions in a physical model, the relative error of LSPIV measurements was less than 1.5%. Furthermore, Bandini et al. (2022) revealed that LSPIV could effectively reconstruct river velocity profiles with a high degree of accuracy, achieving a precision of just a few centimeters per second and coefficients of determination (R^2) exceeding 0.7 in half of the investigated cases. Recently, LSPIV has been employed in flood events to measure flow velocities (e.g. Le Coz et al., 2010; Guillén et al., 2017; Leitão et al., 2018; Lin et al., 2024; Masafu & Williams, 2024). Moreover, recent research has highlighted the potential of integrating LSPIV with advanced technologies such as infrared quantitative imagery (Legleiter & Kinzel, 2021; Schweitzer & Cowen, 2021), deep learning (e.g. Ansari et al., 2023; Wang et al., 2024a) and satellite platforms (e.g. Legleiter & Kinzel, 2021 (see Figure 2.6); Masafu & Williams, 2024), further expanding its applicability and enhancing its measurement capabilities in urban floods.

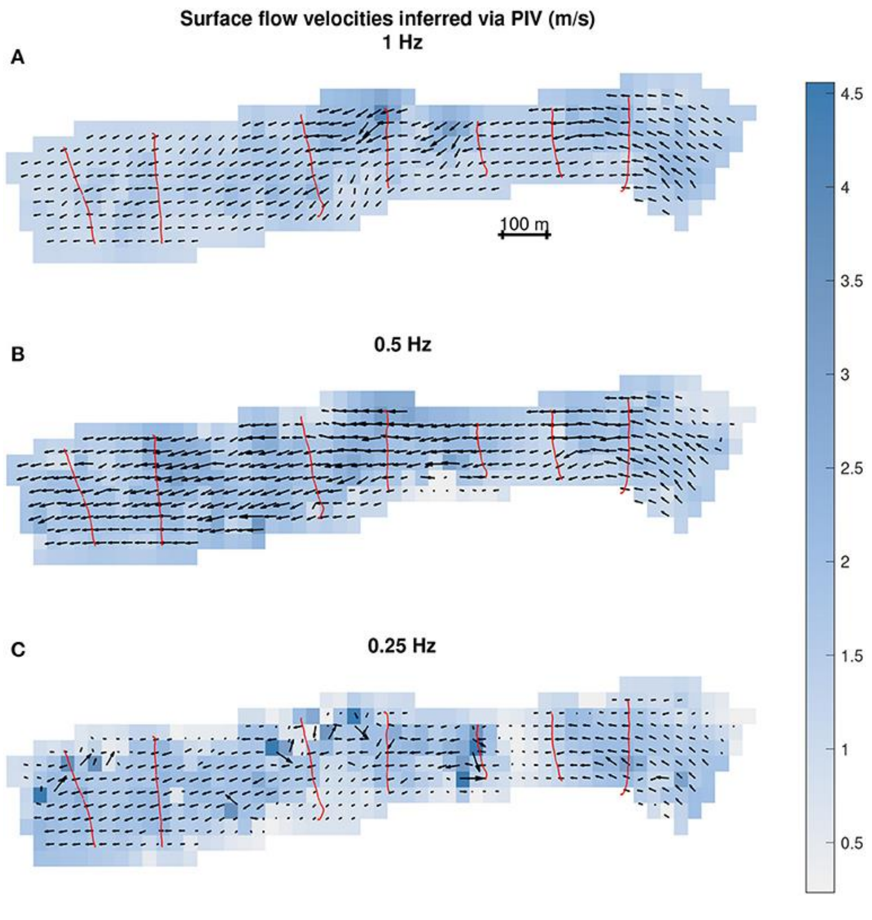

Figure 2.6. Maps of PIV-derived surface flow velocities for different frame rates of satellite video: (A) 1 Hz, (B) 0.5 Hz, and (C) 0.25 Hz. The locations of the ADCP velocity measurements used for

accuracy assessment are shown in red. (Legleiter & Kinzel, 2021)

LSPIV requires a clear and consistent identification of certain flow surface features or surface tracers to ensure a correct estimation of instantaneous velocity vectors from cross-correlation calculation in consecutive frames (Dal Sasso et al., 2021). High tracer density is crucial for accurate velocity estimates using traditional LSPIV. Otherwise, the instantaneous velocity vectors derived from no-tracer zones will be different (usually lower) from those vectors derived from other zones, which underestimates the final velocity after time-averaging. However, favourable tracer conditions were rarely encountered both in experimental and field studies (Muste et al., 2004; Lewis & Rhoads, 2015; Yu et al., 2015; Dal Sasso et al., 2020), which becomes one of the major limitations of traditional LSPIV (Tauro et al., 2017).

2.2 Hydrodynamic modeling

Since fluvial urban floods are directly induced by river overtopping, the performance of fluvial urban flood models highly relies on the accuracy of modeling the river flow behaviors. The major concern of urban flood management is the flood inundation extent. Thus, most urban flood numerical models are hydraulic models, which means the sediment transport process was usually neglected.

Due to the shallowness of floodwater compared to the channel width and the dimension of urban areas, the vertical flow velocity is usually neglected. Thus, the hydraulic urban flood models are mainly one-dimensional (1D), two-dimensional (2D), and 1D-2D coupled. In the next few sections, literature focusing on the hydraulic modeling of fluvial urban floods will be reviewed.

2.2.1 1D modeling

1D models are driven by the 1D Saint-Venant equations, which are based on several assumptions: the flow is one-dimensional, the water level across the section is horizontal, the streamline curvature is small and vertical accelerations are negligible, the effects of boundary friction and turbulence can be accounted for using resistance laws analogous to those for steady flow conditions, and the average channel bed slope is small so the cosine of the angle can be replaced by unity (Cunge et al., 1980; Gilles & Moore, 2010). The continuity and momentum equations of 1D Saint-Venant equations are given as:

Continuity equation:

$$\frac{\partial A}{\partial t}+\frac{\partial AU}{\partial x}=0 \tag{2.2}$$

Momentum equation:

$$\frac{1}{g}\frac{\partial U}{\partial t}+\frac{U}{g}\frac{\partial U}{\partial x}+\frac{\partial h}{\partial x}-S_0=-S_f \tag{2.3}$$

Where A is cross-sectional flow area, t is time, U is longitudinal flow velocity, h is flow depth, g is gravitational acceleration, S_0 is bed slope, and S_f is friction slope.

The commonly-used 1D numerical software to simulate urban floods includes HEC-RAS 1D (e.g. Demir & Kisi., 2015; Dasallas et al., 2019) and MIKE 11 (e.g. Jakob et al., 2014; Lu et al., 2024). The characteristics of 1D models is that the surface terrain is described by a sequence of the river and floodplain cross sections perpendicular to flow direction and only the cross-sectional-averaged velocity and water depth are computed. 1D models are widely used in simulating fluvial urban floods because the computational cost is saved to the largest extent while maintaining the accuracy of floodwater depth, which is the major concern of urban flood management. With the support from detailed urban DEM data, 1D models are also capable of modeling the inland floodwater inundation extent (e.g. Demir & Kisi., 2015; Rahimzadeh et al., 2019)

However, most previous studies using 1D models to simulate the urban floods only carried out the steady-state simulation of flood peaks (e.g. Demir & Kisi, 2015; Dasallas et al., 2019), which could not simulate the flood propagation process properly. It also remains unknown if stand-alone simulation of flood peaks as opposed to using the full flood hydrograph would bring any difference to the inundation extent. In addition, some 1D urban flood models lacked comprehensive calibration and validation (e.g. Demir & Kisi, 2015). Moreover, the assumptions of 1D models no longer hold if simulating flood inundation at large river bends or river confluences. For overbank flow, interaction with the floodplain results in highly complex fluid movement with at least 2D properties (Gilles & Moore, 2010), which 1D models are not able to simulate. Bates & De Roo (2000) also found that subjectivity of cross-section placement would bring uncertainty to the overall accuracy of a 1D hydraulic model.

2.2.2 2D modeling

Different from 1D models, 2D models define the model domain by a continuous surface composed of meshes, and it allows flow to move in both longitudinal and lateral directions. 2D models can provide much more detail than 1D models and simulate the flow behaviors in a more efficient and cost-effective manner compared to 3D models (Tu et al., 2017). 2D models are governed by the depth-averaged Navier-Stokes equations, commonly called the 2D shallow water equations. The non-conservative form of 2D shallow water equations are given as:

Continuity Equation:

$$\frac{\partial h}{\partial t}+\frac{\partial (hu)}{\partial x}+\frac{\partial (hv)}{\partial y}=0 \tag{2.4}$$

Momentum Equations:

$$\begin{aligned}\frac{\partial (hu)}{\partial t}+\frac{\partial (hu^2)}{\partial x}+\frac{\partial (huv)}{\partial y}+gh\frac{\partial h}{\partial x}-f_{Cor}v \\ = -gh\frac{\partial Z_b}{\partial x}-gn^2u\frac{\sqrt{u^2+v^2}}{h^{1/3}}+\frac{1}{\rho_w}\left[\frac{\partial (h\tau_{xx})}{\partial x}+\frac{\partial \left(h\tau_{xy}\right)}{\partial y}\right]\end{aligned} \tag{2.5}$$

$$\begin{aligned}\frac{\partial (hv)}{\partial t}+\frac{\partial (huv)}{\partial x}+\frac{\partial (hv^2)}{\partial y}+gh\frac{\partial h}{\partial y}+f_{Cor}u \\ = -gh\frac{\partial Z_b}{\partial x}-gn^2u\frac{\sqrt{u^2+v^2}}{h^{1/3}}+\frac{1}{\rho_w}\left[\frac{\partial \left(h\tau_{yx}\right)}{\partial x}+\frac{\partial \left(h\tau_{yy}\right)}{\partial y}\right]\end{aligned} \tag{2.6}$$

where t is time; h is the local water depth; u and v are the depth-averaged velocity components in the x and y directions, respectively; g is the gravitational acceleration; f_{cor} is the Coriolis coefficient associated with the Coriolis force; Z_b is the bed surface elevation; ρ_w is water density; τ_{xx}, τ_{xy}, τ_{yx} and τ_{yy} are the depth-averaged Reynolds stresses; n is the Manning roughness. Frequently used commercial 2D flood model packages include MIKE 21, HEC-RAS 2D, Delftt-3D, LISFLOOD-FP, TELEMAC, TUFLOW, Infoworks 2D RS/CS, JFLOW, SOBEK, and DIVAST.

Compared to 1D models, 2D models are more commonly used in urban flood models (e.g. Bisht et al., 2016; Dasallas et al., 2019; Horváth et al., 2020; Farooq et al., 2019; Mustafa & Szydłowski, 2021; Marangoz & Anilan, 2022; Yu et al., 2022; Devi & Kuiry, 2024). Van Emelen et al. (2012) demonstrated that even if 3D models may improve the accuracy of the simulated results for a breach flood event, 2D models appear to be satisfactory for predicting flows in complex situations with a reasonable computational and meshing effort. However, it is reported by Bates & De Roo (2000) that flow at the transition region between river channel and floodplain has been shown to develop a 3D flow field due to intense shear layers, which 2D models are not able to simulate. Furthermore, as with many 1D studies, a significant number of 2D modeling studies lack adequate calibration or validation to substantiate their results. In many cases, the calibration or validation procedures are insufficiently detailed (e.g., Jakob et al., 2014; Bisht et al., 2016; Li et al., 2016; Farooq et al., 2019; Yang et al., 2022), making it challenging for readers to fully understand the robustness of the modeling approach. Additionally, some studies face limitations in the volume or variety of calibration data, which may be inadequate to capture the complexity of the modeled processes (e.g., Parsapour-Moghaddam et al., 2019b; Aureli et al., 2021; Nguyen et al., 2021). In other instances, calibration results fall short of acceptable standards, reflecting limitations in the model's predictive capability (e.g., Li et al., 2008; Dasallas et al., 2019). Consequently, these deficiencies collectively restrict the reliability and generalizability of the modeling outcomes.

In order to reduce the computation time and reduce numerical instability, when modeling the flooding process, the momentum equations are often simplified by neglecting the inertial terms and assuming that the flow is mainly driven by the balance between water surface slope and adjusted bottom resistance. This simplification is the so-called "diffusive wave approximation of the momentum equations" or "diffusive wave equations". After implementing the diffusive wave approximation, the momentum equations could be rewritten as (Costabile et al., 2017):

$$\frac{\partial H}{\partial x} + \frac{n^2 u\sqrt{u^2+v^2}}{h^{4/3}} = 0 \tag{2.7}$$

$$\frac{\partial H}{\partial y} + \frac{n^2 v\sqrt{u^2+v^2}}{h^{4/3}} = 0 \tag{2.8}$$

in which $H = h + Z_b$, where z is the bed level.

Beretta et al., (2018) showed that adoption of 2D diffusive wave model to represent urban buildings is a good option to model floodwater heights, even for unsteady discharge with rapid change in time. However, Costabile et al. (2017) suggested that the use of diffusive-type models is inappropriate in urban environment due to the poor predictions around the buildings, as opposed to the shallow water equations. Moreover, simplified models such as diffusive and inertial models were unable to simulate hydraulic jumps, wake zones, and back-water effects, as reported by Neal et al. (2009, 2011).

Other than the 2D diffusive wave model, Soares-Frazão et al. (2008) introduced the 2D porosity models for large-scale modeling, which define a storage (or conveyance) porosity as the fraction of the plan view (or cross section) area available to the flow and modify the fluxes and source terms in shallow-water equations accordingly. The porosity models showed much lower computational cost than the classical shallow-water equations (Soares-Frazão et al., 2008). Kim et al., (2015) examined the errors of both isotropic and anisotropic porosity models and showed that porosity model errors are smaller than structural model errors, and that porosity model errors in both depth and velocity are substantially smaller for anisotropic versus isotropic porosity models. Velickovic et al. (2017) included the drag coefficients and the amplification factor to the porosity models, accounting for the non-alignment of the main streets to the main flow direction. Results showed that the modified porosity model proved to be accurate regarding the prediction of the total depth drop through the city. However, the performance was not accurate in the case where the urban area was both rotated and anisotropic. In addition, introducing two additional variables (i.e. drag coefficients and the amplification factor) to porosity models brings additional workload in terms of model calibration in real cases, which weakens the advantage of porosity models.

Costabile et al. (2020) benchmarked the abovementioned three numerical hydrodynamic flood inundation models (shallow water model, diffusive model, and porosity model) both in experimental and field environment. Results show that for the urban areas, the shallow water model has provided the best prediction among all three models, when comparing observed and simulated water depths. Furthermore, Costabile et al. (2020) recommended that shallow water models should be the unavoidable reference tool when local estimation of flood hazard/vulnerability is one of the model concerns.

2.2.3 1D-2D coupled modeling

As it can be seen from the last two chapters, 1D models' main advantage is the low-computational cost with accurate simplification of instream flow behaviors. However, the performance of 1D models is limited in the inland urban areas with complex landscape. In contrast, 2D models perform better than 1D models in terms of the flow transition from channel to floodplain and simulating the bidirectional flow behavior in the urban areas. However, the computational cost of 2D models is higher than 1D models. Gilles & Moore (2010) mentioned that a 1D numerical model of the river channel complemented by a 2D model of the floodplain provides improvements in hydraulic modeling accuracy and computational efficiency. Thus, 1D-2D coupled modeling has become a prevailing choice in urban flood modeling (e.g. Jakob et al., 2014; Li et al., 2016; Dasallas et al., 2019; Ngo et al., 2023). Most 1D-2D coupling works used two sets of numerical software that were built under the same framework, such as:

- **HEC-RAS 1D-2D**. In the latest version of HEC-RAS, the ability of performing 1D-2D coupled unsteady-flow routing within the unsteady flow model was added, allowing work on a larger river system as well as the areas that require a higher level of hydrodynamic precision such as the urban areas. The 1D-2D coupling method is performed by setting up a lateral connection using a lateral structure. The flow over the structure is determined using the weir equation or 2D flow equations. However, the results from a comparative study done by Betsholtz & Nordlof (2017) showed that the parameters describing the 1D-2D coupling in HEC-RAS will have large impact on model stability and model results. Furthermore, it was concluded by the authors that the 1D-2D model easily becomes unstable when the water surface elevation is approximately the same as the elevation of lateral structure.

- **MIKE FLOOD (MIKE 11 + MIKE 21)**. MIKE FLOOD is a tool that integrates the MIKE HYDRO River for rivers, MIKE URBAN for collection systems and MIKE 21 for 2D surface flow into a single, dynamically coupled modeling system using several types of links between MIKE 11 and MIKE 21, including the standard link, lateral link, and structure link (DHI, 2019) (see Figure 2.7). These types of links allow model boundary conditions to be controlled by a rating curve, which is useful when modeling unsteady conditions (Gilles & Moore, 2010). MIKE FLOOD has been widely used in urban flood flooding in recent years (e.g. Li et al., 2016; Zhou et al., 2022; Chen et al., 2023a, 2023b; Pariartha et al., 2023; Deopa et al., 2024). The 2D model, MIKE 21, can also be coupled with the 1D drainage model, MIKE URBAN, to simulate the urban drainage behavior during floods. One example is Li et al. (2016), who studied a small county situated beside a river confluence. Both the full flood hydrography (i.e. unsteady flow) and the urban drainage system are considered in Li et al. (2016). Although the coupling calculation of MIKE FLOOD can obtain an accurate and comprehensive urban flood distribution information, it requires detailed data to build the model and the computational cost is relatively high.

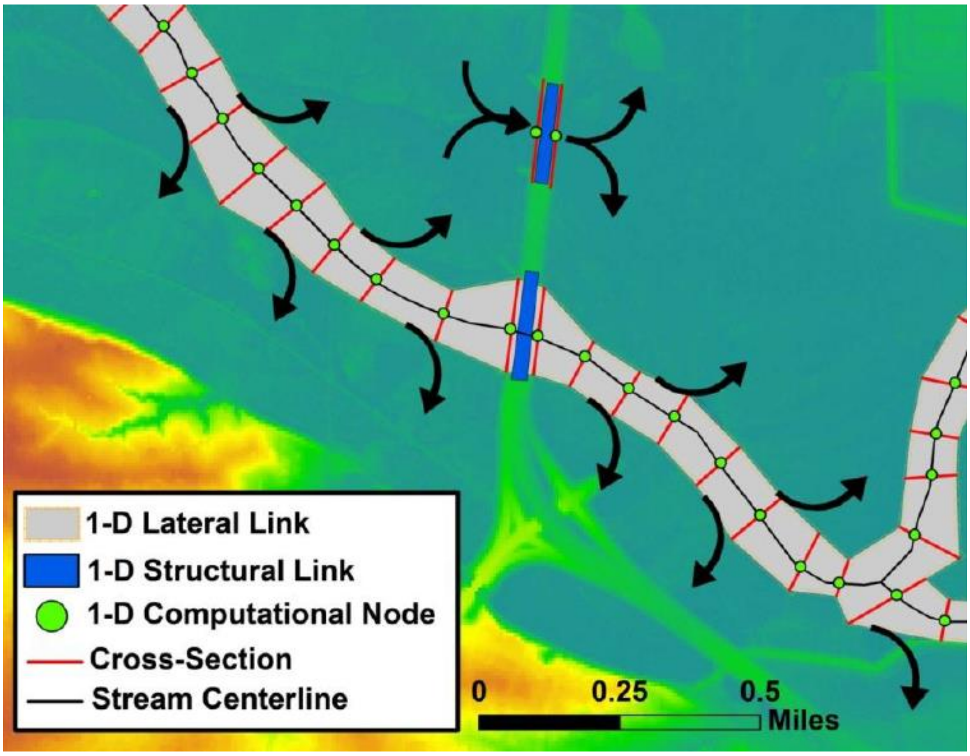

Figure 2.7. MIKE FLOOD allows coupling of 1D hydraulic models to a 2D computation mesh using standard, lateral, and structure links (Gilles & Moore, 2010).

- **LISFLOOD-FP (1D river + 2D inundation).** LISFLOOD-FP is a raster-based flood inundation model developed by the research group from the University of Bristol (Bates & De Roo, 2000). Unlike other models, LISFLOOD-FP was specifically designed to predict flood inundation and ignored or minimized the secondary processes by local-inertial approximation (Bates & De Roo, 2000; Dazzi et al., 2021). The model includes a number of numerical solvers available for calculating floodplain flow (1D on 2D grids) and channel flow (kinematic approximation of the 1D St. Venant equations) using simplified shallow water equations (Bates et al., 2013; Neal et al., 2009, 2011). Neal et al. (2011) developed a new sub-grid flood inundation model using LISFLOOD-FP for large-scale data sparse areas and showed its better performance compared with traditional 1D, 2D, and 1D/2D models. Dazzi et al. (2021) benchmarked two flood models with different governing equations: PARFLOOD, which solves the fully dynamic shallow water equations, and LISFLOOD-FP, which solves the simplified equations. The results indicate that LISFLOOD-FP offers a viable alternative to fully dynamic models, balancing accuracy with computational efficiency. In contrast, the GPU-parallelized code PARFLOOD demonstrates superior efficiency for high-resolution simulations involving millions of cells, despite its more complex numerical scheme.

2.2.4 Model choices in confluence floods

While 2D and 1D-2D coupled models are commonly suitable and widely applied for fluvial urban flood simulations, they may be less appropriate in modeling confluence floods. Open channel confluences are characterized by pronounced secondary flows and complex 3D turbulent structures (Best, 1987; Lewis & Rhoads, 2018; Yuan et al., 2021; Xu et al., 2022), leading to the use of 3D models for studying confluence hydrodynamics (e.g., Bradbrook et al., 2000; Baranya et al., 2013; Sukhodolov et al., 2017; Constantinescu et al., 2011; Dai et al., 2020; Pandey & Mohapatra, 2022; Yan et al., 2024). However, fluvial urban flood modeling often requires large model domains and fine mesh resolutions, imposing substantial computational costs. To the author's point of view, 2D models remain the preferred choice over 3D models, especially for unsteady flood simulations in confluence floods.

In the evaluation of a 2D model's performance at a tidal confluence, Xie et al. (2018) asserted that a 2D model is a suitable compromise for confluences with a significant width-to-depth ratio, provided that secondary flow corrections are incorporated in the model. Horváth et al. (2020) assessed the performance of various shallow-water schemes during an overbank confluence flood event, finding that 2D models can accurately predict both the spatial distribution and temporal fluctuations of water levels. While these studies do not specifically target urban environments, they underscore the potential of employing 2D models for simulating urban confluence floods. Nevertheless, numerical investigations of urban confluence flooding remain less common than studies focused on confluence hydrodynamics and urban flooding in straight channels. Neal et al. (2009) explored an urban confluence flood event using a 1D/2D coupled model, LISFLOOD-FP, which was validated against over 200 spatially distributed debris wrack and water level measurements throughout the city. Despite an overall average error of 0.32 m, the model exhibited greater errors of about 0.8 m in densely populated areas and near confluence regions, indicating limited model performance in urban confluences. Li et al. (2016) developed a 1D/2D coupled hydrodynamic model using MIKE FLOOD to analyze the inundation extent of confluence floods with varying recurrence intervals in Taining County, China. However, their study did not treat inland buildings as impermeable within the computational cells. Additionally, Yang et al. (2022) employed a 2D morphodynamic model to investigate urban flood inundation patterns during a flash flood event at a river confluence, revealing that the enlargement of flash floods in confluence streams is primarily driven by inflows. Nonetheless, the model developed in this study was not validated against observed flood inundation data. In conclusion, there is a pressing need for further exploration of urban confluence flooding through 2D hydrodynamic modeling, accompanied by rigorous validation to ensure the accuracy and effectiveness of the models used.

2.3 Morphodynamic modeling

2.3.1 Necessity of morphodynamic modeling

It is well recognized that rivers are usually accompanied with pronounced sediment transport processes during extreme flood events, which can result in significant morphological changes, such as in-channel deposition and bank erosion (Guan et al., 2016; Tu et al., 2017; Parsapour-Moghaddam et al., 2019b; Reisenbüchler et al., 2019; Yu et al., 2022). However, a literature review done by Vázquez-Tarrío et al. (2023) revealed that only 2% to 5% of the total flood hazard publications has explicitly considered sediment transport. The fact that morphodynamic process was rarely considered in fluvial floods modeling is probably due to (1) the relatively high computational cost, (2) increased labor efforts to collect sedimentary data and validate the model, (3) uncertainty regarding the improvement of the model's overall performance.

Tu et al. (2017) used a coupled 2D hydrodynamic and sediment transport model, National Center for Computational Hydro-science and Engineering (CCHE2D) model, to evaluate the impact of different management strategies on flood inundation and sediment dynamics during extreme flood events in California. They found that sediment transport significantly affects flood inundation depth and extent. Reisenbüchler et al. (2019) applied an integrative hydro-morphological model using TELEMAC-MASCARET to simulate the 2013 flood event in the Saalach River, Germany. They showed that including sediment transport provides a more accurate representation of flood dynamics and the influence of man-made structures on flood risk. Dysarz (2020) developed a methodology using HEC-RAS and Python scripting to assess the long-term impact of sediment transport on flood hazards in the Warta River, Poland. They demonstrated that sediment transport processes are crucial for accurate flood hazard mapping and risk assessment. Yang et al. (2022) conducted a numerical investigation on a flash urban flood event in Sanjiang Town, China, using a 2D hydrodynamic model coupled with sediment transport and bed update equations. Results show that the flash flood enlargement in bifurcation streams is largely affected by sediment deposition, which emphasized the need for integrated hydrodynamic and sediment transport models to accurately predict flood behavior. Overall, these studies underscore the necessity of incorporating sediment transport modules to achieve realistic flood behaviors and flood risk assessments in fluvial floods. Noteworthy, Vázquez-Tarrío et al. (2023) pointed out that most studies on the influence of sediment transport on flood risk have focused on mountain rivers, which are highly sensitive systems to changes in sediment supply.

Some other studies argued that morphodynamic modeling may not be necessary in certain cases. Staines & Carrivick (2015) examined the 1999 jökulhlaup in Iceland using a hydrodynamic model and a morphodynamic model to illustrate how sediment transport impacts flood conveyance. Their findings suggested that, while sediment transport affects the flood timing, it did not significantly alter the peak flood depth and velocity. Similarly, Wong et al. (2014) assessed hydraulic model sensitivity to channel erosion during extreme fluvial floods in Cockermouth, UK, using a 1D-2D coupled hydraulic model in a Monte-Carlo uncertainty framework. Their results indicated that short-term morphodynamic changes have a minor impact on flood inundation. Ahilan et al. (2016) investigated the sediment dynamics on a restored urban floodplain, employing a 2D hydro-morphodynamic model to simulate flow and sediment deposition. They found that, while the floodplain influences sediment retention and flow attenuation, sediment transport has minimal impact on flood resilience in long-term scenarios. These studies suggest that including sediment transport modules in fluvial urban flood models might not be necessary when the short-term or local morphological changes are minor relative to the overall inundation scale or other model uncertainties, which emphasizes the importance of context-specific model simplifications.

Thus, it remains unclear how flood-induced morphological changes impact the extent of urban inundation. There are no quantitative standards to guide model users in choosing the appropriate numerical model (Vázquez-Tarrío et al., 2023). To the author's point of view, the choice of using a hydrodynamic model or a morphodynamic model should be context-dependent, with careful consideration based on the following factors:

- Flood intensity. For extreme flood events, morphodynamic processes such as river bed deposition and channel planform adjustments may substantially influence flow patterns and flood routing. In such cases, a morphodynamic model would likely provide more realistic insights.

- The morphodynamic evolution records. If the river channel experienced significant morphological changes in previous flood events, incorporating morphodynamics can be valuable in accurately capturing potential adjustments in channel form and flow pathways.

- The availability of field data. Morphodynamic models usually require detailed sedimentary data such as sediment gradations, bed stratigraphy, bedload transport rate, etc., which may not always be available. In data-limited settings, a hydrodynamic model might be preferable, as it can offer a practical balance between model accuracy and data requirements.

- The computational costs. Morphodynamic models are typically more resource-intensive due to their complexity. If computational efficiency is a priority or if only flow predictions are needed without considering bed changes, a hydrodynamic model may be more suitable.

2.3.2 Sediment transport coupling

There are two modeling approaches in morphodynamic modeling of fluvial floods: fully-coupled (or strong-coupled) hydro-morphodynamic (FCHM) modeling and loosely-coupled hydro-morphodynamic (LCHM) modeling. In each time step, hydrodynamics, sediment transport and bed surface updating are computed simultaneously in FCHM models (Correia et al., 1992) while separately (i.e. one after another) in LSHM models (Park & Jain, 1986, 1987).

FCHM models has become well developed and widely used in different situations in recent few years. The interactions between the flow, sediment and bed evolution are strongly dynamic in large flood events. Thus, FCHM is apparently a better choice in terms of accuracy and reliability compared to LCHM models when simulating a flood event. However, a fully coupled fluid/solid interaction algorithm needs to converge to a stable solution at every physical time step in FCHM models, which significantly increases the computational cost compared to LCHM models (Khosronejad et al., 2011). The computational cost of FCHM will further increase as the model scale, simulation time, and flow unsteadiness increases. That is probably why most FCHM models were only used in small-scale domains (e.g. Simpson & Castelltort, 2006; Li & Duffy, 2011; Guan et al., 2014) or relatively large-scale domains but in very short time scales (e.g. Cao et al., 2004; Li & Duffy, 2011; Guan et al., 2016; Sreekumar et al., 2023) or under steady-state flow conditions (e.g. Hu et al., 2020).

LCHM models might appear unsuitable for morphodynamic modeling in extreme flood events. Nevertheless, Cao et al. (2011) evaluated LCHM models across multiple time scales of fluvial processes under strong unsteady flow conditions with bedload transport, revealing that bedload transport rapidly adapts with local flow capacity as sediment exchange with the bed supersedes the advection of mean flow. Cao et al. (2011) further concluded that, in fluvial processes dominated by bedload transport, the feedback from bed deformation is negligible to bedload transport, supporting LCHM modeling as an appropriate approach in flood modeling. More recently, Mahdizadeh & Sharifi (2020) reported that, across all flow regimes, the performance of LCHM models was comparable to FCHM models when the Courant-Friedrichs-Lewy (CFL) number in LCHM models was kept below 0.3. These findings provide a theoretical basis for using LCHM models in bedload-dominated fluvial flood scenarios.

In addition, there are many morphodynamic modeling studies that used LCHM models in extreme flood situations and achieved good results. For example, in the work done by Thapa et al. (2023), the modeled post-flood grain size distribution (GSD) coincides with the measured data well using CAESAR-Lisflood. Lai et al. (2024) used the TELEMAC-MASCARET-Sisyphe framework to develop a sedimentation hazard map of urban areas subject to hyper-concentrated flash flood. The bed surface change calculated by the model was in agreement with the survey data. Recently, a lot of studies have used one of the LCHM models, Delft3D, to model morphodynamic changes during strong unsteady flow conditions and successfully validated their model performance against measured velocities, sediment transport rate and/or post-event bathymetry data (e.g. Staines & Carrivick, 2015; Williams et al., 2016; Yuill et al., 2016; Lotsari et al., 2018; Yu et al., 2022; Wang et al., 2022; Wu et al., 2023; Siemes et al., 2024; Wang et al., 2024b), showing that Delft3D can be potential choice in modeling fluvial urban floods with morphodynamic processes.

2.3.3 Flood morphodynamics

While flood-induced morphological changes have been extensively documented across numerous studies (e.g., Wintenberger et al., 2015; Wu et al., 2016; Brooke et al., 2022; Wang et al., 2022), the causal mechanisms remain partially unclear. Baynes et al. (2023) observed substantial variation in sediment production and mobilization across three catchments under the same hydrological event. Similarly, Wang et al. (2018) noted that two in-channel bars underwent distinct erosion and deposition processes during a flood, despite comparable flow and sediment conditions during the flood event. Ramirez &

Allison (2013) likewise reported that the size and slope of in-channel sand bars did not show consistent correlation with flood discharge. Conversely, Eaton & Lapointe (2001) found that channel morphology remained qualitatively similar despite significant differences in transport intensity between two flood events. Collectively, these findings highlight the complex, multi-parametric, and non-linear relationship between flood magnitude and resultant morphological changes. Thus, spatially distributed and temporally continuous flow and/or sediment transport data are crucial for understanding morphodynamic processes during floods.

Williams et al. (2015) successfully linked periodic measurements of spatially distributed bedload transport with observed morphological changes in a gravel-bed river across a series of flood events; however, this study underscored the extensive efforts required to investigate flood-induced morphological changes in a river reach through field survey. Alternatively, numerical modeling can efficiently and cost-effectively provide spatially distributed hydrodynamic and sedimentary data throughout a flood event. For instance, Li et al. (2008) developed a morphodynamic model to generate a spatially distributed sediment budget and identify aggradation and degradation zones in a wandering gravel-bed river. However, substantial discrepancies between modeled and observed bedload transport rates limited the reliability of the model's predictions. Hauer & Habersack (2009) applied a hydrodynamic model to examine the morphodynamics of a 1000-year flood, observing that rapid lateral constriction and expansion in valley geometry caused scouring and aggradation in inundated areas. However, sediment transport processes remained ambiguous in a hydrodynamic model. Staines & Carrivick (2015) simulated a glacial lake outburst flood using a morphodynamic model in Delft3D and found widespread bed activation during the rising limb and greater organization with typical bedform development during the recession. Despite these insights, model validation against measured data was unsatisfactory, and certain local-scale morphological changes remained unexplained. Also using Delft3D, Lotsari et al. (2018) modeled morphodynamic processes during bankfull floods in a gravel-bed ephemeral river. Contrary to Staines & Carrivick (2015), Lotsari et al. (2018) found that the timing of major depositional or erosional events varied with flood magnitude. Hamidifar et al. (2024) highlighted that the impact of morphodynamic variations and sediment transport on flooding is contingent upon specific local morphological conditions. Thus, the interactions between flood hydrodynamics and flood morphodynamic processes remain unclear and require further investigations through numerical models.

2.3.4 Management of in-channel bars

In river morphology, bars are elevated sandy or gravelly bedforms within river channels that typically remain exposed at normal water levels but become submerged during high water events, such as floods. Bars represent one of the most prevalent geophysical features in fluvial systems. Based on formation regions, bars are classified as mid-channel bars, bank-attached bars, and river mouth bars (Church, 1992), and by sediment size, they are further categorized as gravel or sand bars. Fundamentally, bars develop where sediment supply exceeds the sediment transport capacity of the flow.

In gravel-bed rivers, bars tend to form and grow during floods due to the substantial bedload carried by floodwaters (Parsapour-Moghaddam et al., 2019b; Wintenberger et al., 2015). After the flood events, these flood-induced gravel bars become stabilized as flow velocity decreases. Subsequent riparian vegetation colonization on the exposed bar surface further stabilizes the in-channel bars (Rood et al., 2019). Gravel bar formation is a critical step in the natural river migration process and provides crucial habitat for benthic invertebrates, waterbirds, and fish species (Zeng et al., 2015; Parsapour-Moghaddam et al., 2019a). However, in managed rivers, bars can obstruct channels, create navigation challenges, and pose flood risks to nearby communities (Petit et al., 1996). Flood risks may increase when riparian vegetation on the bar surface adds resistance to the flow, leading to sediment accumulation around the bar during subsequent floods (Church et al., 2001; Rood et al., 2019), creating a "vicious cycle" of bar and vegetation growth.

Since the late 19th century, instream gravel extraction and bar removal have been widely implemented as a cost-effective means to provide construction aggregate, mitigate flood risks, and maintain navigability in channels (Kondolf, 1997; Sear & Archer, 1998; Church et al., 2001; Wishart et al., 2008). However, gravel removal can disrupt the active sediment balance, causing the flow to become sediment-starved (Kondolf, 1997), potentially resulting in channel incision, bed coarsening, undermining of structures, and loss of aquatic habitats (Kori & Mathada, 2012). A field study by Wishart et al. (2008) suggested that sediment removal from vegetated bars (indicating long-term sediment storage) might reduce the risk of creating sediment deficits and could be a safer method to mitigate flood risks, though this approach remains unproven.

From the author's point of view, bar realignment may serve as an alternative approach to bar management in place of bar removal. Bar realignment involves adjusting the spatial layout of instream bars within the channel without significantly altering their overall volume. Theoretically, bar realignment offers several potential advantages over bar removal:

- Bar realignment preserves the total volume of instream bars, thereby maintaining the sediment budget at the reach scale. Accordingly, it is reasonable to speculate that appropriate bar realignment poses a lower risk of downstream incision than bar removal.
- By repositioning instream bars, local flow fields and sediment transport patterns are altered, potentially creating conditions conducive to inhibiting future bar growth and promoting channel stabilization. These changes may also contribute to reducing future flood levels.
- Proper bar realignment could enhance the diversity of river flow and channel bed conditions, which in turn may foster new habitats and promote recreational uses of the river, such as swimming, surfing, and kayaking.

2.4 Summary of research gaps

This section summarizes the major research gaps in fluvial urban floods based on the literature review. They are listed as follows:

- Numerical modeling of fluvial urban floods lacks comprehensive and rigorous model calibration and validation, both in hydrodynamic and morphodynamic modeling. For hydrodynamic models, in order to test the model ability of reproducing the actual flood dynamics, model validation against flow velocity collected from different flow stages (i.e. low flow, high flow, and overbank floods) is necessary, yet was rarely included in previous studies. In addition, inland floodwater velocity data was rarely collected by researchers and thus has not been used as one of the validation datasets in fluvial flood modeling. As for morphodynamic models, model validation against measured post-flood bathymetry is an important step to show the model's performance, which was also not carried out in many relevant studies.
- Numerical modeling usually requires a reliable data source of flow discharge and water surface elevation as the model boundary conditions. A flow rating curve (or "Q-H" relationship) can be used to derive water surface elevation data from discharge data of a design flood event. Flow rating curves usually follow the form of a "power law" based on the uniform flow assumption and Manning's flow resistance equation. In river confluences, researchers found that the traditional

power law is no longer valid for upstream portions due to the backwater effect. However, due to the presence of the flow recovery zone in river confluences, it remains unknown if the flow rating curve will follow the traditional power law at the confluence outlet. Thus, comprehensive field measurements need to be carried out to fill this research gap.

- Open channel confluences are important nodes in river flow networks, but are susceptible to fluvial floods due to flow convergence. Previous studies have used numerical models to simulate flood inundation at river confluences. However, the inundation dynamics at river confluences was rarely investigated. One of the key characteristics of confluence flow is the confluence hydrodynamic zones, whose features may vary with discharge ratio, confluence junction angle, channel width, etc. Previous studies have reported the water surface elevation variation as a function of discharge ratio at river confluences. However, those studies were mostly carried out in experimental models. It remains unknown if the discharge ratio will have an impact on the flood inundation extent and/or inundation processes at river confluences.

- Conducting field survey during floods poses significant potential risks to both personnel and equipment. In this context, Large Scale Particle Image Velocimetry (LSPIV) can be a potential solution to measure floodwater velocity remotely. However, traditional LSPIV requires a dense surface tracer condition to correctly identify the surface velocity, which has rarely occurred both in experimental and field studies. Alternative approaches such as Ensemble Correlation (EC), Large-Scale Particle Tracking Velocimetry (LSPTV), and Seeding Density Index (SDI) have the potential to derive flow velocities under low tracer density conditions. However, those approaches have their own limitations such as inability to process turbulent flow and high computational cost. Thus, a new LSPIV algorithm needs to be developed to overcome the abovementioned limitations.

- Due to the lack of continuous-in-time-and-space hydrodynamic and sedimentary data, detailed analyses of local-scale morphodynamic processes such as bar formation and bank erosion during fluvial floods are insufficient. Morphodynamic modeling can provide such a dataset during a flood event, as long as it is carefully calibrated and validated. However, such an advantage has not been fully exploited in previous studies. In addition, few studies have Modeled the flood morphodynamics during large floods (i.e. recurrence interval > 50 years). It also remains unknown if local-scale morphological processes (i.e. erosion and deposition) develop along with the flood hydrograph (i.e. rise and fall) or become dominant at certain flood stages.

- Instream bar removal has been widely implemented as a cost-effective method to mitigate flood risks since the late 19th century. However, the potential risk of sediment deficits and channel instability due to bar removal has limits its application in recent years. Some researchers found that sediment removal from vegetated bars (indicating long-term sediment storage) might reduce the risk of creating sediment deficits and could be a safer method to mitigate flood risks, though this remains unproven. In addition, the new concept of bar realignment has not been explored in the literature and remains an unproven practice. Thus, research gaps and opportunities persist in evaluating instream gravel management practices in relation to flood mitigation, river morphology, aquatic and riparian habitats, and recreational use.

Chapter 3. Thesis outlines, objectives, and novelties

3.1 Project 1

3.1.1 Title

Gravel-bed river morphodynamic processes throughout an 80-year flood event from numerical modeling: implications for flood regulation strategies

3.1.2 Publication status

Submitted to *Journal of Hydrology,* under review.

3.1.3 Objective

This project aims to understand the morphodynamic process of a gravel-bed river during an extreme flood event using modeled data including the temporal and spatial distributions of flow velocity, bedload transport rate, surface sediment sizes, and cumulative morphological changes. We also aim to develop flood regulation strategies accordingly from the perspective of flood-induced morphological changes.

3.1.4 Novelty

The major novelty of this study is that we are the first study to use continuous-in-space-and-time flow velocity, sediment transport, surface sorting, and bed surface evolution data produced by a calibrated and validated morphodynamic model to examine the local-scale river morphodynamic processes throughout a large flood event (i.e. return period > 50 years). With the help of these abundant and reliable model-produced data, we found that the timings of morphological changes during the flood differ for different morphodynamic units (MUs) but are similar for similar MUs despite planform differences between sub-reaches. We also found that bedload transport rates are more sensitive to flow velocities than bed sediment sizes in the Bow River case, due to the greater spatial and temporal variance of velocities during the flood. In regard to flood regulation strategies, it is demonstrated that, with the same flood peak and duration, a regulated flood event with a brief rising period, rather than a long-lasting rising period, might result in less bank erosion and bar growth.

3.2 Project 2

3.2.1 Title

Impact evaluation of instream bar management using morphodynamic modeling

3.2.2 Publication status

Published in the *Journal of Environmental Management.*

Citation: Yu, Q., Rennie, C. D., Slaney, J. M., & Parsapour-Moghaddam, P. (2022). Impact evaluation of instream bar management using morphodynamic modeling. *Journal of Environmental Management*, 318, 115564. https://doi.org/10.1016/j.jenvman.2022.115564

3.2.3 Objective

This project aims to evaluate the impacts of a conventional river management plan of bar removal and a novel plan of bar realignment using a morphodynamic model. Impacts were evaluated in terms of river planform evolution, flood mitigation, aquatic habitat protection and river recreation realization.

3.2.4 Novelty

We propose a new in-channel bar management strategy, “bar realignment”, and tested its performance in a gravel-bed river. We show that appropriate bar realignment can protect aquatic habitat and provide river recreation opportunities while bar removal performs better in terms of lowering the future flood peak level. The findings indicate that manipulation on instream bars has little morphological impact to the downstream reach. We also found that creating a less obstructed channel is the fundamental strategy in flood mitigation.

3.3 Project 3

3.3.1 Title

TiFA: an efficient and robust LSPIV algorithm based on joint distribution analysis

3.3.2 Publication status

Submitted to *Water Resources Research*, under review.

3.3.3 Objective

This project aims to develop a new Large-Scale Particle Image Velocimetry (LSPIV) algorithm to overcome the limitations of the traditional LSPIV algorithm, which is unable to accurately identify flow velocities under low tracer density conditions

3.3.4 Novelty

A new LSPIV algorithm, Time Frequency Analysis (TiFA), is developed and tested in a physical model and two field cases. TiFA showed the highest overall accuracy and lowest computation cost in data analysis, especially under low tracer density conditions, compared to other image velocimetry algorithms including Traditional LSPIV, Ensemble Correlation (EC), Large-Scale Particle Tracking Velocimetry (LSPTV), and Seeding Density Index (SDI).

3.4 Project 4

3.4.1 Title

Inundation dynamics of an extreme urban confluence flood: insights from in-situ measurements, remote sensing, and hydrodynamic modeling

3.4.2 Publication status

Submitted to *Journal of Hydrology*, under review.

3.4.3 Objective

This project aims to understand the inundation dynamics of an extreme urban confluence flood using a hydrodynamic model, specifically, to answer the question "is flood inundation at river confluences a function of discharge ratio, flow unsteadiness, or the total discharge?". We also aim to explore the form of the flow rating curve at the confluence outlet using multi-source field data.

3.4.4 Novelty

This is the first study to use multi-source field data to develop the flow rating curve at the confluence outlet. The developed rating curve shows that the total discharge and water level follow a power-law function, with minimal influence from confluence discharge ratio. We found that the developed rating curve showed a distinct segmentation behavior, with flow depth increasing more quickly in the overbank stage than the in-channel stage, which is probably due to the combined effects of change in roughness and friction slope. This rating curve was used as the downstream boundary condition for the numerical model, which was calibrated using measured in-channel flow velocities and validated with observed flood extent. Additionally, for the first time the model was validated using measured overbank urban flood velocities. Numerical model results show that confluence flood inundation extent is mainly a function of total flow discharge, with minimal impact from discharge ratio or flow unsteadiness.

Chapter 4. Gravel-bed river morphodynamic processes throughout an 80-year flood event from numerical modeling: implications for flood regulation strategies

4.1 Abstract

Due in part to the lack of continuous-in-space-and-time flow and sediment transport data, the river morphodynamic processes during large floods are not fully understood. This study developed a two-dimensional (2-D) morphodynamic model to study the morphodynamic process of a gravel-bed river during a flood event with a return period of 80 years in Calgary, Canada. The model was calibrated against velocimetry data and validated against post-flood bathymetry data. Temporal and spatial distributions of flow velocity, bedload transport rate, surface sediment sizes, and cumulative morphological changes throughout the flood are presented and analyzed. Results show that the timings of morphological changes during the flood differ for different morphodynamic units (MUs) but are similar for similar MUs despite planform differences between sub-reaches. It is demonstrated that, with the same flood peak and duration, a regulated flood event with a brief rising period, rather than a long-lasting rising period, might result in less bank erosion and bar growth. We also found that bedload transport rates are more sensitive to flow velocities than bed sediment sizes in the Bow River case, due to the greater spatial and temporal variance of velocities during the flood.

4.2 Introduction

4.2.1 Background

The histories of alluvial rivers are mostly written by floods. Although flood-induced morphological changes have been comprehensively documented in many studies (e.g. Bartholdy & Billi, 2002; Brooke et al., 2022; Wang et al., 2022; Wintenberger et al., 2015; Wu et al., 2016), cause and effect are not all clear. Baynes et al. (2023) found that the sediment production and mobilization in three catchments differed significantly under the same hydrological event, mainly due to the difference in channel steepness. Wang et al. (2018) discovered that two in-channel bars experienced different erosion and deposition processes during a flood event, even though the flow and sediment conditions were similar. Similarly, Ramirez & Allison (2013) found that the size and steepness of in-channel sand bars did not present a consistent relationship with the flood discharge. In contrast, Eaton & Lapointe (2001) found that despite the disparity in the transport intensity of the two flood events, the channel morphology remained qualitatively similar. These findings demonstrate the complex, multi-parametric, and non-linear relationship between flood magnitude and flood-induced morphological changes. Thus, spatially-distributed and temporally-continuous flow and/or sediment transport data are necessary to understand the morphodynamic process during flood events. Williams et al. (2015) collected periodic measurements of spatially distributed bedload transport in a gravel-bed river during a series of flood events and linked these with observed morphological changes. Although successful, this study demonstrated the considerable effort required to understand the flood-induced morphological changes in a river reach through field work.

Numerical modeling, in contrast, is capable of providing spatially distributed hydrodynamic and sedimentary datasets throughout a flood event in an efficient and cost-effective way. For example, Li et al. (2008) developed a morphodynamic model to produce a distributed sediment budget and to identify the zones of aggradation and degradation in a wandering gravel-bed river. However, relatively large discrepancies between the modeled and observed bedload transport rate reduced reliability of the model predictions. Hauer & Habersack (2009) used a hydrodynamic model to study the morphodynamics of a 1000-year flood and found that lateral constriction and expansion of the valley geometry over short distances led to scouring and aggradation within the inundated areas during the event. However, the detailed sediment transport processes were unclear. Staines & Carrivick (2015) reconstructed a glacier lake outburst flood event using a morphodynamic model in Delft3D. Results showed widespread activation of the bed surface during the rising limb whereas more organization and typical bed form development occurred during the falling limb. However, the model validation against the measured data was unsatisfactory and some local-scale morphological changes also remained unexplained. Lotsari et al. (2018) simulated the morphodynamic process during bankfull floods in a gravel-bed ephemeral river using Delft3D. Different from the findings in Staines & Carrivick (2015), results in Lotsari et al. (2018) showed that the timing of major deposition or erosion varied with the magnitude of flood events. Hamidifar et al. (2024) discovered that the effects of morphodynamic variations and sediment transport on flooding may vary based on the specific local morphological conditions. Hamidifar et al., (2024) also pointed out that the interaction between flood morphodynamic processes and flood hydrodynamics remains unclear and a number of relevant topics are still in debate.

There are two modeling approaches in flood morphodynamic Modeling: fully-coupled hydro-morphodynamic (FCHM) modeling and loosely-coupled hydro-morphodynamic (LCHM) modeling. Hydrodynamics, sediment transport and bed surface updating are computed simultaneously in FCHM models (Correia et al., 1992) while separately (i.e. one after another) in LSHM models (Park & Jain, 1986, 1987) in a single time step. Intuitively, it is easy to draw a conclusion that LCHM models are not suitable for morphodynamic modeling in extreme flood events. However, Cao et al. (2011) evaluated the performance of LCHM models under multiple time scales of fluvial processes with bed load transport under strong unsteady flow conditions and found that bedload transport can quickly adjust to the local flow capacity, as sediment exchange with the bed dominates over the advection of bed load sediment by the mean flow. Cao et al. (2011) further concluded that in fluvial processes involving bedload transport, the feedback effects of bed deformation are minimal, making LCHM modeling a suitable approach in this context. Recently, Mahdizadeh and Sharifi (2020) reported that the performance of LCHM models in all flow regimes was as good as the peroformance of FCHM models, when using a Courant-Friedrichs-Lewy (CFL) number smaller than 0.3 in LCHM models. Those findings provide theoretical foundations for using LCHM models in bedload-dominated fluvial floods. In addition, fluid-solid interaction needs to converge at every physical time step in FCHM models, which increases the computational cost compared to LCHM models (Khosronejad et al., 2011). The computational cost of FCHM models will further increase as the model scale, spatial resolution, simulation time, and flow unsteadiness increases, thus FCHM models have rarely been used in modeling long-duration extreme flood events in large-scale rivers.

In order to balance the computational cost and accuracy, in this paper, one of the widely-used LCHM models, Delft3D, was used to simulate a 100-year flood event for 120 hours in a large river.

4.2.2 Research gaps

In summary, there are still some challenges and research gaps in studying the mechanisms of morphodynamic processes during floods:

(1) **Local-scale morphodynamic processes during floods are poorly understood**. Detailed analysis of local-scale morphodynamic processes such as bar formation and bank erosion during floods are insufficient due to the lack of continuous-in-time-and-space hydrodynamic and sedimentary data. It remains unknown if local-scale morphological processes develop along with the flood hydrograph or become dominant during certain stages of the flood.

(2) **Morphodynamic modeling has not been fully exploited**. Morphodynamic modeling can provide continuous-in-space-and-time maps of flow velocity, bedload transport rate, surface sediment sizes, and cumulative morphological changes throughout a flood event. However, such an advantage was not fully exploited in previous studies (see Table 4.1). In addition, Table 4.1 showed that relatively few previous studies have modeled morphodynamics during large floods (i.e. recurrence interval > 50 years).

(3) **Existing morphodynamic models are not well developed.** A number of existing morphodynamic models are not validated against the observed post-flood DEM and/or not statistically evaluated (Table 4.1), which makes the modeled results less reliable and model interpretation less trustworthy. In addition, model setups in terms of bed stratigraphy are often unrealistic (e.g. He et al., 2020; Khosronejad et al., 2016).

4.2.3 Objectives & novelty

The objectives of this study are to (1) develop a morphodynamic model that can reproduce the river morphological changes caused by an 80-year flood in the Bow River in Calgary, Canada, and (2) use the modeled flow velocity, sediment transport, surface sorting and cumulative deposition or erosion to analyze the flood morphodynamics.

Table 4.1. Summary of previous morphodynamic modeling studies on riverine flood events.

Study	Flood recurrence interval	Field data used for validation	Evaluation metric(s) for validation	Temporal morphodynamic processes analyzed			
				Flow field	Sediment transport	Surface sorting	$CDE*$
Bartholdy & Billi (2002)	1.5 & 20	Not mentioned	Not mentioned	Yes	No	No	No
Li et al.(2008)	2 - 3	S_b*	Not mentioned	Yes	Yes	No	No
Lotsari et al. (2014)	1 - 2	WSE, U, ΔV, & $DEM*$	MAE & R^2 *	Yes	No	No	Yes
Worni et al. (2012, 2014)	$GLOF$	DEM	MAE	Yes	No	No	No
Staines & Carrivick (2015)	$GLOF$	Not mentioned	Not mentioned	Yes	Yes	No	Yes
Guan et al. (2015a, 2015b, 2016)	$GLOF$	DEM	MAE	No	No	No	Yes
Iwasaki et al. (2016)	12	DEM	Not mentioned	Yes	No	No	×
Khosronejad et al. (2016)	100	U	RE	Yes	No	No	Yes
Williams et al. (2016)	Not mentioned	$\Delta V*$, DEM	MAE	No	No	No	No
Tu et al. (2017)	10,50, 100,200	WSE	Not mentioned	No	No	No	Yes
Lotsari et al. (2018)	1 - 3	WSE, ΔV, DEM	RE	No	No	No	Yes
He et al. (2020)	1 & 100	WSE, U, S_s*	$RMSE$, NSE, & $R*$	No	Yes	No	No
Tu et al. (2020)	1,10, 50,200	Q	NSE	No	No	No	Yes
Hu et al. (2021)	2	DEM	Not mentioned	Yes	No	No	Yes
Li et al. (2021)	10000	Not mentioned	Not mentioned	No	No	No	Yes
Scamardo et al. (2022)	8	WSE	Not mentioned	No	Yes	No	Yes
Wang et al. (2022)	Not mentioned	WSE, U	$RMSE$, NSE, & R	No	Yes	No	Yes
Yassine et al. (2023)	100	WSE, DEM	$RMSE$, BSS	No	No	No	Yes
Han et al. (2023)	1 - 3	Braiding index	Not mentioned	Yes	No	No	Yes
Wang et al. (2024b)	5,10,20, 50,100	Not mentioned	Not mentioned	Yes	Yes	No	×
This study	80	U, DEM	R^2, NSE, BSS & MAE	Yes	Yes	Yes	Yes

* CDE = Cumulative deposition and/or erosion; $GLOF$ = Glacier lake outburst flood; DEM = Digital elevation model; WSE = Water surface elevation; U = Flow velocity; ΔV = Volumetric changes; Q = discharge; S_b = Bedload transport rate; S_s = Suspended sediment transport rate; BSS =Brier skill score; MAE = Mean absolute error; $RMSE$ = Root mean square error; RE = Relative error; NSE = Nash–Sutcliffe model efficiency coefficient; R = Correlation coefficient; R^2 = Coefficient of determination

The major novelty of this study is that we are the first to use continuous-in-space-and-time flow velocity, sediment transport, surface sorting, and bed surface evolution data produced by a calibrated and validated morphodynamic model to examine the local-scale river morphodynamic processes throughout a large flood event (i.e. return period > 50 years). With the help of these abundant and reliable model-produced data, the morphodynamic processes throughout the flood event are reconstructed from which the drivers of local-scale morphological changes are identified. The timing during the flood of morphological changes for various morphodynamic units is elucidated. Sensitivity analysis on bedload transport is also performed, from which greater understanding of flood morphodynamics is obtained. Finally, we propose a new flood regulation strategy based on the findings to help mitigate bank erosion and bar growth during floods.

4.3 Study area and field data

The Bow River is a meandering/wandering gravel-bed river located in southern Alberta, Canada (Figure 4.1a). Streamflow rate in the Bow River varies considerably from year to year, which has made the Bow River subject to frequent periods of drought as well as serious flooding (Rood et al., 2019). To regulate the river flow, several reservoirs were constructed upstream of the City of Calgary in the 20th century. The reservoirs also cut off the sediment supply and resulted in some surface armoring (Klohn Crippen Berger, 2016). In late June 2013, with continuous heavy rainfall and rapid snow-melting in the Rocky Mountains, the Bow River witnessed the highest flow of the century-long records (Pomeroy et al., 2016). The return period of the 2013 flood has been estimated to be 80 years, although this estimation includes pre-gauge flow estimates based on historical flood marks (Klohn Crippen Berger, 2016). The 2013 flood produced up to 100 m of lateral bank erosion distances in several locations of the Bow river as well as creation or expansion of extensive, barren, gravel bars and islands (Rood et al., 2019; Slaney et al., 2019). By the year of 2022, those gravel bars have been mostly vegetated.

The model domain of this study is a river reach that passes through downtown Calgary (Figure 4.1b). The total length of this reach is about 3.3 km and the average channel width is about 85 m. During the 2013 flood, this reach witnessed distinct bar formation as well as bank erosion (see Figure 4.2), which provide the basis of studying the morphodynamic processes during the flood. In addition, abundant field data are available (Table 4.2) in this reach, which provide essential information to develop a numerical model. In order to be concise and clear, sites frequently mentioned in this paper are named using abbreviations as follows (see Figure 4.1b):

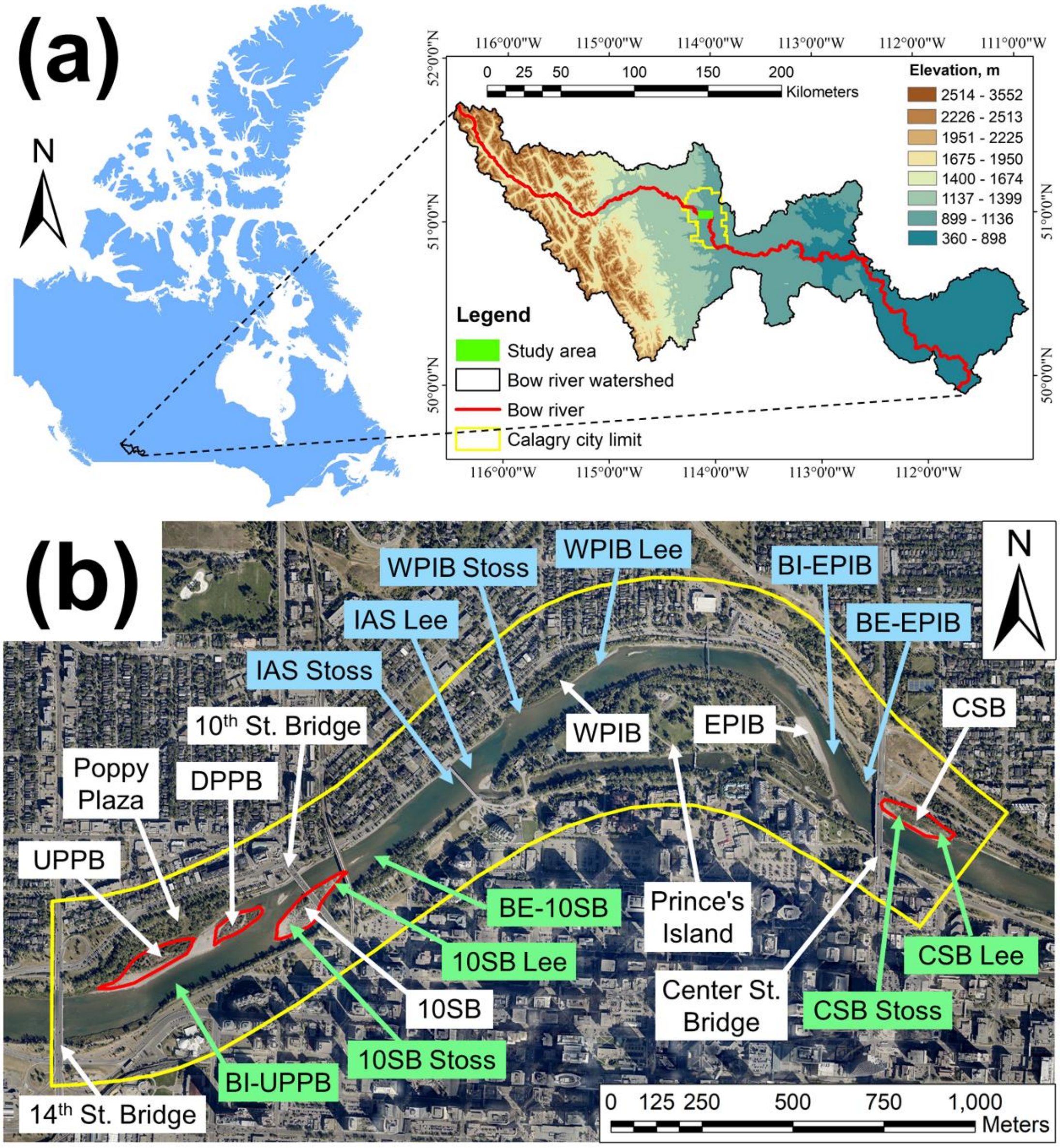

Figure 4.1. (a) The location and topography of the Bow River watershed (courtesy of Dr. Atakan Erdem, University of Calgary). (b) The model domain (the yellow polygon) and site names superimposed on the post-flood aerial photograph (imagery collected on September 11, 2020. © Esri, Maxar, Earthstar geographic, and the GIS User Community). Flow goes from left to right.

- In-channel bars are named as Upstream Poppy Plaza Bar (UPPB), Downstream Poppy Plaza Bar (DPPB), 10th St. Bar (10SB), West Prince Island Bar (WPIB), East Prince Island Bar (EPIB), and Center St. Bar (CSB).

- Names of sites where detailed morphodynamic processes will be numerically investigated (see Figure 4.7, 4.8, & 4.9) are written in green boxes in Figure 4.1b.

Those sites are: Bed Incision near UPPB (BI-UPPB), Stoss side of 10SB (10SB Stoss), Lee side of 10SB (10SB Lee), Bank Erosion near 10SB (BE-10SB), CSB Stoss, and CSB Lee. Together those sites will be referred to as “Set No.1”.

- Names of sites where only the timings of morphological changes will be numerically investigated (see Figure 4.10) are written in blue boxes in Figure 4.1b. Those sites are: Stoss side of Ice Anchor Site (IAS Stoss), IAS Lee, WPIB Stoss, WPIB Lee, Bed Incision near EPIB (BI-EPIB), Bank Erosion near EPIB (BE-EPIB). The so-called “ice anchor site” is an in-channel hole that was artificially-excavated to collect ice in winter. It was infilled during the 2013 flood (refer to Yu et al., 2022 for more information). Together those sites will be referred to as “Set No.2”.

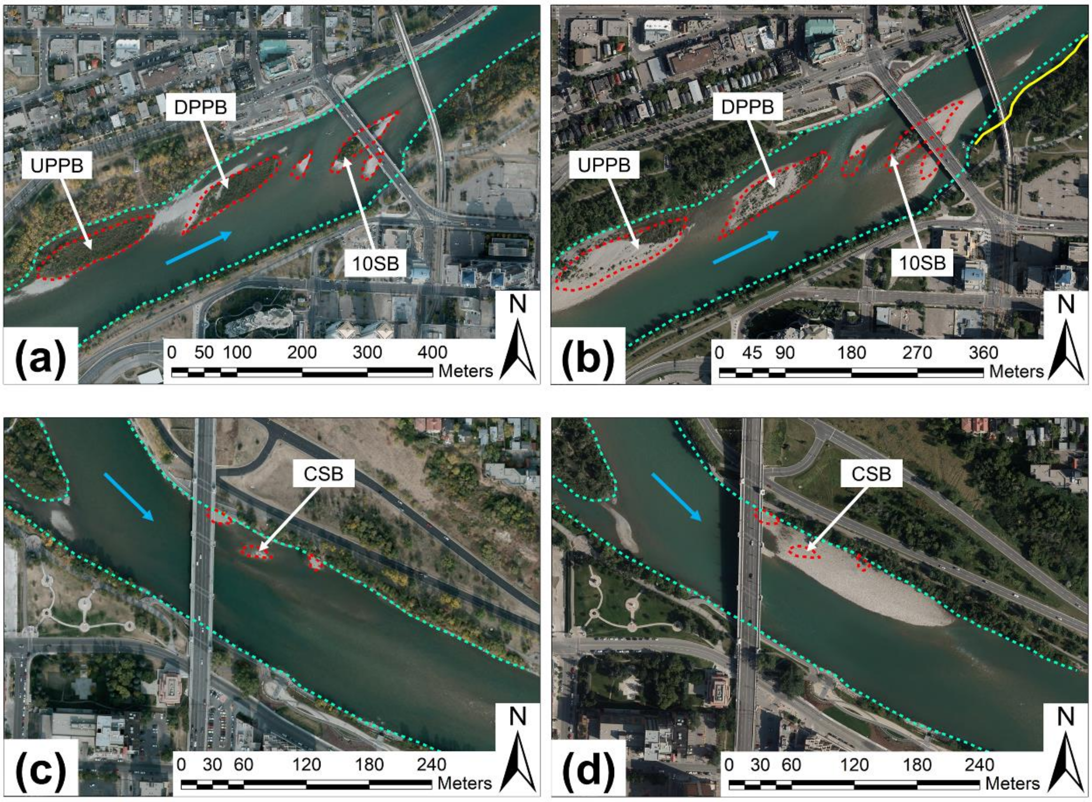

Figure 4.2. Aerial photographs of the Bow River before (September, 2012; flow discharge $\approx 70\ m^3/s$; sub-figure “a” & “c”) and after (August, 2013; flow discharge $\approx 150\ m^3/s$; sub-figure “b” & “d”) the 2013 flood near the 10SB site (sub-figure “a” & “b”) and the CSB site (sub-figure “c” & “d”). The red and cyan dotted-lines mark the in-channel bars above the water surface and river banks before the 2013 flood, respectively. The yellow solid line in (b) marks a part of the river bank after the 2013 flood, in order to show the bank erosion. The blue arrows mark the flow direction.

Table 4.2. Summary of the available field data in the model domain.

Field data	Collection time	Location	Usage in the model	Data source
Pre-flood bathymetry[#1]	2010/9/9	Whole model domain	Input	Golder Associates Ltd. (2011, 2015)
Post-flood bathymetry	2013/10/28	Whole model domain	Input; validation	Golder Associates Ltd. (2015)
Post-flood velocimetry[#2]	2013/9/9	Near UPPB, DPPB, and 10SB	Calibration	Golder Associates Ltd. (2015)
Post-flood river bed	Year 2016	Near UPPB, DPPB, and 10SB	Input	Klohn Crippen Berger (2016)
Discharge & water level	Year 2013, Daily	Hydrometric station[#4]	Input	Water Survey of Canada (2024)

[#1] In-channel and dry-land bathymetry data were collected using ADCP (Acoustic Doppler Current Profiler) (Golder Associates Ltd., 2011) and using LiDAR (Light Detection and Ranging) (Golder Associates Ltd., 2015), respectively.

[#2] Velocimetry data were collected using ADCP.

[#3] Bed sediments data include surface and sub-surface samples.

[#4] Hydrometric station is about 500 m downstream of CSB. Refer to Yu et al. (2022) for its location on map.

4.4 Methodology

Note that the model used in this study was initially developed in Yu et al. (2022) [Chapter 5 in this thesis]. Most model settings herein are directly adopted. Modifications are made to improve the model performance. Only critical model settings and modifications are illustrated in this section. Please refer to Yu et al. (2022) for other relevant information.

4.4.1 Delft3D platform

This study utilized one of the LCHM models, Delft3D-FLOW, to simulate the morphodynamic process during the flood. Delft3D-FLOW is an open-source hydro-morphodynamic 2-D/quasi-3-D modeling suite for integral water solutions. Delft3D has been used by many researchers to model the morphodynamic changes during strong unsteady flow conditions, including extreme floods. Its reliability has been tested by validation against measured flow, sediment transport rate and/or post-event bathymetry data (e.g. Staines & Carrivick, 2015; Williams et al., 2016; Yuill et al., 2016; Javernick et al., 2018; Lotsari et al., 2018; Yu et al., 2022; Wang et al., 2022; Wu et al., 2023; Siemes et al., 2024; Wang et al., 2024b). Delft3D-FLOW uses a horizontal structured grid where variables are arranged in a staggered manner. The Navier-Stokes equations are solved for incompressible fluid under the shallow water and Boussinesq assumptions using finite-difference/finite-volume methods (Deltares, 2020). The advection-diffusion (mass-balance) equation is used for suspended load transport calculation and empirical formulations are used for bedload transport calculation. The Fluid-Structure Interactions (FSI) are solved using one-way coupling. The bed surface elevation and composition are dynamically updated at each computational time step by solving the Exner (1925) equation either with or without a bed stratigraphy model (Hirano, 1971).

4.4.2 Hydrodynamic model

First, a 2-D hydrodynamic model was developed in order to calibrate the background horizontal eddy viscosity (used to model 2-D turbulence) and Manning roughness (used to model bottom shear stress) using the post-flood velocimetry data (see Table 4.1 & Figure 4.3). The post-flood bathymetry data (see Table 4.1) were used as the model input. Considering the need of modeling the in-channel bridge piers (width ≈ 6 m) at 10th St. Bridges and Center St. Bridges, the initial average grid size was set as 6.5 m. Steady-state discharge of 103 m^3/s and water surface elevation of 1041.27 m were used as the model upstream and downstream boundary conditions, respectively. Due to the model stability restriction when using an explicit scheme, the initial time step was set as 0.023 min so that the Courant-Friedrichs-Lewy (CFL) number was less than 1. The initial background horizontal eddy viscosity was set as 0.1 m^2/s. The initial Manning roughness coefficient was set as 0.030 s/[$m^{1/3}$], based on the recommended range for gravel-bed surfaces (i.e. 0.028 - 0.035 s/[$m^{1/3}$]) in Benson & Dalrymple (1967).

4.4.3 Calibration

The background horizontal eddy viscosity and Manning roughness coefficient were calibrated independently (i.e. one parameter was adjusted while keeping the other constant), followed by the model sensitivity analysis on grid size. The following statistical parameters were used to evaluate the model performance:

$$R^2 = \left[\frac{\sum_{i=1}^{N}(O_i - \bar{O})(P_i - \bar{P})}{\sqrt{\sum_{i=1}^{N}(O_i - \bar{O})^2}\sqrt{\sum_{i=1}^{N}(P_i - \bar{P})^2}} \right]^2 \tag{4.1}$$

$$NSE = 1 - \frac{\sum_{i=1}^{N}(O_i - P_i)^2}{\sum_{i=1}^{N}(O_i - \bar{O})^2} \tag{4.2}$$

$$MAE = \frac{\sum_{i=1}^{N}|O_i - P_i|}{N} \tag{4.3}$$

$$BSS = 1 - \frac{\langle (P_e - O_e)^2 \rangle}{\langle (B_e - O_e)^2 \rangle} \tag{4.4}$$

where R^2 is the coefficient of determination between the observed and predicted data, O_i and P_i, respectively; i is the sequence number of a sample point, N is the total number of sample points; $\bar{O}$ and $\bar{P}$ are the means of the observed and predicted data, respectively; NSE is the Nash–Sutcliffe model efficiency coefficient (Nash & Sutcliffe, 1970); MAE is the mean absolute error. BSS is the Brier Skill Score (Brier, 1950), P_e represents the ensemble predicted post-flood DEM data series, O_e represents the ensemble observed post-flood DEM data series, and B_e stands for the ensemble baseline predictions, which are the observed pre-flood DEM data series. The angle brackets (< >) signify the mean value.

Calibration results demonstrated that the best combination of the background horizontal eddy viscosity and Manning roughness coefficient is 0.1 m^2/s and 0.035 $s/[m^{1/3}]$, respectively. Sensitivity analysis on grid size was carried out by comparing the model results of using different grid sizes (i.e. 3m and 6m). Results showed that the grid size of 6.5 m is sufficient to reproduce the actual flow behaviours (see the grid layout in Figure A1 from Appendix A). The comparison between the measured and modeled velocity using the calibrated parameters is shown in Figure 4.3. The statistical evaluation can be found in Table 4.4. Although errors are relatively high at cross-sections No.1, 3, 4, 5, 15, 16 and 18, the overall modeled velocity matched well with the measured velocity and the performance was evaluated as “good” (see Table 4.4). Thus, the model calibration is considered as successful.

4.4.4 Morphodynamic model

The morphodynamic model was developed to reproduce the morphodynamic changes observed to have occurred during the 2013 flood. Most settings were directly adopted from the hydrodynamic model. Only differences are elucidated herein:

- **Bathymetry.** Since there were no high flows in the year of 2011 and 2012 that would cause significant sediment transport, the bathymetry data collected on Sep 9, 2010 were used as the pre-flood bathymetry input;

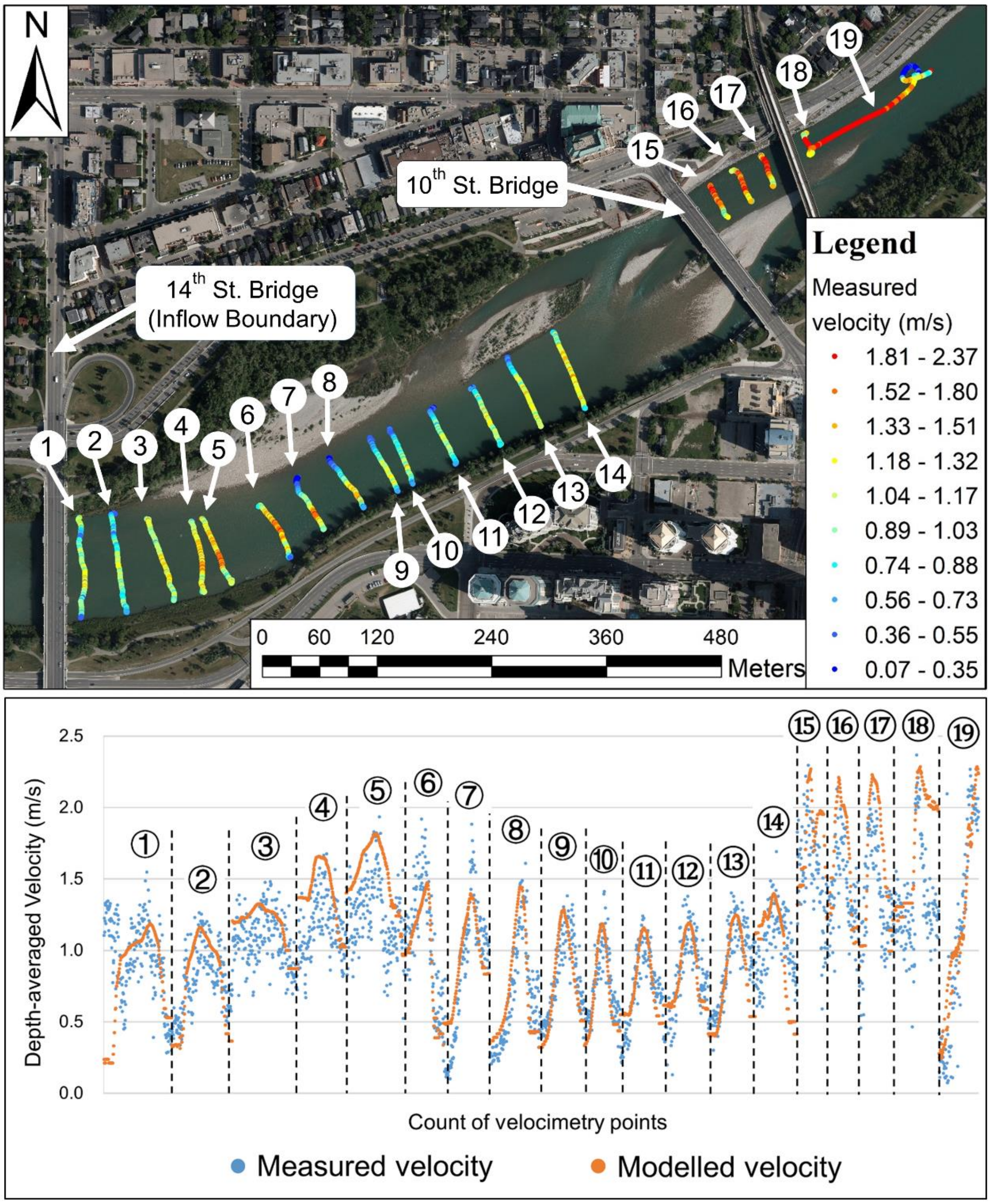

Figure 4.3. Upper image: measured depth-averaged flow velocity on Sep 9th, 2013. Background aerial photograph was taken in August, 2013. Blue arrow indicates the flow direction. Lower image: comparison between the measured and modeled velocity. Velocimetry points are sequenced from upstream to downstream, from the north bank to the south bank. "1" - "19" denote the numbers of survey cross-sections.

- **Bed stratigraphy.** In order to simulate the bed armouring in the Bow River, the bed stratigraphy model (Hirano, 1971) was used, which consists of two types of bed layers: the surface layer and the bookkeeping layer(s). Sediments in the surface layer are well-mixed and only they can directly interact with the flow. Once the surface layer is eroded, it gets replenished by the sediments from the topmost bookkeeping layer below. Once external sediments deposit on the surface layer, first they get well-mixed with the contents in the surface layer and then redundant sediments are pushed down to the topmost bookkeeping layer. As a result, the thickness of the surface layer is kept constant while the thickness and number of bookkeeping layer(s) changes accordingly. Detailed formulation of the Hirano active layer model can be found in Viparelli et al. (2010).

- **Sediment sizes.** The surface and subsurface grain size distributions (GSD) of bed materials in the study region are shown in Figure 4.4. In order to reproduce the non-uniformity of bed sediments, we used a combination of several non-uniform sediment fractions in the numerical model, as shown in Table 4.3.

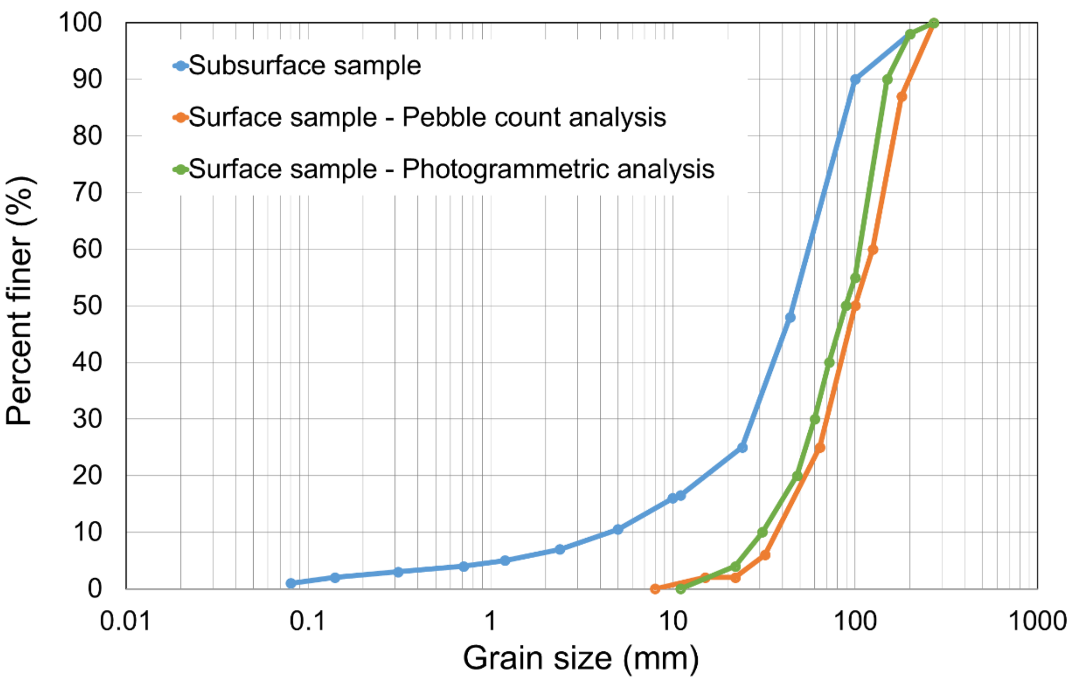

Figure 4.4. Grain size distribution (GSD) of the surface and sub-surface sediments, based on field survey data in 2016 (Klohn Crippen Berger, 2016).

- **Roughness.** Manning roughnesses of the inundated places with low, medium, and high vegetation were set as 0.045 s/[m$^{1/3}$], 0.055 s/[m$^{1/3}$], and 0.065 s/[m$^{1/3}$], respectively, according to Chow (1959).

- **Sediment transport**. Gauged data showed that sediments were mainly transported in the form of bedload in the model domain (Water Survey of Canada, 2024), which makes bedload the key control on the river morphology (Leopold, 1992). Thus, suspended loads were not modeled. Places having bank protection measures were considered as non-erodible in the model. The hiding and exposure effect was taken into account using the formulation developed by Parker et al. (1982).

- **Boundary conditions.** The hydrograph of the 2013 flood (see Figure 4.6) recorded at the hydrometric station was used as the model boundary conditions, with flow discharge as the inflow boundary and water level as the downstream boundary. Due to the lack of measured bedload transport data at model boundaries during the flood, Neumann boundary condition (i.e. gradient of sediment transport rate perpendicular to an open boundary equals to zero) (Roelvink & Walstra, 2004) was applied at the model boundaries. This means that the bedload entering or leaving the model boundaries will be adapted to the local flow conditions and very little accretion or erosion should occur at the model boundaries (Deltares, 2020).

Table 4.3. Initial thicknesses and contents of bed stratigraphy layers.

Layers	Initial thickness (m)	D_{50} of layer (mm)	D_{90} of layer (mm)	Sediment fractions	Sediment D_{50} (mm)	Mass fraction in the layer
Surface layer	0.3[#1]	97.5	179.9	#1	42	1/3
				#2	96	1/3
				#3	146	1/3
Bookkeeping layer	0.4*10 = 4[#2]	48.7	109.7	#4	12	1/3
				#5	48	1/3
				#6	89	1/3

[#1]Thickness was equal to armouring layer thickness in field.

[#2]The initial bookkeeping layer contains 10 sub-layers with initial thicknesses of each sub-layer of 0.4 m.

4.4.5 Validation

In the model validation stage, a number of model variables were tested in order to find the ideal combination to achieve the best model performance:

- **Bedload transport formula**. Meyer-Peter & Müller (1948), Soulsby (1997), and Van Rijn (2007) were tested in Yu et al. (2022). This study further tested the performance of Wilcock & Crowe (2003) and Gaeuman (2009). Results showed that Van Rijn (2007) produced the smallest error. The bedload transport formulation of Van Rijn (2007) is given in Section 3.6 and discussed in Section 5.3.

- **Bed-slope effects on bedload.** Recent studies highlighted the importance of the bed slope parameterization on bedload and associated morphological changes in Delft3D (Baar et al. 2019). Delft3D offers two formulations on bed-slope effects. The first uses Bagnold (1966) for longitudinal slope effects and Ikeda (1986) for transverse slope effects. The second uses Koch & Flokstra (1980). Both options were tested in this study. Results showed that Koch & Flokstra (1980) produced the smallest error.

- **Model dimension.** Sensitivity analysis on the model dimension showed that a 2-D model performed better than a quasi-3-D model. This is probably because, unlike other 3D software (e.g., Flow3D), the quasi-3D version of Delft3D does not solve the three-dimensional Navier-Stokes equations. There is no vertical momentum exchange between vertical layers, which may cause inaccurate prediction of the velocity profile including the near-bed velocities, particularly when simulating a strongly unsteady flood event.

- **Time step.** Following on Mahdizadeh & Sharifi (2020)'s findings, we did a sensitivity analysis by comparing the morphodynamic model results of using time step = 0.001 min (CFL number = 0.2) versus the results of using time step = 0.005 min (CFL number = 0.9). There was not much difference between these two cases, thus, 0.005min was set as the final time step.

- **Manning roughness and eddy viscosity.** We re-calibrated the Manning roughness and eddy viscosity during the 2013 flood simulation. The resulting bed elevation results demonstrated that the ideal combination of Manning roughness and eddy viscosity remain 0.035 s/[$m^{1/3}$] and 0.1 m^2/s, respectively.

The statistical analysis was carried out by comparing the modeled post-flood DEM with the measured post-flood DEM for the entire model domain. Results are shown in Table 4.4. Model performances near 10SB and CSB are shown in Figure 4.5. Although the model underestimated the bar height and scour depth, it successfully predicted the growth and formation of flood-induced bars both in terms of locations and areas. Thus, the developed model was considered as satisfactory and eligible for the analysis of flood morphodynamic processes.

Table 4.4. Summary of the statistical analysis results of the model calibration and validation.

Model stage	**Quantity**	**Statistical parameters**	**Value**	**Quality evaluation**
Model calibration (hydrodynamic)	Depth-averaged flow velocity	R^2	64%	Good[#1#2]
		NSE	56%	
		MAE	0.198 m/s	
Model validation (morphodynamic)	Post-flood DEM	BSS	0.397	Good[#4]
		MAE[#3]	0.535 m	

[#1] The evaluation criteria for R^2 is adopted from Seong et al. (2015): Excellent ($0.8 < R^2 \leq 1$); Very good ($0.7 < R^2 \leq 0.8$); Good ($0.6 < R^2 \leq 0.7$); Poor ($R^2 \leq 0.6$).

[#2] The evaluation criteria for NSE is adopted from Moriasi et al. (2007): Excellent ($0.75 < NSE \leq 1$); Very good ($0.65 < NSE \leq 0.75$); Good ($0.5 < NSE \leq 0.65$); Poor ($NSE \leq 0.5$).

[#3] Places with minor measured morphological changes (i.e. < 0.1m) during the 2013 flood were excluded from the dataset before calculating the MAE.

[#4] The evaluation criteria for BSS is adopted from Sutherland et al. (2004): Excellent ($0.5 < BSS \leq 1$); Good ($0.2 < BSS \leq 0.5$); Fair ($0.1 < BSS \leq 0.2$); Poor ($0.0 < BSS \leq 0.1$); Bad ($BSS \leq 0$).

4.4.6 Bedload formulation

In this study, current-induced (i.e. without the presence of waves) bedload transport rate is calculated using the empirical formula developed by Van Rijn (2007):

$$S_b = 0.5 \cdot \rho_s \cdot D_{50} \cdot u'_* \cdot D_*^{-0.3} \cdot T_b \tag{4.5}$$

where S_b is the magnitude of bedload transport rate per unit width [kg/m/s], ρ_s is the bulk density of sediment [kg/m^3], D_{50} is the median diameter of sediment [m], u'_* is the effective bed shear velocity [m/s], formulated as:

$$u'_* = (g \cdot u_c)^{0.5} \ \bar{V}/C \tag{4.6}$$

where g is gravity [= 9.81 m/s^2], $\bar{V}$ is the depth-averaged velocity [m/s], C is the Chézy coefficient [m$^{0.5}$/s] (calculated from local water depth and user-defined Manning's roughness), u_c is the efficiency factor [-], formulated as:

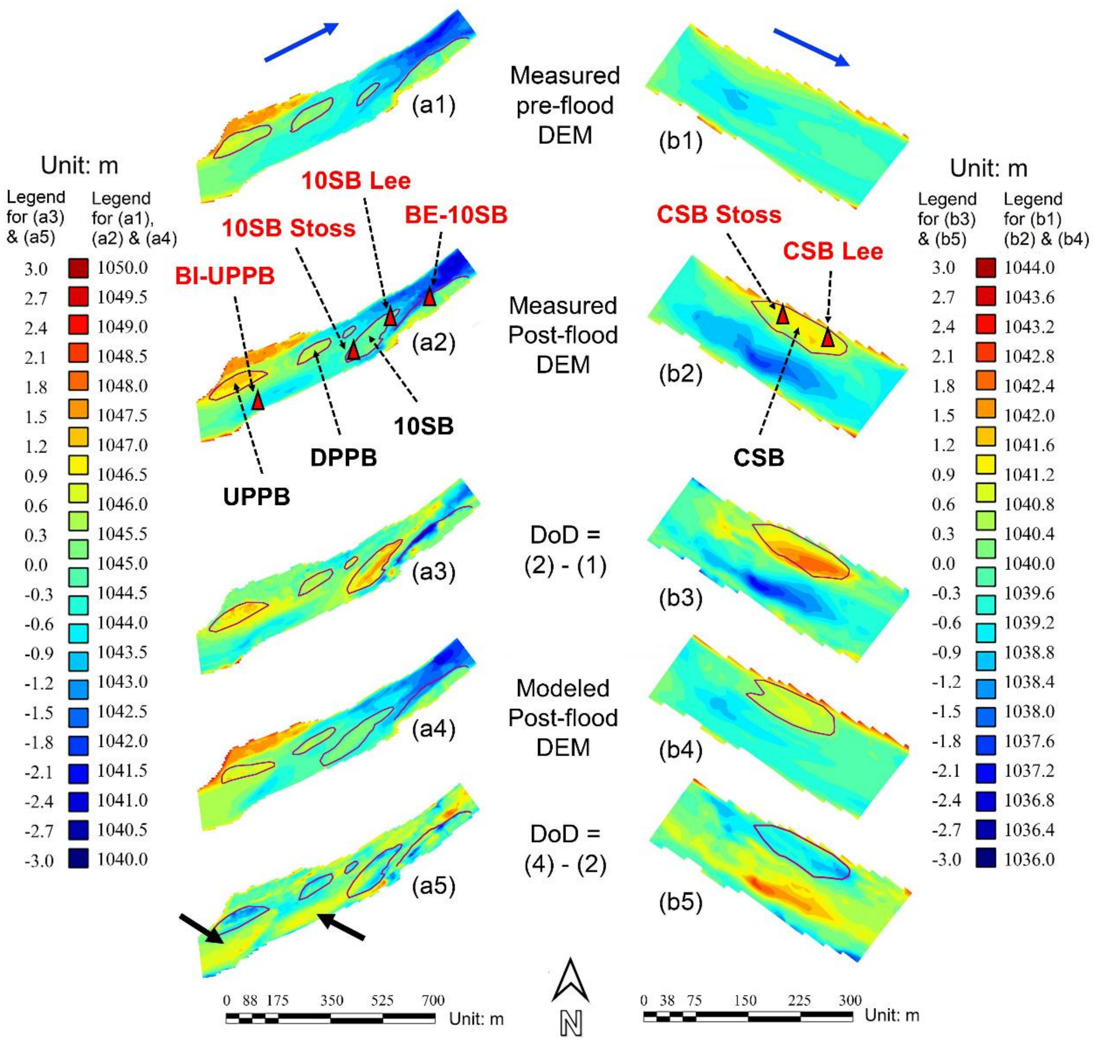

Figure 4.5. (a1 & b1) Measured pre-flood DEM, (a2 & b2) Measured post-flood DEM, (a3 & b3) Difference of DEM (DoD) between measured post-flood and pre-flood DEM (Blue represents erosion, while red represents deposition), (a4 & b4) modeled post-flood DEM, and (a5 & b5) DoD between the modeled and measured post-flood DEM around 10SB and CSB, respectively (Blue represents underestimation of the actual bed level, while red represents overestimation of the actual bed level). Blue arrows indicate the flow directions. Polygons mark the bar locations. Polylines in (a1) - (a5) outline the pre-flood river bank at BE-10SB. Note: bridge piers are not included in the color maps for better illustration.

$$u_c = f_c'/f_c \tag{4.7}$$

where f_c' is the grain-related friction factor [-], formulated as:

$$f_c' = 0.24 \cdot log10(12H/3D_{90})^{-2} \tag{4.8}$$

where H is the water depth [m], D_{90} is the particle diameter representing the 90% cumulative percentile value in bed sediment [m], f_c is the total friction factor [-], formulated as:

$$f_c = 0.24 \cdot log10(12H/3k_s)^{-2} \tag{4.9}$$

where k_s is the roughness height [m], formulated as:

$$k_s = 30.303 \cdot H/[e(e^{K \cdot C/g^{0.5}} - 1)] \tag{4.10}$$

where K is the von Kármán constant [= 0.41].

D_* is the non-dimensional particle diameter [-], formulated as:

$$D_* = D_{50}[(s-1)g/\nu^2]^{1/3} \tag{4.11}$$

where s is the relative density of sediment particle to water [-], ν is the kinematic viscosity of water [= 1.002 *10^{-6} m^2/s, in 20℃].

T_b is the dimensionless excess bed shear ratio [-], formulated as:

$$T_b = \frac{\tau_b' - \tau_{b,cr}}{\tau_{b,cr}} \tag{4.12}$$

where τ_b' is the effective bed shear stress [N/m^2], formulated as:

$$\tau_b' = \rho_w {u_*'}^2 \tag{4.13}$$

where ρ_w is the density of water [kg/m^3].

$\tau_{b,cr}$ is the critical bed shear stress [N/m^2], formulated as:

$$\tau_{b,cr} = (\rho_s - \rho_w) g D_{50} \theta_{cr} \tag{4.14}$$

where θ_{cr} is the threshold parameter calculated from the classical Shields curve [-], formulated as:

$$\theta_{cr} = \begin{cases} 0.24 D_*^{-1} & (1 < D_* < 4) \\ 0.14 D_*^{-0.64} & (4 \le D_* < 10) \\ 0.04 D_*^{-0.1} & (10 \le D_* < 20) \\ 0.013 D_*^{0.29} & (20 \le D_* < 150) \\ 0.055 & (D_* \ge 150) \end{cases} \tag{4.15}$$

4.5 Results

4.5.1 Global morphological changes

Unless otherwise stated, all physical quantities/phenomena described and discussed hereafter are “modeled” quantities/phenomena. The word “modeled” is omitted in order to be concise. Figure 4.6 shows the time history of cumulative deposition, erosion, and net volume in the entire model domain along with the flood hydrograph. We divide the 2013 flood hydrograph into three periods for better interpretation of the results: the rising period (from the beginning to 1686.5 m^3/s), the peak period (from 1686.5 m^3/s to 1662.7 m^3/s), and the falling period (the rest of the flood hydrograph). We selected some typical flood stages from each period to investigate the flow and sediment transport patterns (see Figure 4.8 & 4.9). Those flow stages are marked by the yellow dots in Figure 4.6 and their information is summarized in Table 4.5.

Figure 4.6 shows that the growth rate of deposition or erosion is relatively low until Rising Stage 2, indicating the time when most bed sediments were mobilized. About 70% of total deposition and 90% of total erosion occurred during the rising and peak periods of the 2013 flood. This result coincides with the findings in Staines & Carrivick (2015) and Williams et al. (2016).

Table 4.5. Information of the selected flood stages during the 2013 flood.

Flood stages	Time from the beginning (hours)	Instant flow discharge (m^3/s)
Rising Stage 1	12	224.0
Rising Stage 2	28	917.0
Peak Stage 1	36	1686.5
Peak Stage 2	60	1662.7
Falling Stage 1	84	1227.3
Falling Stage 2	108	845.7
Falling Stage 3	132	696.8

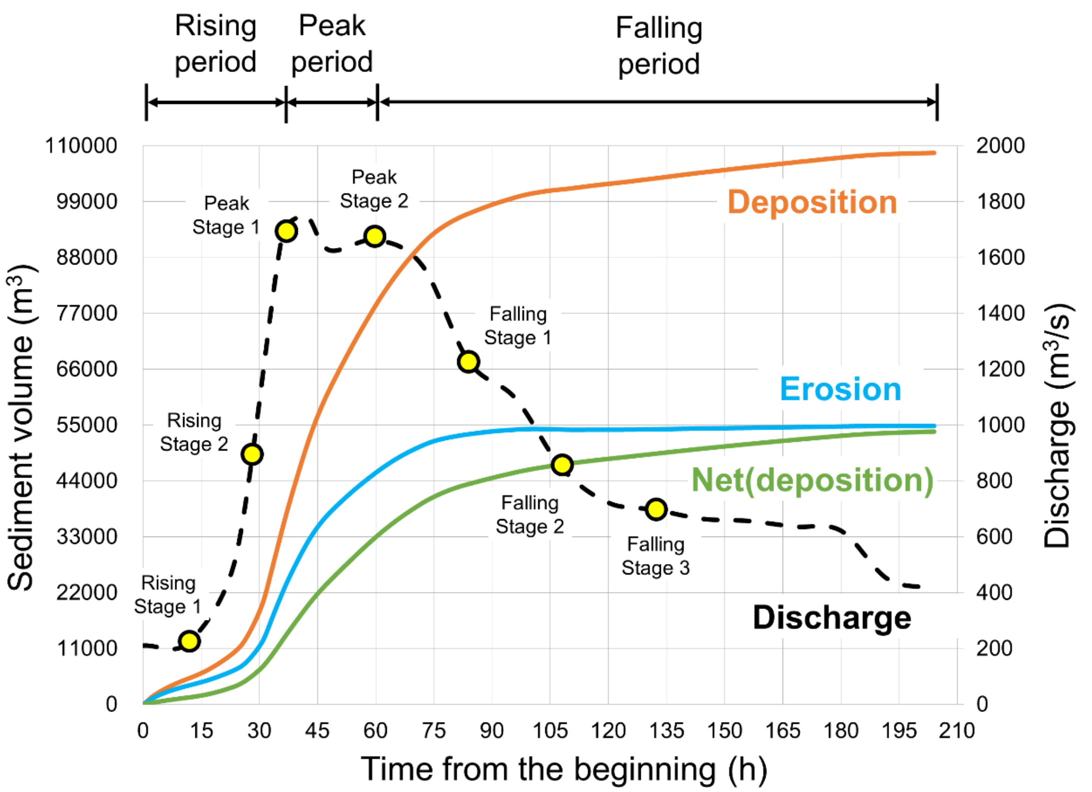

Figure 4.6. Time history of cumulative deposition, erosion, and net volume in the river channel along with the flood hydrograph. Yellow dots mark the typical flow stages in which the hydrodynamic and sedimentary patterns are investigated in Figure 4.8 & 4.9.

4.5.2 Local morphological changes

Major morphological changes happened around 10SB and CSB during the 2013 flood. Thus, detailed morphodynamic processes will be presented (section 4.2 & 4.3) and numerically investigated (section 5.1.1 & 5.1.2) at six selected sites (i.e. Set No.1) around 10SB and CSB. Note that those selected sites have the same erosional or depositional behaviors in the model as observed in the field data.

Figure 4.7 shows the time history of modeled cumulative volumetric change (CVC) at Set No.1 along with the flood hydrograph. A rise of CVC indicates deposition while a drop of CVC indicates erosion. Model results show continuous bed incision at BI-UPPB throughout the flood: the changing rate of erosion was relatively low during the rising period, suddenly increased during the peak period, and then decreased following the trend of declining discharge during the falling period. Deposition at 10SB Stoss mainly happened during the rising and peak periods while deposition at 10SB Lee mainly occurred during the falling period. The erosion process at BE-10SB mainly took place during the peak period. Interestingly, BE-10SB was continuously backfilled during the falling period. Deposition processes at CSB Lee and CSB Stoss were similar, both mainly happened during the rising and peak periods.

4.5.3 Flow and sediment transport

In this section, we present the modeling results of depth-averaged flow velocity ($\bar{V}$), bedload transport rate (S_b), median diameter of the computational surface layer (D_{50}), and cumulative deposition and/or erosion (CDE) around 10SB (Figure 4.8) and CSB (Figure 4.9) at 7 selected flood stages. The initial D_{50} of the surface layer is $97.5\ mm$, indicated by the orange color in Figure 4.8c & 4.9c.

At the 10SB site, flow velocity as well as bedload transport rate were higher at the model inflow boundary than immediately after the inflow boundary during the rising and peak period (see the arrow in Figure 4.8a3). Accordingly, deposition occurred immediately after the inflow boundary (see the upstream arrow in Figure 4.8d4). The bed surface near the inflow boundary became fine during the rising period (see arrows in Figure 4.8, c1-c3), became coarse during the peak period (Figure 4.8, c3-c4), then stayed coarse during the falling period (Figure 4.8, c4-c7). A region of high velocity and bedload transport rate (arrows in Figure 4.8, b3-b5) existed at BI-UPPB, associated with local scour (Figure 4.7a). Interestingly, surface sediments at BI-UPPB slightly coarsened before Rising Stage 2 (Figure 4.8, c1-c2), continuously fined during the peak period (Figure 4.8, c2-c4) then slightly coarsened during the falling period (Figure 4.8, c4-c7). Velocity (Figure 4.8, a3-a5) and bedload transport rate (Figure 4.8, b3-b5) dropped immediately downstream of BI-UPPB. Accordingly, deposition occurred at 10SB Stoss (Figure 4.8, d3-d5). Surface sediments at 10SB Stoss became finer and finer during the rising and peak periods (Figure 4.8, c1-c4). The longitudinal gradient of flow velocity and bedload transport rate (arrows in Figure 4.8, b2-b4) gradually increased near BE-10SB during the rising period. Bank erosion (arrows in Figure 4.8d4) and surface coarsening (Figure 4.8, c1-c4) occurred at BE-10SB and its opposite bank.

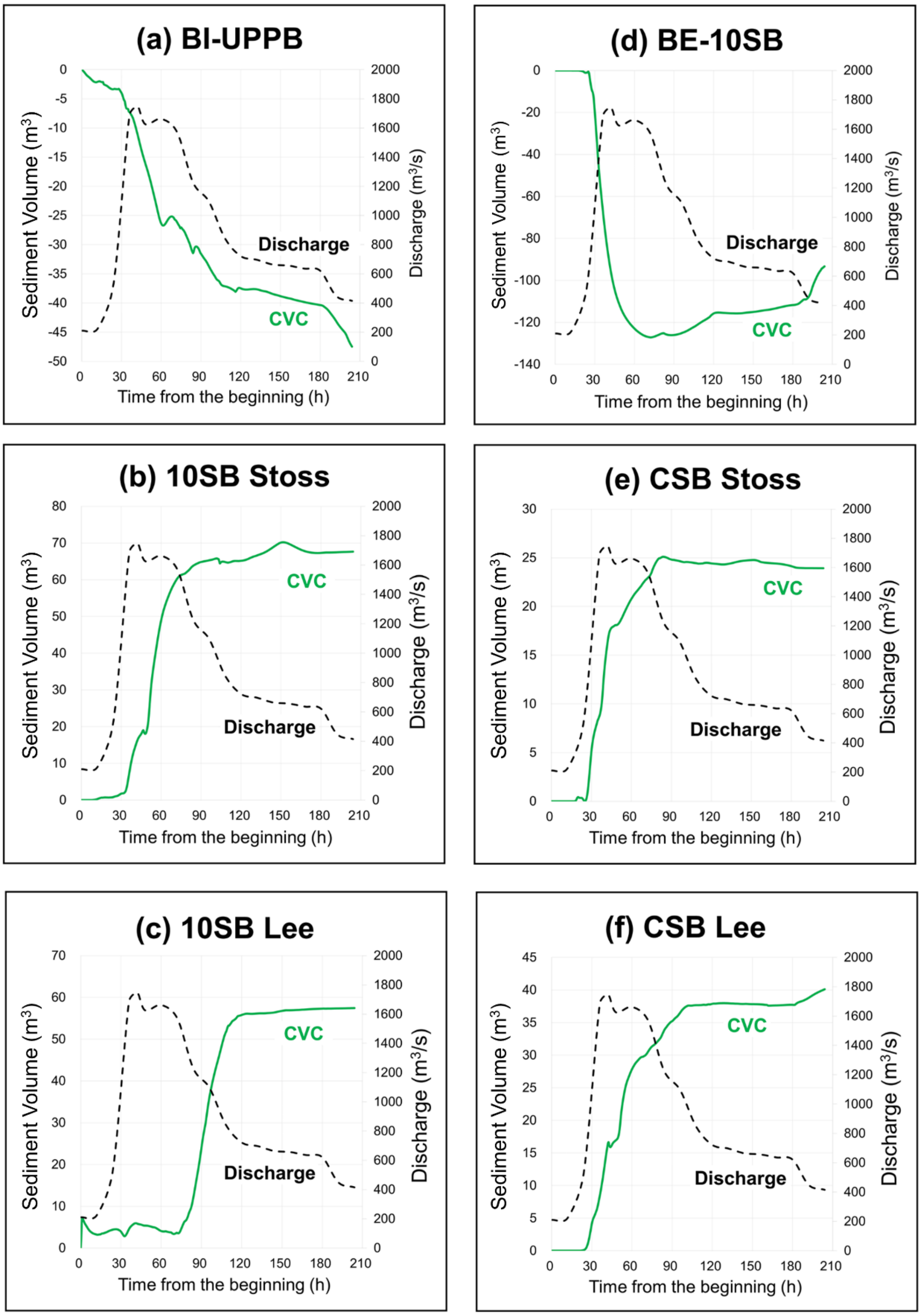

Figure 4.7. Time history of modeled cumulative volumetric change (CVC) curve along with the

flood hydrograph at Set No.1: (a) “BI-UPPB”, (b) “10SB Stoss”, (c) “10SB Lee”, (d) “BE-10SB”, (e) “CSB Stoss”, and (f) “CSB Lee”.

As for the CSB site, during the rising period, flow velocities were higher upstream than downstream of the Center Street Bridge (Figure 4.9a2). Such flow pattern is also reflected on the bedload transport rate map (Figure 4.9b2). Accordingly, minor deposition (Figure 4.9, d2-d3) along with surface fining (Figure 4.9, c2-c3) occurred downstream of the bridge piers in the mid-channel. Three high-flow-velocity regions can be seen at Peak Stage 1: the north region, the middle region, the south region (arrows in Figure 4.9a3). Velocity and bedload transport rate gradient increased along the north bank while decreased along the mid-channel (Figure 4.9, a3-a5, b3-b5). Accordingly, deposition (the upper arrow in Figure 4.9d4) started to grow at CSB while deposition growth in the mid-channel ceased (the lower arrow in Figure 4.9d4). Interestingly, the places with relatively fine surface in the mid channel seemed to split into two (arrows in Figure 4.9c3). One shifted to the north bank and then propagated to CSB Lee while the other one went downstream and gradually coarsened (arrows in Figure 4.9 c3-c5). After the Falling Stage 1, both the bed morphology (Figure 4.9, d5-d7) and the surface D_{50} (Figure 4.9 c5-c7) were relatively stable.

4.6 Discussion

4.6.1 Flood morphodynamics

4.6.1.1 Near 10SB

The pre-flood river channel is narrower at the inflow boundary (active channel width $\approx$ 87 m) than right after the inflow boundary (active channel width $\approx$ 128 m), which results in a negative flow velocity gradient (see the arrow in Figure 4.8a3) and thus a negative bedload gradient along the channel right after the inflow boundary. During the flood rising period, due to the relatively low flow rate, the fine sediment fraction (i.e. Sediment #1) was first fed into the model and deposited right after the inflow boundary due to the negative bedload gradient and resulted in surface fining (see arrows in Figure 4.8, c1-c3). After reaching to the flood peak, the coarser sediment fraction (i.e. Sediment #2) was initiated, fed into the model, deposited right after the inflow boundary (see upstream arrows in Figure 4.8, d4-d6), and resulted in surface coarsening (see arrows in Figure 4.8, c4-c6), also due to the negative bedload gradient at this place. However, such deposition right after the inflow boundary was not observed in reality (see the upstream arrow in Figure 4.5a5). An intuitive explanation is that the implementation of bedload Neumann boundary condition did not represent the actual bedload transport pattern at the inflow boundary (i.e. the boundary effect), which also occurred in other morphodynamic studies using Delft3D (e.g. Staines & Carrivick, 2015; Williams et al., 2016). With this in mind, we had tried to move the inflow boundary to further upstream to eliminate this boundary effect; however, results were not improved but even worse, both globally and locally (refer to Yu et al., 2022 for more details). Another possible explanation is that the transverse flow and bedload transport is not properly modeled as the channel expands near UPPB. If properly modeled, the excessive deposition right after the inflow boundary would have been transported further north to form UPPB such that it would better fit with the measurements (see Figure 4.5a5).

The pre-flood river channel is narrower at BI-UPPB (active channel width $\approx$ 106 m) than right after the inflow boundary (active channel width $\approx$ 128 m), which induced a positive velocity gradient (Figure 4.8a2) at BI-UPPB along the channel and resulted in minor bed incision at BI-UPPB during the rising period. As UPPB developed during the peak period (see upstream arrows in Figure 4.8, d4-d6), the channel was further constricted. This induced an even higher positive bedload gradient (see arrows in Figure 4.8, b3-b5) as well as a higher rate of scouring at BI-UPPB during the peak period (Figure 4.7a). The size of UPPB became stable during the falling period, thus bedload gradient at BI-UPPB dropped and the steepness of the CVC curve decreased, following the trend of declining discharge afterwards (Figure 4.7a). Interestingly, surface sediments at BI-UPPB slightly coarsened before Rising Stage 2 (Figure 4.8, c1-c2), continuously fined during the peak period (Figure 4.8, c2-c4) then slightly coarsened during the falling period (Figure 4.8, c4-c7). The initial coarsening process corresponds to the removal of the finest sediment fraction (i.e. Sediment #1) in the surface layer during the rising period. The following fining process corresponds to the continuous replenishment of fine sediment fractions (i.e. Sediment #4 & #5) from the bookkeeping layer to the surface layer due to the removal of relatively coarse sediment fractions (i.e. Sediment #2 & #3) in the surface layer during the peak period. The succeeding coarsening process corresponds to exhaustion of relatively fine sediment fractions (i.e. Sediment #1, #2, #4 & #5), leaving the relatively coarse sediment fraction (i.e. Sediment #6) in the surface layer during the falling period. Such “coarsening – fining - coarsening” process corresponds to the process of “armouring layer breakup - exposure of the substrate - armouring layer reestablishment” in reality during floods (Orrú et al., 2016; Parker & Klingeman, 1982; Vericat et al., 2006).

During the rising and peak periods, the surface layer at 10SB Stoss became finer and finer (Figure 4.8, c1-c4), indicating a continuous accumulation of finer sediments. This results from the lowering of longitudinal flow velocity (Figure 4.8, a1-a4) brought by the flow splitting into the north side channel of DPPB as well as the channel widening after passing DPPB. The surface fining at the wake zone behind the bridge piers is indicative of minor deposition at 10SB Lee during the rising and peak periods (Figure 4.7c). In addition, Figure 4.7 shows that the start-to-rise point of the CVC curve at 10SB Lee ($\approx$ 74 hours from the beginning, Figure 4.7c) corresponds to the time when deposition at 10SB Stoss (Figure 4.7b) and erosion at BE-10SB (Figure 4.7d) has fully developed, which implies that the development of 10SB Lee was probably associated with the wake behind 10SB Stoss as well as downstream channel widening. While mid-event field measurements are not available for direct validation of the predicted morphodynamic processes, the reasonability of predicted processes has been ascertained by comparison to previous literature. For example, the time lag between the CVC curve of 10SB Lee and that of 10SB Stoss (Figure 4.7, b & c) indicates that 10SB grew from the stoss side towards the lee side, which coincides with the finding in Ashworth (1996). However, both the stoss and lee side of 10SB are fine-sized sediments, which is inconsistent with the field observation in Ashworth (1996) and Li et al. (2014) where sediments were coarser at the stoss side than the less side of mid-channel bars. Such inconsistency may possibly be due to flow deceleration upstream of the bridge piers in the middle of 10SB, and/or continuous contribution of subsurface sediments from scour at BI-UPPB. During the falling period, due to the channel deepening at BI-UPPB and deposition growth at 10SB Stoss, the region with the highest longitudinal velocity gradient (arrows in Figure 4.8, a4-a6) gradually shifted to upstream, which corresponds to the growth of 10SB Stoss towards upstream (see arrows in the middle of Figure 4.8, d4-d5). However, such growth was not observed in the field data (see the downstream arrow in Figure 4.5a5), probably also due to unrealistic modeling of the transverse flow and bedload transport in Delft3D as the flow splits at DPPB and 10SB.

4.6.1.2 Near CSB

During the rising period, the flow velocities were higher upstream than downstream of the Center Street Bridge (Figure 4.9, a1-a2) due to the channel widening (active channel width $\approx$ 80m upstream of the bridge piers and active channel width $\approx$ 100m downstream of the bridge piers, see Figure 4.2c). The longitudinal decreasing flow velocity (Figure 4.9, a2-a3) and associated decreasing bedload transport rate (Figure

4.9, b2-b3) resulted in the deposition (Figure 4.9, d2-d3) as well as surface fining (Figure 4.9, c2-c3) behind the bridge piers.

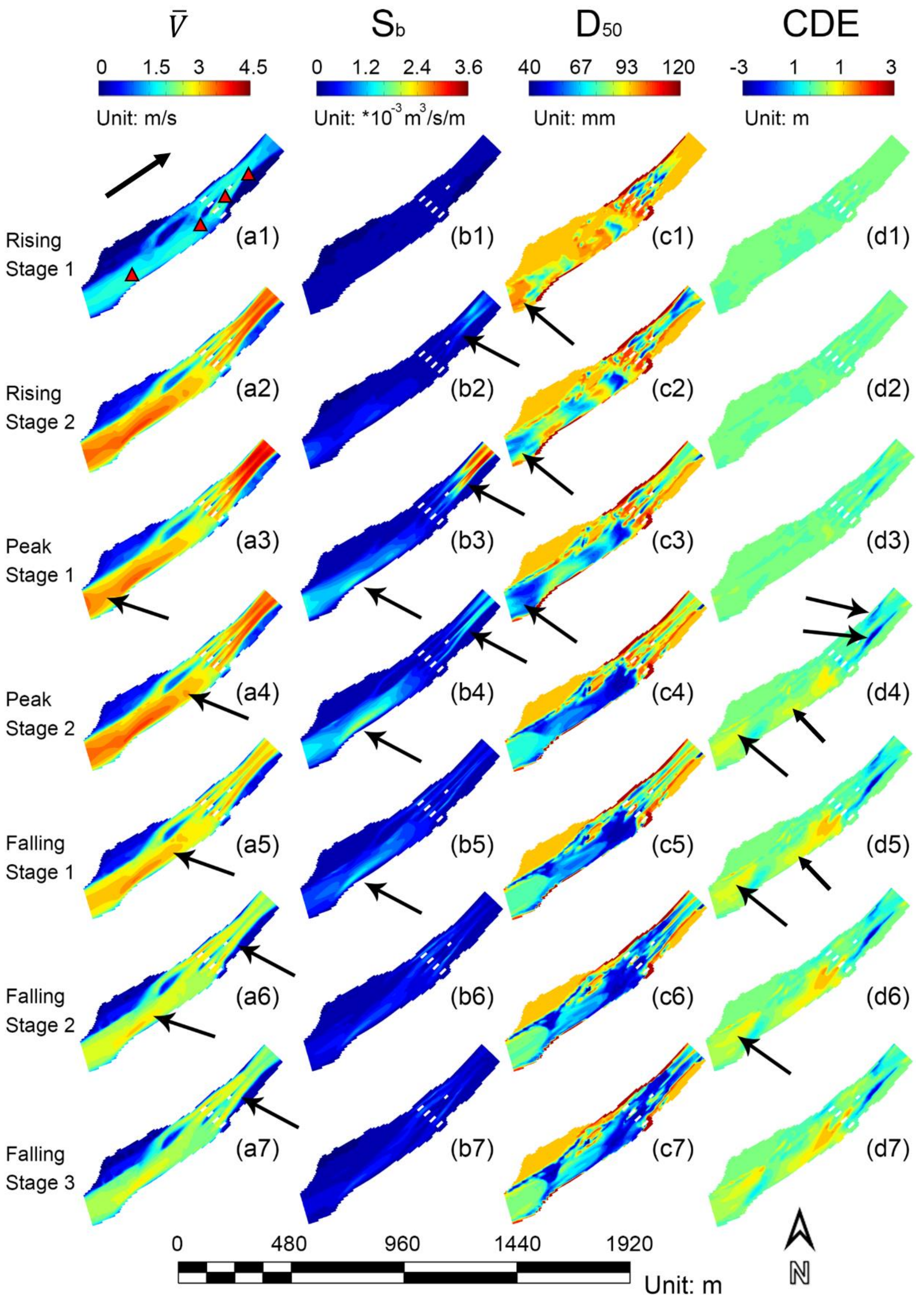

Figure 4.8. Maps of (a1-a7) $\bar{V}$, (b1-b7) S_b, (c1-c7) surface D_{50}, and (d1-d7) CDE at the seven flood stages near 10SB. Red triangles in (a1) mark the locations of "BI-UPPB", "10SB Stoss", "10SB Lee", and "BE-10SB", respectively, from upstream to downstream. The black arrow in (a1) indicates the flow direction. White boxes in color maps are in-channel bridge piers.

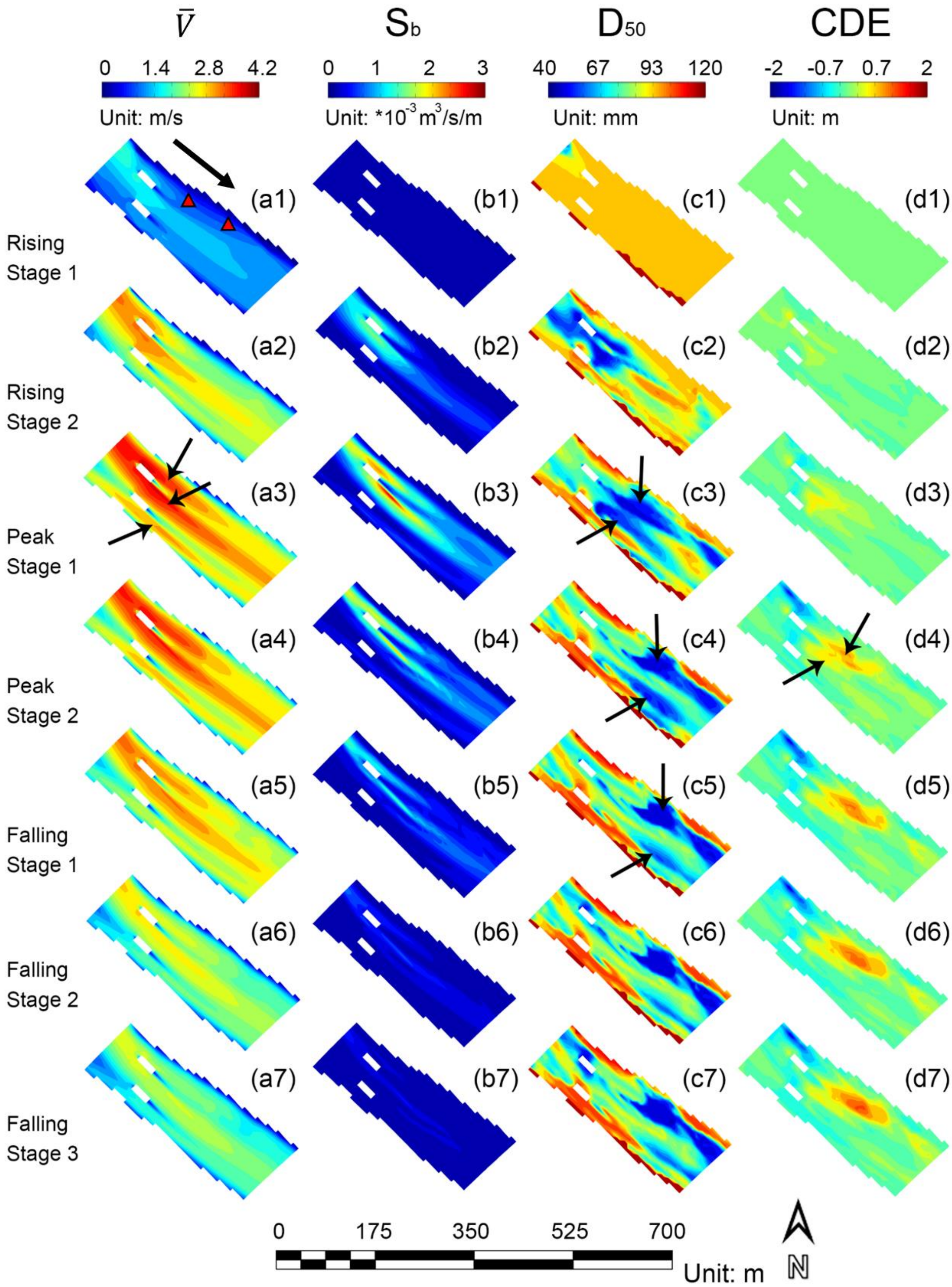

Figure 4.9. Maps of (a1-a7) $\bar{V}$, (b1-b7) S_b, (c1-c7) surface D_{50}, and (d1-d7) CDE at the seven flood stages near CSB. Red triangles in (a1) mark the locations of "CSB Stoss" and "CSB Lee", respectively, from upstream to downstream. The black arrow in (a1) indicates the flow direction. White boxes in color maps are in-channel bridge piers.

Interestingly, there are three high-velocity flow regions around CSB from Peak Stage 1 to Falling Stage 1: the north region, the middle region, and the south region. A higher flow velocity gradient along the river can be seen at the north region (Figure 4.9, a3-

a4) compared to other regions, due to the combination of channel widening and flow separation at the river bend, and caused the deposition at CSB Stoss and CSB Lee (Figure 4.9, d3-d5) as well as the surface fining (Figure 4.9, c3-c5) at this site, similar to the formation of a point bar in a meandering planform. Deposition at CSB mainly happened during the rising and peak stages, which is consistent with the field observation in Wu et al. (2016). Noteworthy, the places of fine surfaces near CSB gradually moved from CSB Stoss to CSB Lee from the Peak Stage 1 to Falling Stage 1 (see the upper arrows in Figure 4.9, c3-c5), which is possibly due to the presence of the middle region of high flow. The modeled result of surface coarsening at the stoss side of CSB while fining at the lee side of CSB is also consistent with the field observation of the grain size distribution on point-bar surfaces in Ghinassi et al., (2018), Julien & Anthony (2002), and Hagstrom et al., (2018). The south region of high flow resulted from the inflow from the secondary channel at the south side of the Prince's Island (see Figure 4.1b) during the peak period. The inflow from the secondary channel partly constricted the main flow path and caused the high flow velocity in the middle region stay high along the mid channel. The middle region of high flow velocity acted as a pathway for bedload conveyance, resulting in the transport of fine sediments towards downstream (see the lower arrows in Figure 4.9, c3-c5).

During the falling period, inflow from the secondary channel diminished and the high flow regions gradually vanished due to the growth of CSB. The combination of these two factors resulted in a relatively uniform flow field and thus minor bed elevation changes.

4.6.1.3 Summing-up

In the Bow River case, it seems the spatial variation of pre-flood channel planform (e.g. widening, narrowing, curvature, etc.) brought a spatial variation to the local flow field, led to a spatially-varied bedload transport pattern, and eventually resulted in local deposition or erosion during the flood according to the law of continuity. Such qualitative relationship between the spatial variation of channel planform and potential morphological changes coincides with the findings in other gravel-bed rivers (e.g. Luchi et al., 2012; Parker et al., 2010; Righini et al., 2017) and also in bedrock rivers (e.g. Hauer & Habersack, 2009; Righini et al., 2017; Yanites, B. J., 2018).

However, simply relating the flood-induced morphological changes to the pre-flood planform neglects the dynamic updating and coupling process between flow and channel morphology during the flood. Figure 4.7 already demonstrates such a non-linear relationship between flow magnitudes and local-scale flood-induced morphological changes. It also overlooks the impact of surface sediment sorting on bedload transport, which should be assessed through sensitivity analysis. Thus, those two topics will be further investigated and discussed in the next few sections.

4.6.2 Timing of morphological changes

Figure 4.7 implies that, for Set No.1, the timings of morphological changes during the 2013 flood varies with different morphodynamic units (MUs) (i.e. a mid-channel bar, a bank-attached bar, bank erosion, bed incision, etc.), which coincides with the field observation in Hooke & Yorke (2011). In order to see if similar timings of morphological changes exist for similar MUs across different reaches, we investigated the timings of morphological changes for a different set of MUs (i.e. Set No.2) in the model domain (see Figure 4.10). Same as those sites in Set No.1, the selected sites in Set No.2 also have the same erosional or depositional behaviors in the model as in the field. Also note that since there are no other mid-channel bars formed in the model domain except for 10SB during the 2013 flood, we had to select a mid-channel sediment-infilling site (i.e. the Ice Anchor Site, "IAS") as a substitute.

In order to quantitatively evaluate the proportion of cumulative morphological changes during different flood periods for a certain MU, we introduce a dimensionless morphological development index, η, formulated as:

$$\eta_i = \frac{CVC_{i,\quad end} - CVC_{i,\quad beginning}}{abs(CVC_{3,\quad end})} \tag{4.16}$$

where i=1, 2, and 3, representing the rising period, peak period and falling period, respectively. $CVC_{i,\quad end}$ and $CVC_{i,\quad beginning}$ are the cumulative volumetric changes at the end and the beginning of the flood period i, respectively. A higher value of η indicates more morphological changes during that period in the overall flood event. This enables the comparison of morphological development process among different flood periods for the same MU or among different MUs for the same flood period. The quantitative analysis results are shown in Figure 4.11.

Figure 4.11 show that bank erosion mainly happened during the rising and peak periods while bed incision mainly occurred during the peak and falling periods. Such difference reflects the different mechanism of those two erosional processes: for a gravel-bed river, bed incision required the removal of surface armouring (i.e. surface activation) as a prerequisite, which mainly happens during the rising period (Figure 4.8, c1-c2; also in Staines & Carrivick, 2015). In contrast, according to the bank erosion routine in Delft-3D, dry bank cells will receive a percentage of erosion from adjacent eroded wet cells, regardless of the sediment composition of bank cells and flood stages. Interestingly, both bank erosion sites underwent continuous deposition (Figure 4.7d & Figure 4.10d) during the falling period. We believe both deposition processes are related to the growth of upstream bars (i.e. 10SB and EPIB) during the rising and peak periods. The larger bar locally constricted the river channel and induced bank erosion immediately downstream (i.e. BE-10SB & BE-EPIB) during the rising and peak stage. Once the flow subsided the increased width caused by bank erosion resulted in flow deceleration, thus deposition occurred at the erosion sites during the falling stage.

Deposition at both the stoss and lee sides of bank-attached bars mainly happened during the rising and peak period. This is because bank-attached bars formed at the places where the flow path widened at one side of the channel, which resulted in flow separation and negative longitudinal bedload gradients along the widening side of the channel. Such negative bedload gradients lasted from Rising Stage 2 to Falling Stage 1 (e.g. Figure 4.9, b2-b5) and caused the formation of bank-attached bars. As the bank-attached bars developed, channel widening and flow separation was gradually mitigated thus minor deposition happened during the falling period. Notably, the development indices are higher at lee sides than stoss sides for mid-channel bars during the falling period, which indicates lee deposition lags behind stoss deposition.

In contrast, deposition on the stoss and lee sides of mid-channel bars mainly happened during the peak and falling periods, respectively. Different from bank-attached bars, mid-channel bars formed at the places where the channel widened at both sides (Hooke & Yorke, 2011; Klösch et al., 2015; Luchi et al., 2010), which brings negative bedload transport gradients dominating at mid-channel. Different from the case in bank-attached bars, mid-channel bedload gradients were only high enough to cause notable deposition during the peak period (e.g. Figure 4.8, b3-b4). This coincides with the field observations of Klösch et al. (2015) where the mid-channel was shown to accrete when it was submerged during flood events. As the stoss sides of mid-channel bars developed, flow widening effects were mitigated until no further stoss growth occurred. However, the fully developed stoss sides introduced wake effects that induced deposition on the lees of mid-channel bars during the falling period.

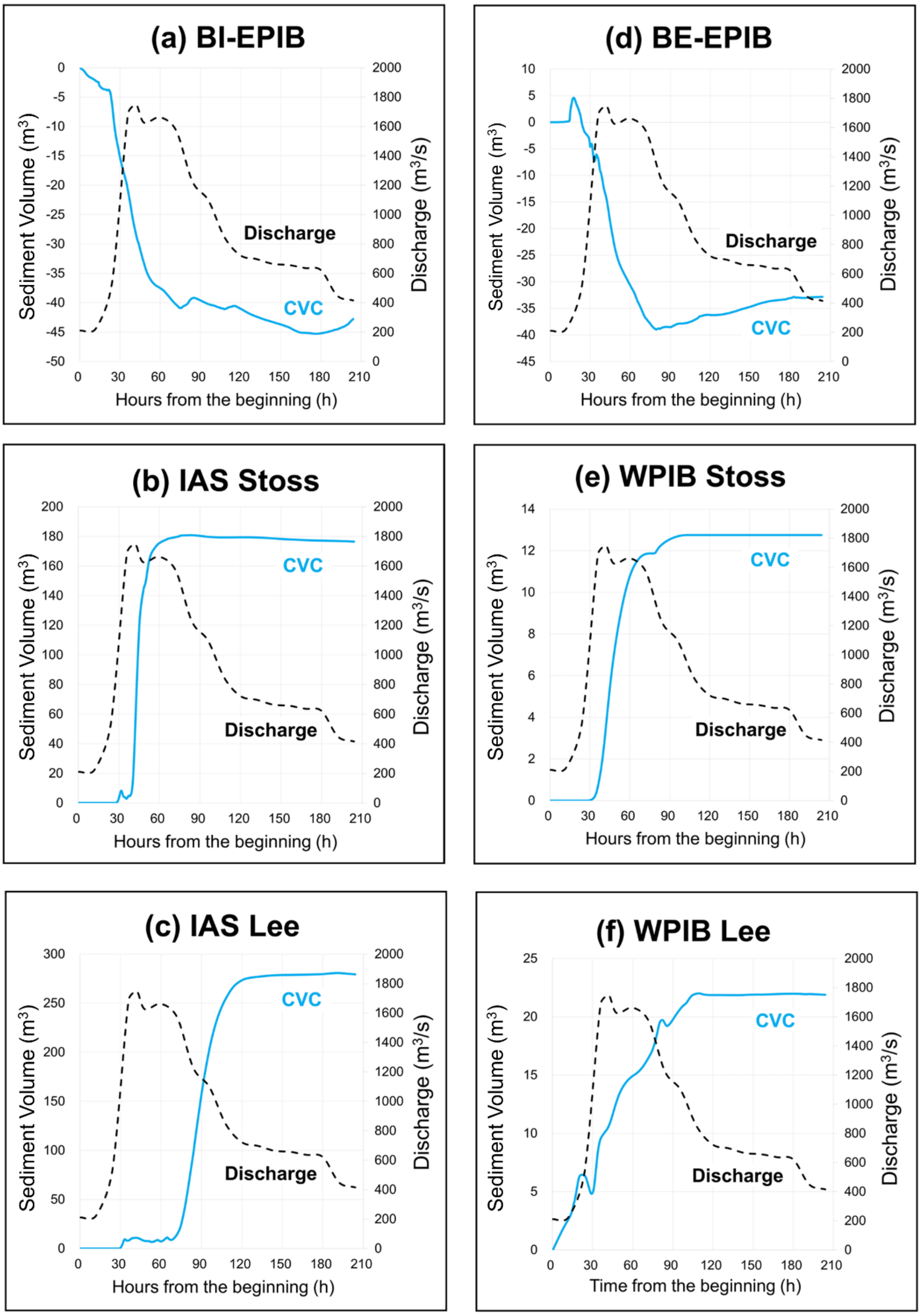

Figure 4.10. Time history of modeled cumulative volumetric change (CVC) curve along with the flood hydrograph at Set No.2: (a) "BI-EPIB", (b) "IAS Stoss", (c) "IAS Lee", (d) "BE-EPIB", (e) "WPIB Stoss", and (f) "WPIB Lee".

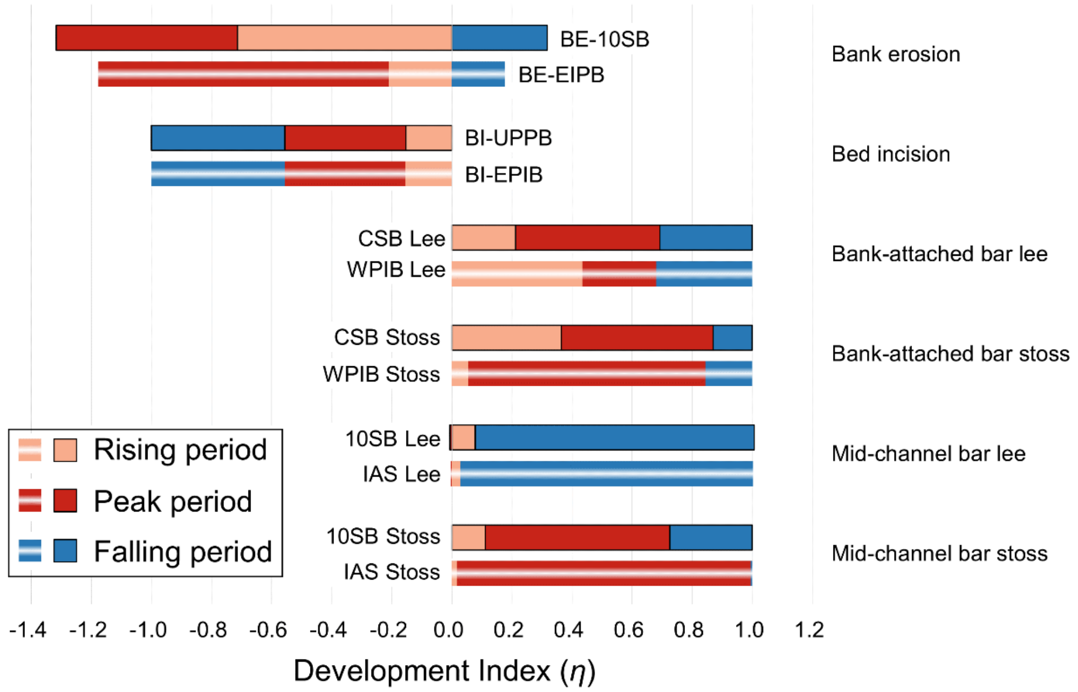

Figure 4.11. Stacked histograms of the dimensionless morphological development indices (η) of three flood periods for different MUs during the 2013 flood. Solid color bars are for Set No.1 and lined color bars are for Set No.2.

In summary, the developments of MUs during the flood event are non-linear in time. The timings of morphological changes during the flood event differ for different MUs but are similar for similar MUs, despite the planform differences across different reaches. These findings suggest that flood-induced erosion and deposition at the local morphodynamic unit scale are not likely to be ascertained using approaches based on reach averaged stream power (e.g. Hooke, 2016; Magilligan et al., 2015; Righini et al., 2017). In addition, these findings may also explain why the timing of major deposition or erosion varied with the flood magnitudes in Staines & Carrivick (2015): because the overall timing of deposition or erosion during the flood depends on the local timings of different MUs, whose dominance can vary with the flood magnitude as well as the sediment budget.

4.6.3 Bedload sensitivity analysis

Although bedload transport rate is dependent on multiple factors, it is considered to be mainly a function of flow strength and sediment size, upon which most bedload transport formulae are built. However, the relative sensitivity of bedload to these two parameters is still in debate (e.g. Cohen et al., 2022; Fernández & Garcia, 2017). In addition, the spatial and temporal sensitivity of bedload transport rate to flow velocity and sediment size during a flood event has not been evaluated in previous studies. In this section we analyze this sensitivity analytically (i.e., in the formula level) and compare with the model results (i.e., in the appearance level).

Taking ρ_s = 2650 kg/m^3, s = 2.65, g = 9.81 m/s^2, Manning's n = 0.035 s/[m$^{1/3}$], and $D_{90} = 2D_{50}$ (Van Rijn, 1993; also true in the Bow River case), and substituting Eq. (4.6) – (4.15) into Eq. (4.5), we can get the bedload transport rate as a function of depth-averaged flow velocity ($\bar{V}$), water depth (H), and median sediment size (D_{50}). Figure 4.12a & b show the variation of S_b as a function of $\bar{V}$ and D_{50} at different water depths and at different sediment size ranges.

Figure 4.12a shows that, for sand (D_{50}= 0.065mm - 2 mm) and very fine gravels (D_{50} = 2mm - 6 mm), bedload transport rate modeled by Van Rijn (2007) is more sensitive to velocity than sediment sizes, especially at the fine sand ranges (D_{50} = 0.065mm - 0.65 mm). But for medium and coarse gravels (D_{50} = 6mm - 150mm), which were the majorities in the Bow River, bedload transport rate modeled by Van Rijn (2007) is almost equally sensitive to D_{50} and $\bar{V}$, and is becoming more and more sensitive to D_{50} as the water depth increases. Interestingly, the apparent sensitivity is contrary: in the Bow River case, the spatial distribution of S_b showed a higher correlation with the spatial distribution of $\bar{V}$ compared to the spatial distribution of D_{50} at a given flood stage (Figure 4.12c). In addition, Figure 4.12c shows that correlation between S_b and $\bar{V}$ mostly increased as the flood rose and decreased as the flood fell, while the correlation between D_{50} and $\bar{V}$ varied more irregularly. Thus, Figure 4.12 seems to imply that the bedload sensitivity pattern in the appearance level is contradictory with that in the formula level. We attribute this inconsistency to different dependency on changes in flow velocity and surface D_{50} during a large flood in nature (demonstrated in Figure A2 in Appendix A). The change of surface D_{50} is either from the sediments in bedload (at deposition) or from the sediments in the substrate (at erosion), determined by the spatial gradient of bedload transport, which makes the interaction between D_{50} and S_b a "self-feedback" and "towards-equilibrium" process. In contrast, flow velocity is dependent on external factors such as channel planform, flood discharge, and roughness. Although the spatial variation of bedload can change channel planform and surface roughness via local deposition/erosion and the updating of surface D_{50}, respectively, and thus influence flow velocity, this is minimal compared to temporal changes in velocity with discharge during a flood. Thus, flow velocity can quickly vary during a large flood event but the change of D_{50} is relatively small and lagging. For example, at BI-UPPB, the modeled flow velocity increased from 1.74 m/s to 2.63 m/s and bedload transport rate increased from 6.9×10^{-6} m^3/s/m to 2.5×10^{-5} m^3/s/m during the first 24 hours. In contrast, D_{50} only slightly increased from 0.097 m to 0.102 m during the same period at that site. Such different dependency and temporal variation patterns of $\bar{V}$ and D_{50} results in the similar variation patterns between S_b and $\bar{V}$ but different variation patterns between S_b and D_{50}.

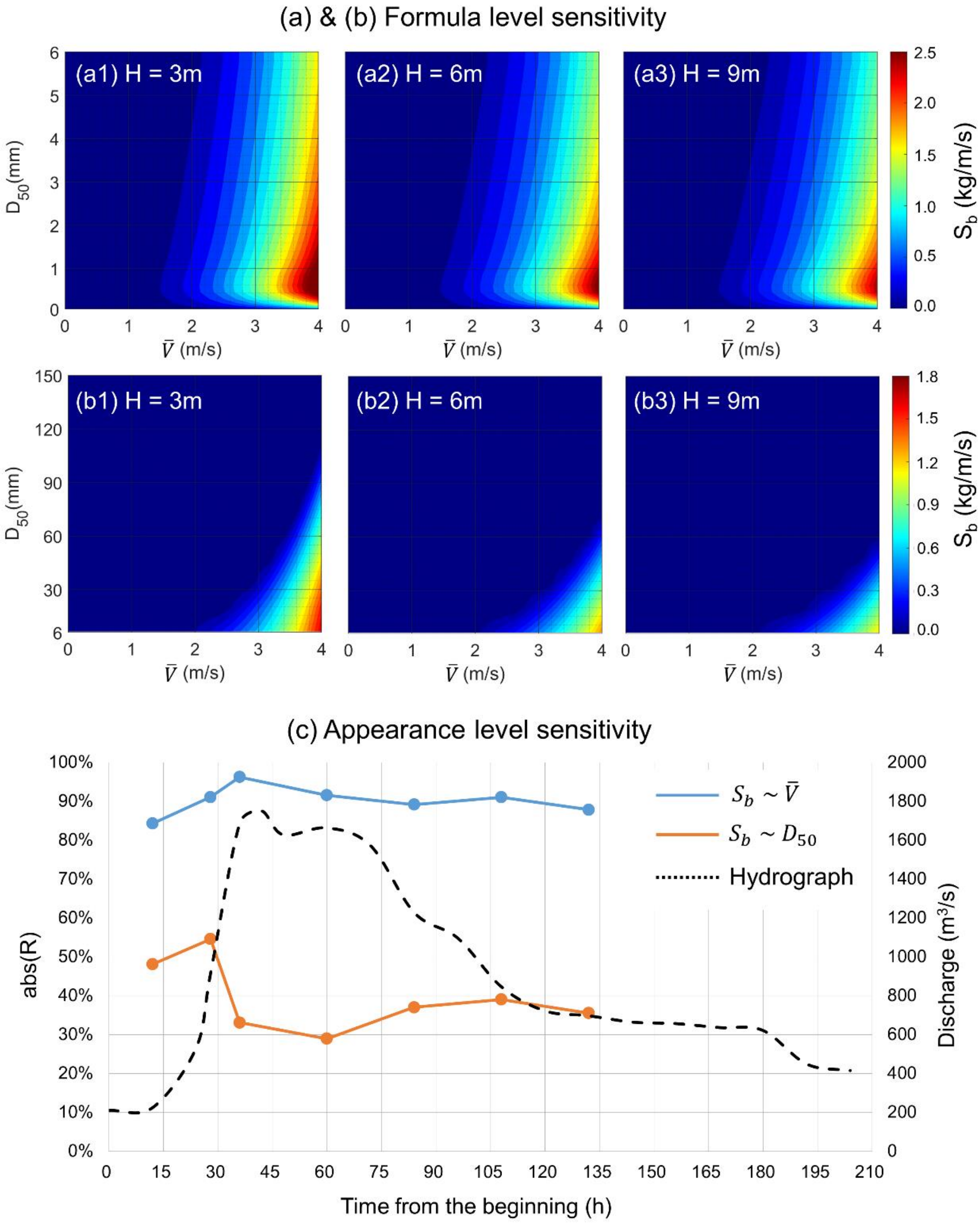

Figure 4.12. (a) bedload transport rate (S_b) as a function of depth-averaged flow velocity ($\bar{V}$) and median diameter of the computational surface layer (D_{50} = 0.065mm - 6 mm) when water depth (H) is (a1) 3 m, (a2) 6 m, and (a3) 9 m. (b) bedload transport rate (S_b) as a function of depth-averaged flow velocity ($\bar{V}$) and median diameter of the computational surface layer (D_{50} = 6 mm – 150 mm) when water depth (H) is (b1) 3 m, (b2) 6 m, and (b3) 9 m. Note that the average water

depth in the model domain varied from 1.6 m to 4.8 m during the 2013 flood. (c) The absolute correlation R between $\bar{V}$ and S_b, and between D_{50} and S_b in the entire model domain at 7 different flood stages.

To summarize, although bedload transport rate is equally sensitive to $\bar{V}$ and D_{50}in the formula level for medium and coarse gravels, the model results suggest bedload transport rate is more dominated by flow velocity rather than sediment size due to the greater spatial and temporal variance of velocity than grain size during a large flood event. This finding implies that when building a morphodynamic model for a real river reach, detailed field data of the horizontal distribution of surface sediment sizes might be less necessary as model input than an accurate flow hydrograph and channel bathymetry.

4.6.4 Implications for flood regulation

In some urban catchments, flood-induced bank erosion and bar formation need to be managed properly in order to mitigate associated risks (e.g. Yu et al., 2022). To this end, traditional approaches involve rip-rap installation to stabilize and protect the riverbanks and periodic dredging to clear in-channel deposits. The sensitivity analysis on bedload transport implies that solving the flow problems rather than the sediment problems could be much more effective and efficient in flood risk mitigation. With this in mind, combined with the finding on the timing of morphological changes of different MUs during floods, we propose the following new flood regulation strategy in urban catchments downstream of reservoirs to minimize morphodynamic changes and associated flood hazards: While maintaining the same flood peak and flood duration, regulating the flood event such that it has a short-lasting rising period, rather than a long-lasting rising period, might bring less potential bank erosion and bar growth to downstream reaches. In order to test this hypothesis, we ran the validated morphodynamic model under a “reversed” 2013 flood event, where flood peak, duration and total volume were the same as the original 2013 flood event (i.e., same stream power) but the rising period lasted longer than the original 2013 flood event. It turned out that the reversed 2013 flood event produced more deposition and erosion compared to the original 2013 flood (see Table 4.6), especially around 10SB and CSB where major flood-induced morphological changes occurred (see Figure S2-c).

In engineering practice, although it is not common to adjust the duration of a certain flood phase on purpose in a regulated river, this study provides the theoretical foundation for decision makers to shorten or lengthen certain flood phases to intervene downstream morphological evolution process when there is an opportunity and it is safe to do so. Iñiguez et al. (2019) showed that historical flood events with different phase durations can exist in the same regulated river, which demonstrates the potential of the abovementioned regulation opportunity. We believe that flood regulation and management is a multidisciplinary systemic endeavor that involves hydrology, river hydraulics, sediment transport and risk evaluation. The purpose of us raising such a flood regulation strategy is to add "potential downstream morphological impacts" to the decision tree.

Table 4.6. Modeled total volumetric changes of a "reversed" 2013 flood compared with the original 2013 flood.

Scenarios	Total deposition volume (m^3)	Total erosion volume (m^3)
Original 2013 flood hydrograph	108581.5	54878.2
Reversed 2013 flood hydrograph	119203.2 (+9.8%)[#]	58199.9 (+6.1%)[#]

[#] Numbers in brackets indicate the relative volumetric difference compared to the original 2013 flood.

4.7 Limitations and future concerns

This study demonstrates that a calibrated and validated morphodynamic model can serve as a powerful and efficient tool for investigating flow and sediment transport behaviors during a flood event. At the same time, there are some limitations that can be improved in future:

- **Representation of the actual morphodynamic processes.** Although the developed model has been validated against the measured post-flood DEM, it remains uncertain whether a morphodynamic model that successfully reproduced the observed post-event morphological changes can also reproduce the actual morphodynamic processes during the event, including the timing of morphological changes. More comprehensive field observations and accompanying modeling are required to answer this question.

- **Generalization of the findings.** This study only investigated the morphodynamic processes at a portion of a bedload-dominant gravel-bed river during a large flood event. More MUs should be investigated at other portions of the Bow River to derive more generalized findings. In addition, it's highly possible that Van Rijn (2007) may not be the ideal bedload model for other fluvial systems, where different bedload sensitivity patterns could appear, both in terms of the formula level and the appearance level. Thus, it remains unknown if the findings from this study remain valid for other alluvial rivers (e.g. sand-bed rivers; braided rivers) and under other types of floods (e.g. bankfull floods, outburst floods).

- **FCHM models.** Although the study done by Mahdizadeh and Sharifi (2020) showed that LCHM models can have equivalent performance to FCHM models, their performance has not been evaluated in extreme fluvial floods in large-scale rivers. Future studies could focus on this topic and provide more robust evidence regarding model selection in large floods.

4.8 Conclusion

In this study, we developed a morphodynamic model to simulate the morphological changes in a gravel-bed river during an 80-year flood event. Notably, the modeled "breakup – reestablishment" process of the surface armouring layer as well as the modeled surface sorting process at CSB are both in line with the field observations in previous relevant studies (e.g. Orrú et al., 2016; Parker & Klingeman, 1982; Vericat et al., 2006), which demonstrate the reliability of the model. We used the modeled flow and sedimentary data to analyze the morphodynamic process during the flood and found that:

- Although most deposition and erosion occurred during the rising and peak periods of the 2013 flood in the global scale, timings of local morphological changes vary for different morphodynamic units, but are similar for similar morphodynamic units, despite the planform differences across different reaches in the Bow River case. Specifically, bank erosion and the growth of bank-attached bars mainly happened during the rising and peak periods. Bed incision mainly happened during the peak and falling periods. The stoss sides of mid-channel bars mainly formed during the peak period while the lee sides of mid-channel bars mainly formed during the falling period.

- The bedload transport formula developed by Van Rijn (2007) is the most reliable one to depict the bedload transport pattern in the Bow River case among other empirical formula. Although bedload transport rate is almost equally sensitive to depth-averaged flow velocity and medium sediment size for medium and coarse gravels in the formula level, the model results suggest bedload transport rate is more sensitive to depth-averaged flow velocity rather than medium sediment size, due to the greater spatial and temporal variance of velocities than grain sizes during a large flood event.

- From the practical perspective, with the same flood peak and duration, a regulated flood event with a short-lasting rising period, rather than a long-lasting rising period, might bring less potential bank erosion and bar growth to downstream reaches and vice versa according to the modeled results in the Bow River case.
- More comprehensive field observations and modeling works in different alluvial rivers (e.g. sand-bed rivers; braided rivers) and under different types of floods (e.g. bankfull floods, outburst floods) are required to solidify and generalize the findings of this study.

Chapter 5. Impact evaluation of instream bar management using morphodynamic modeling

5.1 Abstract

The Bow River's 2013 flood was the costliest natural disaster in the City of Calgary's history. Flood-induced bar growth and subsequent riparian vegetation colonization at many locations has constricted the river channel, which increases flood risk. Although bar removal has been widely employed as a flood mitigation strategy, its effectiveness and associated impacts are still uncertain. This study employs Delft3D to develop a two-dimensional (2D) morphodynamic model in order to evaluate the impacts of a conventional plan of bar removal and a novel plan of bar realignment in terms of flood mitigation, aquatic habitat protection and river recreation realization. A hydrodynamic model was firstly developed and calibrated using post-flood spatially distributed velocimetry data. A morphodynamic model was then developed and validated using post-flood bed elevation survey data. Then, the future channel response and flood peak levels using different bar management plans were modeled and compared. Results show that appropriate bar realignment can protect aquatic habitat and provide river recreation opportunities while bar removal performs the better in terms of lowering the future flood peak level. The findings indicate that manipulation on instream bars has little morphological impact to downstream reach and creating a less obstructed channel is the fundamental strategy in flood mitigation.

5.2 Introduction

In river morphology, bars are elevated sandy or gravelly bedforms in river channels that are usually exposed at normal water level while submerged at high water level (i.e. floods). Bars are one of the most common geophysical features in fluvial systems. Based on the different regions of bar formation, bars can be classified as mid-channel bars, bank-attached bars, and river mouth bars (Church 1992), and based on sediment size, as gravel bars or sand bars. Fundamentally, bars form at the places where sediment supply rate is higher than the sediment transport capacity of the flow.

In gravel-bed rivers, bars are likely to be created and grow during floods due to the excessive amount of bedload carried by floodwater (Mat Salleh & Ariffin, 2013; Parsapour-Moghaddam et al., 2019b; Wintenberger et al., 2015). After floods, those flood-induced gravel bars become stabilized due to the drop of flow velocity. Subsequent riparian vegetation colonization on the exposed bar surface can further stabilize the bars (Rood et al., 2019). Gravel bar formation is part of a rivers natural migration process and provides important habitat for benthic invertebrates, waterbirds, and fish species (Church et al.,2000; Kondolf & Wolman, 1993; Miller et al., 1983; Rempel et al., 2012; Zeng et al., 2015; Parsapour-Moghaddam et al., 2019a). However, when bars form on managed rivers, they may block the channel, cause navigation difficulties, and pose future flood risks to riverine societies (Petit et al., 1996). The flood risk can increase when riparian vegetation colonization on the bar surface induces additional resistance to the flow, thus cause sediment aggregation around the bar during the next flood event (Church et al., 2001; Rood et al., 2019), resulting in a “vicious circle” of bar and vegetation growth.

Since the late 19th century, instream gravel extraction and bar removal has been widely applied as a cost-effective way to supply aggregate to the construction industry as well as mitigate flood risks and ensure channel navigation (Church et al., 2001; Kondolf, 1997; Sear & Archer, 1998; Wishart et al., 2008). However, gravel removal may generate a deficit in the active fluvial sediment balance, such that the flow becomes sediment-starved (Kondolf, 1997), resulting in consequences such as channel incision, bed coarsening, undermining of structures, and destruction of aquatic habitat (e.g. Brown et al., 1998; Collins & Dunne, 1989, 1990; Pauley et al., 1989; Petit et al., 1996; Sear & Archer, 1998; Surian, 1999; Kori & Mathada, 2012). A field study done by Wishart et al. (2008) suggested that removing sediment from vegetated bars (indicative of long-term storage) is considered to be less likely to generate a deficit in the active fluvial sediment balance and possibly a safe method to mitigate flood risk, yet not proven.

Bar realignment could be an alternative bar management plan as opposed to bar removal. Bar realignment refers to the modification of the layout of instream bars within the channel without significantly changing the total volume of bars. Theoretically, bar realignment could have the following advantages compared with bar removal:

- Bar realignment can preserve the volume of instream bars, which brings no disturbance to the reach-scale sediment budget. Thus, it is reasonable to speculate that appropriate bar realignment is less likely to cause downstream incision compared to bar removal;
- By realigning instream bars, the local flow field and sediment transport patterns will be altered. This alteration could result in a favorable condition in terms of inhibiting future bar growth and channel stabilization, and possibly, lowering the future flood level;
- Appropriate bar realignment has the potential to increase the diversity of river flow & channel bed conditions. This diversity can potentially provide an ideal condition for new habitat as well as the realization of river recreation (e.g. swimming, surfing, kayaking, etc.);

However, to the best of the authors' knowledge, the practice of bar realignment has not been addressed in the literature and is therefore unproven. In summary, there are still research gaps and also opportunities in the evaluation of instream gravel management in terms of flood mitigation, morphology, aquatic/riparian habitat, and recreation.

Morphodynamic modeling could be an efficient tool to study those impacts of instream gravel management. Once properly calibrated and validated, morphodynamic modeling has the potential to predict future consequences of different gravel management plans under different flow conditions. Nonetheless, the morphodynamic studies on gravel management are extremely scarce (e.g. Li et al., 2008; Parsapour-Moghaddam et al., 2019b; Yuill et al., 2016) and preliminary: first, those models are not properly calibrated/validated due to the lack of reliable field data. In addition, those models have very limited ability to evaluate downstream channel response due to gravel management. In summary, the powerful tool of morphodynamic modeling hasn't been fully exploited in the field of instream gravel management.

The objective of this study is to evaluate the performance of three instream gravel bar management plans in Bow River, Calgary in terms of morphological impacts, future flood risks, aquatic habitat protection, and possible river recreation use through morphodynamic modeling.

The major novelty of this study is that we propose a new instream bar management strategy of bar realignment and demonstrate its promising applications in river engineering. This study demonstrates that manipulations on long-term vegetated gravel bars have little morphological impacts to downstream areas, which fills a research gap in instream bar management. This study also implies that a more efficient strategy in fluvial flood mitigation is to create a uniform, less obstructed river bed, compared to river bed widening or lowering.

This study was carried out using the Delft3D platform. A hydrodynamic model was first developed and calibrated against existing velocimetry data. Then, a morphodynamic model was developed to simulate a large flood event and validated against the post-flood bathymetric survey data. Afterwards, three bar management plans: “do nothing”, “bar removal”, and “bar realignment” were implemented respectively by altering the river bed DEM (Digital Elevation Model). Following that, future performances of those plans were evaluated numerically and compared in terms of flood peak levels as well as morphological impacts.

5.3 Study area and data

The Bow River, located in southern Alberta, Canada, originates from Canadian Rocky Mountains and ends at the confluence with the Oldman River (Figure 5.1a & 1b). It has a length of approximately 645 km. It flows through three geographic regions: the mountains, the foothills, and the prairies (Veiga et al., 2015). The reach that passes through the City of Calgary (will be noted as “the Calgary reach” hereafter) is situated at the geological transition region between foothills and prairies. According to the “conveyor belt” model raised by Kondolf (1994), the Calgary reach is the “zone of transport”, which is characterized by gravel-sized bed sediment, channel meandering, and distinct instream bar formation. Several upstream reservoirs have cut off gravel transport, resulting in some surface armoring in the Calgary reach.

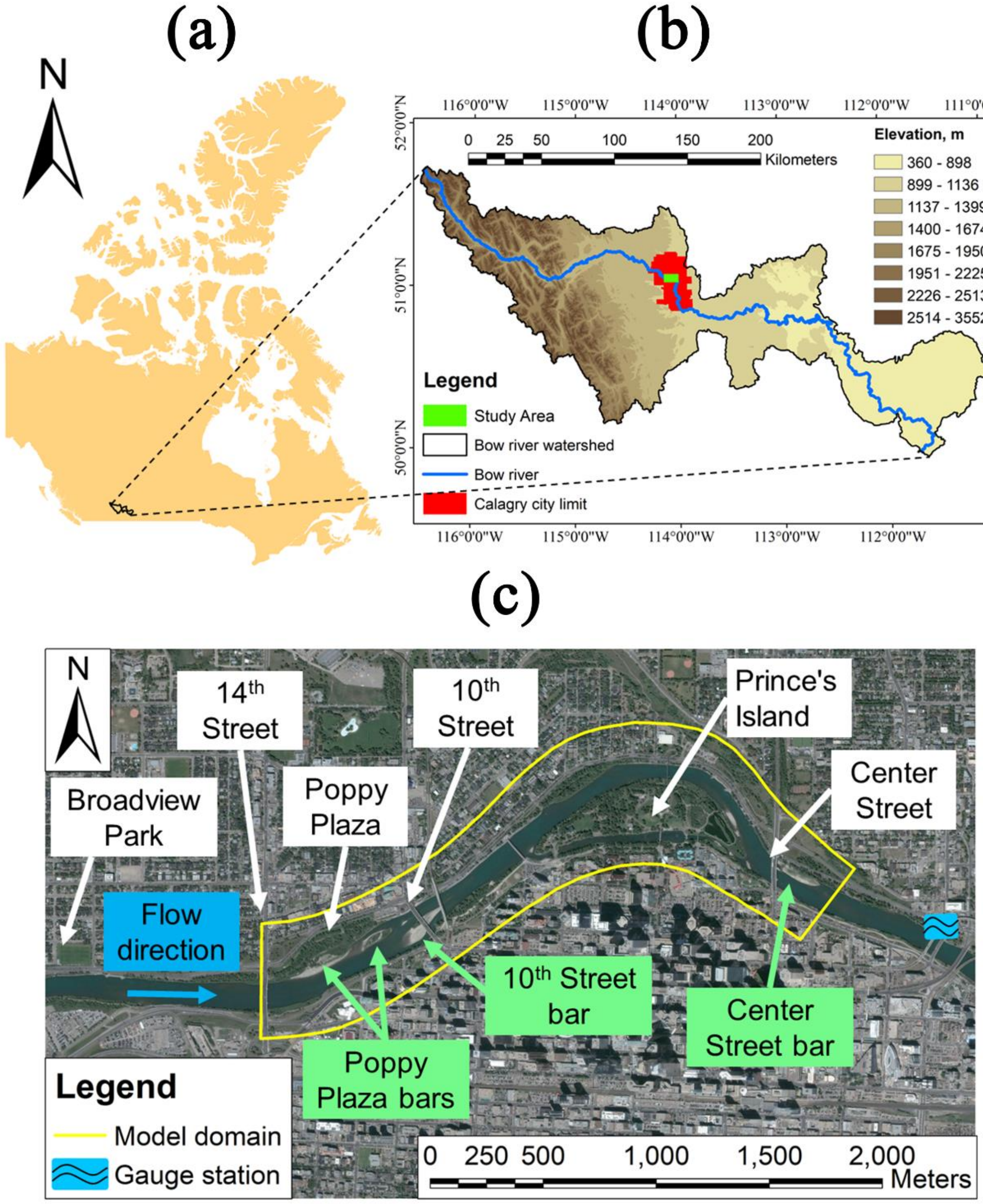

Figure 5.1. (a) The location of Bow River watershed in Canada. (b) The topography (courtesy of Dr. Atakan Erdem, University of Calgary) along the Bow River flow path (the blue line) and the location of the study area (the green area). (c) The model domain (the yellow polygon) and important landmarks. Background satellite image was taken in the year 2021, © Maxmar technologies, Google Image.

In late June 2013, with continuous heavy rainfall and rapidly melting alpine snow, the Bow River witnessed the highest flow of the century-long records (Pomeroy et al., 2016). The flood inundated the downtown Central Business District (CBD) of Calgary, and resulted in the evacuation of 26 communities in Calgary and a total cost of $5 billion across southern Alberta, which makes the 2013 flood one of costliest flood events in

Canada's history (Government of Alberta, 2014). The 2013 flood also produced up to 100 m of bank erosion in several locations of the Bow river as well as creation or expansion of extensive, barren, gravel bars and islands (Rood et al., 2019; Slaney et al., 2019). By the year of 2021, those gravel bars have been mostly vegetated, especially the largest ones that are close to the downtown CBD of Calgary: Poppy Plaza bars and 10th St. Bars (Figure 5.1c). Those bars might pose a flood risk to the city, thus, three alternate options have been considered for their management:

① **"Bar removal".** Bars will be fully removed in order to reduce future flood risks;

② **"Do nothing".** Bars will stay in the channel in order to avoid any possible consequences brought by human intervention;

③ **"Bar realignment".** Bars will be realigned to new sites without changing the total volume of instream bars significantly in order to fulfill multiple needs: reduce future flood risks, restore/create aquatic habitat, minimize downstream morphological impacts, and create a river surf wave park (Surf Anywhere, 2020) near the 10th St. bar.

The model domain starts from the 14 St. SW Bridge to the Center Street bar in the Bow River (See Figure 5.1c). The total length of this reach is about 3.3 km. The average width of this reach is about 85 m. The reasons and advantages of choosing this reach as the model domain are:

- **Distinct bar growth.** During the 2013 flood, this reach witnessed distinct bar formation and growth (See Figure 5.2), which provides the basis of model validation and implementation of different bar management plans;
- **Complete dataset support.** Abundant survey data and gauged data are available (See Table 5.1) in this reach, which provide essential supports to build and test the numerical model.

5.4 Methodology

This study utilized Delft3D-FLOW to simulate the flow, sediment transport, and morphological updating process. In the hydrodynamic aspects, Delft3D-FLOW solves the Navier-Stokes equations for an incompressible fluid, under the shallow water and the Boussinesq assumptions (Deltares, 2020). In the morphodynamic aspects, Delft3D-FLOW solves the advection-diffusion (mass-balance) equation for suspended load transport and standard (e.g. Van Rijn, 1993) or user-defined formulations for bedload transport. The bed elevation is dynamically updated at each computational time-step by solving the Exner (1925) equation. Delft3D-FLOW has been widely used in several hydro-morphodynamic studies (e.g. Kasvi et al., 2015; Parsapour-Moghaddam et al., 2017, 2019a, 2019b; Williams et al., 2016; Yuill et al., 2016) and proved its powerful and reliable performance.

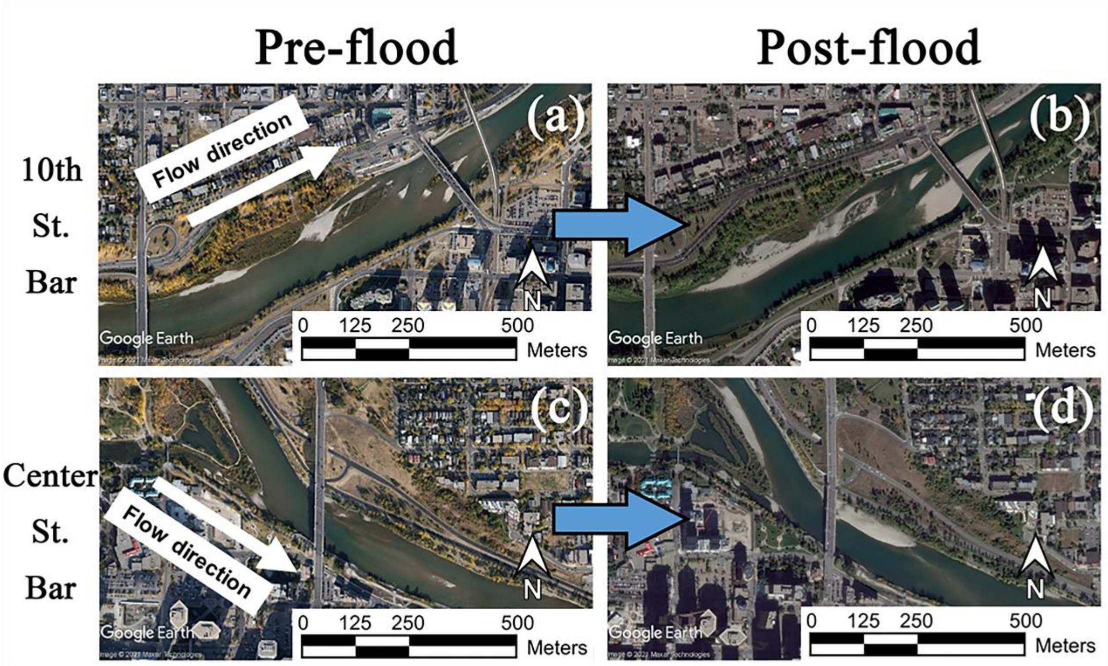

Figure 5.2. Aerial photographs of the Bow River before (Sep, 2012; $Q \approx 70\ m^3/s$; sub-figure "a" & "c") and after (Sep, 2014; $Q \approx 95\ m^3/s$; sub-figure "b" & "d") the 2013 flood for the 10th St. bar (sub-figure "a" & "b") and the Center St. bar (sub-figure "c" & "d"). Image © Maxmar technologies, Google Image.

5.4.1 Hydrodynamic model

A 2-D hydrodynamic model was initially developed under a low-flow condition for which velocity data were collected following the 2013 flood, without considering the sediment transport or morphological updating process. The velocity data were used to calibrate important model variables such as background horizontal eddy viscosity (used to model 2D turbulence as well as dispersion) and Manning roughness (used to model boundary shear stress), as will be covered in the next section.

The model domain covers the river channel and a portion of floodplains (See Figure 5.1c) in order to accommodate overbank flow and any possible bank erosion. Grid size was determined by considering the tradeoff between the computational cost and the desired model details as well as considering the dimension of instream bridge piers at the 10 St. SW Bridge (width $\approx$ 6 m). Given all these considerations, the initial average grid size was set as 6.9 m. The maximum orthogonality and aspect ratio of the model grid are 0.009 and 1.44, respectively, which are both within the recommended range by Deltares (2020).

Table 5.1. Summary of the available dataset in the model domain.

<table>
<tr><th colspan="2">Data type</th><th>Date</th><th>Coverage</th><th>Spatial Resolution</th><th>Source</th></tr>
<tr><td rowspan="5">Survey data</td><td rowspan="2">Bed elevation[#1]</td><td>2010/9/9</td><td rowspan="2">Whole model domain</td><td rowspan="2">River bed: 2.5 m x 40 m
Dry land: 0.2 m x 0.2 m</td><td>Golder Associates (2011)</td></tr>
<tr><td>2013/10/28</td><td>Golder Associates (2015)</td></tr>
<tr><td>Velocimetry (ADCP)</td><td>2013/9/9</td><td>A portion[#2] of the model domain</td><td>0.5 m x 100 m</td><td>Golder Associates (2015)</td></tr>
<tr><td rowspan="2">Bed sediment gradation</td><td>Year 1986</td><td>N.A.</td><td>Surface layer</td><td>Northwest Hydraulic Consultants Ltd. (1986)</td></tr>
<tr><td>Year 2016</td><td>10 St. Bridge & Center St. Bridge</td><td>Surface layer, Sub-surface layer</td><td>Klohn Crippen Berger (2016)</td></tr>
<tr><td rowspan="3">Gauged[#3] data</td><td>Discharge</td><td>1911-2019, Daily</td><td rowspan="3">N.A.</td><td rowspan="3">N.A.</td><td rowspan="3">Water Survey of Canada (2024)</td></tr>
<tr><td>Water level</td><td>2012-2019, Daily</td></tr>
<tr><td>Bedload rate</td><td>1972-1978, Daily</td></tr>
</table>

[#1] Data were collected using ADCP (Acoustic Doppler Current Profiler), land-based RTK (Real-Time Kinematic) GPS, and LiDAR (Light Detection and Ranging).

[#2] See Figure 3 for more details of the velocimetry survey coverage.

[#3] See Figure 1c for the location of the hydrometric gauge station.

The post-flood bed elevation survey data (surveyed on Oct 28, 2013) were used as the bathymetry input. Bridge piers were implemented by using “dry cells” in the model domain. Gauged discharge of 103 m^3/s and water level of 41.27 m (referenced based on the mean sea level) were used as the model upstream and downstream boundary conditions, respectively. Steady-state flow was used in the hydrodynamic model due to the negligible variation of discharge and water level within a day. Trial runs showed that the equilibrium state could be reached in the real-event time of 3 hours, which was then set as the event duration of the hydrodynamic model. The time step was determined as 0.023 min, considering the requirement that the Courant number should be smaller than 1. The initial background horizontal eddy viscosity was set as 0.1 m^2/s, which was adopted from Parsapour-Moghaddam et al. (2019b). The initial Manning roughness was set as 0.03, based on the recommended roughness for gravel-bed (0.028-0.035) in Phillips & Tadayon (2006).

5.4.2 Calibration & sensitivity analysis

Figure 5.3 shows the post-flood velocimetry survey routes and velocity magnitude, which was collected on Sep 9th, 2013 using RTK-ADCP, and were post-processed using in-house Matlab codes (Rennie & Church 2010). Although the velocimetry survey only covered the first 1/3 portion of the model domain, the calibration parameters determined from the first 1/3 portion could be applied to the remaining 2/3 portion of the model domain as there is the little variation of channel surface and flow properties between those two portions.

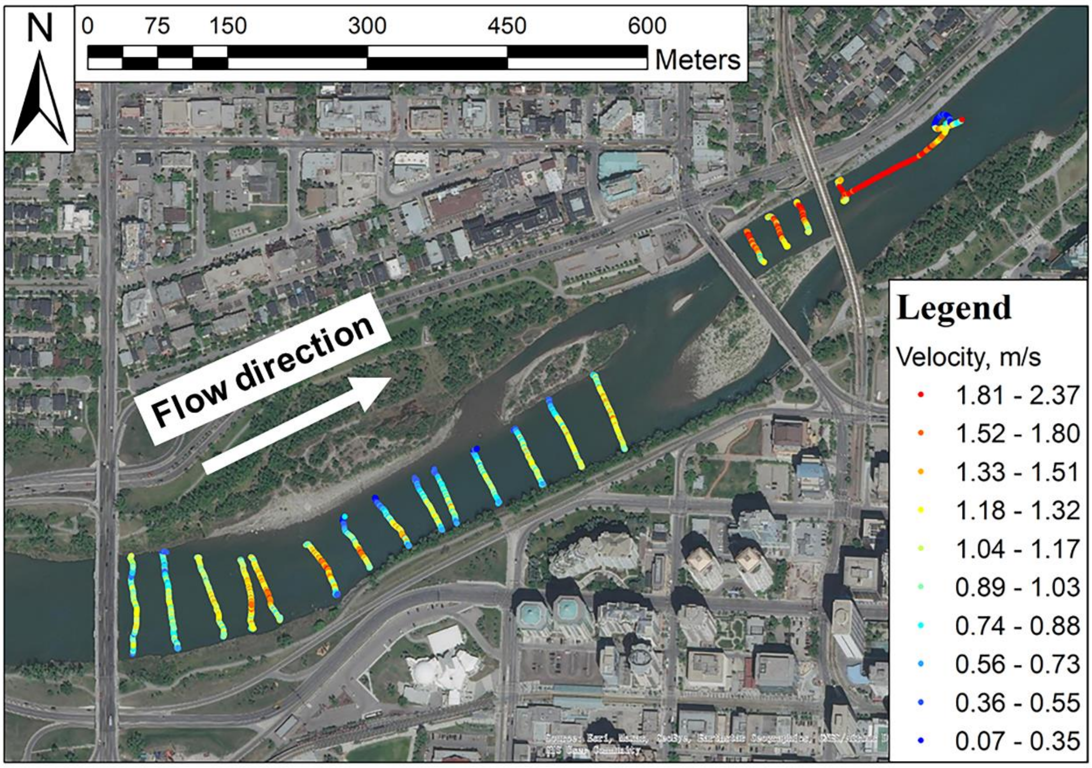

Figure 5.3. Post-flood (Date: 2013/9/9; $Q \approx 103\ m^3/s$) velocimetry survey routes and depth-averaged velocity magnitude. Background satellite image was taken in year 2021, © Maxmar technologies, Google Image.

Table 5.2 shows the scenarios of model calibration and sensitivity analysis and the associated statistical results by comparing the modeled and measured values. The background horizontal eddy viscosity, grid size, and Manning roughness are calibrated using the following approach: First, different values of background horizontal eddy viscosity were trialed while keeping the other two variables constant (E series). After the optimal value of eddy viscosity was determined, the same procedure was done for Manning roughness (M series), and then the grid size (G series). modeled velocities were triangularly interpolated to the locations of velocimetry survey points before carrying out the statistical analysis in order to eliminate the errors induced by spatial deviation between measured and modeled velocity points. The following statistical parameters were used in the statistical analysis:

$$R = \frac{\sum_{i=1}^{N}(O_i - \bar{O})(P_i - \bar{P})}{\sqrt{\sum_{i=1}^{N}(O_i - \bar{O})^2}\sqrt{\sum_{i=1}^{N}(P_i - \bar{P})^2}} \tag{5.1}$$

$$MAE = \frac{\sum_{i=1}^{N}|O_i - P_i|}{N} \tag{5.2}$$

where R is the Correlation R between the observed and predicted data, O_i and P_i, respectively; i is the sequence number of a sample point, N is the total number of sample points; $\bar{O}$ and $\bar{P}$ are the means of the observed and predicted data, respectively; MAE is the mean absolute error.

Table 5.2. Model calibration and sensitivity analysis scenarios and corresponding statistical results.

Scenario	Setups			Statistical results	
	Grid size (m)	Eddy viscosity, m^2/s	Manning roughness	Correlation R	MAE, (m/s)
E 0.1	6.5	0.1	0.030	0.797	0.226
E 0.5		0.5		0.790	0.219
E 10		10.0		0.713	0.217
M 0.03	6.5	0.1	0.030	0.797	0.226
M 0.035			0.035	0.793	0.198
M 0.04			0.040	0.785	0.194
G1.1	1.1	0.1	0.035	0.804	0.190
G3.4	3.4			0.803	0.190
G6.5	6.5			0.793	0.198
G10.2	10.2			0.736	0.234

Table 5.2 shows little statistical difference among case “E0.1”, “E0.5” and “E10” in terms of the MAE, which indicates that the model results are not sensitive to background horizontal eddy viscosity. In order to pursue a higher correlation between the measured and modeled data, optimal background horizontal eddy viscosity was set as 0.1 m^2/s. The case “M0.035” has signification lower errors compared to case “M0.03”, while higher correlation R compared to the case “M0.04”. Thus, the optimal Manning roughness was set as 0.035. There is little statistical difference among case “G1.1”, “G3.4” and “G6.5” in terms of correlation R and MAE, which means that a model with an average grid size of 6.5 m is sufficient to reproduce the real flow behaviours. Thus, the average grid size of 6.5 m, Manning roughness of 0.035, and background horizontal eddy viscosity of 0.1 m^2/s were determined as the calibrated parameters.

Figure 5.4 shows the comparison between the measured and modeled velocity as well as the differences at each velocimetry survey point when using the calibrated parameters. Relatively large errors can be seen in the first five cross-sections after the 14^{th} St., which is probably because the model is unable to consider the impacts of the 14^{th} St. bridge piers to the flow field immediately downstream. Overall, the modeled velocity matched with the measured velocity within a reasonable range, with a good correlation and a relatively low MAE. Thus, the calibration process is considered to be successful.

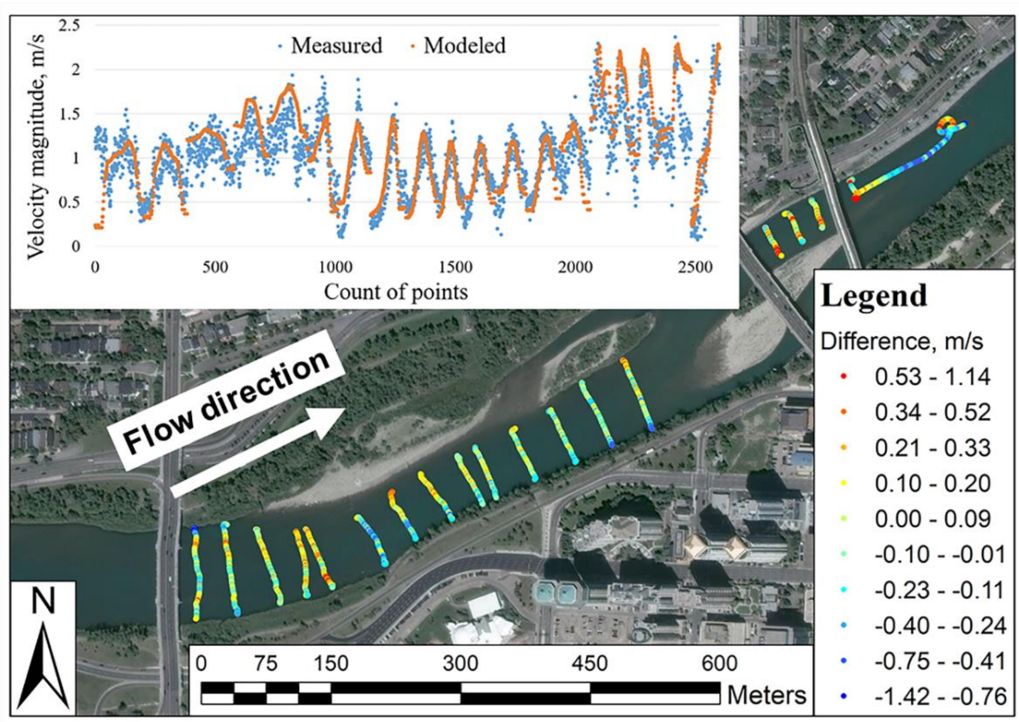

Figure 5.4. Comparison between the measured and modeled velocity as well as the differences at each velocimetry survey point when using the calibrated parameters. The imbedded plot shows the direct comparison between the modeled (yellow dots) and measured (blue dots) velocity: Points are sequenced from upstream to downstream, from left bank to right bank. The color map shows the velocity difference between the measured and modeled velocity: "Difference = modeled velocity – measured velocity".

5.4.3 Morphodynamic model

The morphodynamic model allows for the simulation of bed elevation updating and sediment transport. Most settings were directly adopted from the hydrodynamic model. Here only the differences are elucidated:

- **Bathymetry.** Since there were no high flows in year 2011 and 2012 that would cause significant sediment transport, the survey data on Sep 9, 2010 were used as the initial pre-flood bathymetry input for the morphodynamic model;

- **Roughness.** Manning roughness at vegetated places (i.e. bar surface, Prince's Island) was modified based on the suggested values in Phillips & Tadayon (2006). Places having bank protection structures were considered as none-erodible surfaces.

- **Bed stratigraphy.** Bed armouring was modeled by means of the bed stratigraphy module in Delft3D-FLOW, which consists two bed layers: the surface layer and the bookkeeping layer. Only sediments in the surface layer can directly interact with the flow. Once the surface layer is eroded, it gets replenished by the sediments from the bookkeeping layer below. Redundant sediments in the surface layer are pushed down to the bookkeeping layer if sediment deposits at the surface layer (Deltares, 2020). As such, the thickness of the surface layer is kept constant while the thickness of bookkeeping layer changes accordingly.

- **Sediment transport.** The thickness and sediment composition in each bed layer are shown in Table 5.3, which was based on the 1986 and 2016 bed surveys (see Table 5.1). Gauged data showed that sediments were mainly transported in the form of bedload in the model domain (Water Survey of Canada, 2024), which makes bedload the key control on the river morphology (Leopold, 1992; Williams et al., 2016). Thus, the suspended loads were not modeled. During the bedload transport process, small grains could be hidden from a current by larger, more exposed grains, known as the hiding-exposure effect. This effect is taken into account in this study by modifying the effective critical shear stress for different grain classes, using the formulation proposed by Parker et al. (1983). Bedload transport is also affected by bed level gradients. This effect is considered using the formulation proposed by

Koch & Flokstra (1980). Different bedload transport formulas were trialed in the model validation stage, which will be covered in the next section.

Table 5.3. Sediment composition in each bed stratigraphy layer

Layer	Initial thickness (m)	Sediment fractions	Median diameter (mm)	Mass fraction in the layer
Surface layer	0.3[#1]	No. 1	22.6	33%
		No. 2	89.4	33%
		No. 3	172.9	34%
Bookkeeping layer	4.0	No. 4	1.2	33%
		No. 5	30.9	33%
		No. 6	101.3	34%

- **Boundary conditions.** The hydrograph of the 2013 flood (See Figure 5.5) was used as the boundary conditions of the morphodynamic model. Due to the lack of measured bedload transport data at model boundaries during the flood, Neumann boundary condition (i.e. sediment concentration gradient perpendicular to an open boundary equals to zero) was applied at the model boundaries to calculate the input/output bedload transport rate. This means that the bedload entering or leaving the model boundaries will be near-perfectly adapted to the local flow conditions (Deltares, 2020), which is mostly the case in the Bow River based on the historical gauged data (Water Survey of Canada, 2024).

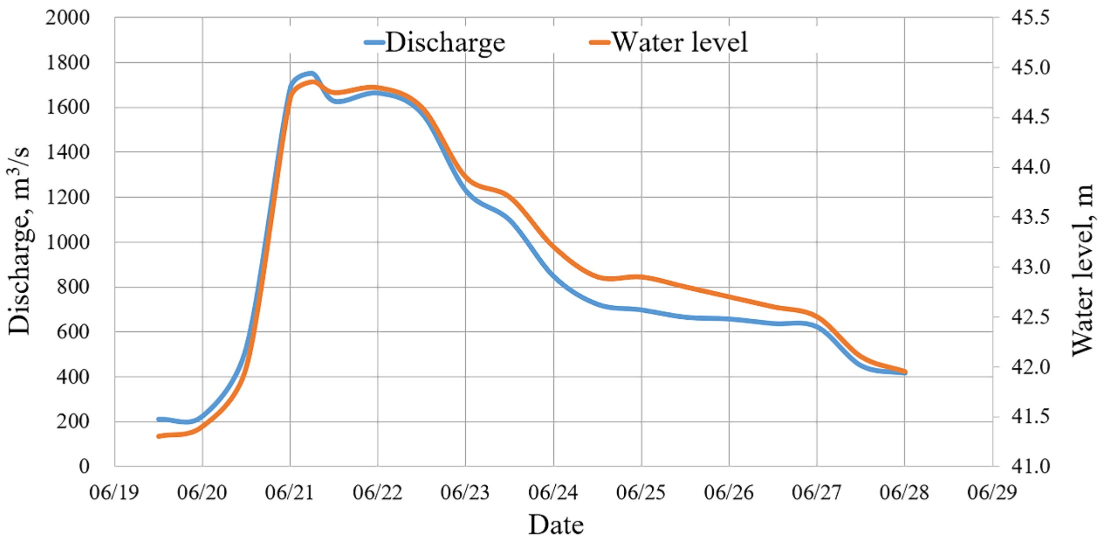

Figure 5.5. Hydrograph of the Calgary 2013 flood. Data were collected at the river gauge station 05BH004 (Water Survey of Canada, 2024)

5.4.4 Validation & sensitivity analysis

In this section, the influences of different sediment transport formulas, model dimension, and the location of the inflow boundary to the model performance were assessed by running several model scenarios. Results of those scenarios were evaluated by comparing the modeled and measured post-flood bed elevation in terms of MAE (Table 5.4).

Table 5.4. Model validation and sensitivity analysis scenarios and corresponding statistical results.

Case	Setups			Statistical results	
	Sediment transport formula	Model dimension	Inflow boundary location	Overall MAE, m	MAE at bars, m
Case 1	Van Rijn (1993)	2D	Broadview Park	0.688	0.593
Case 2	Van Rijn (1993)	2D	14 St. SW Bridge	0.692	0.371
Case 3	Van Rijn (1993)	3D#1	14 St. SW Bridge	1.483	0.734
Case 4	Soulsby/Van Rijn (1997)	2D	14 St. SW Bridge	0.607	0.446
Case 5	Meyer-Peter-Muller (1948)	2D	14 St. SW Bridge	0.643	0.478

#1 the developed 3D model has 4 flow layers and uses k-Epsilon model for 3D turbulence closure

Three bedload transport formulas were trialed: Van Rijn (1993), Soulsby/Van Rijn (1997), and Meyer-Peter-Muller (1948) (case 2, 4, & 5 in Table 5.4). It could be seen that Van Rijn (1993) produced the closest prediction in terms of the bar formation while Soulsby/Van Rijn (1997) produced the closest overall prediction. Since bar management and accurate prediction of subsequent bar formation are the major concerns in this study, Van Rijn (1993) was used in the following modeling works.

There was some concern that the upstream boundary (at 14 St. SW Bridge) is very close to the Poppy Plaza bars as well as the 10th St. bars (See Figure 5.1c). This proximity might result in inaccurate sediment transport predictions at those bars, with the implementation of Neumann boundary condition. Thus, the model sensitivity to the upstream boundary location was analyzed by moving the original upstream boundary 900 m further upstream to the Broadview Park (See Figure 5.1c) and compared the results (case 1 & 2 in Table 5.4). The model sensitivity to the model dimension was also analyzed by changing the dimension from 2D to 3D and comparing the results (case 2 & 3 in Table 5.4). It could be seen that changing the upstream boundary location or the model dimension didn't bring better results. Thus, the original upstream boundary and a model dimension of 2D were adopted in the following modeling works.

Figure 5.6 shows the measured pre-flood bed elevation, measured post-flood bed elevation, modeled post-flood bed elevation using the validated settings, and the difference between the modeled and measured post-flood bed elevation. It can be seen that the model overestimated the post-flood bed elevation at the ice anchor site (dashed circle in Figure 5.6a) and near the outer bend. The model also overestimated the volume of the 10th St. bar. Nonetheless, the developed model successfully reproduced the bar growth during the 2013 flood with respect to both location and height. The overall bed form produced by the model was also similar to the measured one, especially around the 10th St. bar and Poppy Plaza bars. From our perspective, the developed model was considered to be valid and ready for the simulations of bar management plans. However, the overestimation of deposition needs to be considered when interpreting the simulation results.

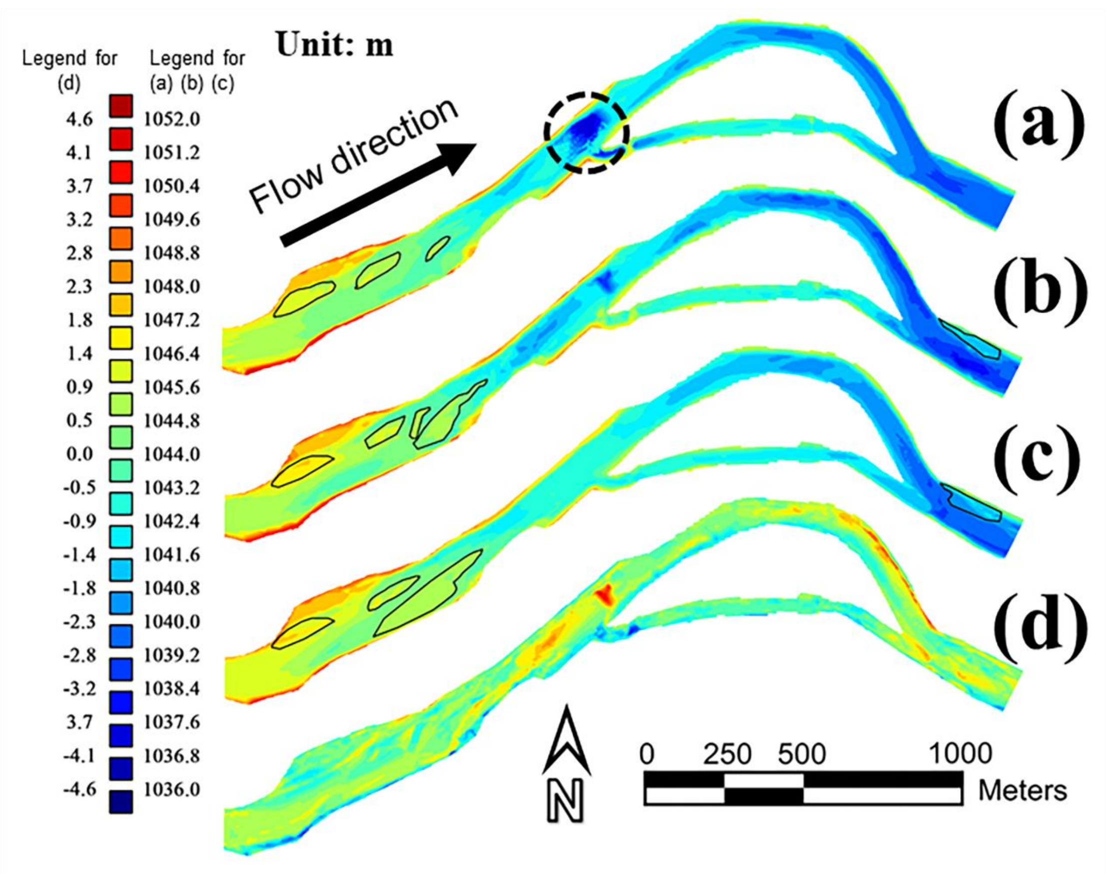

Figure 5.6. (a) Measured pre-flood bed elevation map (triangular interpolated from the ADCP survey points). Polygons mark the observed locations of channel bars. Dashed circle marks the ice anchor site; (b) Measured post-flood bed elevation map (triangular interpolated from the ADCP survey points). Polygons mark the observed locations of channel bars; (c) modeled post-flood bed elevation map using the validated settings. Polygons mark the modeled locations of channel bars; (d) Difference between the measured and modeled maps (Difference = modeled value – measured value). Floodplains are excluded from the map for better illustration.

5.4.5 Bar management plans

Bar management was carried out for the 10th St. bar and the Poppy Plaza bars (see Figure 5.1c). The measured post-flood DEM was modified to reflect the implementation of different bar management plans. Those original vegetated and non-erodible places will be kept by using the same Manning roughness unless they are modified or removed in the proposed management plans. Three bar management plans (see Figure 5.7) were implemented and modeled in this study:

(1) "Do nothing". The river bars were not modified (Figure 5.7a). This plan was designed to avoid any possible negative consequences brought by human intervention. It is also a reference option to the other two bar management plans.

(2) "Bar removal". All gravel bars around the 10th St. Bridge as well as the Poppy Plaza were removed from the channel (Figure 5.7b) to lower the future flood peak to the largest extent. A constant stream-wise bed surface slope was assigned at the removal sites in order to smoothly connect the upstream and downstream edge of the removal sites.

(3) "Bar realignment". The bar realignment plan was designed (Figure 5.7c) in order to ① restore the active channel width, ② reduce flow blockage due to the bars, ③ create new aquatic habitat, ④ create a river recreation park for surfing and kayaking. In order to minimize the possible negative consequences brought by human intervention, the total instream sediment volume before and after the bar realignment action is maintained. First, 10th St. bars will be cleared. Some of the cleared volume will be piled up to construct a wall at the middle of the channel, functioning as a flow guider and a divider. The surface of the dividing wall will be covered with riprap to prevent erosion (i.e. non-erodible). The south side of the wall will be used to construct a recreation park. Then, a side channel will be excavated at the north side of the Poppy Plaza bars, functioning as a shallow channel for fish spawning habitat. Finally, the removed gravels were realigned to the top and the tail of the bars near the Poppy Plaza.

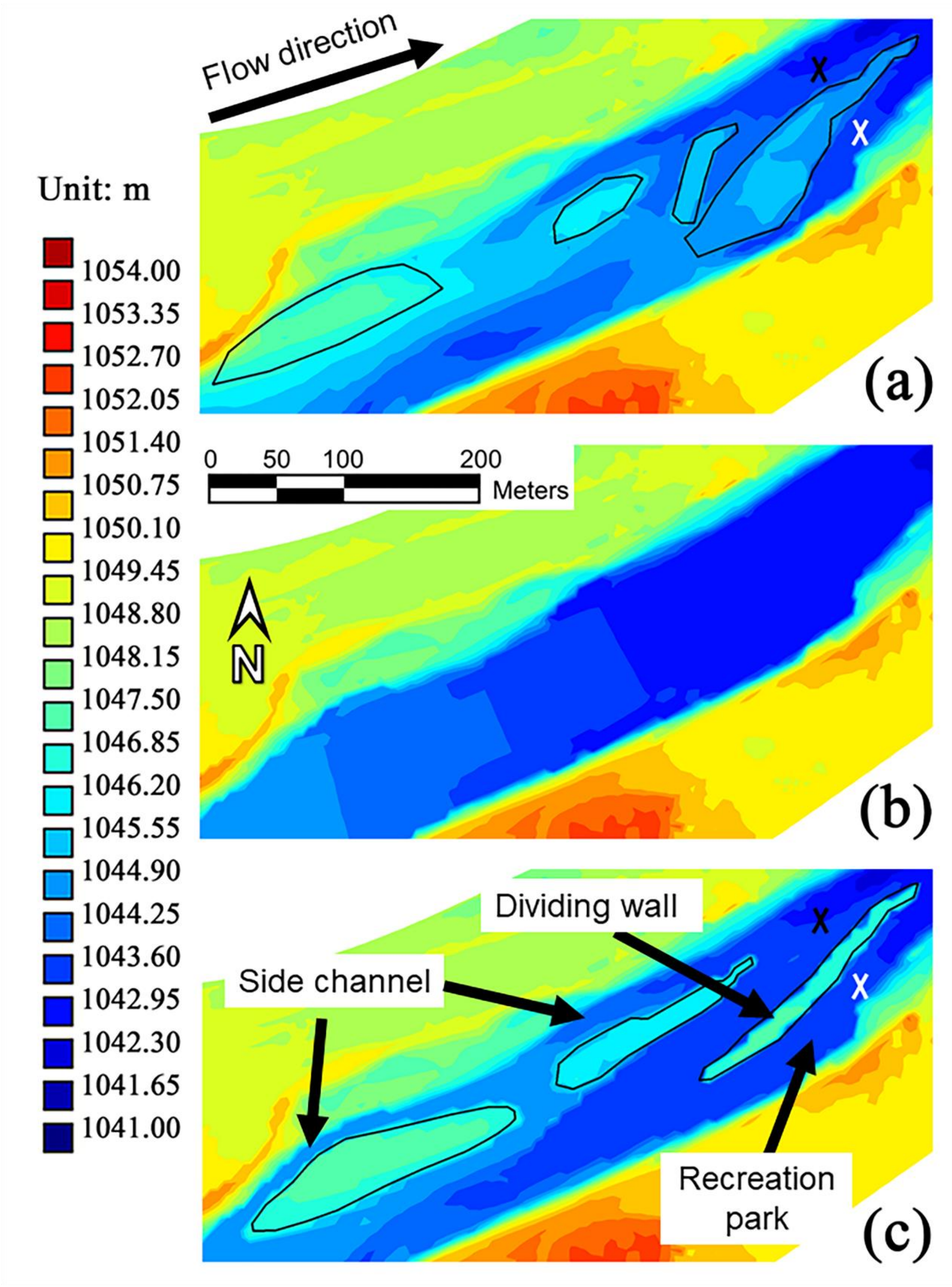

Figure 5.7. Bed elevation map of bar management plans: (a) no management; (b) bar removal; (c) bar realignment. Polygons mark the locations of channel bars. Black and white crosses mark the modeled velocity inspection sites during the long-term simulation (see Figure 5.12 for details). Black crosses: left side channel; white crosses: right side channel.

5.4.6 Design hydrographs

A future flood hydrograph is required for the morphodynamic model to simulate the performance of different bar management plans. In order to make the future hydrography closer to the reality, the hydrography was designed based on the historical daily instantaneous flow records from 1911 to 2021 (Water Survey of Canada, 2024). First, according to the study done by Slaney et al. (2019), significant bedload transport is expected to begin at around an 8-year flood ($Q \approx 700\ m^3/s$) for the Bow River. Thus, those floods with the peak discharge less than $700\ m^3/s$ were filtered out from the records. The remaining floods were two 10-year floods, one 25-year flood, one 35-year flood, and one 100-year flood. Then, the hydrograph of those floods was directly adopted and arranged together in 16 days (See Figure 5.8). Two 10-year floods were compacted in the first 4 days to represent an equivalent simulation of about 20 years, which will be noted as the "short-term" period hereafter. The entire hydrograph (i.e. 16 days) is equivalent to a simulation of about 100 years, which will be noted as the "long-term" period hereafter.

In Delft3D-FLOW, the morphological updating process could be accelerated by using the "morphological time scale factor", *MorFac*, in order to save the computational cost. *MorFac* has been used by a number studies to model the time-consuming long-term morphological process (e.g., Lesser et al., 2004; Moerman, 2011; Mool et al., 2017; Parsapour-Moghaddam et al., 2019b; Schuurman et al., 2013; Williams et al., 2016). *Morfac* is implemented in the sediment continuity equation of Delft3D-FLOW:

$$\Delta_{SED}^{(m',n')} = \frac{\Delta t \cdot f_{MorFac}}{A^{(m',n')}} \cdot \left[Q_u^{(m'-1,n')} - Q_u^{(m',n')} + Q_v^{(m',n'-1)} - Q_v^{(m',n')} \right] \tag{5.3}$$

where $\Delta_{SED}^{(m',n')}$ is the change in quantity of bottom sediment at computational cell (m',n') [kg/m^2]; Δt is the computational time step [s]; f_{MorFac} is the user-defined morphological time scale factor, *MorFac* [-]; $A^{(m',n')}$ is the area of cell (m',n') $[m^2]$; $Q_u^{(m',n')}$ is the computed bedload sediment transport rate in the u direction at cell (m',n') [kg/s].

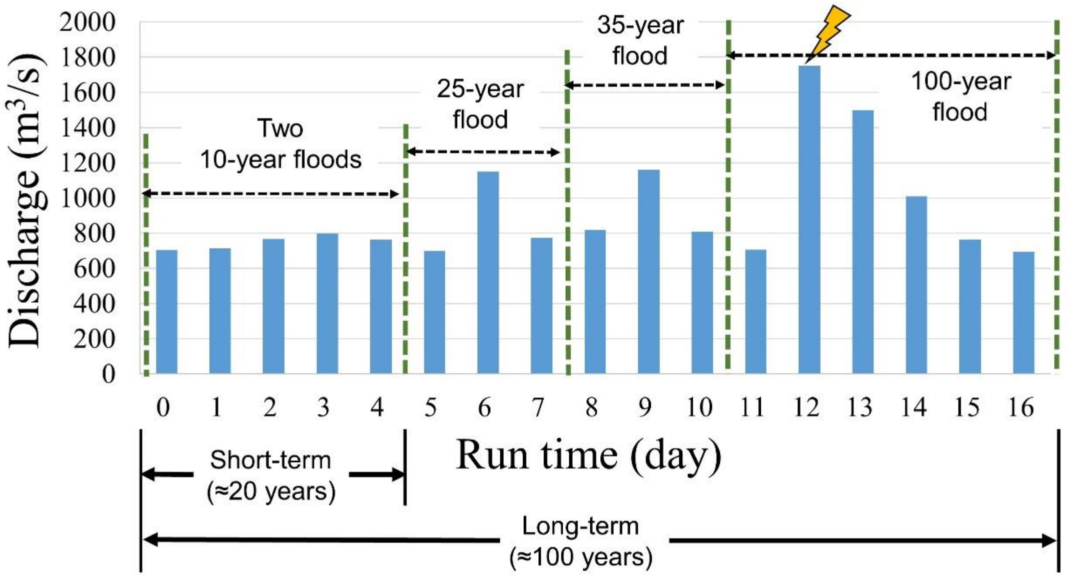

Figure 5.8. The designed future hydrograph. The lighting bolt symbols represent the flood peaks that are going to be investigated and compared between different bar managements in terms of flood mitigation.

The model sensitivity to *MorFac* needs to be analyzed prior to use, as recommended by Delft3D (Deltares, 2020). To do this, we designed three model scenarios with different combinations of *MorFac* and the simulated event time while keeping the total equivalent event time as well as the time step the same: ① *MorFac* = 1, simulated event time = 16 days, equivalent event time = 16×1 = 16 days; ② *MorFac* = 5, simulated event time = 3.2 days, equivalent event time = 3.2×5 = 16 days; ③ *MorFac* = 10, simulated event time = 1.6 days, equivalent event time = 1.6×10 = 16 days. We ran those three scenarios with the bar management plan of "do nothing". Results showed very little differences between case ① and case ② in terms of the developed bed morphology (See Figure B1, a & b in Appendix B). In contract, no bed level change were found in case ③ (See Figure B1-c in Appendix B), which indicates the large model instability when using *MorFac* = 10. Thus, *MorFac* = 5 was adopted in subsequent simulations.

5.5 Results

In all three bar management plans, the morphological evolution pattern of the short-term and long-term simulations was similar. In addition, a similar pattern of flood mitigation could be found between the 35-year flood and the 100-year flood for all bar management plans. Thus, only the results of long-term morphological evolution as well as the 100-year flood of different bar management plans are presented herein. The results of short-term morphological evolution as well as the 30-year flood peak level of different bar management plans can be found in Figure B2 & B3 from Appendix B

5.5.1 Morphological impacts

Figure 5.9 & 5.10 shows the cumulative deposition (or erosion) map and bed elevation map of different bar management plans after the long-term simulation, respectively. The simulation results show that:

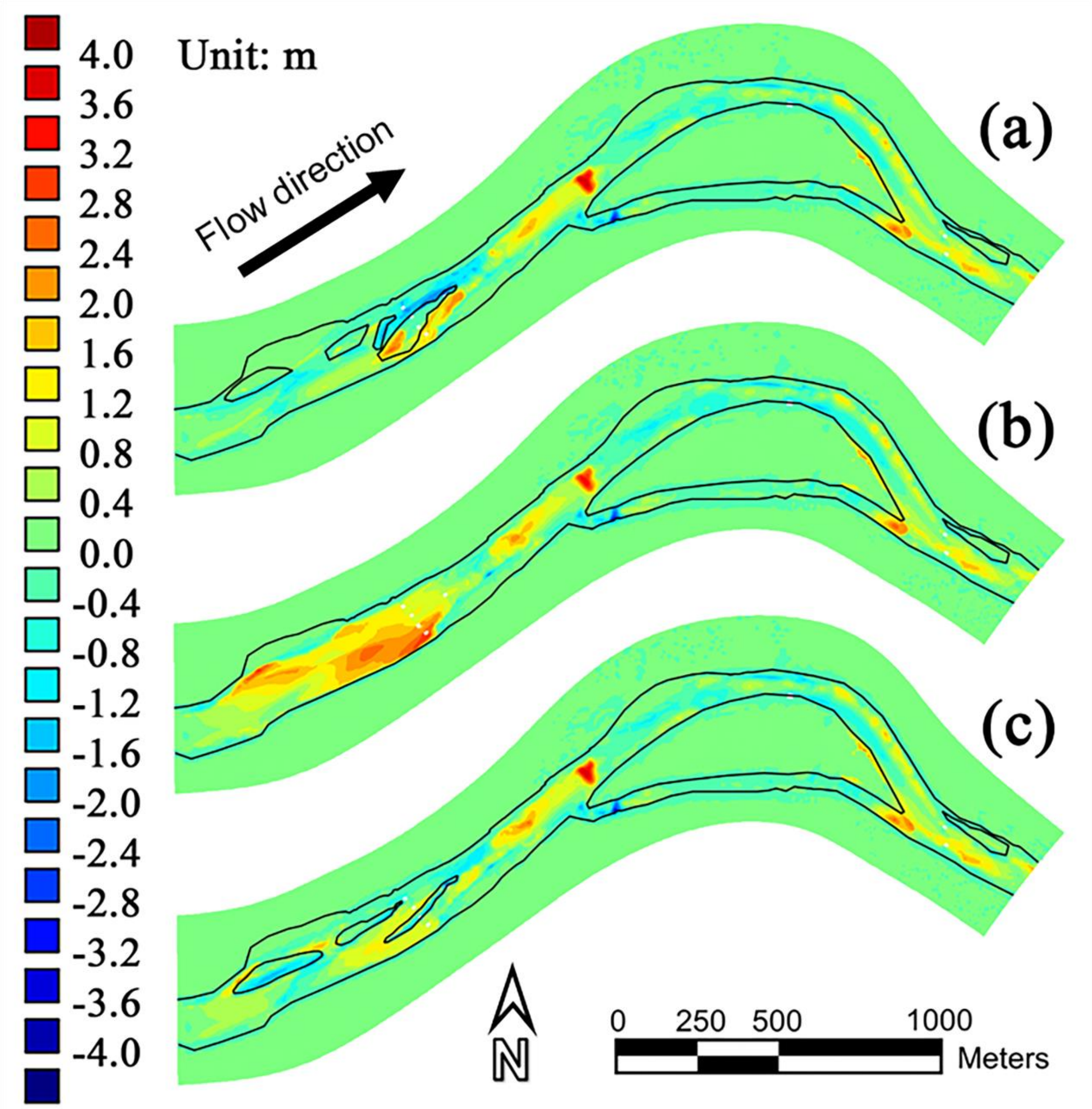

Figure 5.9. Cumulative deposition (red) and erosion (blue) map of different bar management plans after the long-term simulation: (a) Do nothing; (b) bar removal; (c) bar realignment. Polygons show the channel boundary and the channel bars before the run.

- **Do nothing.** If nothing is done on the instream bars, deposition will keep occurring at the tip and the right side of the 10th St. bar while erosion will happen at the left side of the 10th St. bar (Figure 5.9a) after the long-term simulation, which will result in a total occupancy of the right side of the river channel and a deep scour hole near the bridge piers (Figure 5.10a).

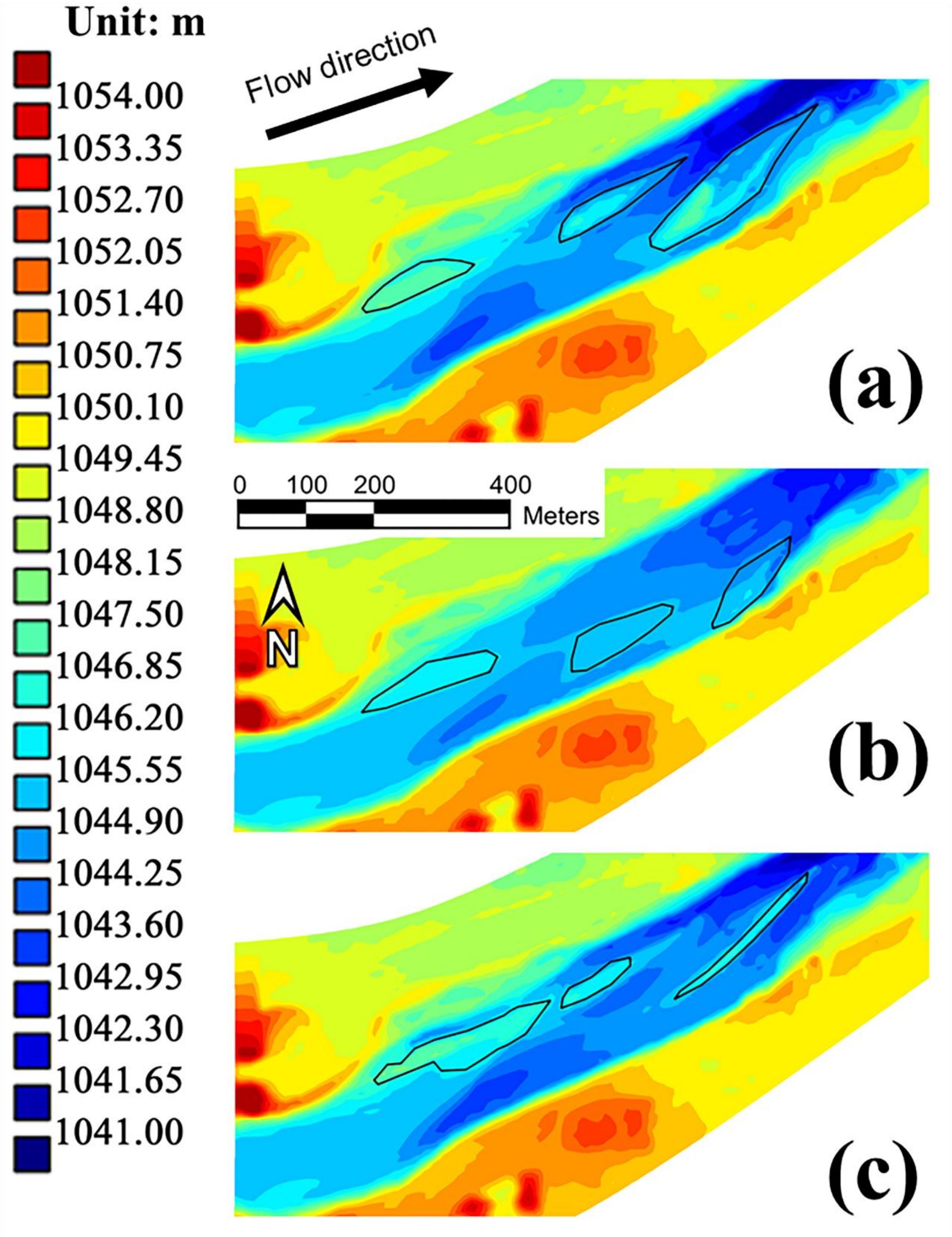

Figure 5.10. The bed elevation map of different bar management plans after the long-term simulation. (a) Do nothing; (b) bar removal; (c) bar realignment. Polygons show the channel bars after the run.

- **Bar removal.** As for the bar removal plan, abundant deposition happens at the bar removal sites. If comparing with the original bars, it can be seen that the new bars deposit at similar locations but with smaller dimension and lower height, compared to the original bars (Figure 5.7a and 5.10b). Different from the “do nothing” plan, the overall bed form will be nearly uniform and flat after the long-term simulation following bar removal.

- **Bar realignment.** In the bar realignment plan, minor deposition is predicted to happen around the tip of the dividing wall as well as at the entrance of the side channel near the Poppy Plaza bars (Figure 5.9c). The overall bed form at the bar management site does not change too much, compared with the other two management plans. No deep scour hole or high-elevated bars are observed in the results of bar realignment.

Noteworthy, similar downstream morphological impacts are predicted by the model regardless of the choice of bar management plans, which are: deposition is predicted to happen at the beginning and the end of the river bend while slight erosion will happen at the channel bed within the river bend. The long-term simulation results did not show any clear bank erosion for all three bar management plans.

5.5.2 100-year flood peak level

Figure 5.11 shows the flood mitigation performance of bar removal and bar realignment in terms of the modeled 100-year flood peak level. The mitigation performance was evaluated by calculating the 100-year flood peak level difference between the manipulation plans (i.e. bar realignment and bar removal) and the “do nothing” plan.

Bar removal is predicted to lower the 100-year flood peak by 0.26 m on average at the bar management site (dashed rectangle in Figure 5.11a). In contrast, bar realignment lowers the flood peak by 0.07 m on average at the bar management site (dashed rectangle in Figure 5.11b). Noteworthy, the flood peak level is predicted to be increased by about 0.15 m near the dividing wall in the bar realignment plan. No obvious flood level change is found for the downstream reaches in either case. In addition, by investigating the overbank flood extent, it can be seen that bar removal is predicted to result in a slightly smaller overbank flood extent compared to bar realignment (red arrows in Figure 5.11).

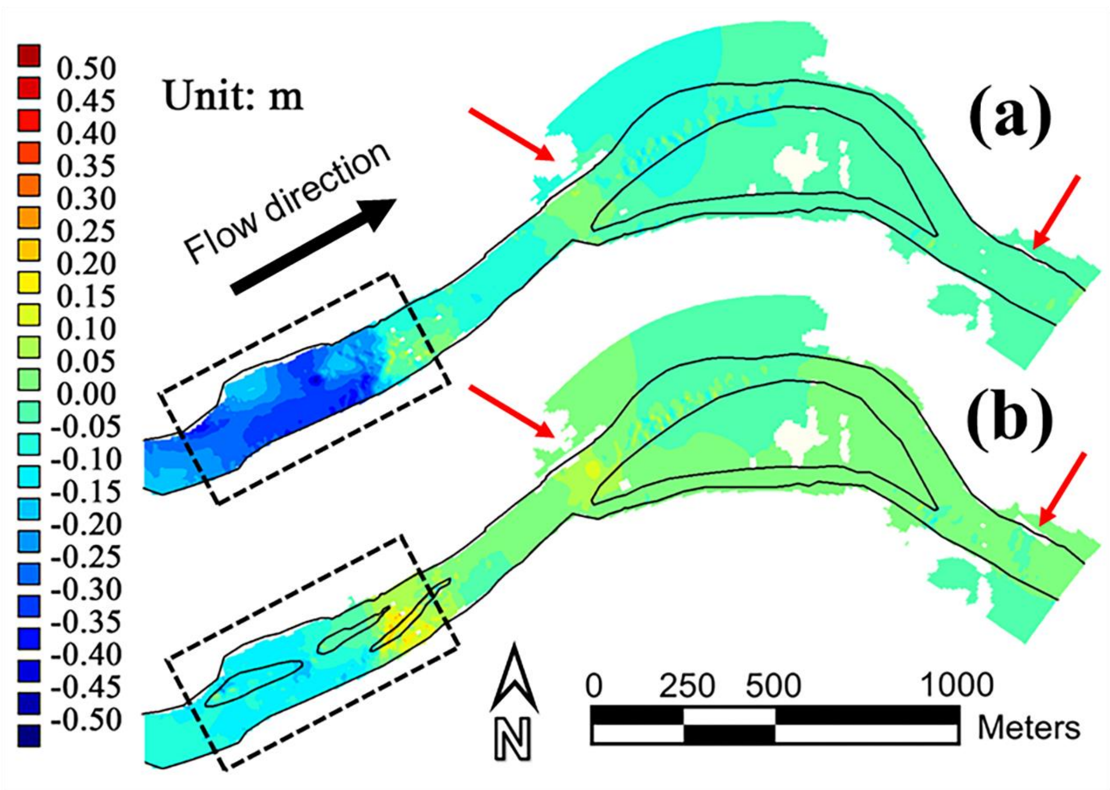

Figure 5.11. The 100-year flood peak level difference (a) between "bar removal" and "do nothing" (Difference = bar removal – do nothing), (b) between "bar realignment" and "do nothing" (Difference = bar realignment – do nothing). Red arrows show the locations of flood extent differences between bar removal and "do nothing". Dashed rectangles represent the "bar management site"

5.6 Discussion

5.6.1 Morphological impacts

If nothing is done to the instream bars around the 10th St. Bridge, deposition is predicted to happen at the tip of the 10th St. bar in the following flood events. The deposition site is right ahead of the site of dense vegetation at the 10th St. bar surface, which suggests that riparian vegetation colonization on the bar surface would probably induce additional resistance to the flow, thus cause sediment aggregation around the bar during the next flood event. Deposition is also observed in the right side channel (looking from upstream) near the 10th St. bar, which is probably owing to the low flow velocity in the right side channel (the orange dashed line in Figure 5.12). Figure 5.10a shows the deposition at the right side channel would block the right side channel, which makes the floodwater mostly go through the left side channel. As a result, velocity in the left side channel dominates (the blue dashed line in Figure 5.12), which further causes significant scour at the left side channel (about 1.5 m deep, see Figure 5.9a). This scour would impact the stability of the bridge piers and also the left channel bank. In summary, the “do nothing” plan is predicted to result in a narrower and deeper river channel at the bar management site after a long-term period, compared to the original river channel.

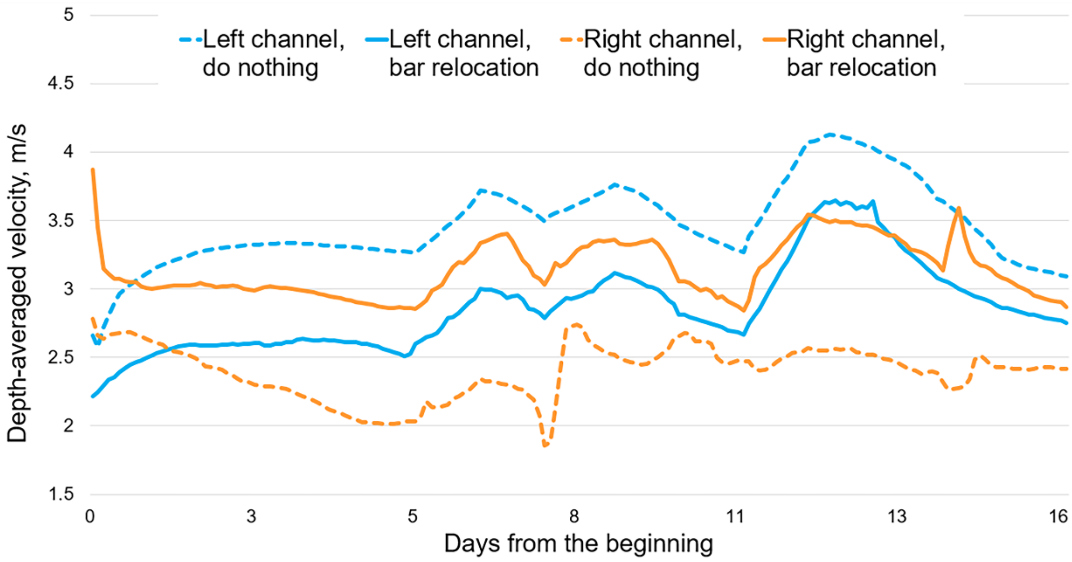

Figure 5.12. Time-series of modeled velocity at the right side channel (orange lines) and left side channel (blue lines) near the 10th St. bar/dividing wall for the “do nothing” plan (dashed lines) and bar relocation plan (solid lines) during the long-term simulation. Velocity inspection sites are marked by black (left side channel) and white crosses (right side channel) in Figure 5.7.

In the bar removal plan, bars are predicted to reoccur at the bar management site after several flood events. This is probably because the channel widens when flow enters the bar management site, which makes the flow velocity drop and thus causes deposition. The bar recurrence phenomenon has been widely observed both from field works (e.g. Church et al., 2001; Collins & Dunne, 1990; Yuill et al., 2016) and numerical studies (e.g. Li et al., 2008; Yuill et al., 2016; Parsapour-Moghaddam et al., 2019b), which reflects the resilience of alluvial river channels to an external disturbance. However, uncertainty remains in terms of the size of the reoccurred bars compared to the original bars: the reoccurred bar in Li et al. (2008) was lower in height compared to the original bar after a simulation of 10 years. In contrast, the reoccurred bars in Parsapour-Moghaddam et al. (2019b) were found to be bigger than the original bars. In this study, the reoccurred bars were both smaller and lower compared to the original bars before the bar removal after the long-term simulation, which coincides with the finding in Li et al. (2008) but different with Parsapour-Moghaddam et al. (2019b). This is probably because the *MorFac* used in Parsapour-Moghaddam et al. (2019b) was 20, which could result in significant model instability issues, as reported by Williams et al. (2016).

Similar to the plan of “do nothing”, the dividing wall in the bar realignment plan also induces blockage to the flow, which results in deposition at the tip of the dividing wall. However, the deposition amount at the tip in the bar realignment plan is much smaller compared to that in the “do nothing” plan (Figure 5.9, a & c). This is because the blockage effect of the thin dividing wall to the flow is smaller than the effect of a wide 10^{th} St. bar. After constructing the dividing wall, the channels on each side of the dividing wall have similar width and thus similar flow velocity (see Figure 5.12), which prevents significant erosion/deposition from happening at both side channels. Overall, the bar realignment plan is predicted to produce the most stable bed form at the bar management site after a long-term simulation compared with the other two plans.

In terms of downstream morphological impacts, both the bar realignment plan and the “do nothing” plan resulted in similar downstream bed morphology between the short-term (Figure B2, a & c in Appendix B) and long-term simulation (Figure 5.9, a & c). This is because both of these two plans preserve the instream sediment volume, which brings little impact to the overall bedload transport pattern at the reach scale. Different from the bar realignment plan and the “do nothing” plan, very little deposition is found at the ice anchor site in the bar removal plan after the short-term simulation (Figure B2-b in Appendix B). This is because bar removal clears and widens the river channel and create a large area of “sediment-starving” regions at the beginning of the simulation. These regions capture most of the sediment coming from upstream and prevent them from going further downstream during the two 10-year floods. As the sediment accumulates in these regions, the “sediment-starving” situation is mitigated. Thus, after the two 10-year floods, much less subsequent deposition happens at the bar removal site, compared to the depostion during the two 10-year floods (i.e. not much difference at the bar removal site between Figure B2b & Figure 5.9b). Excessive sediment is transported further downstream to the ice anchor site and deposits (Figure 5.9b). Excessive sediment is transported further downstream to the ice anchor site and deposits (Figure 5.9b). It could be seen that although bar removal may generate a short-term sediment deficit to the downstream reach, this deficit could be mitigated or even eliminated in a long-term period. As for the further downstream places (i.e. around Prince’s Island and Center St. Bridge), the morphological evolution pattern is similar among all three management plans, both in short-term and long-term, which demonstrates the impact range of such intervention is very limited (about 1 km). In the end, the downstream morphological patterns of the three different bar management are predicted to be similar, which agrees with the filed work results in Wishart et al., (2008).

Thus, it could be concluded that manipulation on vegetated bars has little morphological impacts to downstream reach.

5.6.2 Flood mitigation

Figure 5.11 indicates that the "do nothing" plan has the highest 100-year flood peak level at the bar management site among all three bar management plans, which confirms the hypothesis that the existing bars pose a high flood risk to the city. Figure 5.11 also shows that the bar removal plan results in a lower 100-year flood peak level at the bar management site and a slightly smaller downstream flood extent, compared to the bar realignment plan. Similar results could be found for the 30-year flood peak level (see Figure B3 in Appendix B). Thus, based on the simulation results, the bar removal plan performs the best in terms of flood risk mitigation among the three bar management plans. However, the constructability and impacts of wholesale dredging in bar removal are significant and likely not practice in this case. As for the bar realignment plan, in order to preserve the volume of instream bars, some excessive sediment is piled up to form the dividing wall at the design stage. This high-elevated dividing wall is considered to increase the 100-year flood peak level near the dividing wall. Regardless, the designed bar realignment plan in this study does mitigate the flood risk at most places of the bar management site, which demonstrates the potential of generic bar realignment actions in terms of flood mitigation. In other words, if instream bars are realigned in a different way, it is reasonable to believe that the new plan will result in an even better flood mitigation effect. In addition, some combination of the bar removal and realignment options might also present a good option in terms of flood mitigation.

There is an interesting phenomenon in the relation between flood peak mitigation and bed elevation change: bar removal is predicted to lower the 100-year flood peak by 0.26 m on average at the bar management site (Figure 5.11a), compared with the "do nothing" plan. However, the average bed elevation difference at the bar management site between bar removal and "do nothing" at the time of 100-year flood peak is only 0.0029 m (see Figure 5.13). This high inconsistency indicates that the quantitative bed elevation difference between those two cases at the time of 100-year flood peak is not the fundamental cause of the flood peak reduction. To the authors' point of view, this reduction is because the bar removal case brings a more uniform and less obstructed bed form compared to the "do nothing" case at the time of 100-year flood peak, which resulted in a lower flow resistance and thus greater ability to convey flood water. In comparison, the average bed elevation difference at the bar management site between bar realignment and "do nothing" at the time of 100-year flood peak is 0.07 m (Figure 5.11b). Since the sediment volume in the bar realignment case is preserved, the mitigation to the flood water blockage is limited. Thus, the quantitative bed elevation difference becomes dominant in the determination of the flood peak reduction, which is 0.07 m in average at the bar management site (Figure 5.13). It could be learned that simply relating the lowering of flood peak level to the lowering of river bed level could be misleading, as the propagation of floodwater is a continuous and highly dynamic progress. Flood peak could still be lowered through altering the river bed form and lowering flow resistance, with or without lowering of river bed level. The approach of creating a uniform, less obstructed river bed form needs to be paid more attention in terms of fluvial flood mitigation.

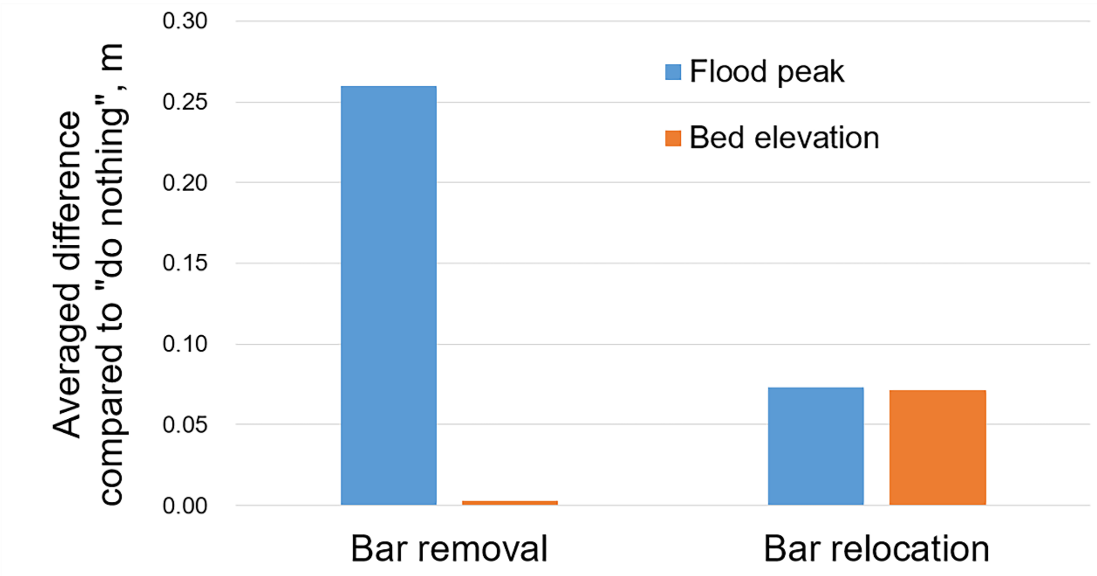

Figure 5.13. The average flood peak difference and bed elevation difference at the bar management site between bar removal (or bar realignment) and "do nothing" at the 100-year flood peak. Difference = "do nothing" - "bar removal" (or "bar realignment").

5.6.3 Aquatic habitat & river recreation

Figure B2b (in Appendix B) shows that after total bar removal, it will likely require several bed mobilizing flood events and thus possibly decades for the bars to reform. During those years, the bed morphology at the bar removal site will be relatively flat and uniform, which is generally unfavorable for fish habitat. Even after the recurrence of the instream bars, the overall bed morphology is still more uniform and lower in variety compared to the bar realignment plan or "do nothing" plan. In contrast, after the long-term run of using the bar realignment plan, although the entrance to the designed fish-spawning side channel near the Poppy Plaza bar is blocked, the side channel is still accessible during high-flow, which could provide refuge for fish during floods. In addition, the bed form variety in the bar realignment plan is quite high and remains relatively stable without significant deposition or erosion after a quite long term. This provides a favorable condition for aquatic ecosystem development for fish, water birds, as well as aquatic plants. In summary, the bar realignment plan performs better in terms of the protection of aquatic habitat compared to the bar removal plan.

At the design stage of different bar management plans, a river recreation park was proposed at the right side of the dividing wall in the bar realignment plan. According to the long-term simulation results (Figure 5.11c), no significant deposition or erosion occurs at the right side channel, which indicates that the river recreation park could maintain its normal functionality for a long time without maintenance works such as dredging. In contrast, this site was both filled with sedimentation in the bar removal plan and the "do nothing" plan. In conclusion, the bar realignment performs the best in terms of the realization of river recreation purpose among all three bar management plans.

5.6.4 Limitations and future concerns

The use of numerical models always involves a compromise between the computational cost and model details. In addition, numerical models also require a series of assumptions to represent and simplify the actual physical process and properties, which brings additional uncertainties to the results. Limitations of this study are addressed herein for further improvement:

- In order to save computational cost, the model domain only includes a part of the dry land, which prevents the floodwater to propagate further across the inland model boundary. Nonetheless, the modeled flood inundation areas match with the observed flood extent (Zhang & Crawford, 2020). Thus, this limitation was not considered to influence the model results, especially the morphodynamic aspect. Future study could extend the model domain so that the overall flood extent could also be used as a validation parameter.

- Impact from climate change is not considered in the design hydrograph, which limits the application of the projection results. Nonetheless, this study mainly focuses on the comparative study of the performance of different bar management plans. Thus, results are still meaningful to understand instream bar management and guide engineering practice. Climate change could be introduced in future studies to study the resulted bed form of a pre-selected bar management plan in a more accurate manner.

- Delft-3D is not capable of modeling the colonization process of bar surface vegetation during a series of flood events. In reality, the bar removal option might create new bars that quickly vegetate and become permanent, they may be even more stable, grow even faster, and result in even higher flood levels at the bar management site than the model assumes. Thus, the actual flood mitigation effect of bar removal might not be that good. Again, since this study is mainly a comparative study and the colonization process is not considered for all three cases, results are still meaningful.

5.7 Conclusion

In this study, we developed a high-resolution morphodynamic model to reproduce the flood-induced morphological change in the Bow River, Calgary. We then utilized the developed morphodynamic model to evaluate the performance of three gravel bar management plans in terms of morphological impacts, flood mitigation, aquatic habitat protection, and possible river recreation use. This study demonstrates the consequences of instream bar management to the riverine environment and shows the great potential of a morphodynamic model as an impact and risk assessment tool. Several conclusions could be drawn herein:

- If no management action is taken to deal with the flood-induced instream bars in Bow River, the river channel is predicted to become narrower and deeper near those bars, which brings instability issues to the bridge piers and a high flood risk to the riverine neighborhood.

- Bar removal may bring a sediment deficit at the removal site, which induces bars recurrence in the Bow River case. The reoccurred bars are predicted to be both smaller and lower compared to the original bars. Although bar removal presents the best flood mitigation effect among all three plans, the constructability and ecological impacts of wholesale dredging should not be overlooked.

- Bar realignment plan can stabilize the channel bed thus performs better in terms of aquatic habitat protection as well as the realization of river recreation in the Bow River case. Although the proposed bar realignment plan in this study has limited ability to mitigate flood risk due to the construction of a dividing wall, it is reasonable to speculate that a different realignment strategy could have better mitigation effects.

- The downstream morphology could be affected in a short-term if the bar management plan brings sediment deficit to the Bow River reach (i.e. bar removal). However, no matter which plan is applied, the downstream morphological patterns are predicted to be similar in a long-term. Thus, manipulation on vegetated instream gravel bars does not have obvious morphological impact to the downstream river reach.
- Simply relating the lowering of flood peak level to the lowering of river bed level could be misleading because the propagation of floodwater is a continuous and highly dynamic progress. Creating a uniform, less obstructed river bed is believed to be the fundamental strategy in flood mitigation.

Chapter 6. TiFA: An Efficient and Robust LSPIV Algorithm Based on Joint Distribution Analysis

6.1 Abstract

The incapability of processing flow velocities under low tracer density conditions is one of the limitations of the traditional Large-Scale Particle Image Velocimetry (LSPIV). This study developed a new LSPIV algorithm, Time Frequency Analysis (TiFA), to overcome such a limitation, enhance computational efficiency, and improve the accuracy of derived velocities. TiFA investigates the temporal joint distribution pattern of two velocity components at each location. By assuming that the valid velocities follow a quasi-normal distribution in the velocity time series, TiFA can quickly and accurately separate the valid velocities from background noise and outliers. The performance of TiFA was evaluated by comparing with other algorithms including Traditional LSPIV, Ensemble Correlation (EC), Large-Scale Particle Tracking Velocimetry (LSPTV), and Seeding Density Index (SDI) in an experimental hydraulic model and two field cases. TiFA showed the highest overall accuracy and lowest computation cost in data analysis, especially under low tracer density conditions. In addition, TiFA showed its unique ability of automatically filtering out velocity data from low-quality zones such as no-tracer zones and surface glare zones. TiFA also showed its potential in processing turbulent flow. In summary, the newly-developed algorithm, TiFA, has demonstrated strong capability and competence in various flow and tracer scenarios, making it a valuable candidate for future applications.

6.2 Introduction

Flow velocity measurement is the fundamental step of understanding flow behaviors. Velocities can be measured using either intrusive or nonintrusive techniques. Intrusive techniques involve placing instruments, such as propeller current meters, electromagnetic current meters, Acoustic Doppler Velocimetry (ADV) and Acoustic Doppler Current Profilers (ADCP), into the flow to measure velocity. However, intrusive techniques become inefficient for situations that require knowledge of the spatial distribution of flow velocities over a large area. As an alternative, nonintrusive techniques can measure a wide range of flow movement simultaneously using camera recordings (which provide particle locations at different time steps) and control points (which provide reference distance). Commonly used nonintrusive approaches include Particle Image Velocimetry (PIV), Particle Tracking Velocimetry (PTV), Kanade Lucas Tomasi Image Velocimetry (KLT-IV) (Perks, 2020), Space-Time Image Velocimetry (STIV) (Fujita et al., 2007), Surface Structure Image Velocimetry (SSIV) (Leitão et al., 2018), and Optical Tracking Velocimetry (OTV) (Tauro et al., 2018b).

Large Scale Particle Image Velocity (LSPIV) is one of the PIV approaches that can be applied in large-scale flow domains such as rivers to measure surface flow velocities (Fujita et al., 1997). Its reliability and performance have been tested in many different scenarios. For example, Muste et al. (2004) showed that the relative error of LSPIV was less than 1.5% under ideal conditions in a physical model. Bandini et al. (2022) showed that LSPIV could reconstruct the river velocity profile with an accuracy of a few centimeters/seconds and coefficient of determinations (R^2) larger than 0.7 (in half of the cases larger than 0.85). LSPIV has been applied in many different situations such as measuring velocities in ship-induced waves (Fleit & Baranya, 2022), near hydraulic structures (Strelnikova et al., 2020; Kantoush et al., 2011), in steep bedrock canyons (Ansari et al., 2018), and during flood events (Le Coz et al., 2010; Lin et al., 2024). Recent studies also showed the capability of integrating LSPIV with artificial intelligence (Ansari et al., 2023) and satellite platform (Legleiter & Kinzel III, 2021; Masafu & Williams, 2024).

LSPIV requires a clear and consistent identification of certain flow surface features to ensure a correct estimation of instantaneous velocity vectors from cross-correlation calculation in consecutive frames (Dal Sasso et al., 2021). Natural surface features such as ripples and foams can be used in LSPIV when there is enough turbulence (Liu et al., 2021; Li & Yan, 2022). However, such conditions do not always exist in all rivers at all times. Artificial surface tracers are commonly introduced to the flow by seeding the study area with particles such as wood chips (Detert et al., 2017), rice cereal (Duan et al., 2023), eco foams (Strelnikova et al., 2020), and fluorescent particles (Naves et al., 2019) to facilitate image interpretation. Either way, high tracer density is crucial for accurate velocity estimates using traditional LSPIV. Otherwise, the instantaneous velocity vectors derived from no-tracer zones will be different (usually lower) from those vectors derived from other zones, which underestimates the final velocity after time-averaging. However, favourable tracer conditions were rarely encountered both in experimental and field studies (Muste et al., 2004; Lewis & Rhoads, 2015; Yu et al., 2015; Tauro et al., 2017; Dal Sasso et al., 2020), which becomes one of the major limitations of traditional LSPIV (Tauro et al., 2017).

There are several options to deal with the velocity processing issue under low tracer density conditions:

- **Ensemble Correlation (EC).** EC was originally developed by Santiago et al. (1998) as a velocity vector processing algorithm in MicroPIV. It was then introduced to LSPIV by Meinhart et al. (2000). Since then, EC has been further refined and improved through various studies (Westerweel et al., 2004; Sciacchitano et al., 2012; Theunissen & Edwards, 2018; Edwards et al., 2020). It showed improved performance in many different low tracer density situations (e.g. Jeon et al., 2014; Strelnikova et al., 2020; Ljubičić et al., 2024), compared to traditional LSPIV. In addition, as a subsidiary tool of traditional LSPIV, EC does not involve additional user-defined parameters. However, EC showed limited ability in turbulent flow situations (Strelnikova et al., 2020). In addition, since EC does not involve any data filtering process, EC users could not tell if the processed velocity vectors are derived from the movement of the tracers or merely from background noise. Moreover, EC showed a high computational cost and unreliable correlation results when processing a large number of frames in large-scale domains (Strelnikova et al., 2020).
- **Large-Scale Particle Tracking Velocimetry (LSPTV)**. Different from LSPIV, where velocities are associated with integration windows, velocities derived from LSPTV are associated with surface tracers. In this way, LSPTV avoids generating velocities from the places where there are no tracers. Recent studies have shown that LSPTV is an optimal choice as opposed to traditional LSPIV under low tracer density conditions (Tauro et al.,2017; Dal Sasso et al., 2020) and in unsteady flows (Tauro et al., 2018a). However, LSPTV requires the size and shape of the tracers

to be clear, uniform and consistent across frame pairs (Gharahjeh & Aydin, 2016; Dal Sasso et al., 2020; Pearce et al., 2020). In addition, Jolley et al. (2021) reported that detecting erroneous vectors is more challenging in LSPTV due to its unstructured features (i.e., does not conform to a gridded system as LSPIV does).

- **Seeding Density Index (SDI)**. SDI was developed by Pizarro et al. (2020a), tested in field cases and further improved by Pizarro et al., (2020b) and Dal Sasso et al. (2021). The advantage of SDI is that it focuses only on those frames where tracers are relatively dense and disregards the others for a specific region, which indirectly increases the tracer density and significantly reduces the computational loads at the selected region. However, the performance of SDI highly relies on the selection of the Area of Interest (AOI): a smaller size of AOI will produce better results (Dal Sasso et al., 2021), but a smaller size of AOI might also increase the computational cost globally.

In order to overcome the limitations of the abovementioned algorithms and improve the accuracy and efficiency of surface velocimetry processing under low tracer density conditions, we developed a new LSPIV algorithm named Time Frequency Analysis (TiFA). TiFA investigates the temporal joint distribution pattern of two velocity components at each location. Then, by assuming that the valid velocities follow a quasi-normal distribution in the velocity time series, TiFA can quickly separate the valid velocities from background noise and outliers. TiFA was applied to estimate flow velocities from video footage of an experimental hydraulic model (will be noted as "physical model" hereafter) and two field cases. The performance of TiFA was evaluated by comparing velocity results to those derived using the other aforementioned algorithms including the traditional LSPIV, EC, LSPTV, and SDI. The newly developed algorithm, TiFA, demonstrated the highest overall accuracy and lowest computation cost in data analysis among all five algorithms, especially under low tracer density conditions. In addition, TiFA showed its unique ability of automatically filtering out velocity data from low-quality zones such as no-tracer zones and surface glare zones. TiFA also showed its potential in identifying the average flow velocity from a turbulent flow region.

6.3 Methodology

6.3.1 Image velocimetry algorithms

This section introduces the concepts and data process procedures of five image velocimetry algorithms that were used in this study. All images used in the analysis were orthorectified. The data process procedures are also illustrated in Figure 6.1.

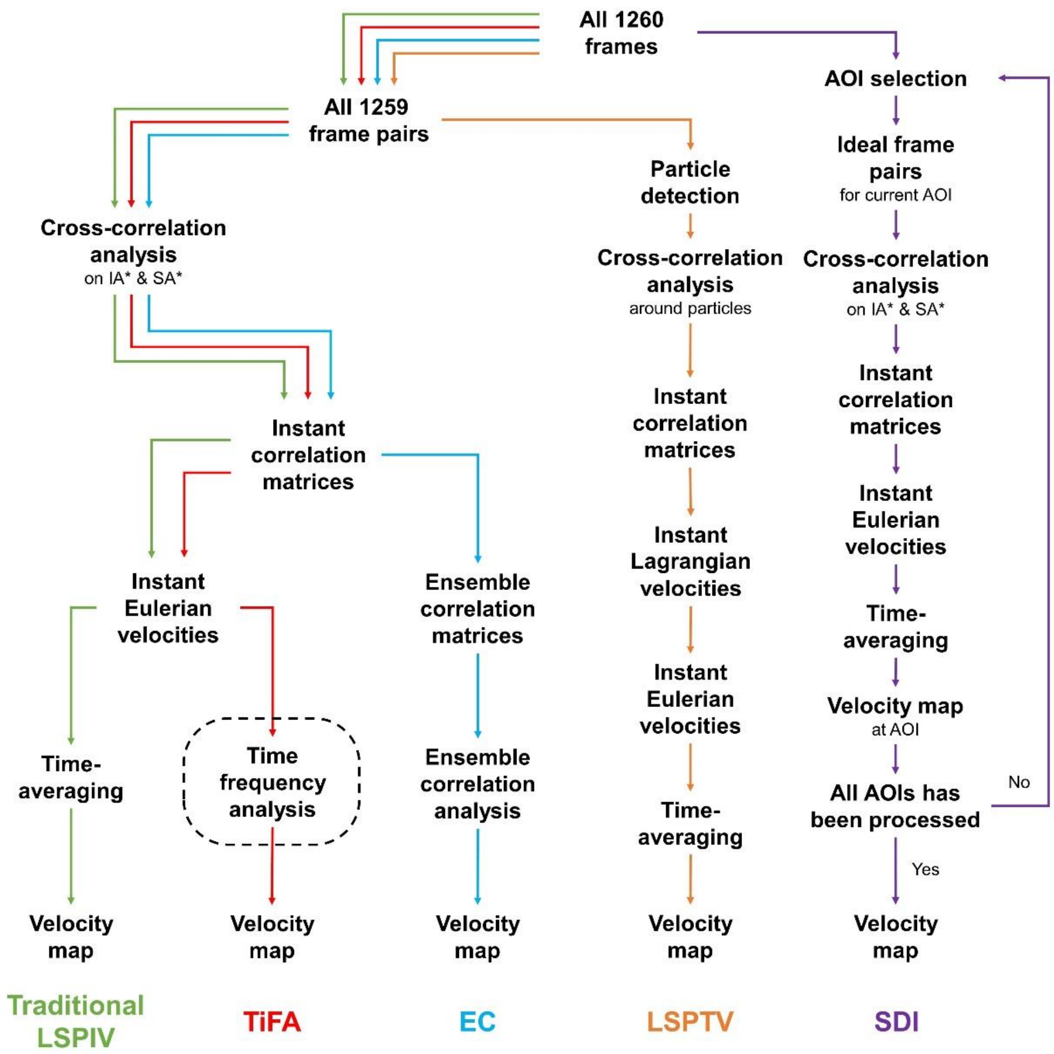

Figure 6.1. Data process procedures of different surface velocimetry algorithms: Traditional LSPIV, TiFA, EC, LSPTV, and SDI. "IA" is the abbreviation for "Interrogation Area". "SA" is the abbreviation for "Search Area".

6.3.1.1 Traditional LSPIV

At a specific region (i.e., determined by the interrogation area), traditional LSPIV first calculates the instantaneous correlation matrix ($M_{t=1}$) from one frame pair by performing cross-correlation analysis in neighboring regions (i.e. search area). Then, the instantaneous velocity vector ($V_{t=1}$) is determined by searching the peak value from the instantaneous correlation matrix. This process is repeated for all frame pairs to derive a time series of instantaneous velocity vectors ($V_{t=1}$, $V_{t=2}$, $V_{t=3}$, … , $V_{t=T}$) at that region. The final velocity vector ($\bar{V}$) at that region is determined by averaging all instantaneous velocity vectors. This process is repeated for all regions across the frame to generate a complete spatially-distributed velocity map. More details of traditional LSPIV algorithms can be found in (Raffel et al., 2018).

The freeware RIVeR version 2.6 (Patalano et al., 2017) with PIVlab version 2.59 (Thielicke et al., 2021; Thielicke, 2022) was used in this study to perform traditional LSPIV analysis. Traditional LSPIV algorithm used the Fast Fourier Transformation (FFT) window deformation method to perform correlation analysis on each Interrogation Area (IA) and the neighboring Search Area (SA). As recommended by Raffel et al. (2018), two correlation search passes were used in this study, with the IA size of the second pass equal to half of the IA size of the first pass. Recent studies have shown that the results of traditional LSPIV are sensitive to the size of IA (Pearce et al., 2020). In this regard, for a specific case, RIVeR provides three alternative IA sizes for the second pass based on the overall displacement of particles, particle counts, and practical experience and then the median of those three IA sizes is selected as the final IA size. Gaussian 2x3-point interpolation was used to fit the correlation peak, which could bring the resolution to the sub-pixel level (Hou et al., 2022). Background noise and outliers were marked as not a number (NaN) values using a standard deviation filter along with a magnitude notch filter. Then, time series of instantaneous velocities at different sites were averaged (all NaN values were excluded before the averaging) to produce a final velocity map.

6.3.1.2 EC

Different from traditional LSPIV, EC uses the time series of instantaneous correlation matrices ($M_{t=1}$, $M_{t=2}$, M, … , $M_{t=T-1}$) at a specific velocity site to calculate an ensemble correlation matrix (M_{sum}=$\sum_{t=1}^{T-1} M_t$). The final velocity vector at that site is determined from the peak of the ensemble correlation matrix (M_{sum}). This process is repeated for all regions across the frame to generate a velocity map. By operating on instantaneous correlation matrices rather than instantaneous velocity vectors, EC “dilutes” the random, erroneous peak correlation values (from background errors and outliers) and "concentrates" the consistent, valid peak correlation values (from tracers). A detailed description of EC can be found in Meinhart et al. (2000).

The freeware RIVeR version 2.6 with PIVlab version 2.59 was also used to perform the image velocimetry analysis using EC. Similar to the approach adopted for traditional LSPIV, two correlation search passes were used in EC. In order to make the comparison of computational cost among different algorithms meaningful, the same settings of IA and step size in each search pass were applied to EC, as they were in traditional LSPIV. Different from traditional LSPIV or TiFA, data post-processing (e.g., filtering, interpolation, etc.) is not feasible in EC, as EC generates a final velocity map directly from the consecutive frame series, without any intermediate stages or accessible data.

6.3.1.3 LSPTV

The freeware PTVlab version 2.59 (Patalano, 2024) was used to perform the LSPTV analysis. First, a Gaussian mask was used to detect and mark the locations of surface tracers in all frames with the help of three user-defined filtering parameters: correlation threshold, particle size, and intensity threshold. Different from traditional LSPIV, only one correlation search pass was available in LSPTV. The IA size adopted for LSPTV conformed to the IA size adopted for the second pass in traditional LSPIV. Then, the correlation between the IA centered at a specific tracer in one frame and the SAs centered at neighbouring tracers in the next frame was analyzed to determine the locations of the same tracer in consecutive frames, from which the instantaneous velocity vectors for that specific tracer were calculated. The correlation analysis process was repeated for all tracers across all frame pairs to generate a Lagrangian velocity map, which was then converted to the Eulerian form to produce a complete velocity map by taking the time-averaged values at different sites. A detailed description of LSPTV can be found in Brevis et al. (2011).

6.3.1.4 SDI

Different from other algorithms focusing on velocity recognition and post-processing, the Seeding Density Index (SDI), introduced by (Pizarro et al., 2020a), aims at image pre-processing by selecting the most informative sequence of frames from the video. SDI is defined as:

$$SDI = \; {D_T}^{0.1}/(\frac{\rho_c}{\rho_{cv1}}) \tag{6.1}$$

where D_T, ρ_c, and ρ_{cv1} are the empirical spatial clustering level of tracers [-], the seeding density [particles per pixel (ppp)], and the converging seeding density at the Poisson case ($D_T = 1$) [ppp], respectively. D_T is computed as

$$D_T = [Var(N)/E(N)]/1 \tag{6.2}$$

where $Var(N)$ and $E(N)$ are the spatial variance and mean value of the number of tracers in the AOI, respectively). ρ_{cv1} was estimated as 1.52×10^{-3} ppp in Pizarro et al. (2020a).

In SDI, first, an AOI (usually the smallest area that covers all probe measurements) was first selected. Then, an optimal frame window was determined based on two criteria: (a) the maximization of the number of frames, subject to (b) the minimization of SDI (Pizarro et al., 2020b). Next, the velocimetry analysis was carried out from those selected frame series using traditional LSPIV. A detailed description of the SDI-based method can be found in Pizarro et al., (2020a), Pizarro et al., (2020b) and Dal Sasso et al., (2021). In order to make the comparison of computational cost among different algorithms meaningful, the same settings were applied in SDI, as they were in traditional LSPIV.

6.3.1.5 TiFA

At a certain site in a specific flow case, each velocity vector from the velocity time series can either be a "valid velocity" (recognized from actual tracer movement), or "invalid velocity" (recognized from background noise, surface random fluctuation, surface glares, camera movement, etc.). We can assume that, in steady-state flow, at each site, valid velocities in the velocity time series will follow a quasi-normal distribution with its peak frequency corresponding to the actual local time-averaged flow velocity. The invalid velocities due to the background noise (if there are any) will also follow a quasi-normal distribution with its peak frequency corresponding to "velocity≈0". The invalid velocities due to other factors will follow a quasi-uniform distribution. TiFA was developed based on these assumptions. Readers can download the full Matlab code of TiFA (with comments and usage instructions) from the "Data Availability Statement" section for free. TiFA's algorithm is illustrated in Figure 6.2 and described in detail as follows:

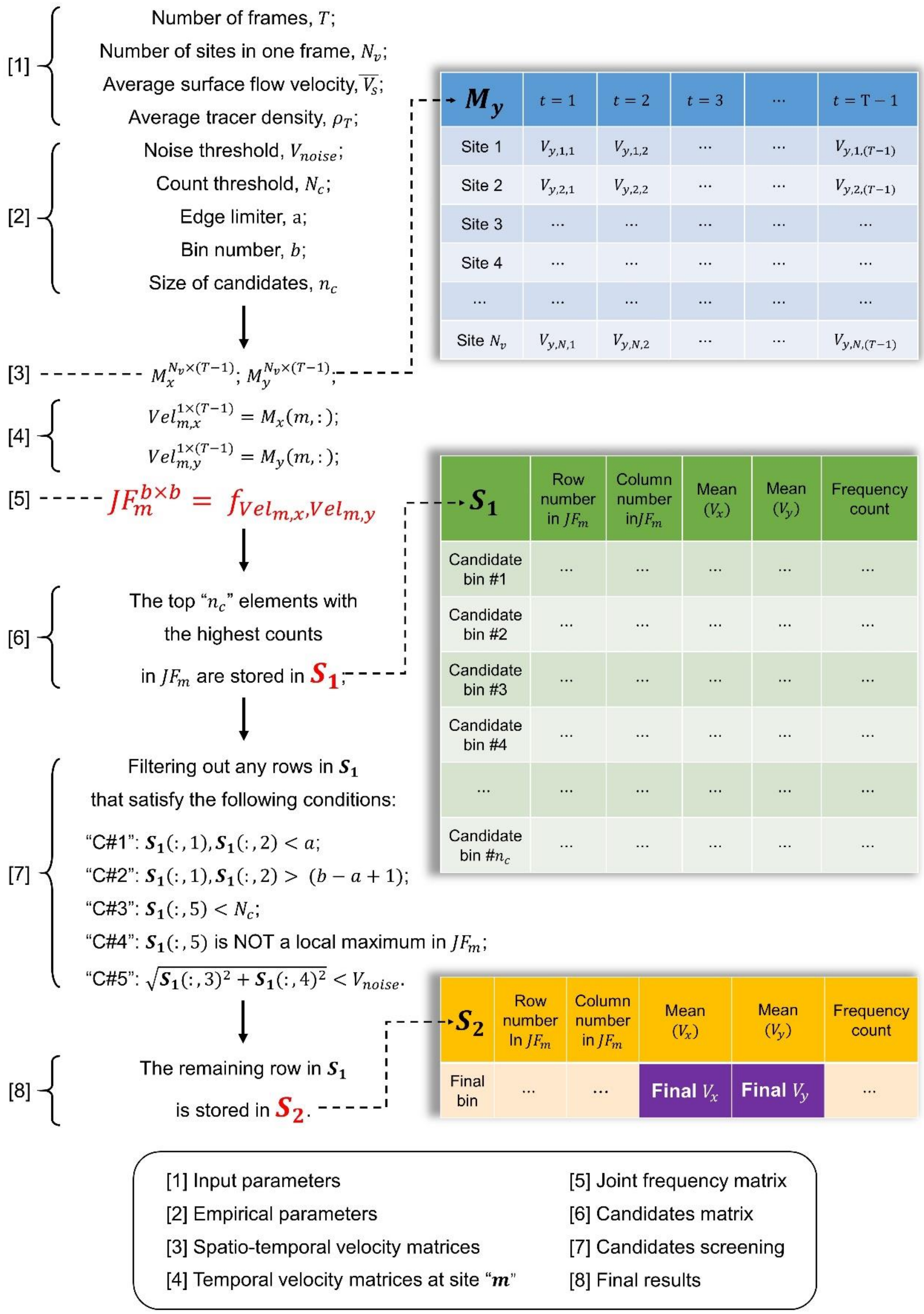

Figure 6.2. Illustration of the full algorithm of TiFA and associated matrices' structures. "x" is the axis in the image width direction while "y" is the axis in the image height direction.

- The total number of frames (T), total number of velocity sites in one frame (N_v), and the instantaneous velocities matrices in the x and y direction ([3] in Figure 6.2) generated from traditional LSPIV were known input parameters. A user needs to estimate the overall average surface flow velocity ($\overline{V_s}$) and the overall average tracer density (ρ_T) of the target flow, which are the user-defined input parameters ([1] in Figure 6.2). Other input parameters ([2] in Figure 6.2) are derived from the above-mentioned input parameters using the empirical formulas provided below:

$$V_{noise} = \ 0.23 \cdot \overline{V_s} \tag{6.3}$$

$$N_c = \ 17543.86 \cdot \rho_T \tag{6.4}$$

$$a = \ min[(T/100), 2] \tag{6.5}$$

$$b = round(\sqrt{T-1}); \tag{6.6}$$

$$n_c = round[(T-1) \cdot \ 5\%] \tag{6.7}$$

where V_{noise} is the noise threshold [pixel/frame], $\overline{V_s}$ is the overall average surface flow velocity of the target flow [pixel/frame], N_c is the count threshold [-], ρ_T is the overall average surface tracer density of the target flow [ppp], a is the edge limiter [-, integer], T is the total number of frames [-, integer], b is the total bin number of the joint distribution histogram [-, integer], n_c is the number of velocity candidates [-, integer].

- For a certain velocity site "m" ($1 \leq m \leq N_v$), TiFA investigates the temporal joint distribution pattern of two velocity components, $Vel_{m,x}$ and $Vel_{m,y}$ ([4] in Figure 6.2), by a joint frequency matrix $JF_m^{b\times b} = f_{Vel_{m,x},Vel_{m,y}}$([5] in Figure 6.2). The size of JF_m is calculated from the total number of frames (i.e. sample volume) using the "square root rule" (Eq.4), which ensures the preservation of the distribution pattern of the ensemble. Each row and column of JF_m corresponds to a certain range of V_x and V_y, respectively. Each element in JF_m stands for the total number (i.e. count) of velocities whose two components, V_x and V_y, fall into the velocity ranges determined by the row (ranges of V_x) and column (ranges of V_y) of that element. A figure illustration of the JF_m matrix is provided in Figure 6.3a.

- For a certain site, those bins ranked in top "n_c" based on their frequency counts (i.e., the bin with highest count, the bin with the 2nd highest count, the bin with the 3rd highest count,…, the bin with the ${n_c}^{th}$ highest count) in JF_m will be selected as candidates. Their positions in JF_m (i.e., rows and columns), mean flow velocities, and frequency counts are stored in matrix S_1 ([6] in Figure 6.2). These candidate bins will undergo the following rounds of screening process ([7] in Figure 6.2) to identify the bin storing the actual flow velocity at the investigated site:

(1) "C#1" & "C#2": Candidate bins located near the edges of JF_m will be eliminated, as the corresponding velocities were likely to be outliers.

(2) "C#3": Among the remaining candidates, bins with frequency counts less than N_c will be removed (i.e., "Condition #3" in Figure 6.2), as bins with low frequency counts have a low confidence level in representing the actual flow velocity.

(3) "C#4": From the remaining candidates, bins that do not represent a local maximum of the frequency counts in JF_m (i.e., the highest frequency count among neighbouring bins in JF_m) will be discarded, as we assume that the actual flow velocity should follow a quasi-normal distribution.

(4) "C#5": Finally, among the remaining candidates, bins with an average flow velocity magnitude lower than V_{noise} will be excluded. The remaining bin will be treated as the bin containing the actual flow velocity.

- The valid bin will be stored in the matrix S_2 ([8] in Figure 6.2). $S_2(1,3)$ and $S_2(1,4)$ store the final velocity components, from which the final velocity magnitude was determined. In some cases, there is more than one row in S_2. For those cases, the row with the highest frequency count is used. In rare cases there is more than one row with the same highest frequency count. In those cases, TiFA will further investigate the unimodal temporal frequency distributions of V_x and V_y separately and use the row with the highest sum of the count of their corresponding velocity ranges in the unimodal distributions.

- The above mentioned process was repeated for all velocity sites until generating a complete spatial-distributed velocity map.

To help readers gain a more intuitive understanding of the TiFA algorithm, the image velocimetry results processed by TiFA at a sample location in the physical model (marked by the yellow circle in Figure 6.4b) is shown in Figure 6.3. Note that the original elements in JF_m (i.e. count) in the TiFA code have been converted to $ln(count + 1)$ in Figure 6.3a for better illustration. With the velocity screening condition #3, TiFA can avoid identifying random outliers as the valid velocities. With the velocity screening condition #4, TiFA identifies both the background noise and valid velocities as valid velocity candidates. Then, with the velocity screening condition #5, TiFA can pick out the actual valid velocities and filter out background noise (see Figure 6.3a). With application of all those velocity screening processes, TiFA identifies that valid velocities at the example location should fall into the bin where $V_x \in [7.4, 8.1]$ and $V_y \in [-1.175, -0.625]$. In the end, velocities in the selected bin were averaged to get the final valid velocity as $V_x = 7.77$ pixel/frame and $V_y = -0.91$ pixel/frame at the example location. Figure 6.3(d) shows that the valid V_y generated by TiFA does not correspond to the peak in the unimodal distribution map of V_y, which means that using unimodal distribution map to identify the valid velocity can be unreliable as the high-frequency background noise will not be filtered out.

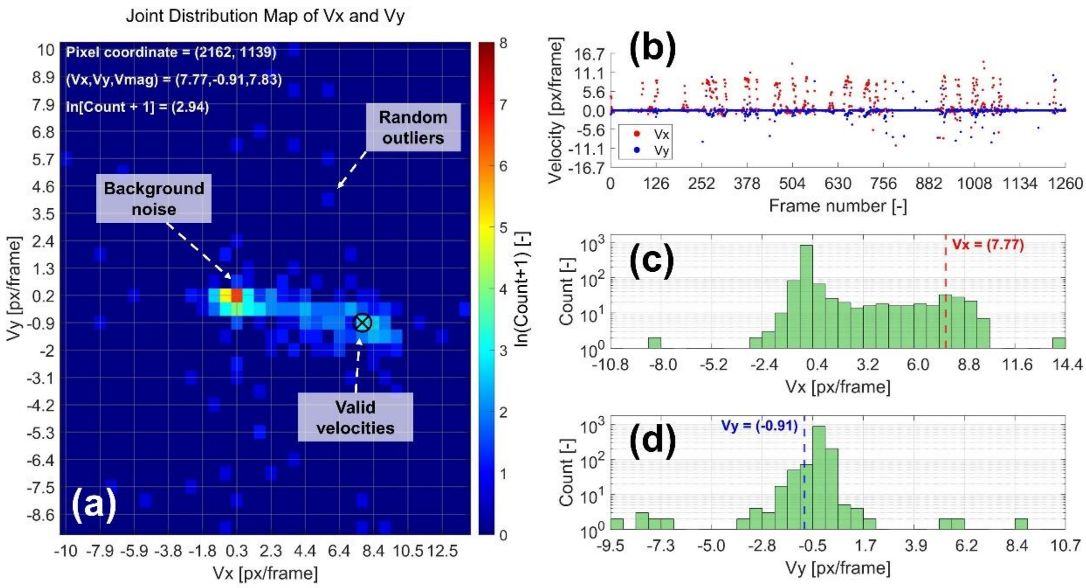

Figure 6.3. Illustration of image velocimetry results processed by TiFA at a sample location (marked by the yellow circle in Figure 6.4b) in the physical model. (a) Joint frequency distribution of V_x and V_y time series. Note that the black circle & cross in (a) mark the selected bin element by TiFA, from which the final velocity magnitude is calculated. (b) Time series of the scattered velocity components; (c) & (d) Unimodal frequency distribution of V_x and V_y time series and the components of TiFA-processed flow velocity (the red dashed line and the blue dashed line). Note that unimodal frequency distribution is not part of TiFA, unless there is more than one row with the same highest frequency count stored in matrix S_2.

6.3.2 Physical model

First, we used a physical model (Figure 6.4a) to test the performance of TiFA and compared it with other image velocimetry algorithms. This section introduces the setups and experimental procedures of the physical model.

The physical model was located in the National Research Council of Canada's Ocean Coastal and River Engineering Research Centre (NRC-OCRE), a Canada research laboratory in Ottawa, Ontario. The three-dimensional model included an approximately 1 km reach of the Bow River near Calgary, Alberta, Canada, represented using an undistorted geometric scale of 1:30. The model was initially designed to evaluate flood management strategies and channel morphodynamics at the study site. The model channel was approximately 30.4 m in length and 5.2 m in width at model-scale.

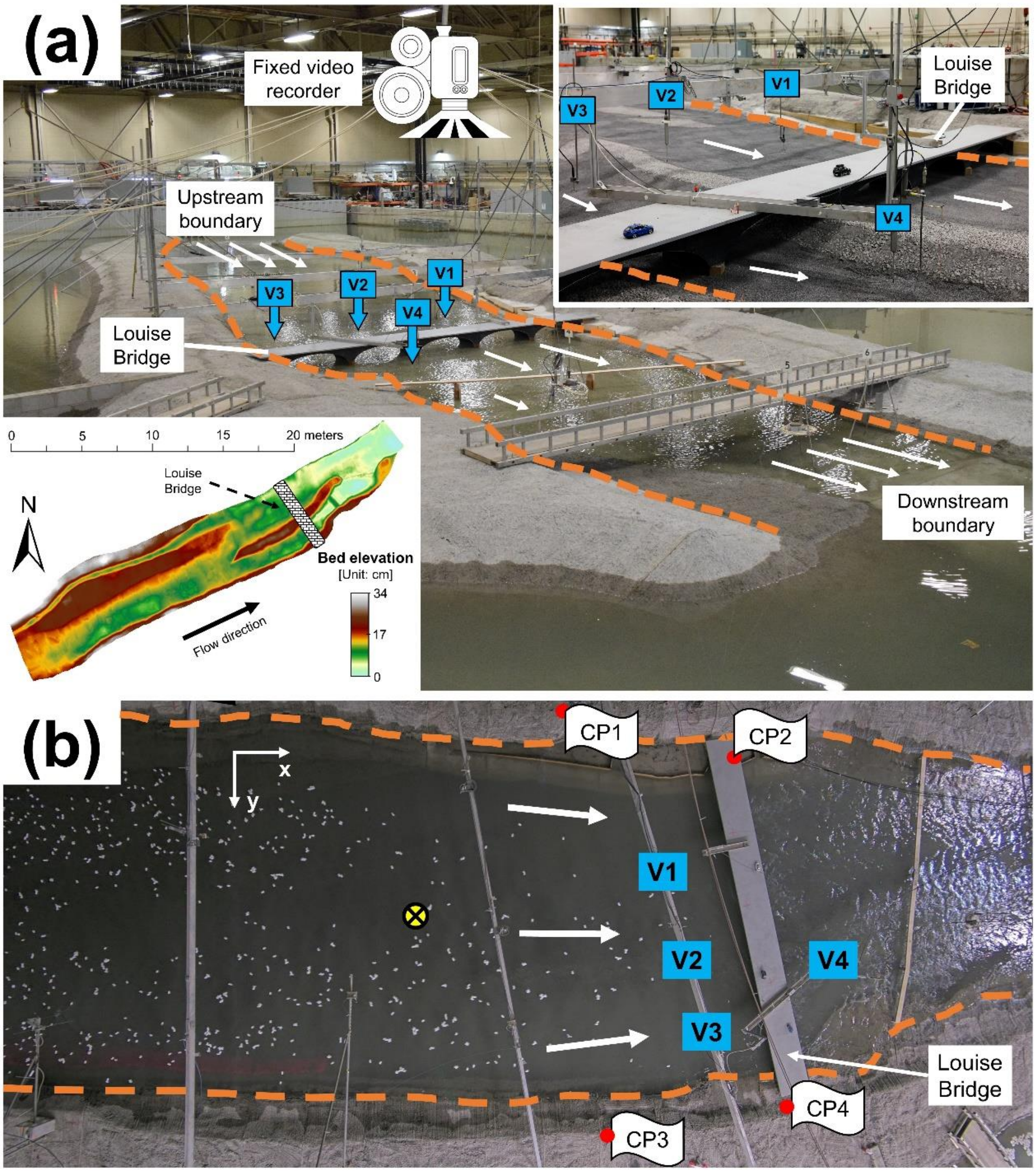

Figure 6.4. (a) Physical model layout, digital elevation model (lower left figure, units are in model scale) of the channel, and velocity measurement sites ("V1", "V2", "V3", and "V4"; upper right figure). (b) An example of a distortion-corrected frame. "CP1" – "CP4" represent the ground control points for rectification and velocity unit conversion. Orange dashed lines mark the river channel boundary. The yellow circle in (b) marks the sample velocity site where the temporal joint

distribution of velocity components and TiFA-processed velocity are investigated (see Figure 6.3).

Flow velocities were interpreted using a single, tested flow condition comprised of a constant discharge of 0.284 m^3/s and a downstream water depth of 0.203 m (model-scale). This coincides with a full-scale flow of 1400 m^3/s, representing an approximately 35-year flood event at the study site. Two *Nortek*® Vectrino ADVs ("V1" & "V3", see Figure 6.4a) and two *Alec*® electromagnetic current meters (ECM) ("V2" & "V4", see Figure 6.4a) were installed in the vicinity of Louise Bridge to measure the flow velocity. Note that measurement site "V4" was located downstream of a bridge pier and was also near a localized channel constriction, where flow is more turbulent. An *AXIS*® P1378-LE Network Camera was mounted to a catwalk above the physical model, looking straight down to collect video data (Figure 6.4b). The size of the video image was 3840 x 2160 pixels, with a resolution of 96 dots per inch (DPI). The recording rate was 30 frames per second (FPS). Ground control points were painted onto the channel banks using spray paint, and surveyed using a HILTI POS 180 (see Figure 6.4b, CP1-CP4). All overhead lights that would cause surface glares were turned off in order to ensure a consistent and uniform light condition, except for the one close to the model downstream boundary (see Figure 6.4b), which would be used to test the performance of different image velocity algorithms in the glare zone.

The experimental procedures are described as follows:

- The desired flow discharge and downstream water level conditions were established and kept constant for the duration of the test.

- Buoyant, biodegradable packing peanuts (made from starch) were introduced to the flow at the upstream boundary for 2 minutes. At the same time, the ADV and ECM probes started to collect velocity data and the camera started to record until all tracers had left the field of view. To avoid surface tracer clusters, the surface tracer density was low (see Table 6.1). Since the surface tracers were manually introduced into the flow, the feeding rate was not constant. Additionally, due to the channel widening near the inflow boundary (Figure 6.4a), the spatial distribution of surface tracers was also uneven. These factors together created the opportunity to evaluate the performance of different algorithms under unfavorable tracer conditions.

- Velocity data from the ADV and ECM instruments were time-averaged and converted to the surface flow velocity using the classical log-law (Keulegan, 1938) and the measured water depth and probe depth.

Table 6.1. Summary of the flow and tracer conditions and user-defined parameters in different cases.

	Physical model	Bradano River	Arrow River
Characteristics	low tracer density surface glares turbulent flow background noise	low tracer density background noise frequent outliers	high tracer density flow in river bends
Number of frames [-]	1260	600	99
IA size [pixel]	32	36	20
$\overline{V_s}$ [#1] [pixel/frame]	5.59	3.47	4.83
V_{noise} calculated from Eq. (1) [pixel/frame]	1.3	0.8	1.1
V_{noise} used in TiFA [pixel/frame]	2.5 [#2]	0.8	1.1
ρ_T [#3] [ppp]	$1.29 * 10^{-4}$	$1.71 * 10^{-4}$	$5.79 * 10^{-4}$
N_c calculated from Eq. (2) [-]	2.3	3.0	10.2
N_c used in TiFA [-]	4 [#2]	3.0	10.2

[#1] "$\overline{V_s}$" stands for average surface flow velocity

[#2] Values are adjusted to filter out data from low-quality zones, which will be discussed in section 4.3.

[#3] "ρ_T" stands for average surface tracer density

- A 42-second segment of the video was selected and exported as 1260 consecutive frames. Lens distortion was then corrected using the intrinsic parameters of the camera (see an example frame in Figure 4b). After that, frames were converted to greyscale and background was removed by subtracting the mean frame. Those converted frames were used to generate surface velocimetry results using the five image velocimetry algorithms. User-defined parameters are summarized in Table 6.1. Readers can access the original video and converted frames from the "Data Availability Statement" section.

- Using four ground control points ("CP1" – "CP4") in the frame (see Figure 4b) and the camera frame rate of 30 FPS, frames were rectified and flow velocity vectors in the camera coordinates (i.e. pixel/frame) were transformed into velocity vectors in the world coordinates (i.e. meter/second).

6.3.3 Field cases

In this section, two field cases from Perks et al. (2020) were introduced to further evaluate the performance of five image velocimetry algorithms.

The first field experiment took place in the valley portion of the Bradano River, located in the Basilicata region of Italy. On 14 October 2016, an experiment was undertaken to explore the optimal setup for surface velocimetry techniques (Dal Sasso et al., 2018). At the time of the experiment, the maximum water depth and average surface velocity were 0.80 m and 0.75 m/s, respectively. Charcoal particles were added to the flow acting as surface tracers. A *DJI*® Phantom 3 Pro Unmanned Aerial Systems (UAS) equipped with a *Sony*® EXMOR 1/2.3 in. (1.10 cm) CMOS camera sensor was deployed to record a video for 1 min 43 s at a pixel resolution of 1920 x 1080 and a frame rate of 24 Hz. A total of 600 images (stabilized, contrast-corrected, orthorectified and converted to greyscale intensity) were extracted from the footage for further analysis. All frames have a resolution of 0.009 m/pixel. Validation data in the form of surface velocities were obtained at 7 points (see Figure 6.5-a1) in a cross section using a Seba® F1 current flowmeter, attached to a tether line. More details about the experiment can be found in Dal Sasso et al. (2018) and Perks et al. (2020). The velocity data and results processed by TiFA at location "7" in the Bradano River case are shown in Figure 6.5 (a3) & (a2), respectively.

The second field experiment was undertaken in the Arrow River, located in Warwickshire, UK., to ascertain the accuracy of different image velocimetry approaches. During the experiment, the average water depth and average surface velocity were 0.22 m and 0.42 m/s, respectively. Ecofoam chips were added to the flow acting as surface tracers. A *GoPro*® Hero 4 mounted at a stationary telescopic pole at a height of approximately 2 m above the water surface was used to collect a video for 5 min 37 s at a pixel resolution of 1920 x 1080 and frame rate of 30 Hz. Datasets of 99 consecutive images (sampled at a frame rate of 5 Hz, orthorectified and converted to greyscale intensity) were extracted from the footage for further analysis. All frames have a resolution of 0.0174 m/pixel. Reference velocity data at 49 sites (see Figure 6.5b1) were obtained using a *Valeport*® 801 electromagnetic current meter. Measurements were made for a period of 30 s just below the water surface, with the time-averaged value being reported. More details about the experiment can be found in Perks et al. (2020). The velocity data and results processed by TiFA at location "36" in the Arrow River case are shown in Figure 6.5 (b3) & (b2), respectively.

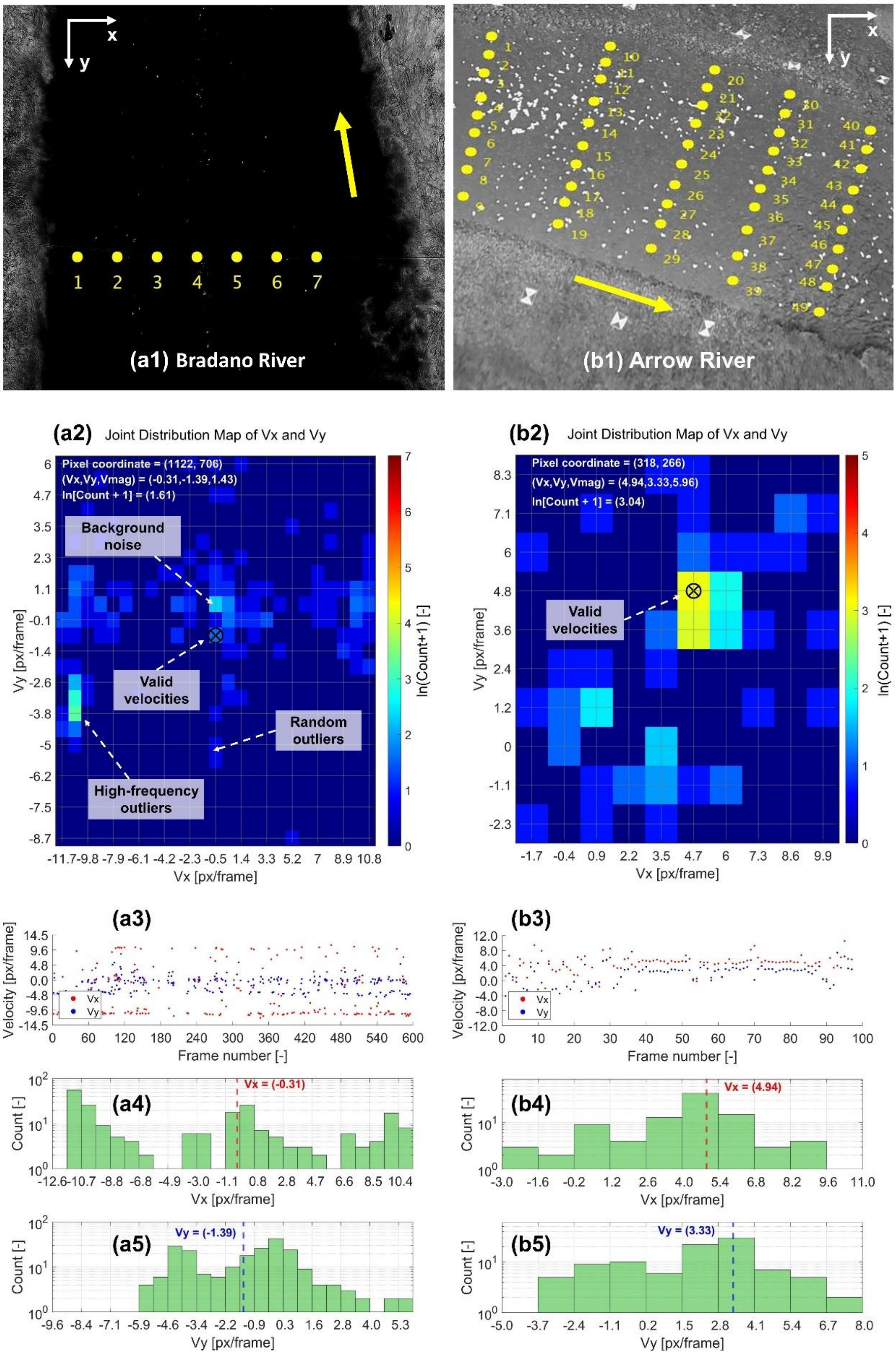

Figure 6.5. (a1) & (b1) A video frame and velocity measurement sites (yellow dots) in the Bradano River case and the Arrow River case (Perks et al., 2020), respectively. Yellow arrows mark the flow direction; (a2) joint frequency distribution of velocity components at the measurement site "7" in the Bradano River case; (a3) Time series of velocity components, (a4 – a5) unimodal frequency

distribution of velocity components, and (b2) joint frequency distribution of velocity components at the measurement site "36" in the Arrow River case (b3) Time series of velocity components, (b4 – b5) unimodal frequency distribution of velocity components, and. The black circle & cross in (a2) & (b2) mark the bin from which the TiFA-processed final velocity is calculated.

The procedures for the five image velocimetry algorithms in the two field cases are similar to those in the physical model case (see Section 2.2). User-defined parameters are summarized in Table 6.1. Note that, in Figure 6.5 (a5), TiFA discarded the element of the highest frequency in the joint frequency matrix JF_m at the sample location owing to the implementation of "Condition #1" & "Condition #2". Velocities corresponding to the discarded element were found to be a systematic error, which is likely due to the error from the camera stabilization algorithm and/or the swinging motion of the tether line in the Bradano River case.

6.4 Results

Note that hereafter "LSPIV" in figures means "traditional LSPIV". Mean Absolute Error (MAE) and the coefficient of determination (R^2) were used to evaluate the performance of different algorithms, and were calculated as follows:

$$MAE = \frac{\sum_{i=1}^{N}|O_i - P_i|}{N} \tag{6.8}$$

$$R^2 = \left[\frac{\sum_{i=1}^{N}(O_i - \bar{O})(P_i - \bar{P})}{\sqrt{\sum_{i=1}^{N}(O_i - \bar{O})^2}\sqrt{\sum_{i=1}^{N}(P_i - \bar{P})^2}}\right]^2 \tag{6.9}$$

where MAE is the mean absolute error; R^2 is the coefficient of determination between the measured data (O_i) and the image velocimetry data (P_i); i is the sequence number of a measured velocity data, N is the total number of measured velocity data; $\bar{O}$ and $\bar{P}$ are the means of the measured and image velocimetry data at all measurement sites, respectively.

6.4.1 Physical model

Figure 6.6 shows the results of five image velocimetry algorithms in the physical model at four measurement locations.

Figure 6.6a shows a significant velocity underestimation using traditional LSPIV and SDI at measurement locations. Figure 6.6b demonstrated the similarly good performance of TiFA, EC, and LSPTV at the measurement locations. Among them, TiFA showed the highest accuracy with the lowest MAE (Figure 6.6b) and the highest R^2 (Figure 6.6c). The MAE of TiFA is 41% lower than the second lowest MAE produced by LSPTV, and the R^2 of TiFA is 100% higher than the second best R^2 value produced by EC. In addition, both TiFA and LSPTV showed more reliable velocity predictions at the turbulent region (i.e. site "V4") than the other three algorithms. This also confirms the relatively inadequate performance of EC in turbulent flow.

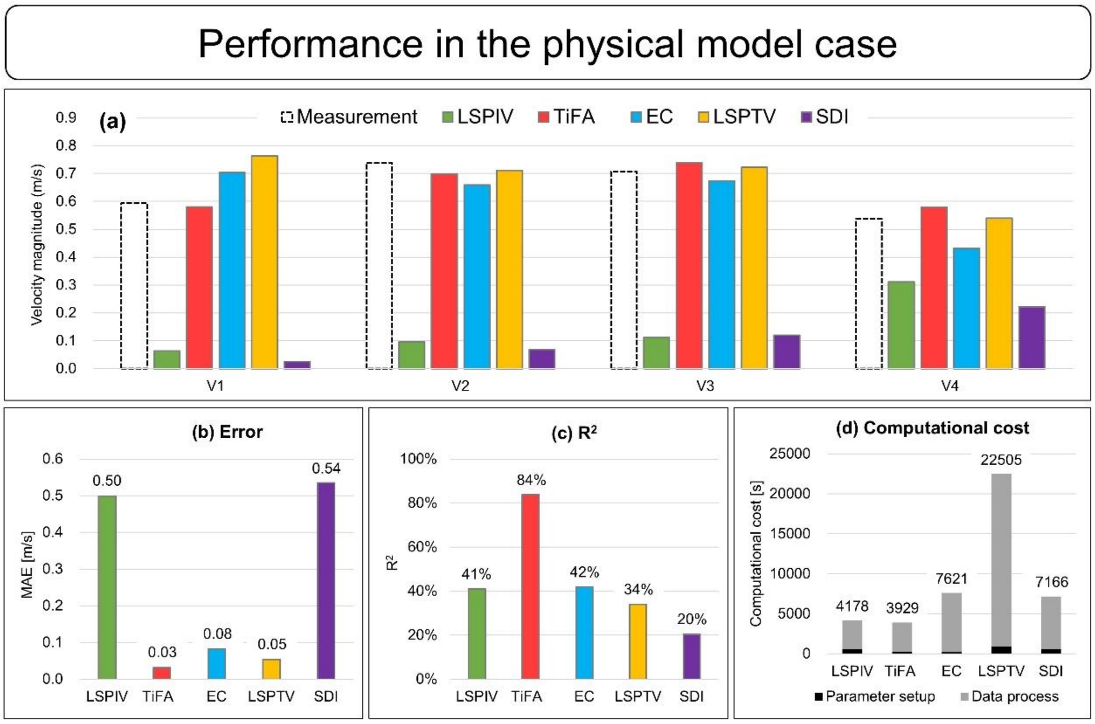

Figure 6.6. Results of five image velocimetry algorithms at the velocity measurement locations in the physical model. (a) Measured velocity versus image velocimetry results at different measurement locations, "V1" - "V4"; (b) MAE of five image velocimetry algorithms; (c) R^2 of five image velocimetry algorithms; (d) Computational cost of five image velocimetry algorithms.

Figure 6.6d shows the computational cost of five image velocimetry algorithms in the physical model case. The working platform was a *DELL*® Precision 5570 Workstation with an *Intel*® *Core*™ i7-12700H processor (14 cores, 4.70 GHz, and 20 threads). The computational cost is the sum of the time spent on the setup of user-defined parameters and data processing (including correlation analysis and data post-processing). The time spent by TiFA on data processing is almost the same as that of traditional LSPIV. However, less parameter setup time was required for TiFA compared to traditional LSPIV. EC requires minimal parameter setup time, but requires higher data processing time compared to LSPIV and TiFA. LSPTV had the highest computational cost of the tested algorithms with regard to both data processing time and parameter setup time. Although being efficient in only processing the selected AOI in SDI, the total computational cost of SDI is still quite high if processing the whole frame area.

Figure 6.7 shows the velocity maps generated from the five image velocimetry algorithms in the physical model. Note that only the velocity map in the AOI that is around the velocity measurement sites was shown in the SDI case as it is adequate to demonstrate SDI's performance.

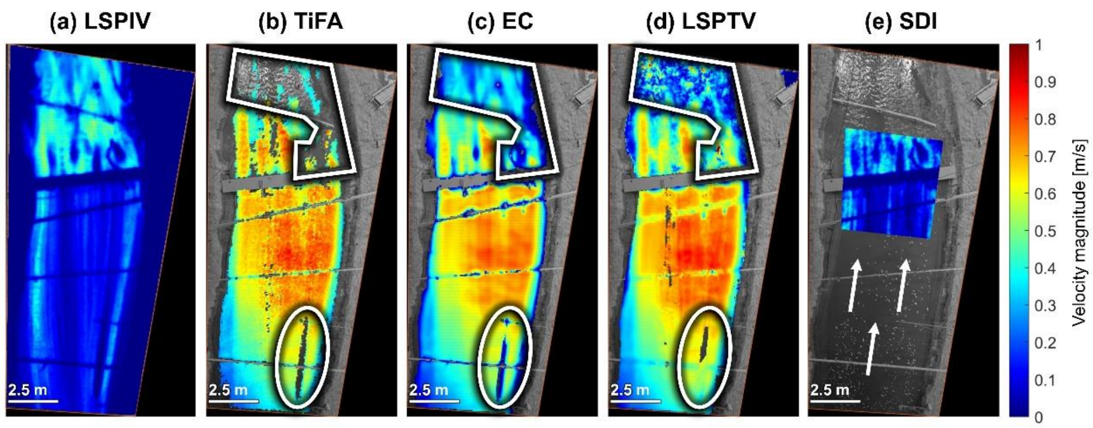

Figure 6.7. Velocity maps of five image velocimetry algorithms in the physical model. (a) Traditional LSPIV; (b) TiFA; (c) EC; (d) LSPTV; (e) SDI. White polygons mark the downstream glare zone. White circles mark the no-tracer region. White arrows mark the flow direction.

Figure 6.7 further confirms the substantial velocity underestimation using traditional LSPIV and SDI. Figure 6.7 also shows the similar performance among TiFA, EC, and LSPTV. Nevertheless, in the high velocity region, overall velocities are slightly higher in LSPTV than TiFA while slightly lower in EC than TiFA. Considering the fact that TiFA produced the smallest error at the velocity measurement sites, we suspect LSPTV and EC might have overestimated and underestimated the overall flow velocity, respectively. In addition, there are large discrepancies between EC and LSPTV in terms of the velocities at the downstream glare zone (see white polygons in Figure 6.7), which demonstrates the uncertainties of EC and LSPTV under unfavorable light conditions. In contrast, TiFA filtered out those uncertain velocities and marked them as NaN. Moreover, there is a region close to the inflow boundary where tracers rarely passed through (see the white circles in Figure 6.7) due to the surface wake produced by a sensor probe in front of it. Velocities in this region were processed as "0" in EC while as "NaN" in TiFA and LSPTV. TiFA had successfully marked the entire no-tracer region while LSPTV and EC only marked a portion of that region. The treatment on glare zones and no-tracer regions demonstrates the strong capability of TiFA in terms of filtering out data with low fidelity.

6.4.2 Field cases

Figure 6.8 & Figure 6.9 show the accuracy and computational cost of five image velocimetry algorithms in the Bradano River case and in the Arrow River case, respectively. The velocity map results in those two cases can be seen in Figure C1 & Figure C2 in Appendix C.

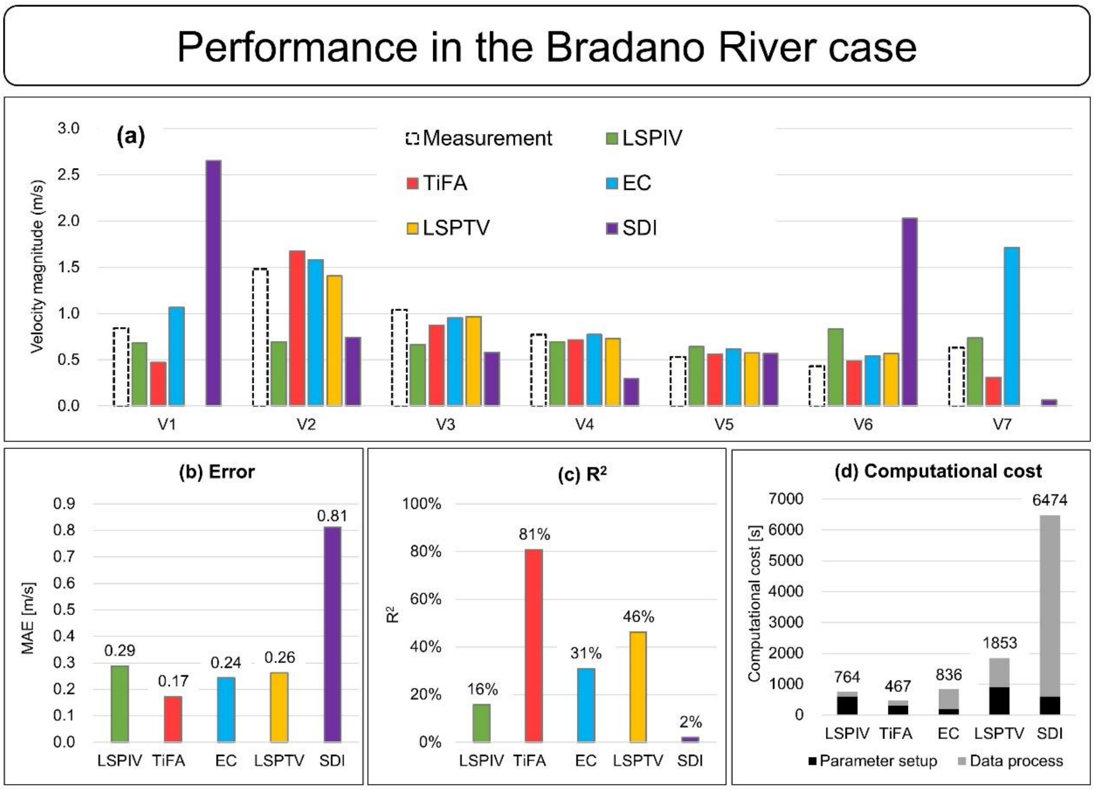

Figure 6.8. Accuracy and computational cost of five image velocimetry algorithms in the Bradano River case. (a) Measured velocity versus image velocimetry results at different measurement locations, V1-V7; (b) MAE of five image velocimetry algorithms; (c) R^2 of five image velocimetry algorithms; (d) Computation cost of five image velocimetry algorithms.

Figure 6.8 shows that the performance of TiFA was still the best both in terms of accuracy and efficiency in the Bradano River case. Unlike the physical model case, traditional LSPIV did not substantially underestimate all flow velocities in the Bradano River case. This is possibly due to the high-frequency residual error (see Figure 6.5-a2) coming from the drone movement correction algorithm in the Bradano River case: the magnitude of the residual error is about 11.6 px/frame, which is much higher than the background noise of about 0.86 px/frame (see Figure 6.5-a2). After time-averaging all velocity data at a certain site in traditional LSPIV, the high-magnitude, high-frequency residual error outweighs the low-magnitude, high-frequency background noise and causes the traditional LSPIV to no longer substantially underestimate flow velocities in the Bradano River case. Nevertheless, the performance of traditional LSPIV is still not acceptable considering an R^2 value of 16% (Figure 6.8c). EC showed moderate performance both in terms of accuracy and efficiency. However, EC substantially overestimated the velocity at site "V7" (Figure 6.8a). Although the overall accuracy of LSPTV is acceptable, it took the second longest time to process velocity data. In addition, LSPTV didn't produce any flow velocity data at site "V1" & "V7" (Figure 6.8a). Similar to the physical model case, SDI produced the highest error in the Bradano River case.

Figure 6.9 shows that, under the favorable tracer condition, TiFA is equally accurate as the other algorithms. Noteworthy, TiFA no longer had the computational cost advantage over EC in the Arrow River case, due to efforts on parameter setup in TiFA. Nevertheless, the computational time TiFA spent on data processing was still much lower than that of EC. The performances of LSPTV, LSPIV, and SDI in the Arrow River are similar to that in previous cases.

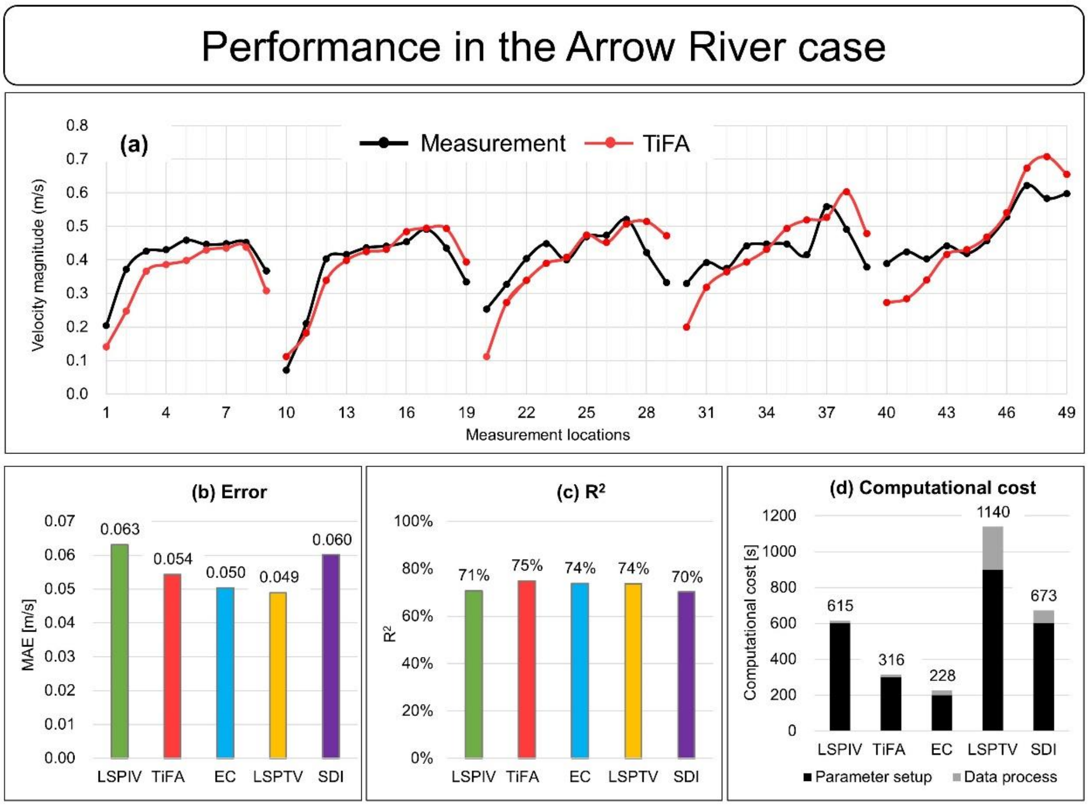

Figure 6.9. Accuracy and computational cost of five image velocimetry algorithms in the Arrow River case. (a) Measured velocity versus TiFA results at different measurement locations. (b) MAE of five image velocimetry algorithms. (c) R^2 of five image velocimetry algorithms. (d) Computation

cost of five image velocimetry algorithms.

6.5 Discussion

6.5.1 Evaluation: Accuracy

In traditional LSPIV, invalid velocities are filtered out using post-process filters such as neighboring filter, standard deviation filter, and magnitude notch filter. However, those filters are constant for each frame, regardless of the variation of local flow conditions, light conditions, and tracer density conditions at different regions. Applying weak filters may preserve noise and outliers, while using harsh ones may discard valid data. In addition, to the best of our knowledge, no filters in PIVlab can filter out the high-frequency outliers in the Bradano River case. Those limitations make the parameter tuning process very challenging in traditional LSPIV, especially under low tracer density conditions. In this regard, time-averaging on the velocity time series could result in great uncertainties, and thus low accuracy (see Figure 6.6b & Figure 6.8c) under low tracer density conditions.

In EC, infrequent velocities are “diluted” and frequent velocities are “concentrated” in the ensemble correlation matrix. By doing so, EC can accurately identify those frequent velocities from the correlation matrices time series regardless of the variation of flow, tracers, or light conditions. However, the identification process relies on the hypothesis that “frequent velocities” and “valid velocities generated from tracer movement” are equivalent at all times. This hypothesis may not hold under the conditions of (1) turbulent flow, where ripples and foams generated from surface fluctuations may interfere (see Figure 6.6a, “V4”); (2) existence of high-frequency outliers, which may be incorrectly recognized as valid velocities (see Figure 6.8a, “V7”); and (3) glare zones and no-tracer zones, where noise may be incorrectly recognized as valid velocities (see Figure 6.7c, the white circle and the white polygon).

Different from EC, all velocities in LSPTV are linked to tracers, which avoids extracting velocity data from background noise, ripples or foams due to surface turbulence. Thus, LSPTV shows a very good overall accuracy under the low tracer density conditions (see Figure 6.6b & Figure 6.8b) and in turbulent regions (Figure 6.6a, “V4”). However, the correlation analysis in LSPTV is based on the identification of surface tracers, which is mainly performed using the greyscale intensity threshold. In this regard, LSPTV may wrongly treat surface glares as surface tracers and produce unreliable results accordingly (see Figure 6.7d). In addition, LSPTV requires a consistent particle shape & intensity between successive frames to produce valid velocity results. Otherwise, it may lose track of particles and produce “NaN” results (see Figure 6.8a, “V1” & “V7”).

The basic principle of TiFA is similar to that of EC, both attempting to link the high-frequency data to the valid data. Different from EC, where high-frequency data are directly treated as valid data, TiFA has the flexibility to filter out invalid data from the high-frequency data by incorporating additional filters (i.e. Figure 6.2, “Condition#1 - #5”). By doing so, TiFA has the ability of (1) generating accurate average velocity estimates in turbulent flow regions (see Figure 6.6a, “V4”); (2) not being affected by high-frequency outliers (see Figure 6.8a, “V7”); (3) filtering out velocities from glares and no-tracer zones (see Figure 6.7b, the white circle and the white polygon). Compared to LSPTV, TiFA is more flexible and robust as it does not require consistent particle shape & intensity to produce velocity results (see Figure 6.8a, “V1” & “V7”). With those advantages, TiFA produced the lowest overall error over the others under the low tracer density conditions (Figure 6.6c & Figure 6.8c). However, since TiFA is built on statistical analysis, the applicability and performance of the algorithm is contingent on the availability of a suitable sample size (i.e. total number of frames). This may explain why TiFA did not show a significant advantage over the others in the Arrow River case (Figure 6.9b & 6.9c) where the sample size was relatively low. It is believed that the performance of TiFA can be improved in the Arrow River case, if provided with more frames (e.g. > 500 frames).

In SDI, an optimal frame window was selected based on the tracer density in the AOI. This image pre-processing technique reduced the background noise to a certain extent. However, SDI did not fully remove background noise. It still requires the same post-processing filters as traditional LSPIV does, thus shares the same limitation as traditional LSPIV. Noteworthy, the optimal frame window determined by SDI is based on the overall tracer density in the AOI. Thus, the local tracer density (e.g. at velocity measurement sites) in the selected frame window might be lower than the overall tracer density in the AOI. In addition, SDI substantially reduced the total number of target frames (e.g., SDI selected 102 frames out of 1260 frames based on the selected AOI), which induced information loss. The decrease of the total number of frames also makes SDI very sensitive to outliers (Figure 6.8a, “V1” & “V6”). As a result, SDI did not perform better than LSPIV in the low tracer density cases as expected (Figure 6.6b & 6.8b).

6.5.2 Evaluation: Efficiency

In traditional LSPIV, the user-defined parameters are mainly the post-process filters. As mentioned before, the tuning process of those parameters can be very challenging under low tracer density conditions. Nevertheless, data processing requirements for traditional LSPIV generally have low computational cost. Thus, the overall efficiency of traditional LSPIV depends on the total number of frames: when the total number of frames is not large (i.e. the Arrow River case), the time spent on user-defined parameters will be dominant, which makes traditional LSPIV relatively inefficient (Figure 6.9d); when there is a large amount of frames (i.e. the physical model case and the Bradano River case), the time spent on data processing will be dominant, which makes traditional LSPIV very efficient (Figure 6.6d & 6.8d).

Compared to traditional LSPIV, EC does not involve any additional user-defined parameters, which makes it very user-friendly. However, the data process time of EC is about 2 to 3 times that of traditional LSPIV. It is suspected that is because, for a certain location, EC needs to compute and store all elements in all instantaneous correlation matrices in the computer Random Access Memory (RAM) in order to calculate the ensemble correlation matrix, which might slow down the computation. In addition, since the number of elements in each correlation matrix is proportional to the square of the IA size, running the multi-pass correlation analysis in such an algorithmic framework probably further increases the computational cost of EC. Therefore, the overall computational cost of EC is about 2 times that of TiFA when the total number of frames and the frame size are medium (Figure 6.8d) or large (Figure 6.6d).

TiFA adopts the correlation analysis framework of traditional LSPIV and does not compute or store any of the time series of correlation matrices as EC does, which makes TiFA more efficient in data analysis than EC. TiFA only involves two input parameters, "average surface flow velocity $\overline{V_s}$" and "average tracer density ρ_T". Those two parameters are easier to determine compared to the post-process filters in traditional LSPIV. Thus, TiFA combines the advantages of traditional LSPIV and EC in terms of the overall framework efficiency, which makes it extremely efficient when the total number of frames and the frame size are medium (Figure 6.8d) or large (Figure 6.6d). When the total number of frames is small, TiFA is comparatively more computationally expensive than EC as it requires more parameter setup effort, yet still ranks the second most efficient among all five algorithms.

The number of user-defined parameters involved in LSPTV is the highest among all algorithms. Parameters in the particle detection stage include “correlation threshold”, “pixel size threshold”, and “intensity threshold”. Parameters in the correlation analysis stage include “IA size”, “minimum correlation”, and “neighbouring similarity level”. Those parameters are dependent on the quality and physical properties of frames and tracers, which are not straightforward to determine. This makes the parameter tuning process in LSPTV very time-consuming. During the data analysis stage, for each frame pair, the computational cost of LSPTV is not only a function of the IA size, but also a function of the total number of tracers, which makes the data analysis also very time consuming. Thus, LSPTV combines the disadvantage of traditional LSPIV and EC in terms of the framework efficiency, which makes it extremely inefficient in various conditions (Figure 6.6d, Figure 6.8d, and Figure 6.9d).

As an image pre-processing algorithm, SDI does not involve many additional user-defined parameters. Thus, the computational time spent on parameter setting in SDI is similar to that in traditional LSPIV. By reducing the total number of target frames, the time spent on the correlation analysis is dramatically reduced in SDI. However, corresponding results are only for the target AOI. In order to cover the entire flow area, the correlation analysis process needs to be looped (Figure 6.1). In this regard, the overall efficiency of SDI is similar to traditional LSPIV (Figure 6.6d, Figure 6.8d, and Figure 6.9d).

6.5.3 User-defined parameters in TiFA

The original user-defined input parameters in TiFA are “Noise threshold V_{noise}” and “Count threshold N_c”. They are applied in velocity screening conditions “Condition #3” & “Condition #5” to filter out noises and ensure the frequency of valid velocities in the velocity time series, respectively. However, the meanings of V_{noise} and N_c are not straightforward. After investigating TiFA’s performance in different cases, we found that V_{noise} and N_c seem to follow a linear relationship with overall average surface velocity “$\overline{V_s}$” and overall surface tracer density “ρ_T”, respectively (see Table 6.1 and Figure C3 in Appendix C). Thus, $\overline{V_s}$ and ρ_T are selected as the user-defined parameters, and V_{noise} and N_c are calculated using the empirical formulas Eq.(1) and Eq.(2). When the target flow is free of glares, users should directly adopt the values of V_{noise} and N_c calculated from the empirical formulas. When there are surface glares, using empirical formulas to determine V_{noise} and N_c will still produce valid results at glare-free regions. Users should exercise judgement to adjust the values of $\overline{V_s}$ and

ρ_T to filter out glares (see Table 6.1), which might impact the results at glare-free regions.

6.5.4 Limitations and future concerns

This study demonstrates the great potential of TiFA in various situations, especially under low tracer density conditions. However, there are several limitations in this study that need to be addressed for future exploration:

- **Sensitivity analysis and optimal settings.** This study aims to show the accuracy and efficiency of TiFA in different situations by comparing with other algorithms. To facilitate comparison, this study used the same IA size for all algorithms in each case. In addition, default values were adopted for some user-defined parameters in this study, such as “minimum correlation” and “neighbouring similarity level” in LSPTV. In addition to the “square root rule”, there are other options to select the optimal bin number that have not been tested in TiFA, such as the Sturges’ rule, Rice’s rule, Freedman-Diaconis rule, and others (Hacine-Gharbi & Ravier, 2021). Therefore, the tested algorithms were not thoroughly optimized in this study and the results presented in this study may not reflect the best results achievable for the tested algorithms. Future works should try to evaluate the accuracy of different algorithms using the optimal settings of user-defined parameters, with a thorough sensitivity analysis.

- **More trials.** There are some other competitive image velocimetry algorithms that are not investigated in this paper such as KLT-IV, STIV, SSIV, and OTV. Future works should consider a more thorough evaluation of TiFA by comparing with those algorithms. In addition, the successful performance of TiFA in turbulent flow was demonstrated at only one localized region in the physical model. More diverse flow conditions should be used to further test TiFA’s performance under different situations, especially in turbulent flow. Moreover, TiFA should also be trialed and further polished in other challenging situations such as the presence of rod-like tracers (e.g. Pizarro et al., 2020a) and irregular shadows (e.g. Dal Sasso et al., 2021).

- **Empirical formula.** The empirical formulas (i.e., Eq. [1] - [5]) presented in this study produced the best velocity results in the physical model and two field cases using TiFA. However, those formulas were not validated against independent data. Thus, it is possible that they will not apply to new data sets. More datasets from different situations are needed to further test and polish the empirical formulas used in TiFA.

6.6 Conclusion

The incapability of processing flow velocities under low tracer density conditions has constrained the application of traditional LSPIV for a long time. This study developed a new LSPIV image velocimetry algorithm, Time Frequency Analysis (TiFA), to overcome such a limitation. We evaluated the performance of TiFA in a physical model and two field cases and compared with other algorithms including traditional LSPIV, Ensemble Correlation (EC), Large-Scale Particle Tracking Velocimetry (LSPTV), and Seeding Density Index (SDI).

Under low tracer density conditions, TiFA showed the highest accuracy among all five algorithms: the coefficient of determination of TiFA ($R^2 \approx 83\%$) is approximately two times higher than that of the second-best performing algorithm ($R^2 \approx 44\%$). Under favorable tracer conditions, TiFA's performance is similar the other algorithms, which demonstrates the robustness and adaptability of TiFA. It was found that the accuracy of different algorithms not only depends on their ability to identify valid flow velocities, but also depends on their ability to recognize and discard invalid velocities. The authors believe the latter mainly determines the image velocimetry accuracy under unfavorable conditions and is the fundamental reason for TiFA's success. In addition, TiFA showed its ability of filtering out velocity data from surface glare zones and no-tracer zones, which LSPTV and EC are not capable of. TiFA also showed its potential of identifying average velocity from turbulent flow regions, where EC generally performs poorly. Since TiFA is based on statistical analysis, its performance is contingent on the availability of a suitable sample size (i.e. number of frames).

As for the computational efficiency, results show that TiFA is the most efficient algorithm among all five algorithms when the total number of frames is medium (i.e. 600 frames) or large (i.e. 1260 frames). When the total number of frames is small (i.e. 99 frames), TiFA's efficiency ranks the second highest as it requites more time on user-defined parameters than EC. Nevertheless, only two user-defined parameters are involved in TiFA: "noise threshold V_{noise}" and "tracer count threshold N_c". We found that those two parameters show linear relationships with the average surface flow velocity and average tracer density, respectively, which are relatively easy to determine.

In summary, the newly-developed image velocimetry algorithm, TiFA, has shown its great competence in various situations, especially under low tracer density conditions. Future studies can work on more trials on TiFA to further improve its accuracy and efficiency.

Chapter 7. Inundation Dynamics of an Extreme Urban Confluence Flood: Insights from In-Situ Measurements, Remote Sensing, and Hydrodynamic Modelling

7.1 Abstract

While the flow characteristics of open channel confluences have been extensively studied, the inundation dynamics of urban confluence floods remain unexplored. This study aims to fill this research gap by investigating a 100-year flood event at the Ottawa-Gatineau (OG) confluence in Canada, utilizing in-situ measurements, remote sensing, and a two-dimensional (2D) hydrodynamic model. A flow rating curve was first developed at the confluence outlet, showing that the total discharge and water level follow a power-law function, with minimal influence from confluence discharge ratio. The developed rating curve also showed a distinct segmentation behavior, where water level increases faster with total flow discharge in the overbank flow stage than that in the in-channel flow stage, probably due to the combined effects of the change of roughness and friction slope. Then, we employed MIKE+ to develop a two dimensional (2D) unsteady hydrodynamic model to study the confluence flood dynamics. The developed 2D model reproduced well the measured inland floodwater velocity and urban flood inundation extent, demonstrating its reliability in simulating large-scale urban confluence floods. Model results show that confluence flood inundation extent is mainly a function of total flow discharge, with minimal impact from discharge ratio or flow unsteadiness. Therefore, using steady-state models may be appropriate in future modeling of urban confluence floods.

7.2 Introduction

Open channel confluences are important nodes in river flow networks. On the one hand, confluences offer great water resources, fishery resources, and waterway transportation convenience to human society (Cao et al., 2023; Wang et al., 2024c). On the other hand, confluences are susceptible to contamination (Yuan et al., 2019; Haque et al., 2024), bank erosion (Lawal & Omosanya, 2023; Kumar et al., 2024), and risks of urban flooding (De Leo et al., 2020; Ravichandran et al., 2024). In recent years, climate change and urbanization have significantly altered both global and local hydrological processes (Qian et al., 2022), which brings additional uncertainties to urban confluence floods.

Numerical modelling is a powerful and cost-effective tool in studying fluvial urban floods. Van Emelen et al. (2012) found that even though three-dimensional (3D) models may improve the accuracy of the simulated results for a fluvial urban flood event, 2D models appear to be satisfactory for predicting flows in complex situations with a reasonable computational and meshing effort. Costabile et al. (2020) benchmarked three flood inundation models including a 2D shallow-water model, a 2D diffusive wave model, and a 2D porosity model in experimental and field environments. Results demonstrated that the 2D shallow-water model produced the best prediction in terms of water depths, which makes 2D shallow-water models more commonly used in fluvial urban flood modelling compared to other types of models (e.g. Bisht et al., 2016; Dasallas et al., 2019; Horváth et al., 2020; Farooq et al., 2019; Mustafa & Szydłowski, 2021; Marangoz & Anilan, 2022; Yu et al., 2022; Devi & Kuiry, 2024).

Although being suitable and widely used in fluvial urban floods simulations, 2D models may no longer be suitable for confluence environments, as the flow features in open channel confluences are characterized by significant secondary flow and 3D turbulent features (Best, 1987; Lewis & Rhoads, 2018; Yuan et al., 2021; Xu et al., 2022), which makes 3D models more widely used in studying confluence hydrodynamics (e.g. Bradbrook et al., 2000; Baranya et al., 2013; Sukhodolov et al., 2017; Constantinescu et al., 2011; Dai et al., 2020; Pandey & Mohapatra, 2022; Yan et al., 2024). However, in the field of fluvial urban flood modeling, relatively large model domain yet small mesh size is usually required with large computational cost, thus 2D models are still preferred over 3D models, particularly for unsteady flood simulations. By evaluating the performance of a 2D model at a tidal confluence, Xie et al. (2018) claimed that for a confluence with a large width-to-depth ratio, a 2D model is an acceptable compromise as long as the secondary flow corrections are included. Horváth et al. (2020) evaluated the performance of different shallow-water schemes in an overbank confluence flood event. Results showed that 2D models can provide accurate prediction in terms of the spatial distribution and temporal variation of water level. Although not focused on urban environments, those numerical studies demonstrate the potential of using 2D models in urban confluence flood simulations. However, numerical studies on urban confluence floods are less prevalent compared to the numerical studies on confluence hydrodynamics and urban floods in straight channels. Neal et al. (2009) used a 1D/2D coupled model, LISFLOOD-FP, to investigate an urban confluence flood event. The model was validated against more than 200 spatially-distributed debris wrack and water level marks across the whole city. Although the overall average error was 0.32m, the model produced the highest errors (≈ 0.8m in average) at densely built-up areas and also near the confluence regions, demonstrating the limited model performance in the urban confluence. Li et al. (2016) developed a 1D/2D coupled hydrodynamic model using MIKE FLOOD to study the inundation extent of confluence floods with different reoccurrence intervals in Taining county, China. However, inland buildings were not considered as impermeable in the computational cells in their study. Yang et al. (2022) utilized a 2D morphodynamic model to study urban flood inundation behaviors during a flash flood event at a river confluence. Results showed that the flash flood enlargement in confluence streams is mainly induced by the inflows. However, the developed model was not validated against any observed flood inundation data. In summary, further investigation of urban confluence flooding through numerical modeling is necessary, with rigorous model validation to ensure the model's accuracy and effectiveness.

One of the key characteristics of confluence flow is the confluence hydrodynamic zones (i.e. CHZ, see Best (1987)), whose features may vary with discharge ratio (Yuan et al., 2016) and water level (Yuan et al., 2021). Thus, validation against spatially distributed flow velocity across the CHZ at different flow stages (i.e. low flow and high flow) is a critical step in evaluating numerical model performance, especially for simplified 2D models. However, insufficient and/or unsatisfactory validation against measured flow velocity at CHZ is a shared imperfection among most numerical studies on confluence hydrodynamics (e.g. Bradbrook et al., 2000; Sukhodolov et al., 2017; Xie et al., 2018; Constantinescu et al., 2011; Dai et al., 2020; Liu et al., 2020; Shi et al., 2022) and on confluence floods (e.g. Li et al., 2016; Aureli et al., 2021; Kim et al., 2021; Nguyen et al., 2021; Yang et al., 2022). Moreover, Bates & De Roo (2000) reported that 2D models may not be suitable for urban inundation modelling as flow at the transition region between river channel and floodplain has strong 3D features due to intense shear. Thus, model validation against inland floodwater velocity is also critical if overland food dynamics is one of the research concerns. However, due to the unpredictability and hazards of floods, very few studies have collected inland floodwater velocity data during fluvial urban flood events (e.g. Brown & Chanson, 2013). To the best of the authors' knowledge, no fluvial urban flood numerical studies have validated their model against inland floodwater velocities in urban areas.

Steady-state models are commonly thought to overestimate the peak flood level, as they do not allow for water storage over the floodplain (Ahmadisharaf et al., 2018). Thus, unsteady models are widely used in studying overland fluvial floods, including confluence floods (e.g. Neal et al., 2009; Li et al., 2016; Xie et al., 2018; Horváth et al., 2020; Yang et al., 2022). However, Naulet et al. (2005) only found a minimal overestimation of 2% in terms of the flood peak when using steady models. Ruiz-Bellet et al. (2017) also argued that the overestimation effect may be diminished in floods with a prolonged, stable peak flow, and virtually equivalent to a steady flow. In confluence studies, Neal et al. (2012) found the maximum water surface difference between a steady model and an unsteady model was 0.345m, using the model developed by Neal et al. (2009). However, as mentioned before, the developed model in Neal et al. (2009) tends to overestimate the observed water level by about 0.8m at confluence regions. Thus, conclusions drawn from that 0.345m difference are inevitably somewhat unconvincing. In summary, the extent to which flow unsteadiness influences the confluence flood dynamics and inundation extent are still unclear. In addition, to the best of the authors' knowledge, no studies have evaluated the confluence inundation extent difference between two numerical models with different tributary unsteadiness (i.e. rising, steady, or falling flow). If the differences are minimal, it would suggest that, in some certain situations, a steady-state model could be used in place of an unsteady flow model to simulate confluence floods to reduce computational cost without producing unrealistic results.

Numerical modeling on confluence floods requires an accurate setting of water surface elevation (WSE) at the model downstream boundary. For an actual flood event, downstream WSEs can be obtained from field recording (e.g. Yang et al., 2022) or from remote sensing (e.g. Gleason & Wang, 2015). However, when simulating a design flood event, the relationship between the confluence flow discharge and downstream WSE (i.e. "Q-H" relationship, or flow rating curve) must be established. Although the unique one-to-one power law Q-H relationship was found invalid upstream of river confluences due to the backwater effect (Hidayat et al.,2011; Liu et al., 2023), it remains uncertain whether the total discharge and WSE at the confluence outlet follows a power-law relationship during confluence floods. It also remains unclear if and how much downstream WSE will be affected by confluent flow discharge ratio and/or flow unsteadiness. On the one hand, the presence of the flow recovery zone may result in a stable energy slope at the confluence outlet (Liu et al., 2023), making the power law potentially applicable. On the other hand, the combined effect of momentum exchange and secondary flow lead to complex spatial variation of water level within the confluence flow zone (Biron et al., 2002; Zhang et al., 2020; Shen et al., 2023), which might invalidate the power law. Some researchers chose to move their downstream model boundaries far away from the confluence region to some known gauge stations (e.g. Ding & Wang, 2012; Shi et al., 2022) to avoid such an uncertainty, which led to unnecessary computational cost. Thus, field measurements are still needed to understand the Q-H relationship at the confluence outlet.

In order to overcome the abovementioned limitations and fill the research gaps in urban confluence floods, we investigated the inundation dynamics of an extreme urban flood event at a large river confluence using multi-source data and unsteady 2D numerical modeling. With the help of in-situ measurements and remote sensing data, we established a flow rating curve at the confluence outlet and found that the total discharge and water level at the confluence outlet follow a power-law function, with minimal influence from confluence discharge ratio. Then we developed a 2D numerical model and validated it against in-channel flow velocity data obtained during different in-channel flow periods, inland floodwater velocity collected during an overland flood event, and flood inundation extent mapped using remote sensing data. The model results demonstrate that under the same time history of total discharge and downstream water level, the overall flood inundation extent at open channel confluences is more sensitive to the total discharge, with minimal impact from discharge ratio or flow unsteadiness. Therefore, using steady-state models is probably appropriate in studying confluence flood inundation.

7.3 Methodology

7.3.1 Study area and background

The Ottawa-Gatineau (OG) confluence is situated on the border between Ontario and Quebec, Canada, where the Gatineau River (tributary) merges with the Ottawa River (main channel) (see Figure 7.1). About 1.4 million people live in the vicinity of the OG confluence region (City of Ottawa, 2024; City of Gatineau, 2024), making it the largest and the most prosperous urban confluence in the Ottawa River watershed. The average width of the Ottawa River upstream of the OG confluence, the Gatineau River, and the Ottawa River immediately downstream of the OG confluence are about 600m, 200m and 300m, respectively. From year 2010 to 2024, the daily average flow discharges of the Ottawa River and the Gatineau River were about 1429 m^3/s and 390 m^3/s, with an average daily confluence discharge ratio of 0.297. Note that, in this study, confluence discharge ratio (will be short-noted as "discharge ratio" hereafter) is defined using the following equation:

$$\alpha = \frac{Q_t}{Q_m} \tag{7.1}$$

where α is the discharge ratio; Q_t is the tributary (i.e. the Gatineau River) flow discharge; Q_m is the main channel upstream (i.e. the Ottawa River) flow discharge, which will be short-noted as the "main channel discharge".

The OG confluence has suffered from multiple overbank floods in history due to the combined effects of heavy rainfall, rapid snowmelt, ice jams, and coincidence of spring annual peaks of two rivers (Buttle et al., 2016). On April 28, 2019, an extreme flood event with a recurrence interval of 100 years took place at the OG confluence, resulting in the evacuation of 111 homes, damage to 923 properties, and insurance costs of 200 million CAD (CBC News 2019a & 2019b; Kirchmeier-Young et al., 2021). The peak discharges of the Ottawa River and the Gatineau River were 6110 m^3/s and 1133 m^3/s during the 2019 flood, respectively (see Figure 7.2). Three urban neighbourhoods were seriously inundated on the north bank of the Gatineau River (Zone A, B, and C in Figure 7.1b). The area of interest (AOI, see the white polygon in Figure 7.1b) of this study was the region covering all open water bodies (including inland floodwater, rivers, and lakes) at the OG confluence during the 2019 flood.

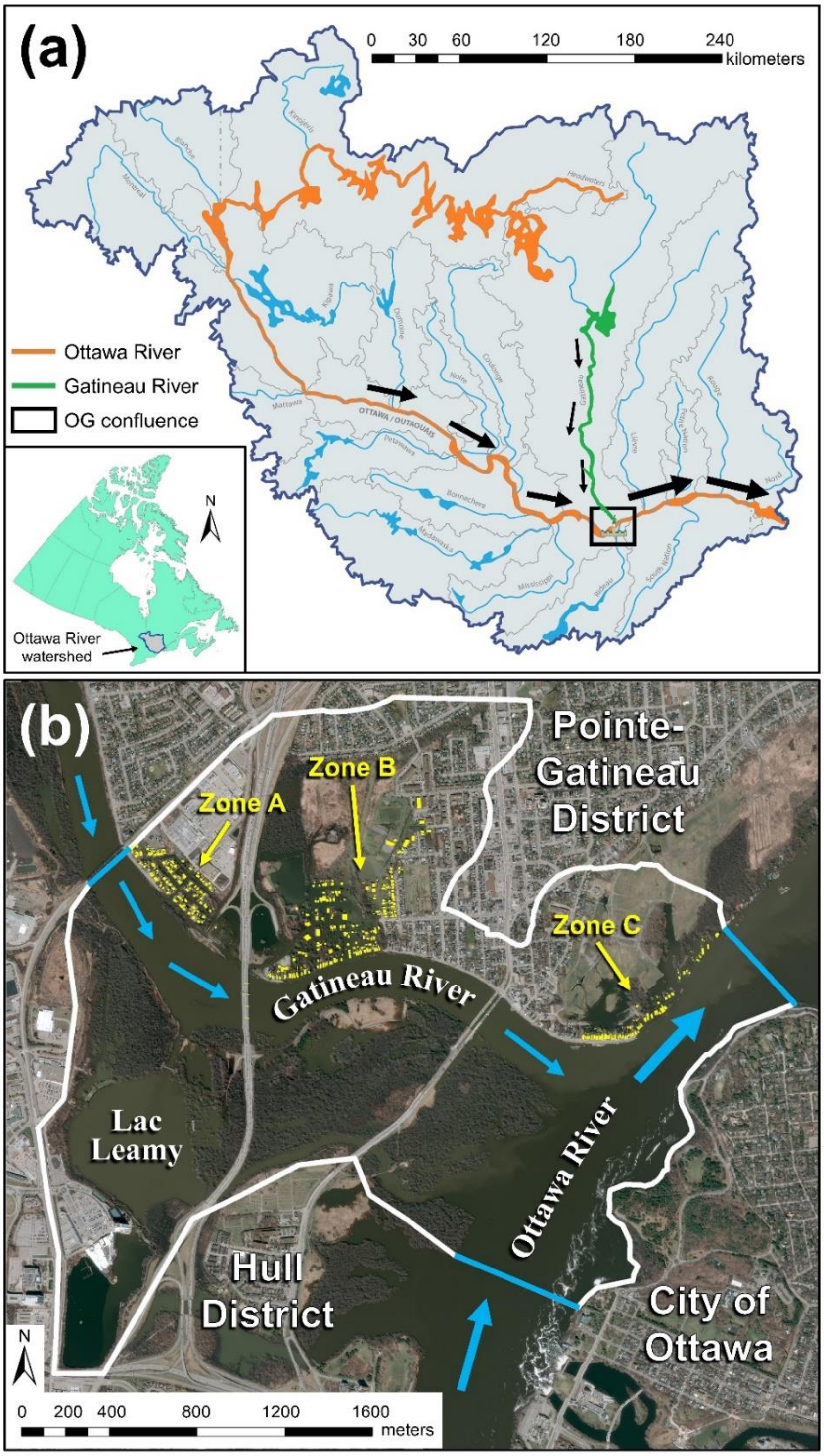

Figure 7.1. (a) Map of Ottawa River watershed (modified after Ottawa RIVERKEEPER (2024)). Black arrows mark the flow directions. (b) Satellite imagery of the OG confluence during the 2019 flood (collected on April 28th, 2019). Blue arrows mark the flow directions. The white polygon marks the numerical model domain. Blue solid lines mark the model inflow boundaries and the downstream boundary. Yellow dots mark the houses and buildings that were inundated during the 2019 flood.

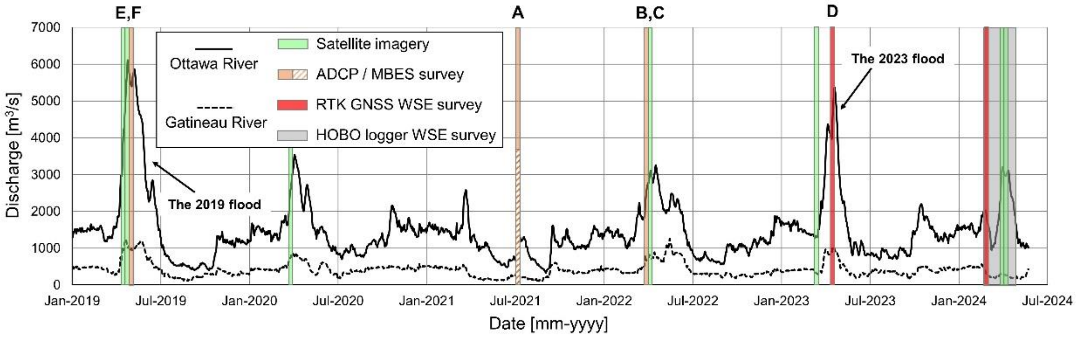

Figure 7.2. Hydrograph of the Ottawa River and Gatineau River from 2019 to 2024 (Water Survey of Canada, 2024; Ottawa River Regulation Planning Board, 2024). Color bars mark the periods when different field data were collected. Note that satellite imageries collected before the year of 2019 are not shown in this figure. Letters "A" - "F" correspond to times when certain data points in Figure 7.8 were collected.

7.3.2 Field data

7.3.2.1 In-situ measurement data

(1) Flow velocity. Inland floodwater velocity was collected using a *SonTek® RiverSurveyor™* M9 Real-Time Kinematic (RTK) Acoustic Doppler Current Profiler (ADCP), tethered by a canoe, at Zone B during the 2019 flood (red lines in Figure 7.3b) on May 1st,2019 (see Figure 7.2). In-channel velocity data were collected using the same equipment, mounted at one side of a motorboat (see Figure 7.3a), during a low flow period in 2021 and a high flow period in 2022 (see Figure 7.2). Raw data were depth-averaged and post-processed using in-house *Matlab®* code (Rennie & Church, 2010). Every eleven neighbouring velocity measurements were spatially averaged to their center to minimize systematic errors. Those velocity data were used to calibrate and validate the numerical model (see Figure 7.4 & Figure 7.5).

(2) Flow discharge. The Ottawa River and the Gatineau River each have a hydrometric station located 15 km (gauge station #02KF005, "Ottawa River at Britannia") and 9 km (gauge station "Gatineau River at Chelsea") upstream of the OG confluence, respectively, to monitor daily river discharge. Note that two smaller rivers, the Rideau Canal and Rideau River, flow into the Ottawa River at sites between the Ottawa River hydrometric station and the OG confluence. Their discharge is also monitored by hydrometric stations. The term "discharge of the Ottawa River" heretofore and hereafter refers to the total discharge of Ottawa River, Rideau Canal and Rideau River. Flow discharge of the Ottawa River and the Gatineau River was also measured by ADCP during the in-channel flow velocimetry campaign, which was used to validate the flow discharge data monitored by hydrometric stations (see Figure 7.4). The relative difference between the ADCP-measured discharge (Q_{ADCP}) and the discharge monitored by hydrometric stations (Q_{hydro}) was 6.8% and 3.1% during the low flow and high flow periods, respectively. The average value between Q_{ADCP} and Q_{hydro} was used in subsequent numerical modelling and analysis.

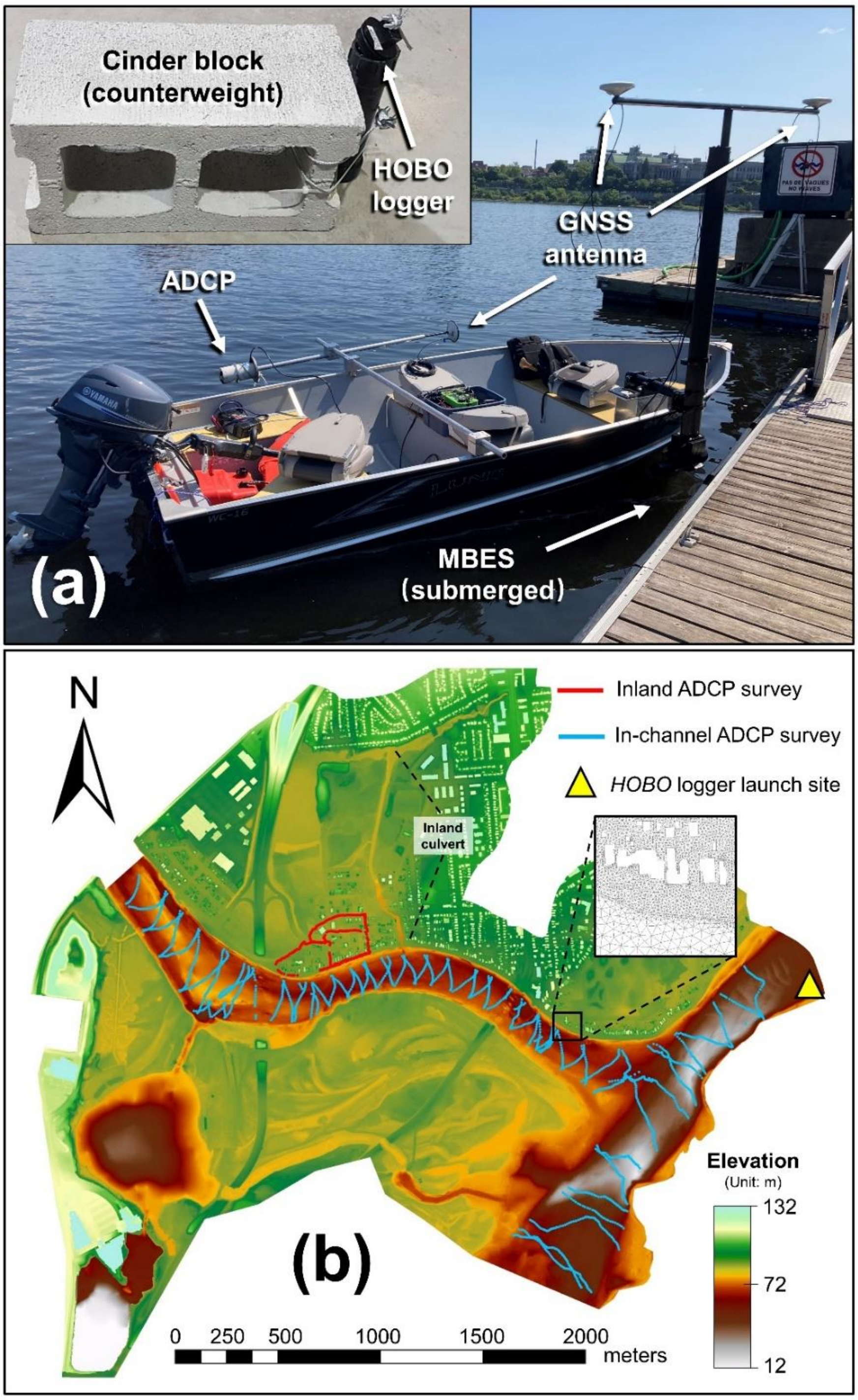

Figure 7.3. (a) Instruments used in the in-situ measurements. (b) The Digital Elevation Model (DEM) of the AOI, an example of the model mesh, inland velocimetry survey sites in 2019, in-channel velocimetry survey sites in 2022, and the *HOBO*® logger deployment site in 2024.

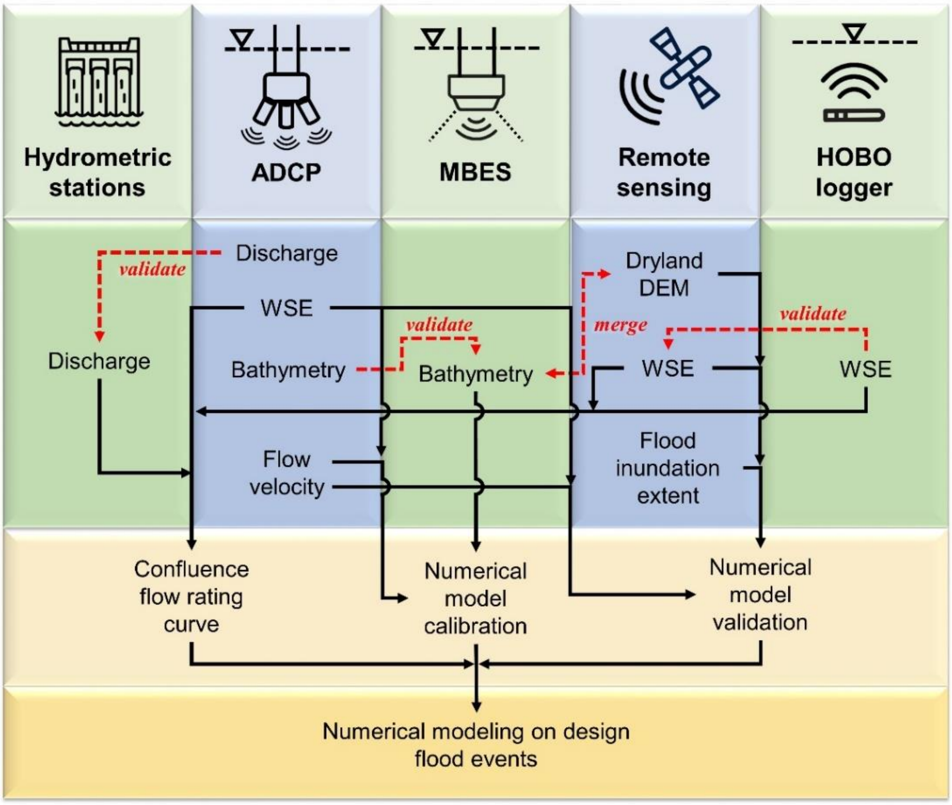

Figure 7.4. Field data and their usage in this study.

(3) Bathymetry. Bathymetry at the AOI was measured using a *NORBIT®* 400kHz 12004 iWBMS wideband multibeam echo-sounder (MBES) mounted at the other side of the motorboat (see Figure 7.3a). The survey took place at the low flow period from July 21st to July 26th, 2021 (see Figure 7.2). High precision positioning data were acquired using an integrated Global Navigation Satellite System/Inertial Navigation System (GNSS/INS) navigation system comprised of a motion unit built in the MBES head and two antennas placed above the MBES head (see Figure 7.3a). The horizontal and vertical resolution of the MBES measurement is 1m and 0.02m, respectively. The beam angle of the MBES was set to 180 ° in order to make sure (1) there were enough overlapping data between parallel survey passes for subsequent post-processing; and (2) bathymetry close to the river banks was included in the measurement. Raw bathymetry data were post-processed using the *QPS®* software packages, Qimera and FMGeocoder Toolbox (FMGT). Bathymetry was also measured by the vertical beam of ADCP, which was used to validate the bathymetry data measured by MBES (see Figure 7.4). The mean difference and mean absolute difference between them was about 0.03m and 0.06m, respectively. Bathymetry data collected by MBES was used as the final bathymetry in subsequent modelling.

(4) **WSE during a freshet season**. During the velocimetry survey campaigns in 2021 and 2022, WSE data at the downstream boundary were also collected using ADCP, which were set as the downstream boundary conditions of calibration runs in the numerical model (see Figure 7.4). Those data were also used to develop the flow rating curve at the OG confluence outlet (see Figure 7.4). Additionally, a *HOBO®* U20 water level logger (see Figure 7.3a) was deployed at the confluence outlet on March 14th, 2024 (see location in Figure 7.3b) to collect real-time (every 15 minutes) water depth data during the 2024 freshet event (from April 1st to May 22nd, 2024, see Figure 7.2), with a measurement accuracy of 0.015 m. The WSE data collected by a land-based Stonex S900A RTK GNSS device at the *HOBO®* logger deployment site was used to validate the *HOBO®* logger data and convert it to WSE data, which were then used to develop the flow rating curve at the OG confluence outlet (see Figure 7.4).

(5) **WSE during an overbank flood season**. On April 26th 2023, another overbank flood event took place at the OG confluence. The 2023 flood just barely overtopped the riverbank without inundating urban areas, which facilitated the in-situ measurement of WSE at the downstream boundary using the RTK GNSS device. The collected data was then used to develop the flow rating curve at the OG confluence outlet (see Figure 7.4).

7.3.2.2 Remote sensing data

(1) **Dryland DEM**. A dryland DEM obtained from the City of Gatineau was collected using airborne Light Detection and Ranging (LiDAR) technique, which can provide a horizontal resolution of 0.1m and vertical resolution of 0.15m. LiDAR signals scattered from vegetation canopies and the ground were differentiated (cf., Clark et al., 2004) to remove surface vegetation from the DEM. The dryland DEM was collected in the fall of 2018, during which the total discharge of the OG confluence was less than 2500 m^3/s. The dryland DEM thus provides an opportunity to identify downstream WSE from high-resolution satellite imageries collected during periods when the total discharge of the OG confluence is higher than 2500 m^3/s. The dryland DEM was merged with the bathymetry data to form a complete surface elevation map as an input for the numerical model (see Figure 7.3b, Figure 7.4).

(2) **Flood inundation extent.** Two pan-sharpened satellite imageries, one collected on April 28th, 2019 (Figure 7.1b) with a horizontal resolution of 0.5m, and the other one collected on April 30th, 2019 with a horizontal resolution of 0.4m, were used to

identify the flood inundation extent of the 2019 flood (see Figure 7.2), which was used to validate the numerical model (see Figure 7.4).

(3) WSE during freshet seasons. Four pan-sharpened satellite imageries (average resolution = 0.5 m) during historical freshet seasons (2500 m^3/s < total discharge < 3500 m^3/s) in 2020, 2022, and 2024 were collected (see Figure 7.2). For a certain satellite imagery, WSE at the downstream boundary was calculated by averaging the inland DEM values at the places where flow touches the drylands (i.e. at flow boundaries). This method has been widely applied in determining the Q-H relationship during floods and has shown good performance (e.g. Tarpanelli et al., 2013; Pavelsky, 2014; Gleason & Wang, 2015). Among those satellite imageries, two were collected at the time when the *HOBO*® logger was also recording WSE data (see Figure 7.2). Thus, those remote-sensed WSE data were used to validate the WSE data collected by the *HOBO*® logger at corresponding dates (see Figure 7.4). The average absolute difference between them is 0.042 m, demonstrating the accuracy of obtaining WSE data from satellite imagery. WSE data derived from the remaining satellite imageries were used to develop the flow rating curve at the OG confluence outlet (see Figure 7.4).

(4) WSE during overbank flood seasons. Three pan-sharpened satellite imageries (resolution = 0.38 m in average) during overbank flow events (total discharge ≥ 3500 m^3/s) in 2019 and 2023 were also obtained (see Figure 7.2). WSE at the downstream boundary was calculated by averaging the inland DEM values at the places where floodwater touches the drylands in the satellite imageries. Those remote-sensed WSE data were used to develop the flow rating curve at the OG confluence outlet (see Figure 7.4). The remote-sensed overbank WSE data during the 2019 flood were also used as the downstream boundary condition of the numerical model at the model validation stage (see Figure 7.4).

7.3.3 Flow rating curve at confluence outlet

With the help of multi-source field data, data series of total discharge and corresponding WSE at the confluence outlet were obtained, from which a flow rating curve was developed. To ensure consistency in the data collection periods, all data series used in the flow rating curve analysis were collected from the rising periods of historical flood events.

According to the Manning's equation (Chow, 1959), for a uniform, gravity-driven, fully-developed, turbulent flow in rough open channels, the flow rating curve at a certain river channel cross-section will follow a power law, which has the form of:

$$Q(H) = \ a_1(H - b_1)^c \tag{7.2}$$

where Q is flow discharge; H is the WSE relative to a given datum (usually the local mean sea level); a_1 is a scaling coefficient related to the characteristics of the section control or channel control; b_1 is a cease-to-flow reference level; and c is an exponent related to the type of hydraulic control (Le Coz et al., 2014). The c value is 1.5 for perfect rectangular channels and is 2.5 for V-shaped channels (WMO, 2010). Thus, the c value range of [1.5, 2.5] was applied as the constraint in the curve-fitting calculations.

Although natural flow is rarely perfectly uniform, the power law derived from the uniform flow assumption was still satisfactory in most field cases (Hrafnkelsson, 2020). However, considering the turbulent flow features and distinct spatial distribution patterns of WSE in river confluences (Biron et al., 2002; Zhang et al., 2020; Shen et al., 2023), especially during flood events, it remains unknown if the flow rating curve at a confluence outlet follows the power law. In this study, first we assumed the flow rating curve at the confluence outlet would follow Eq. (7.2). Then, we used least squares fitting to derive the function of the flow rating curve, based on the observed data series of total discharge and WSE at the confluence outlet, and evaluated the reliability of such fit using the coefficient of determination R^2 (Eq. 7.4). The derived flow rating curves were used to determine the downstream boundary condition for the numerical model as well as to analyze the confluence inundation behavior.

7.3.4 Numerical model

7.3.4.1 Model setup

MIKE+® (*MIKE Plus*) was used in this study to simulate the inundation process of the 2019 urban flood at the OG confluence. *MIKE+* is a comprehensive urban, river, and flood modelling platform. It is featured by the integration of multiple tools and packages including the Modelling of 1D river network (*MIKE HYDRO River*), 2D overland flow (*MIKE 21 FM*), 1D collection systems (*MIKE URBAN*), rainfall (*MIKE ZERO*), water quality (*MIKE ECO Lab*) and sediment transport (*ST*). *MIKE+* and its predecessor, *MIKE FLOOD*, have been widely used in urban flood flooding in recent years (e.g. Li et al., 2016; Zhou et al., 2022; Chen et al., 2023a, 2023b; Pariartha et al., 2023; Deopa et al., 2024).

In this study, the "2D overland" subroutine is applied. It solves the shallow water equations using an explicit finite volume solver (the two-stage explicit second-order Runge-Kutta scheme in this study). The unstructured triangular mesh facilitates using fine grid cells at densely-built urban areas (cell size $\leq$ 5 m^2 in this study) and relatively coarse grid cells at river channels (cell size $\leq$ 50 m^2 in this study) (see Figure 7.3b), which balanced the computational accuracy and the overall efficiency. A sensitivity analysis on grid size was carried out by comparing the modeled in-channel velocity with the measured ones using "cell size $\leq$ 50 m^2" and "cell size $\leq$ 30 m^2" in river channels. Results show that "cell size $\leq$ 50 m^2" is sufficient to reproduce the measured velocity (see section 7.3.4.2 for more details). The total number of computational cells in this study is 611437. During each simulation, the time step was allowed to vary from 0.001 seconds to 0.1 seconds as long as the local Courant-Friedrichs-Lewy (CFL) number remained less than 1. Buildings and bridge piers were set as permanent dry cells. Two upstream boundaries (where inflow discharge of the Gatineau River and the Ottawa River are defined) and one downstream boundary (where WSE is defined) were used in this study. The initial Manning roughness values for paved roads, grasslands, and forests were set as 0.02 $s/m^{1/3}$, 0.03 $s/m^{1/3}$, and 0.05 $s/m^{1/3}$, respectively, based on Chow (1959). These values were subsequently adjusted during the model validation stage (see Section 7.3.4.3), and the final Manning roughness values were adjusted to be 0.01 $s/m^{1/3}$, 0.035 $s/m^{1/3}$, and 0.08 $s/m^{1/3}$, respectively . The method of using surface roughness to represent floodplain surface vegetation has been widely used and proven effective in fluvial floods numerical modeling (Straatsma & Baptist, 2008; Croissant et al, 2018; Chaulagain et al., 2022; Herrera Gómez et al., 2024).

7.3.4.2 Model calibration

Model calibration aims to determine Manning roughness of the river channel and eddy viscosity by comparing the modeled and measured flow velocity (e.g., Williams et al. 2013; Parsapour-Moghaddam & Rennie, 2018; Yu et al., 2022). It can also demonstrate how well a 2D model can reproduce the flow field in a large-scale open channel confluence.

A low flow event in 2021 and a high flow event in 2022 were used as two calibration cases. Average discharge measured by ADCP and hydrometric stations was set as the inflow boundary. WSE measured by ADCP near the downstream boundary was set as the downstream boundary (see Table 7.1, also in Figure 7.8). During each ADCP measurement campaign, flow discharges in the two confluent rivers were relatively stable. Thus, flow conditions were set as steady state during the model calibration stage.

Mean absolute error (MAE), coefficient of determination (R^2), and percent bias (PBIAS) were used to evaluate the calibration and validation results, and were calculated as follows:

$$MAE = \frac{\sum_{i=1}^{N} |O_i - P_i|}{N} \tag{7.3}$$

$$R^2 = \left[\frac{\sum_{i=1}^{N} (O_i - \bar{O})(P_i - \bar{P})}{\sqrt{\sum_{i=1}^{N} (O_i - \bar{O})^2} \sqrt{\sum_{i=1}^{N} (P_i - \bar{P})^2}} \right]^2 \tag{7.4}$$

$$PBIAS = \frac{\sum_{i=1}^{N} (O_i - P_i)}{\sum_{i=1}^{N} O_i} \times 100\% \tag{7.5}$$

where MAE is the mean absolute error; R^2 is the coefficient of determination; $PBIAS$ is the percent bias between the measured depth-averaged velocity (O_i) and modeled depth-averaged velocity (P_i); i is the velocity sequence number, n is the total number of velocity data; $\bar{O}$ and $\bar{P}$ are the means of the measured and modeled depth-averaged velocity, respectively.

Table 7.1. Boundary conditions of calibration and validation runs.

Model stage	Flow event	Upstream discharge [m³/s]		Downstream WSE [m]
		Ottawa River	Gatineau River	
Calibration run1	Low flow, steady (July 23rd, 2021)	1175.35	111.74	41.384
Calibration run2	High flow, steady (April 25th, 2022)	2893.48	751.05	42.677
Validation run1	2019 flood, unsteady (April 28th - 30th, 2019)	5620 → 6110	1133 → 1024	44.900 → 45.043
Validation run2	2019 flood, steady (May 1st, 2019)	6087	1006	45.030

Calibration results are shown in Figure 7.5. Figure 7.5(a) shows that the ideal Manning roughness for the low flow and high flow periods is 0.05 s/m$^{1/3}$ and 0.032 s/m$^{1/3}$, respectively. Manning roughness represents the surface resistance to the flow, which is not only a function of absolute surface properties, but also a function of water depth. Resistance from surface roughness in deep flow is less dominant compared to that in shallow flow, which explains why the calibrated Manning roughness is higher during the low flow simulations. This also implies that the river channel Manning roughness during even higher flow (e.g., the overbank flood event in 2019) should be lower than 0.032 s/m$^{1/3}$, although total compound roughness will also depend upon floodplain roughness. Figure 7.5(b) shows that the model is less sensitive to eddy viscosity than to Manning roughness, which is also reported in other large-scale numerical simulations (e.g. Parsapour-Moghaddam & Rennie, 2018; Yu et al., 2022). Thus, eddy viscosity was set as 0.5 m^2/s in all subsequent modeling. The calibrated parameters produced an overall MAE of 0.07 m/s, R^2 of 77%, and PBIAS of 7.4% in the high flow simulation, which indicates that the 2D model well reproduced confluence flow behaviors during high flow.

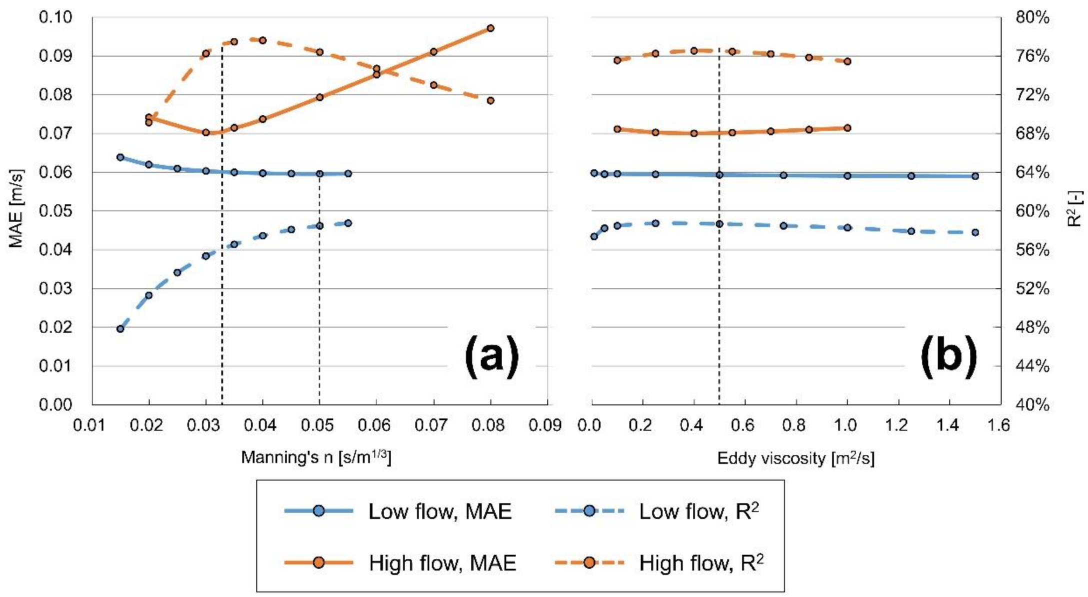

Figure 7.5. Statistical results of "Calibration run1" and "Calibration run2". (a) MAE and R^2 of calibration runs with different Manning roughness and constant eddy viscosity (0.2 m^2/s for low flow runs and 0.5 m^2/s for high flow runs). (b) MAE and R^2 of calibration runs with different eddy viscosity and constant Manning roughness (0.05 s/m$^{1/3}$ for low flow runs and 0.032 s/m$^{1/3}$ for high flow runs).

7.3.4.3 Model validation

The numerical model was then validated against the urban inundation extent derived from two satellite imageries during the 2019 flood (one on April 28th, 2019 and the other one on April 30th, 2019). Those satellite imageries were also used to set up the downstream WSE at corresponding dates. Flow discharge monitored at hydrometric stations on the corresponding dates was set as the upstream boundary. Unsteady simulation was used in the model validation stage, starting from April 28th, 2019 and ending on April 30th, 2019 ("Validation run1" in Table 7.1, also see Figure 7.8c). Manning roughness of the river channel was determined as 0.025 s/m$^{1/3}$, which produced the best match between modeled flood extent with measured flood extent. The numerical model was further validated against the measured inland floodwater velocity collected on May 1st, 2019 ("Validation run2" in Table 7.1, also see Figure 7.8c). A constant flow discharge monitored at the hydrometric stations on May 1st, 2019 was set as the upstream boundary. Downstream WSE was determined from the total discharge, using the developed flow rating curve (see Section 7.4.1).

Figure 7.6 (a) - (d) show the observed and modeled flood extent superimposed on the satellite imagery collected on April 28th, 2019 at Zone A, B, and C. Due to the relatively small WSE variation between April 28th and April 30th (see Table 7.1) and partial cloud coverage at AOI on April 30th, 2019, results are shown at two locations (red polygons in Figure 7.6a & 7.b) where noticeable changes in inundation area were observed between April 28th and April 30th in Figure D1 from Appendix D.We used the critical success index (CSI) to quantitatively evaluate the model performance in reproducing the observed flood inundation extent (Lim & Brandt, 2019; Sreekumar et al., 2024):

$$CSI = \frac{A_c}{A_c + B_c + C_c} \tag{7.6}$$

where A_c is the number of model cells correctly predict the measured flood extent; B_c is the number of model cells overestimate the measured flood extent (i.e. false alarms); C_c is the number of model cells underestimate the measured flood extent (i.e. misses).

To avoid overstating the merits of the developed model, CSI is only calculated at floodplain cells. Due to the partial cloud coverage on April 30th, 2019, CSI is only calculated on April 28th, 2019, which gives a value of 0.88, demonstrating the good performance of the model. Figure 7.6 also demonstrates that, although the numerical model overestimated the flood extent at some locations in Zone A and Zone C (Figure 7.6a & 7.6b), the overall modeled flood event matched with the observed flood extent very well, especially at the most serious inundation area, Zone B. Additionally, Figure 7.6(e) compares the inland floodwater velocity measured by ADCP and modeled in "Validation run2". The validated parameters produced an overall MAE of 0.036 m/s,

R^2 of 85.4%, and PBIAS of -13.5%. Thus, the 2D model well reproduced both the flood inundation extent and overland floodwater hydrodynamic behavior during the 2019 flood event. Consequently, the numerical model can be used to analyze the inundation dynamics at the OG confluence.

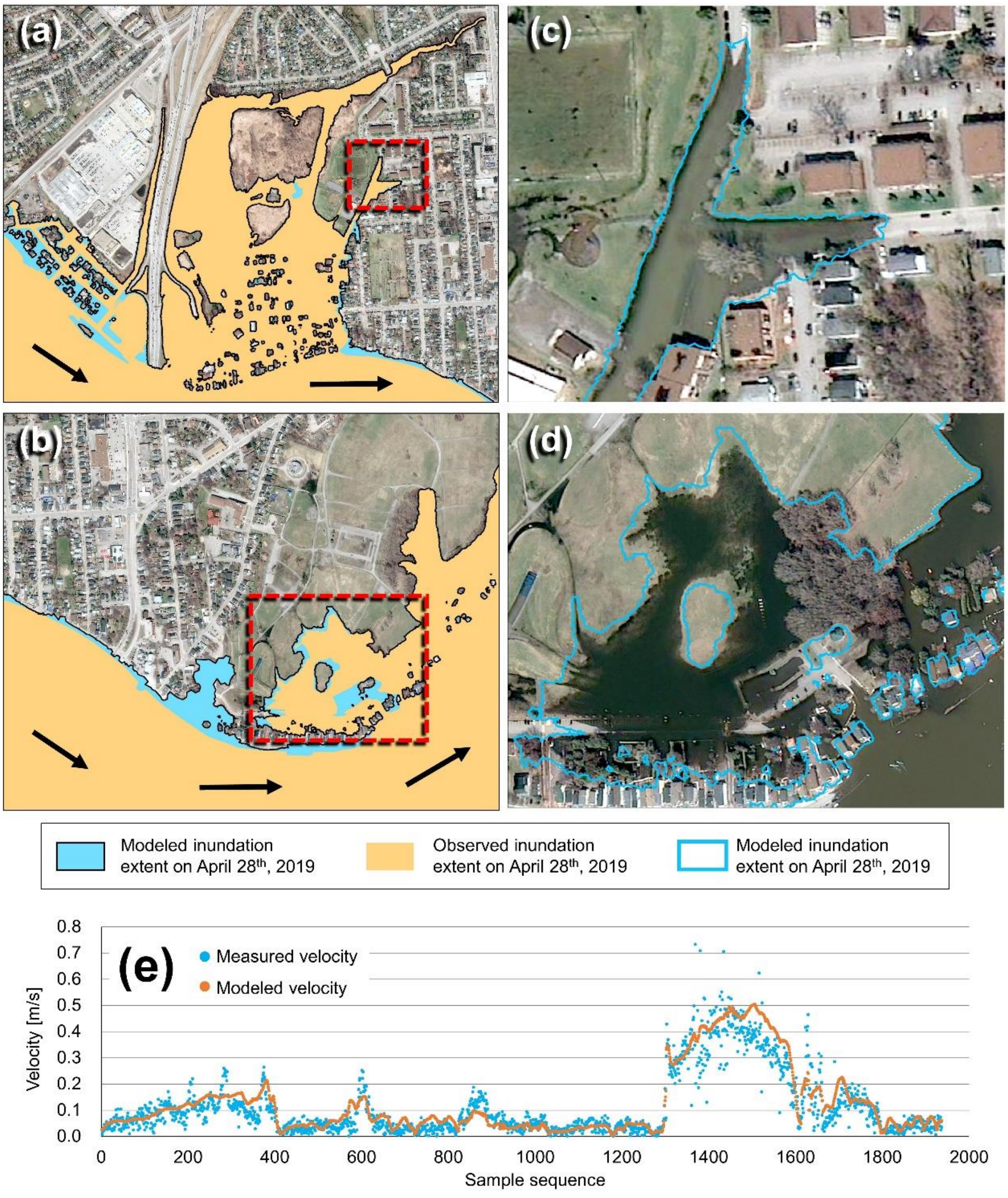

Figure 7.6. Results of "validation run1" and "validation run2". (a) & (b) Modeled flood extent and observed flood extent on April 28th, 2019 at Zone A, B, and C. Background satellite imagery was collected on April 28th, 2019. (c) & (d) Modeled flood extent on April 28that the places marked by the red polygons in Figure 7.6 (a) & (b). Background satellite imagery was collected on April 28th, 2019. Black arrows mark the flow direction. Closed polygons inside the flood inundation extent mark the dry areas. (e) Measured and modeled inland floodwater velocity on May 1st, 2019.

7.3.4.4 Inundation behavior modelling

During the 2019 flood, the Ottawa River experienced rising flow while the Gatineau River experienced falling flow, which brings the question “will the flood inundation process or extent be different if both confluent rivers experience rising flow?”. To the best of the authors' knowledge, this problem has not been addressed in previous studies. Studying this topic can help to gain deeper understanding on how the backwater effect impacts confluence floods and also help to develop flood mitigation strategies accordingly.

Two unsteady flood cases were modeled with equal total discharge hydrographs (see Figure 7.7). In the first case (i.e. “Run 01”), both the Ottawa River and the Gatineau River experience rising flow. In the second case (i.e. “Run 02”), the Ottawa River experiences a rising flow while the Gatineau River experiences a falling flow, similar to the 2019 flood case. The initial total discharge is set as 4967.2 m^3/s in both cases, which equals to the discharge on April 26th, 2023 (the time when floodwater just overtops the bank). The final total discharge is set as 6753 m^3/s in both cases, which equals to the discharge on April 28th, 2019 (the 2019 flood event). Note that the rate of increase of total discharge is two times higher than the gauge records in order to (1) study flood inundation dynamics under strongly unsteady flow, and (2) save computational cost. The total discharge increases over time in both cases, making sure the flow conditions always represent overbank floods in both cases. Such a setting also allows determination of the downstream WSE from the total discharge using the derived flow rating curve (see Section 3.1) at the confluence outlet, as the flow rating curve was developed based on data from rising periods. Note that, at any give time stamp, both total discharge and downstream WSE were kept the same between the two flow scenarios, while discharge ratio differed between the two cases (see Figure 7.7c). The rationale for such setup is discussed in Section 4.2.

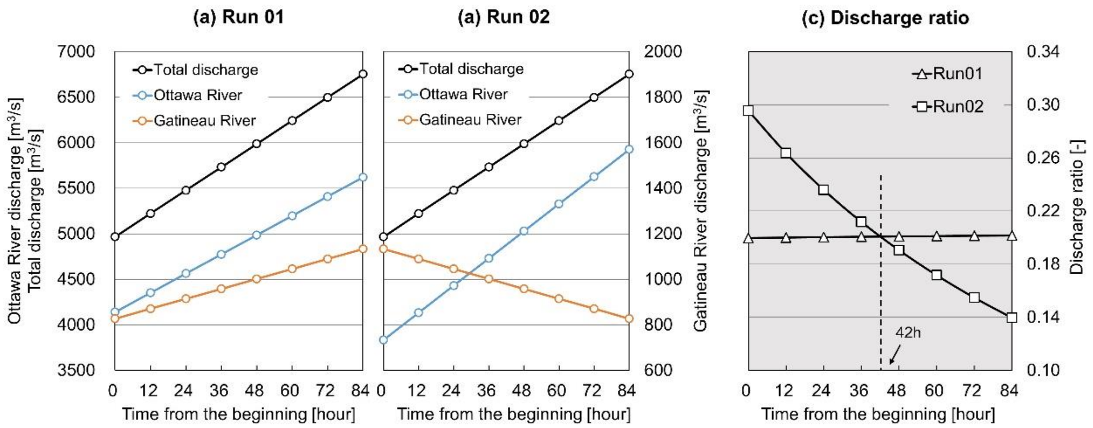

Figure 7.7. (a) & (b) Design flow hydrograph of "Run 01" and "Run 02", respectively. (c) time history of discharge ratio in "Run 01" and "Run 02".

7.4 Results

7.4.1 Flow rating curve at confluence outlet

Figure 7.8a shows the scatter plot of measured water surface elevation and total discharge along with the fitted flow rating curves at the OG confluence outlet. The flow rating curve was divided into three segments named "Phase 1", "Phase 2", and "Phase 3", respectively. WSE of the segmentation point is approximately 42.40 m between Phase 1 and Phase 2, which can be seen from the zoomed-in view (see the lower right embedded figure in Figure 7.8a). Rating curve segmentation has often been observed when flow transitions from in-channel flow (i.e., Phase 2 in this study) to overbank flow (i.e., Phase 3 in this study) (e.g., Yonesi et al., 2013; Lindroth et al., 2020; Naghavi et al., 2022). Therefore, although there is no clear trend difference between Phase 2 and Phase 3 in this study, we still differentiated them to account for the different flood stages they represent. We discuss the possible reasons for no clear segmentation between Phase 2 and Phase 3 in Section 4.1.1. WSE of the segmentation point between Phase 2 and Phase 3 is likely to be 43.66 m (i.e., data point "D"), which corresponds to the bankfull flood stage at the confluence outlet (see Figure 7.8b).

All discharge data used to develop the flow rating curve were collected from hydrometric stations. The majority of WSE data in Phase 1 were collected from the *HOBO*® logger in 2024 with one WSE data collected from the ADCP survey in 2021 (i.e., data point "A" in Figure 7.8a). As for Phase2, WSE data of point "B", "C", and "D" were collected from ADCP, land-based RTK GNSS, and satellite imagery, respectively. The remaining data in Phase 2 (those around the segmentation points) were collected from the *HOBO*® logger. Note that the numerical model boundary conditions in "Calibration run1" (i.e., data point "A" in Figure 7.8a) and "Calibration run2" (i.e., data point "B" in Figure 7.8a) belong to Phase 1 and Phase 2, respectively. WSE data of point "D", "E", and "F" in Phase 3 were collected from satellite imageries.

In this study, a three-segment flow rating curve can be modeled using the following power-law equation sets, assuming a rectangular channel shape (Reitan & Petersen-Øverleir, 2009; Qiu et al., 2021):

$$Q(H) = \begin{cases} \underbrace{K_{S_1}\sqrt{S_f^1}B_{w1}}_{a_1^1}(H - b_1^1)^{c1} \cdots \quad k_1 \le H < k_2(k_1 \ge b_1) \cdots \quad Phase1 \\ \underbrace{K_{S_2}\sqrt{S_f^2}B_{w2}}_{a_1^2}(H - b_1^2)^{c2} \cdots \quad k_2 \le H < k_3(k_2 > b_2) \cdots \quad Phase2 \\ \underbrace{K_{S_3}\sqrt{S_f^3}B_{w3}}_{a_1^2}(H - b_1^3)^{c3} \cdots \quad H \ge k_3(k_3 > b_3) \cdots \quad Phase3 \end{cases} \tag{7.7}$$

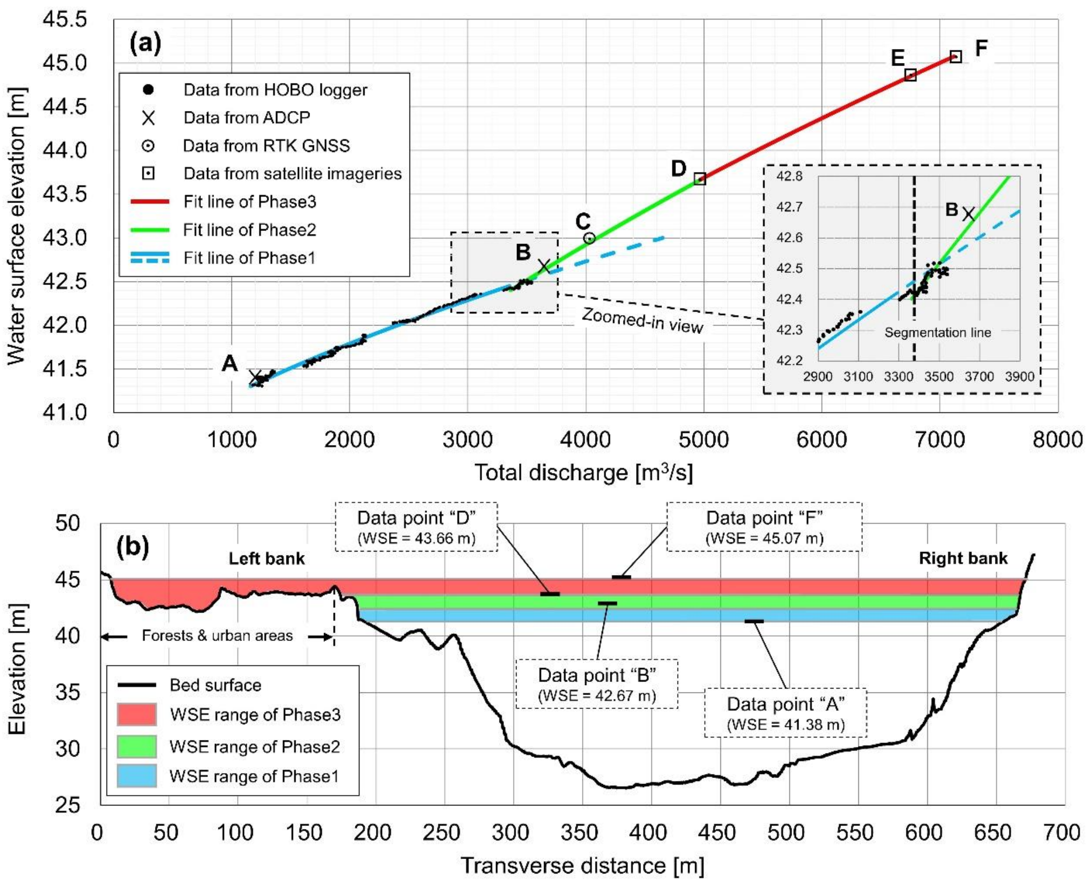

Figure 7.8. (a) Raw data points and fitted flow rating curve segments at the OG confluence outlet (b) the cross-sectional shape of the confluence outlet and WSE data ranges of different rating curve segments.

where K_S is the Strickler flow resistance coefficient [m$^{1/3}$/s]; S_f is the friction slope; B_w is the width of the rectangular channel [m]; The product of K_S, $\sqrt{S_f}$ and B_w is equivalent to the scaling coefficient "a_1" in Eq.(7.2); b_1 is the cross-section offset [m], and c is the exponent related to the type of hydraulic control (Le Coz et al., 2014); k_1, k_2 and k_3 are the activation flow stage [m].

Using least squares fitting, the resulting flow rating curve functions in this study are expressed as:

$$Q(H) = \begin{cases} 984 \cdot (H - 40.184)^{1.500} \cdots & 41.316 \leq H < 42.400 \cdots \quad Phase1 \\ 361 \cdot (H - 38.078)^{1.524} \cdots & 42.400 \leq H < 43.666 \cdots \quad Phase2 \\ 215 \cdot (H - 37.555)^{1.733} \cdots & H \geq 43.666 \cdots \quad Phase3 \end{cases} \quad (7.8)$$

The PBIAS values of fitted flow rating curves for Phase 1, Phase 2 and Phase 3 are -3.31%, 0.48% and 0.13%, respectively, which demonstrates the overall reliability of using the power law (i.e. Eq. 7.2) to describe the flow rating curve at the confluence outlet, especially during Phase 2 and Phase 3. Note that the model with more segments (i.e., will be referred to as “Model-2” hereafter) almost always shows a better fit to the observed data than the model with less or no segment (i.e., will be referred to as “Model-1” hereafter). Thus, it is important to assess whether Model-2 offers a significantly better fit to the data than Model-1 (i.e. the significance of using multi-segment). One common approach to address this issue is to calculate the F-statistic (Chow, 1960):

$$F = \frac{\dfrac{RSS_1 - RSS_2}{p_2 - p_1}}{\dfrac{RSS_2}{N - p_2}} = \frac{RSS_1 - RSS_2}{RSS_2} \cdot \frac{N - p_2}{p_2 - p_1} \quad (7.9)$$

where F is the F-statistic; RSS_1 and RSS_2 are the residual sum of squares of Model-1 and Model-2, respectively; p_1 and p_2 are the number of unknown parameters in Model-1 and Model-2, respectively; N is the total number of observations. In F-test, the null hypothesis (i.e., Model-2 does not provide a significantly better fit than Model-1) will be rejected if the calculated F-statistic is higher than the threshold value of the F-distribution at a specified significance level (e.g., 0.01).

Table 7.2 shows that, in the OG confluence case, the F-statistic of a 2-segments model versus a no-segment model is equal to 2817.0, much higher than the corresponding threshold of 3.9. The F-statistic of a 3-segments model versus a 2-segments model is equal to 9.7, also higher than the corresponding threshold of 3.9. Thus, the 3-segments model offers a significantly better fit to the data than 2-segment model or no-segment model with a confidence level higher than 99%. In other words, it is necessary to use 3-segment to model the flow rating curve at the confluence outlet.

In order to quantitatively describe and analyze rate of increase of WSE as the total discharge varies at different flow stages, here we define a new parameter, S_{QH}, as below:

$$S_{QH} = \frac{\sum_{i=1}^{n-1}(\frac{WSE_{i+1} - WSE_i}{Q_{i+1} - Q_i})}{N - 1} \tag{7.10}$$

where S_{QH} is the average rate of increase of WSE [cm/(m^3/s)]; WSE_i [cm] and Q_i [m^3/s] are the WSE and total discharge at the i^{th} data point in a dataset arranged in ascending order, respectively; and N is the total number of data points in a certain flow rating curve segment. S_{QH} can be interpreted as the reciprocal of the average slope of the rating curve of a certain flow rating curve segment. The calculation results show that the S_{QH} value of Phase 1 is 0.05 cm/(m^3/s) while the S_{QH} value of Phase 2 and Phase 3 is 0.07 cm/(m^3/s), which implies that WSE at confluence outlet increases faster with total flow discharge in Phase 2 and Phase 3 than that in Phase 1.

Table 7.2. F-statistic results of using different segmentation models.

Model-1	Model-2	RSS_1 [(m^3/s)^2]	RSS_2 [(m^3/s)^2]	p_2	p_1	N	$DOF_n^{\#1}$	$DOF_d^{\#2}$	$F_{\alpha=0.01}^{\#3}$	$F^{\#4}$
No segment	Two segments	2.47*10^7	9.93*10^5	6	3	360	3	354	3.9	2817.0
Two segments	Three segments	9.93*10^5	9.17*10^5	9	6	360	3	351	3.9	9.7

#1 DOF_n is the degree of freedom of the numerator, $DOF_n = p_2 - p_1$;

#2 DOF_d is the degree of freedom of the denominator, $DOF_d = N - p_2$;

#3 $F_{\alpha=0.05}^{\#3}$ is the threshold F-statistic under the confidence level of 99% for a certain DOF_n and DOF_d;

#4 $F^{\#4}$ is the F-statistic calculated from Eq.(7.9)

7.4.2 Modeled mid-channel WSE

Urban inundation mainly happened at the Gatineau River side during the 2019 flood. Thus, the WSE variation along the mid channel of Gatineau River at different flood stages and among different flow scenarios was investigated (see Figure 7.9). Figure 7.9a shows the mid-channel WSE difference between “Run 01” and “Run 02” at four different time stamps: 12 hours, 36 hours, 42 hours, and 60 hours. Table 7.3 lists the model boundary conditions at those time stamps in “Run 01” and “Run 02”. The mid-channel WSE difference is calculated as:

$$Diff_{T=t}^{(x,y)} = WSE_{T=t}^{(x,y),Run02} - WSE_{T=t}^{(x,y),Run01} \tag{7.11}$$

where $Diff_{T=t}^{(x,y)}$ is the mid-channel WSE difference between "Run 02" and "Run01" at time stamp t ($t =$ 12 hours, 36 hours, 42 hours, or 60 hours) and at location (x, y). $WSE_{T=t}^{(x,y),Run02}$ and $WSE_{T=t}^{(x,y),Run01}$ are the mid-channel WSE value at the time stamp "t" and at location (x, y) in "Run 02" and "Run01", respectively.

Figure 7.9a shows that the WSE along the Gatineau River mid channel in "Run02" is higher than that in "Run 01" at the earlier stage of the design flood, but this difference diminishes as the flood rises. At the latter stage of the design flood, the situation reverses and the WSE along the Gatineau River mid channel in "Run01" becomes higher than that in "Run 02". Notably, such difference is decreasing towards the tributary confluence mouth along the channel.

Figure 7.9 (b) & (c) show the WSE increment over 24 hrs (i.e., rate of increase of WSE) at two different stages of the flood in "Run 01" and "Run 02", respectively. The orange lines lie below the yellow lines in both Figure 7.9(b) & (c), which indicates that the WSE rises faster in the earlier flood stage than that in the latter stage, both in "Run 01" and "Run 02". In addition, the shape of the orange line is similar to that of the yellow line in both Figure 7.9 (b) or Figure 7.9 (c), which indicates that the spatial distribution of WSE increment speed does not change much over time. Noteworthy, in "Run 01", the WSE increment rate is greater at the upstream end of the domain, with faster increases in WSE near the inundation zones than at the downstream boundary. The situation in "Run 02" is reversed, where the WSE increment rate is lower upstream than downstream.

Table 7.3. Boundary conditions at 12 hours, 36 hours, 42 hours, and 60 hours in "Run 01" and "Run 02".

Case	Time stamp	Ottawa River discharge [m^3/s]	Gatineau River discharge [m^3/s]	Total discharge [m^3/s]	Downstream WSE [m]	Discharge ratio [-]
Run 01	12 hours	4351.60	870.71	5222.31	43.88	0.20
	36 hours	4774.40	958.14	5732.54	44.23	0.20
	42 hours	4880.10	980.00	5860.10	44.31	0.20
	60 hours	5197.20	1045.57	6242.77	44.55	0.20
Run 02	12 hours	4133.03	1089.29	5222.31	43.88	0.26
	36 hours	4730.69	1001.86	5732.54	44.23	0.21
	42 hours	4880.10	980.00	5860.10	44.31	0.20
	60 hours	5328.34	914.43	6242.77	44.55	0.17

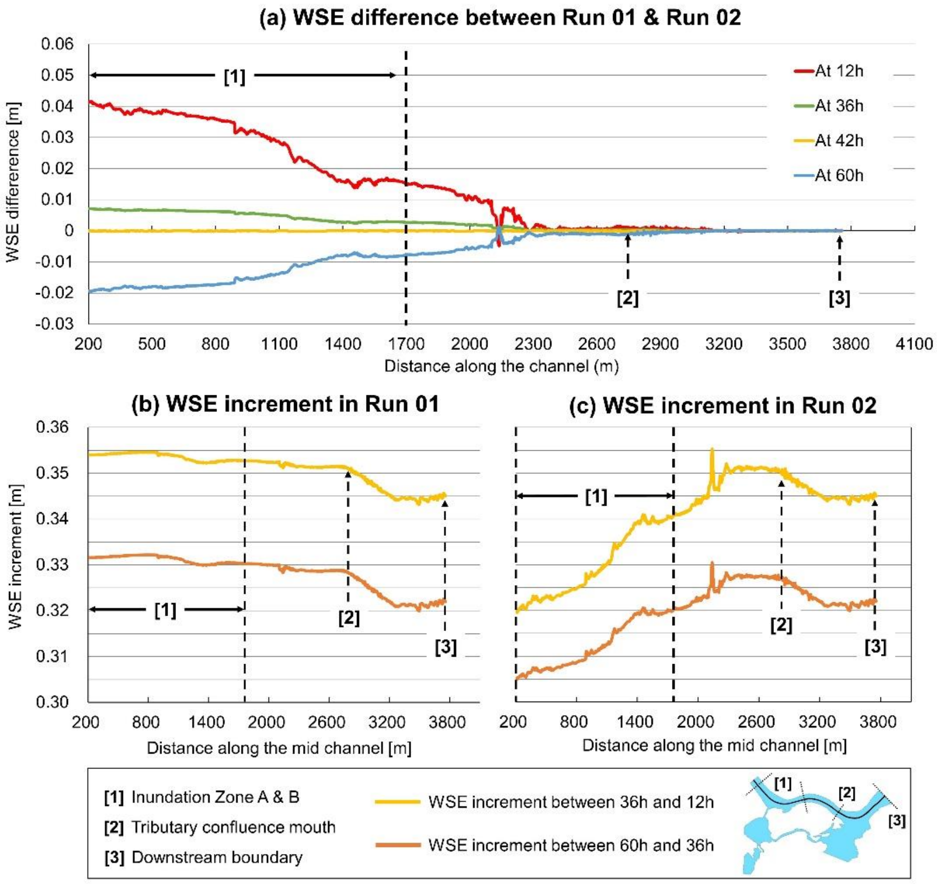

Figure 7.9. Variation of WSE along the mid channel (the mid channel is shown by the black line in the legend box) at different flood stages and between different flow scenarios. (a) mid-channel WSE difference between Run01 and Run02 at different time stamps. (c) & (d) Temporal WSE increment over 24 hrs along the mid channel in "Run 01" and "Run 02", respectively.

7.4.3 Modeled inundation extent

Figure 7.10 shows the modeled flood inundation extent of "Run 01" and "Run 02" at different flood stages. Results show that, at 12 hours, "Run 01" produced a slightly smaller inundation extent in Zone B compared to that in "Run 02" (Figure 7.10a1). At 36 hours, the modeled inundation extent in Zone B is almost identical between "Run 01" and "Run 02" (Figure 7.10a2). At 60 hours, "Run 01" produced a slightly larger inundation extent in Zone B compared to that in "Run 02" (Figure 7.10a3). The overall inundation extent in Zone C between "Run 01" and "Run 02" is almost identical at all three time stamps.

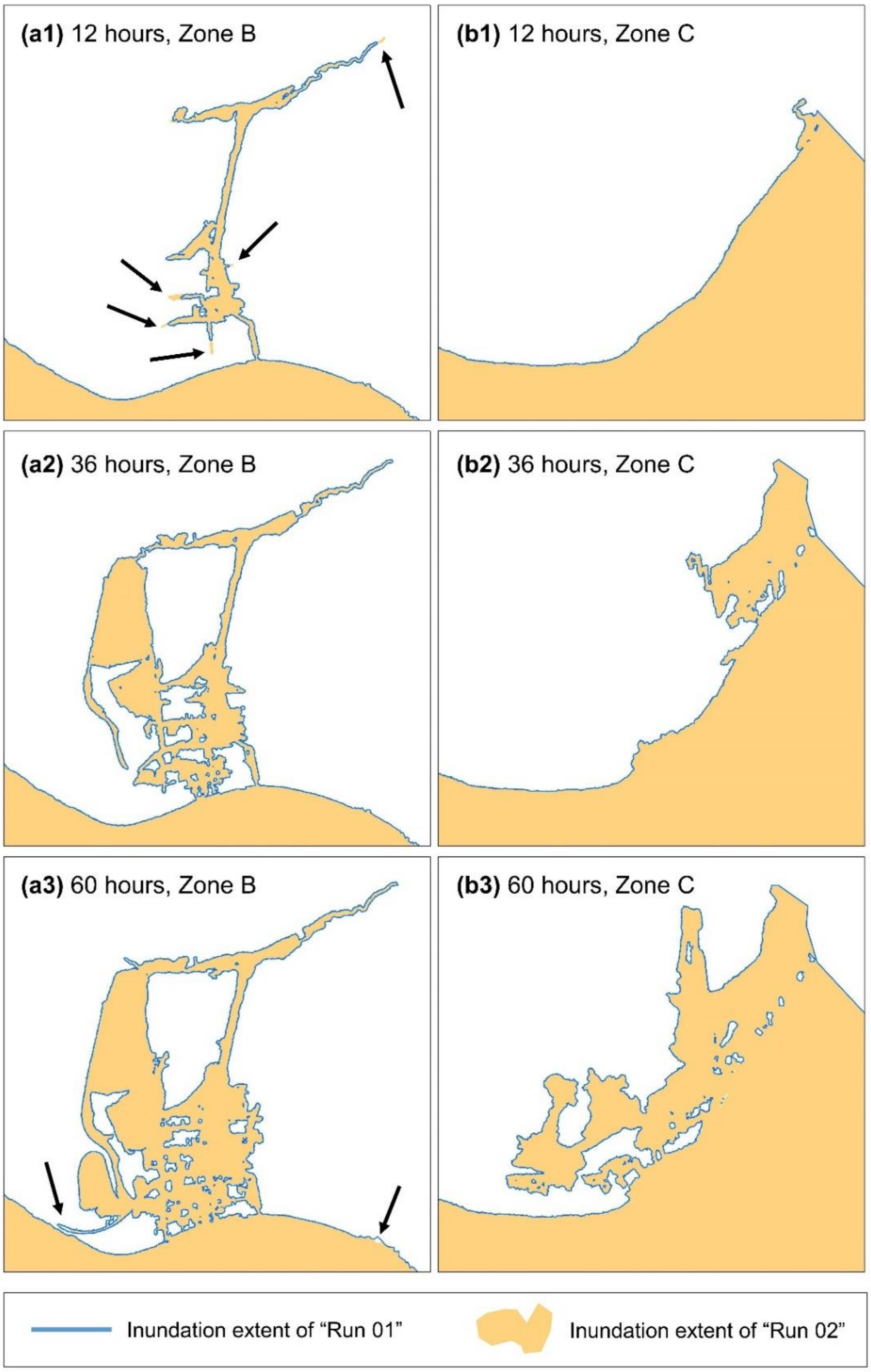

Figure 7.10. Modeled flood inundation extent of "Run 01" and "Run02". (a1), (a2), and (a3) modeled flood inundation extent at Zone B at 12 hours, 36 hours, and 60 hours, respectively. (b1), (b2), and (b3) modeled flood inundation extent at Zone C at 12 hours, 36 hours, and 60 hours, respectively. Polygons inside the flood inundation areas are indicative of dry areas. Black arrows mark the inundation difference between "Run 01" and "Run02".

The inundation process at Zone B is quite different from that at Zone C. Inundation at Zone C is an overbank process throughout the flood event, where floodwater gradually increased until surpassing the bank edge and inundating the inland areas. In contrast, inundation at Zone B starts from an inland culvert (see its location in Figure 7.3b). At 12 hours, Zone B was not directly inundated by the floodwater in the Gatineau River, but by the floodwater from the inland culvert. At 36 hours and 60 hours, inland floodwater at Zone B came from both the inland culvert and the Gatineau River.

7.5 Discussion

7.5.1 Flow rating curve at confluence outlet

7.5.1.1 Segmentation

The segmentation behavior of flow rating curves is common in nature (e.g. Petersen-Øverleir & Reitan, 2005; Birgand et al., 2013; Lindroth et al., 2020; Qiu et al., 2021; Muste et al. 2022; Kang et al., 2024). Factors that may lead to the segmentation includes overbank flow, morphological changes, unsteady flow (known as the hysteresis effect), vegetation growth or decay, backwater, ice cover, etc. (Herschy, 2008).

For a given overbank flow discharge, WSE would be lower in the case with a floodplain compared to the case without a floodplain (i.e., the original shape of channel cross-section is maintained and extrapolated), which causes the overbank flow rating curve to be more gradual (i.e., flatter) than the in-channel flow rating curve in the H (y-axis) – Q (x-axis) plot (e.g., Herschy, 2008; Yonesi et al., 2013; Kavousizadeh & Ahmadi, 2018; Lindroth et al., 2020; Naghavi et al., 2022). However, in the OG confluence case, the upper segments (i.e., Phase 2 & 3) are steeper than the lower segment (i.e., Phase 1) in the H-Q plot. To the best of the authors' knowledge, such a flow rating curve segmentation behavior has not been observed in experimental studies, but has been observed in a few field cases (e.g. Birgand et al., 2013; Sahoo et al., 2014; Kavousizadeh & Ahmadi, 2018; Hrafnkelsson, 2020; Kang et al., 2024; Li et al., 2024). However, none of those studies have provided detailed analysis on this matter.

Herein, we analyze this distinct segmentation behavior from the perspective of rating curve equations. Note that there are no channel constriction sites or dams downstream of the confluence outlet. Thus, the flow rating curve at the confluence outlet is mainly a channel control. Eq.(7.8) shows that the a_1 value in Phase 2 (i.e., $a_1^2 = 361$) is much lower than the a_1 value in Phase 1 (i.e., $a_1^1 = 984$). Consider that "a_1" is the product of K_S, $\sqrt{S_f}$ and B_w, the decrease of "a_1" should arise from the decrease of K_S, $\sqrt{S_f}$ and/or B_w. Figure 7.8b shows that the equivalent flow width, B_w, does not change much from Phase 1 to Phase 2, which does not contribute to the change of the

"a_1" value. Water level increases by about 0.2 m from the end of Phase 1 to the beginning of Phase 2. As a result, the in-channel Manning's n may slightly decrease from Phase 1 to Phase 2, which can result in a minor increase of the Strickler flow resistance coefficient, K_S $(= 1/n)$, and thus cause a slight increase of "a_1" (c.f., Pan et al., 2016). Therefore, the lower value of "a_1" in Phase 2 probably results from the decrease of friction slope, S_f, around data point "B", which outweighs the impact of K_S. The lower value of S_f in Phase 2 is probably due to two reasons:

(1) The hysteresis effect. During flood events, the temporal variation of flow discharge may lag behind the variation of friction slope in open channel flow (Muste et al. 2022). This phenomenon was also recently observed immediately downstream of a confluence flume by Tang et al. (2024). In this regard, the friction slope, S_f, may be smaller when flow approaches to the discharge peak (the time when data points, "B", "C", and "D" were collected in this study) compared to the earlier stages of flow rising periods (the time when *HOBO*® logger data were collected), which contributes to the decrease of the "a_1" value in Phase 2.

(2) The backwater effect. Castelltort et al. (2020) reported a decrease of friction slope immediately downstream of a large confluence during an extreme flood event due to the combined effects of backwatering and downstream constriction, which probably also exists in the OG confluence case. In addition, during the high flow ADCP survey in the OG confluence (corresponds to the data point "B" in Figure 7.8a), although the river bank at the confluence outlet was not overtopped (see Figure 7.8b), we observed in the field that the left bank of the Ottawa River at the upstream confluence junction was inundated, which can also contribute to the decrease of friction slope in the Ottawa River.

Although friction slope data at different flow events were not collected in this study, we provide a calculation sheet in Appendix D using known and assumed data to show that a sudden decrease of friction slope around data point "B" is theoretically possible and can lead to the observed flow rating curve segmentation behavior in this study.

Flow at the confluence outlet changes from in-channel flow to overbank flow at data point "D". Hrafnkelsson (2020) found that the "c" value in Eq. (7.8) was higher during overbank flow stages compared to in-channel flow stages in a trapezoidal shape river channel. Similarly, in this study, the "c" value in Phase 3 ($c_3 = 1.733$) is higher than that in Phase 2 ($c_2 = 1.524$) and in Phase 1 ($c_1 = 1.5$) , which demonstrates the impact of overbank flow to the flow rating curve after data point "D". However, the flow rating curve in Phase 3 still does not show a more gradual trend compared to that in Phase 2, as it would in most overbank flow situations (e.g., Herschy, 2008; Yonesi et al., 2013; Lindroth et al., 2020; Naghavi et al., 2022). This is also probably due to the lower "a_1" value in Phase 3 than that in Phase 2, which offsets the impact of a higher "c" value in Phase 3. Among the three determinants (K_S, $\sqrt{S_f}$ and B_w) of "a_1", the value of B_w may be higher in Phase 3 as the flow width increases from Phase 2 to Phase 3. At the same time, the Manning's n of forests and houses ($n \approx 0.08$ s/m$^{1/3}$) is much higher than that of river channel ($n \approx 0.025$ s/m$^{1/3}$, as shown in section 2.4.3) during overbank flow, which may cause the overall Manning's n to be higher and the value of K_S to be lower in Phase 3. In addition, the hysteresis effect may cause the friction slope, S_f, to be even lower in Phase 3 than that in the earlier stages as the flow reaches to the peak discharge (data points "E" and "F"). Thus, the decrease of both K_S and $\sqrt{S_f}$ probably offsets the increase of B_w and finally results in a lower "a_1" in Phase 3 than that in Phase 2. In summary, the effect of overbank flow to the flow rating curve segmentation was outweighed by the change of floodplain roughness (c.f. Yonesi et al., 2013) and friction slope, which finally results in a similar rating curve shape between Phase 3 and Phase 2.

In summary, the flow rating curve at the confluence outlet can be modeled using the power law in segments. The unique segmentation behavior of the flow rating curve at the OG confluence outlet mainly results from the combined effect of the change of roughness and friction slope, while the impact of overbank flooding appears to be relatively minor. Such a segmentation behavior suggests, when modeling confluence floods, determining downstream WSE from the in-channel flow rating curve may significantly underestimate the flood inundation extent. For example, if using the rating curve of Phase 1 to model the WSE at the peak of the 2019 flood at the OG confluence outlet, the WSE of the downstream boundary will be underestimated by about 1.15m. Additionally, the fact that the S_{QH} value is higher in Phase 2 and Phase 3 than in Phase 1 suggests that the flood inundation extent may increase faster with the flow discharge during overbank flow stage, posing additional risks to riverine neighborhood. Decision-makers should take this into account when developing flood mitigation strategies for cities situated at confluences, especially in terms of the evacuation plan before and during confluence floods.

7.5.1.2 Sensitivity to discharge ratio

The impact of discharge ratio on the flow field and morphodynamic process in open channel confluences has been extensively studied and documented (e.g. Riley et al., 2014; Yuan et al., 2016; Sukhodolov & Sukhodolova, 2019; Yu et al., 2020; Yuan et al., 2021). Spatially-varied WSE has also been reported in open channel confluences under different discharge ratios by different researchers (e.g., Biron et al., 2002; Zhang et al., 2020; Shen et al., 2023). However, due to the limited datasets in those studies, the sensitivity of WSE to discharge ratio at large-scale river confluences has not been investigated. In this study, we intend to tackle this problem by answering the following question: is the WSE at confluence outlet not only a function of total discharge, but also a function of discharge ratio?

In order to address this question, we calculated the correlation R between discharge ratio and residual error of flow discharge using the following equation:

$$R = \frac{\sum_{i=1}^{N}(\alpha_i - \bar{\alpha})(\varepsilon_i - \bar{\varepsilon})}{\sqrt{\sum_{i=1}^{N}(\alpha_i - \bar{\alpha})^2}\sqrt{\sum_{i=1}^{n}(\varepsilon_i - \bar{\varepsilon})^2}} \tag{7.12}$$

where α_i is the discharge ratio of the flow data point indexed with i; $\bar{\alpha}$ is the average discharge ratio of all flow data points; ε_i is the residual error of flow discharge at data point indexed with i, calculated as: $\varepsilon_i = Q_{sim,i} - Q_{obs,i}$, where $Q_{sim,i}$ is the flow discharge calculated from the fitted flow rating curve functions (see Eq. 7.8) at the data point indexed with i and $Q_{obs,i}$ is the measured flow discharge of the data point indexed with i; $\bar{\epsilon}$ is the average residual error of flow discharge of all flow data points.

The calculation gave an R value of 0.108, which indicates the correlation between discharge ratio and residual error of flow discharge is weak. In other words, errors of the developed flow rating curve functions can not be explained by or related solely to discharge ratio. Thus, in the OG confluence case, WSE at the confluence outlet is mainly a function of the total discharge, with only minor impact from the discharge ratio between two confluent rivers. Such a finding provides basis for the numerical model setting of determining the downstream WSE merely from the total discharge in this study, regardless of the discharge ratio variation. This finding also demonstrates that the spatial variation of WSE in open channel confluences under different discharge ratio conditions is probably not comparable to the temporal WSE variation induced by changes in total discharge. Note that the discharge ratio in the collected datasets falls within the range of [0.09, 0.26]. Thus, it is still possible that a larger variation of discharge ratio may have a comparable impact to the downstream WSE. Thus, further field investigations are still required to fully understand this issue.

7.5.2 Impact of tributary unsteadiness on inundation dynamics

In order to study the impact of tributary unsteadiness on confluence flood inundation, downstream WSE was kept the same between “Run 01” and “Run 02” to control variables. Since downstream WSE is mainly a function of total discharge, total discharge was also kept the same between the two flow scenarios. However, the setting of different tributary unsteadiness (i.e. rising or falling tributary flow) between the two flow scenarios resulted in different time histories of discharge ratio (Figure 7.7c). Thus, it is important to note that, only at the “42 hours” time stamp, both the tributary discharge and discharge ratio are identical between “Run 01” and “Run 02” (i.e. the tributary unsteadiness is the only variable, see Figure 7.7c). At all other times, the tributary discharge, discharge ratio, and tributary unsteadiness are different between “Run 01” and “Run 02”.

The Gatineau River discharge is higher at 12 hours in “Run 02” (i.e., 1089.29 m^3/s) than that in “Run 01” (i.e., 870.71 m^3/s), which results in a higher WSE at 12 hours in “Run 02” compared to that in “Run 01” (the red line in Figure 7.9a). As the Gatineau River discharge rises in “Run 01” while drops in “Run 02” (Figure 7.7a & 7.7b), the WSE difference curve between them also goes down (i.e. red line → green line → orange line → blue line in Figure 7.9a). Importantly, at 42 hours, the tributary unsteadiness is the only variable between “Run 01” (i.e., rising flow) and “Run 02” (i.e., falling flow), yet there is barely any WSE difference between “Run 01” and “Run 02” (the orange line in Figure 7.9a). We also carried out an additional steady-state simulation using the boundary conditions at 42 hours. The mid-channel WSE along the tributary channel in the steady-state simulation is also the same as that in “Run 01” or “Run 02”. Thus, given the same total discharge, the tributary mid-channel WSE is mainly a function of the tributary discharge and is not sensitive to tributary flow unsteadiness (i.e., rising, steady-state, or falling). In addition, the model validation against overland floodwater velocity was carried out using a steady-state model in this study. The validation results suggest that steady-state numerical model can reproduce the floodwater dynamics. Considering all those findings, it is worth considering to use steady-state numerical models in future confluence floods simulations to further save computational cost.

Figure 7.9a also shows that the WSE difference between “Run 01” and “Run 02” is not constant along the tributary, but decreases towards downstream (Figure 7.9a), which suggests that impact of tributary discharge on the tributary WSE becomes weaker and impact of total discharge starts to dominate when approaching to the confluence mouth (“[2]” in Figure 7.9a). At the point where the WSE difference between “Run 01” and “Run 02” almost equals to zero (i.e., downstream of the tributary mouth), the tributary discharge no longer affects the local WSE for a given total discharge, as the WSE at the downstream boundary is entirely a function of total discharge.

Figure 7.9b & 7.9c shows that the WSE increment rate in zone “[1]” in “Run 01” is higher than that in “Run 02” between 12 hours and 36 hours and also between 36 hours and 60 hours, which might seem to suggest that the tributary unsteadiness affects the WSE increase rate in the tributary channel. However, these differences arise from the different instantaneous tributary flow discharge between the two cases, not the flow unsteadiness itself. For example, at 200 m downstream of the tributary inflow boundary, the modeled tributary WSE is 44.01 m and 44.05 m at 12 hours in “Run 01” and “Run 02”, respectively. The modeled tributary WSE is almost the same between “Run 01” and “Run 02” at 42 hours, which produces a lower rate of WSE increase in “Run 02” compared to that in “Run 01” between 12 hours and 42 hours. Such a lower rate of WSE increase does not result from different tributary unsteadiness, but is merely due to the higher initial tributary WSE in “Run 02” compared to “Run 01”, which results from a higher initial tributary flow discharge in “Run 02”. Thus, given the same total discharge, the tributary WSE increase rate is related to the tributary WSE at different time stamps, which, as discussed before, results from the real-time tributary flow discharge. The variation of tributary flow unsteadiness does not bring any distinct impact on this matter.

Figure 7.10 (a1) show that, at 12 hours, flood inundation extent in Zone B in “Run 02” is larger than that in “Run 01”. This is because the discharge and WSE (see the red line in Figure 7.9a) of the tributary are both higher in “Run 02” than those in “Run 01”. The flood inundation extent in Zone B at 36 hours (Figure 7.10a2) and 60 hours (Figure 7.10a3) can also be linked to the WSE difference at the Gatineau River at the corresponding time stamp between “Run 01” and “Run 02” (the green and blue lines in Figure 7.9a, respectively). Thus, flood inundation extent at tributary side is directly related to tributary WSE, and as discussed before, related to tributary discharge (or discharge ratio) when total discharge is constant. There is no clear inundation extent difference at Zone C between “Run 01” and “Run 02” (Figure 7.10 b1-b3) at all times. This is because Zone C is near the downstream model boundary, where the same WSE was applied between “Run 01” and “Run 02” at all times. Thus, flood inundation extent downstream of the confluence is directly related to downstream WSE, and as discussed before, related to total discharge, with no clear impact from discharge ratio or flow unsteadiness. We calculated the S_{QH} value in the tributary channel from the modeled tributary discharge and WSE data at 200 m downstream of the tributary inflow boundary during overbank floods. The S_{QH} value in the tributary channel is 0.017 cm/(m^3/s), which is much lower than the S_{QH} value of 0.069 cm/(m^3/s) at the confluence outlet during Phase 2. This suggests that the impact of tributary discharge variation on tributary WSE is not comparable to the impact of total discharge variation on downstream WSE. This also explains why the variation of tributary discharge has a minor impact on the tributary inundation extent (Figure 7.10, a1-a3). In summary, numerical model results show that, under the condition of constant total discharge, WSE and flood inundation extent at the tributary side is mainly a function of real-time tributary flow discharge, regardless of different tributary flow unsteadiness. The overall flood inundation extent at open channel confluences is mainly determined by total discharge, with minimal impact from discharge ratio or flow unsteadiness. Thus, it is probably appropriate to use steady-state numerical models in future confluence floods simulations to further save computational cost.

7.5.3 Limitations and future concerns

This study demonstrates that multi-source field data along with a calibrated and validated numerical model can serve as a powerful tool in investigating urban confluence floods. In this section, we point out some limitations of this study and propose some potential future concerns accordingly:

- **Data volume.** Datasets during extreme floods are quite limited, which constrained the reliability of the developed flow rating curve in Phase 2 and Phase 3 to a certain extent. In addition, we are not fully certain about the friction slope variation across the AOI due to lack of field measurement data.

- **Validation results.** Although the validation results are satisfactory in this study, the reason why the numerical model overestimates the observed flood inundation extent during the 2019 event is still unknown. In addition, flood inundation extent data at different flood stages and during different flood events need to be collected for further model validation.

- **Object diversity.** The variation of discharge ratio is very limited in the OG confluence case. River confluences of different sizes, junction angles, and discharge ratios should be investigated in the future to understand the general flood inundation behaviors.

7.6 Conclusion

In this study, we analyzed the flood inundation behaviors of an extreme urban confluence flood event at the Ottawa-Gatineau confluence using multi-source field data and a 2D hydrodynamic model. We developed a flow rating curve at the confluence outlet using available datasets and found that a segmented power law is applicable. A distinct segmentation behavior was observed in the developed rating curve. Different from the segmentation behavior previously observed in overbank flow situations, WSE at the confluence outlet increases faster with total flow discharge in the overbank flow segment than that in the in-channel flow segment, which is probably due to the combined effects of the change of roughness and friction slope. We found that water surface elevation (WSE) is mainly a function of total discharge and it is not sensitive to discharge ratio in the range of [0.09, 0.26] at the confluence outlet in the OG confluence case. This suggests that the spatial variation of WSE at open channel confluences, as reported in previous studies, is probably not comparable to the temporal variation of WSE with total flow discharge.

This is the first study to validate a fluvial urban flood numerical model against the observed flood inundation extent as well as the inland floodwater velocity. The numerical model reproduced both of two validation datasets with reasonable success, which suggests that a 2D hydrodynamic model is adequate in simulating large-scale urban overland confluence floods. The developed model was used to simulate the inundation dynamics of two design flood events with the same time series of total discharge but different tributary flow unsteadiness (i.e. rising or falling). Under such a condition, the tributary WSE and flood inundation extent are mainly determined by the instantaneous total discharge and the instantaneous tributary discharge, but not the tributary flow unsteadiness in the OG confluence case. The overall flood inundation extent at the OG confluence is thus most sensitive to the total discharge, with only relatively minor impact from discharge ratio, and no apparent influence of flow unsteadiness. This suggests that steady-state numerical models have the potential to be considered for modeling confluence floods to further save computational cost.

The current study is limited to the OG confluence, and further research is needed to obtain generalized conclusions. If such general conclusions can be achieved, they would have significant implications for engineering practice. Specifically, flood managers should focus on the design of “total discharge hydrograph” at river confluences and minimize the magnitude and duration of “total discharge peak” by shifting the peaks of the two confluent flows when possible to mitigate the flood risks. Discharge ratio, flow unsteadiness and hydrodynamic interactions between the two confluent flows are probably not the main issues in confluence flood mitigation. Decision-makers may also need to take the distinct flow rating curve segmentation behavior into account when developing strategies in terms of the evacuation plan before and during confluence floods.

Chapter 8. Conclusions and future work

8.1 Conclusion

This thesis aimed to fill research gaps in fluvial urban floods in terms of flood morphodynamic processes, in-channel bar management, flood velocity data collection, inundation dynamics of confluence floods, model development, etc. The major findings and conclusions are summarized as below:

- In **flood morphodynamics**, we found that the timings of local morphological changes during extreme floods vary for different morphodynamic units, but are similar for similar morphodynamic units, despite the planform differences across different reaches. Numerical model results show that bedload transport rate is more sensitive to depth-averaged flow velocity rather than medium sediment size, due to the greater spatial and temporal variance of velocities than grain sizes during a large flood event. The model results also show that with the same flood peak and duration, a regulated flood event with a short-lasting rising period, rather than a long-lasting rising period, might bring less potential bank erosion and bar growth to downstream reaches and vice versa.
- In **in-channel bar management**, bar removal presents the best flood mitigation effect compared to bar realignment and the "do nothing" plan. However, the constructability and ecological impacts of wholesale dredging should not be overlooked. Bar realignment plan can stabilize the channel bed thus performs better in terms of aquatic habitat protection as well as the realization of river recreation. The downstream morphology of a river could be affected in a short-term if the bar management plan brings sediment deficit to the river reach (i.e. bar removal). However, no matter which bar management plan is applied, the downstream morphological patterns are predicted to be similar after a long term. Thus, manipulation on vegetated instream gravel bars does not have obvious morphological impact to the downstream river reach. The model results also show that creating a uniform, less obstructed river bed is believed to be the fundamental strategy in flood mitigation.
- In **flood velocity data collection**, we developed a new Large-Scale Particle Image Velocimetry (LSPIV) algorithm, Time Frequency Analysis (TiFA), to overcome the limitations of other algorithms including the traditional LSPIV, Ensemble Correlation (EC), Large-Scale Particle Tracking Velocimetry (LSPTV), and

Seeding Density Index (SDI). Among those algorithms, TiFA showed the highest overall accuracy and lowest computation cost in data analysis, especially under low tracer density conditions. In addition, TiFA showed its unique ability of automatically filtering out velocity data from low-quality zones such as no-tracer zones and surface glare zones. TiFA also showed its potential in processing turbulent flow. In summary, the newly-developed algorithm, TiFA, has demonstrated strong capability and competence in various flow and tracer scenarios, making it a valuable candidate for future applications.

- In **confluence inundation dynamics**, we developed a flow rating curve at the outlet of Ottawa-Gatineau confluence using available datasets and found that a segmented power law is applicable. A distinct segmentation behavior was observed in the developed rating curve, which is probably due to the combined effects of the change of roughness and friction slope. We found that water surface elevation (WSE) at the confluence outlet is mainly a function of total discharge with minimal sensitivity to discharge ratio. We are the first study to validate a two-dimensional (2D) hydrodynamic model against the observed flood inundation extent as well as the inland floodwater velocity. The numerical model reproduced both of two validation datasets with reasonable success, which suggests that the 2D model is adequate in simulating large-scale urban overland confluence floods. The numerical model results suggest that the tributary WSE and flood inundation extent are mainly determined by the instantaneous total discharge and the instantaneous tributary discharge, but not the tributary flow unsteadiness. The overall flood inundation extent at open channel confluences is thus most sensitive to the total discharge, with only relatively minor impact from discharge ratio, and no apparent influence of flow unsteadiness. This suggests that steady-state numerical models can be used in modeling confluence floods to further save computational cost.

8.2 Future works

Although this thesis addresses several research gaps in fluvial urban flood modeling, numerous research gaps and challenges remain in the research field. Additionally, this thesis has limitations that require further refinement to enhance its robustness and applicability. Key areas for future work include:

- **The actual river morphodynamic processes during floods.** Although the developed morphodynamic model has been validated against the measured post-flood Digital Elevation Model (DEM), it remains uncertain whether a morphodynamic model that successfully reproduced the observed post-flood morphological changes can also reproduce the actual morphodynamic processes during the flood, including the timing of morphological changes. More comprehensive field observations and accompanying modeling are required to answer this question. In addition, we only investigated the morphodynamic processes at a portion of a bedload-dominant gravel-bed river during a large flood event. More comprehensive field observations and modeling works in different alluvial rivers (e.g. sand-bed rivers; braided rivers) and under different types of floods (e.g. bankfull floods, outburst floods) are required to solidify and generalize the findings.

- **Improvement of model accuracy and representation of actual situations.** Although previous studies show that loose-coupled morphodynamic models can have equivalent performance to fully-coupled morphodynamic models, their performance has not been evaluated in extreme fluvial floods in large-scale rivers. Future studies could focus on this topic and provide more robust evidence regarding model selection in large floods. In addition, impact from climate change is not considered in the design flood hydrograph in the Bow River case, which limits the application of the projection results. Moreover, the morphodynamic model's (Delft-3D) ability to reproduce post-flood bathymetry requires further improvement. Possible improvements in terms of model inner structures include: bedload inflow boundary, interchange between bed stratigraphy layers, dynamic-updating of surface roughness, etc.

- **Enhancement of LSPIV algorithm.** LSPIV holds great potential for development and application in measuring flood velocities. Although the accuracy and efficiency of the newly-developed algorithm, TiFA, are both superior comparing with other algorithms, the empirical formulas used to determine the user-defined parameters in TiFA are not validated against an independent dataset. Thus, more datasets from different situations are needed to further test and polish the empirical formulas used in TiFA. Velocity map results generated from the current version of TiFA are still not smooth. Future work can consider to introduce new tools such as neighboring value analysis to improve TiFA's performance. In addition, there are some other competitive image velocimetry algorithms that are not investigated in this thesis such as KLT-IV, STIV, SSIV, and OTV. Future works should consider a more thorough evaluation of TiFA by comparing with those algorithms. Moreover, more diverse flow and tracer conditions should be used to further test

TiFA's performance

- **More field data during river confluence floods.** Datasets during extreme confluence floods are quite limited in the OG confluence study, especially in terms of the water surface slope data, which constrained the reliability of the interpretation on confluence flow rating curve segmentation behavior to a certain extent. In addition, flood inundation extent data at different flood stages and during different flood events need to be collected to test if a steady-state model works in all flood situations in confluences. Moreover, the variation of discharge ratio is very limited in the OG confluence case. River confluences of different sizes, junction angles, and discharge ratios should be investigated in the future to understand the general flood inundation behaviors.

Appendix A

This appendix archives additional information that supports “Chapter 4: Gravel-bed river morphodynamic processes throughout an 80-year flood event from numerical modeling: implications for flood regulation strategies”. It contains two supplementary figures: Figure A1 shows the computational grid used in this study. Figure A2 described logical relationships of bedload transport rate on surface sediment size and flow velocity. Figure A3 showed the difference in the modeled volumetric changes between the original 2013 flood and the “reversed” 2013 flood, in order to testify the hypothesis on flood regulation strategy that the author proposed in the manuscript.

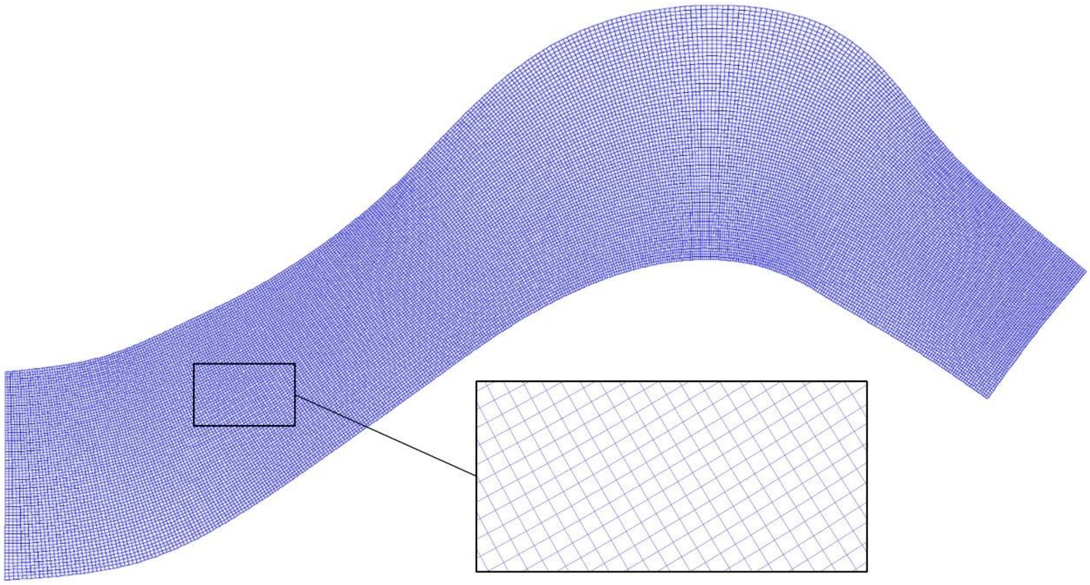

Figure A1. Computational grid used in the study.

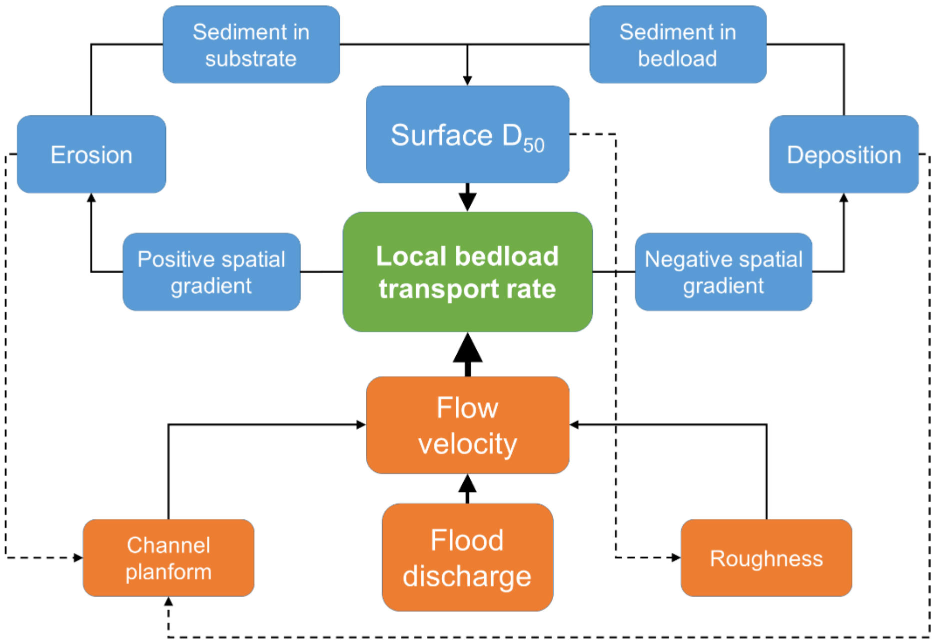

Figure A2. Dependent relationships of bedload transport rate on surface sediment size and flow velocity. Arrows mean "contribute to the change of" or "cause the change of". Thicker arrows imply higher contributions. Dashed lines mean "weak contributions".

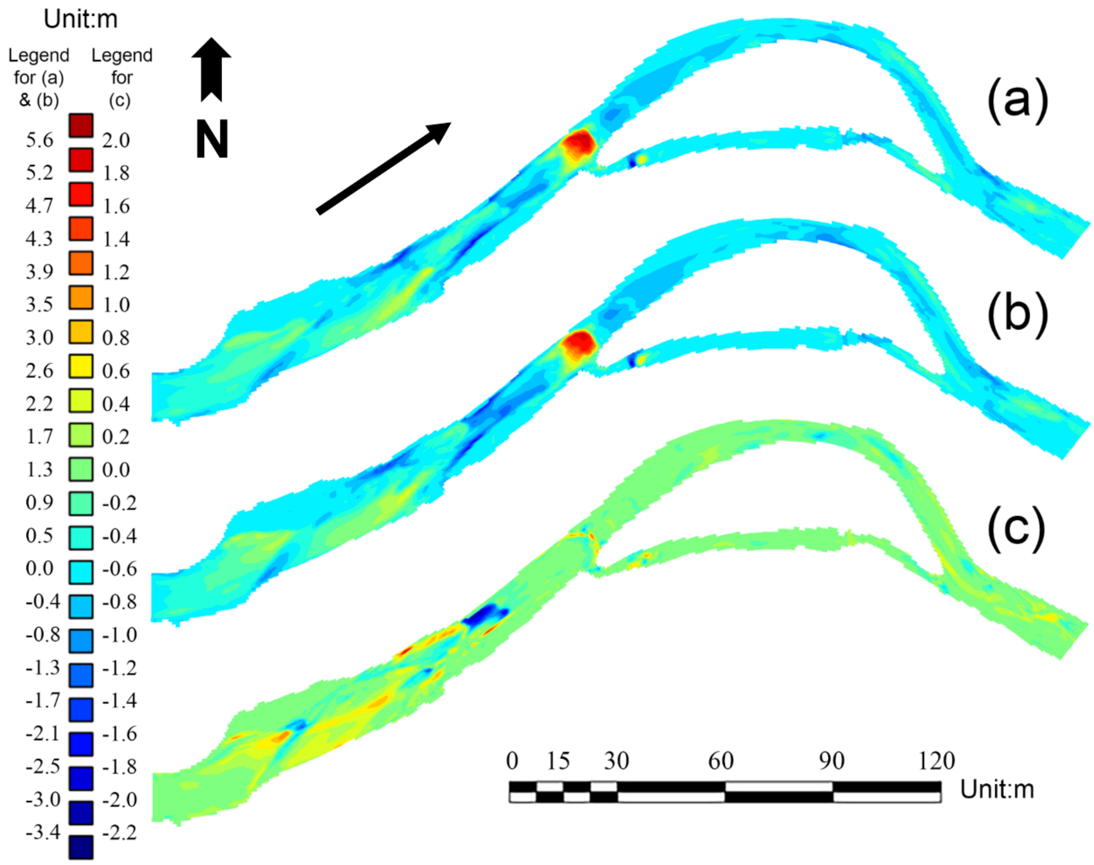

Figure A3. (a) Cumulative deposition or erosion (CDE) map under the original 2013 flood event, (b) CDE map under the "reversed" 2013 flood event, (c) Difference map between "(b)" and "(a)" (i.e. "Difference" = "(b)" – "(a)").

Appendix B

This appendix archives additional information that supports "Chapter 5. Impact evaluation of instream bar management using morphodynamic modeling". It contains:

- Model sensitivity analysis results of the parameter "$MorFac$";
- Cumulative deposition and erosion map of different bar management plans after the short-term simulation;
- 30-year flood peak level difference between "bar removal" and "do nothing", and between "bar relocation" and "do nothing";

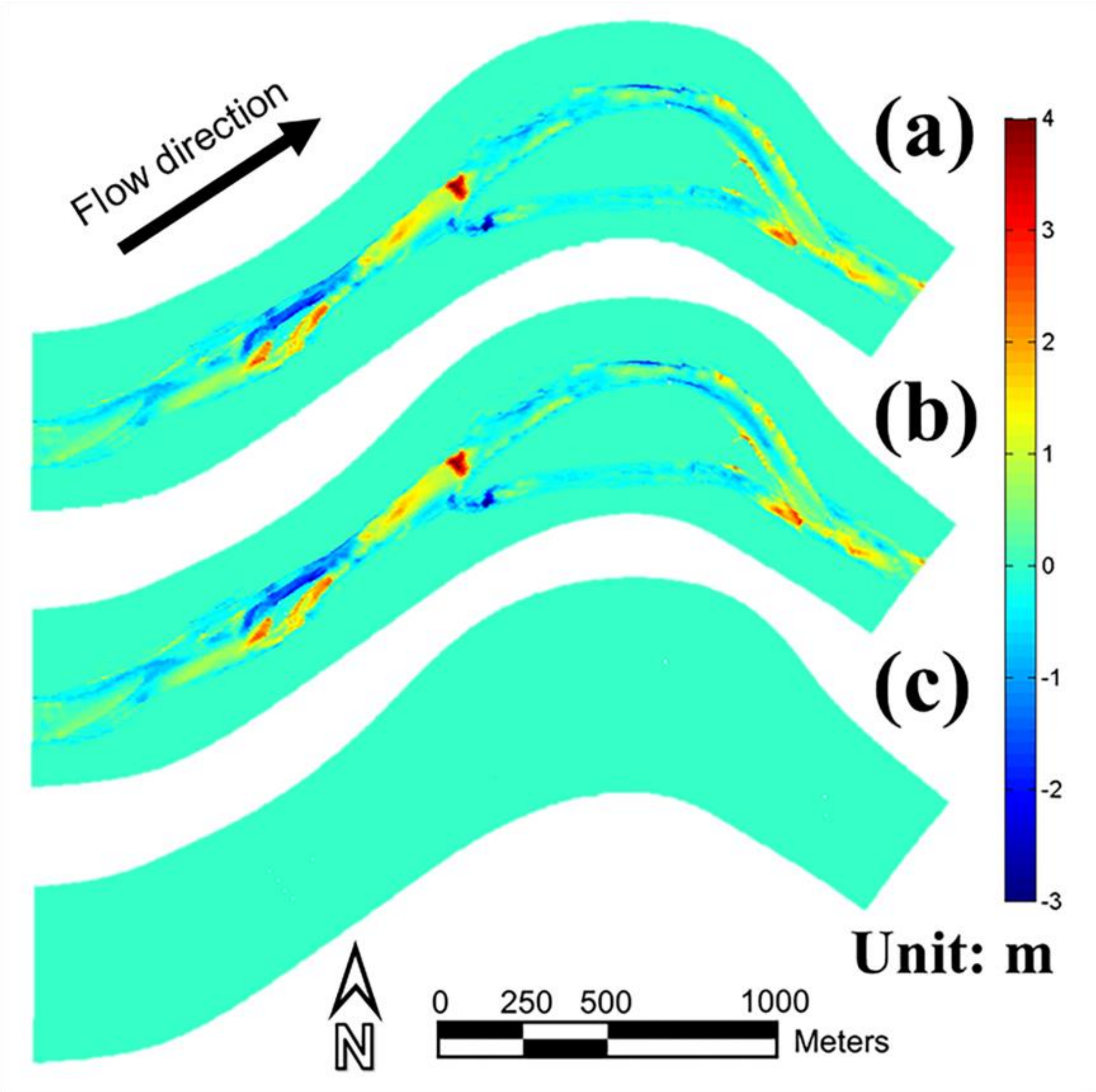

Figure B1. Cumulative deposition and erosion map of using different $MorFac$ after a long-term simulation of the "do nothing" plan (a) $MorFac$ = 1. (b) $MorFac$ = 5. (c) $MorFac$ = 10.

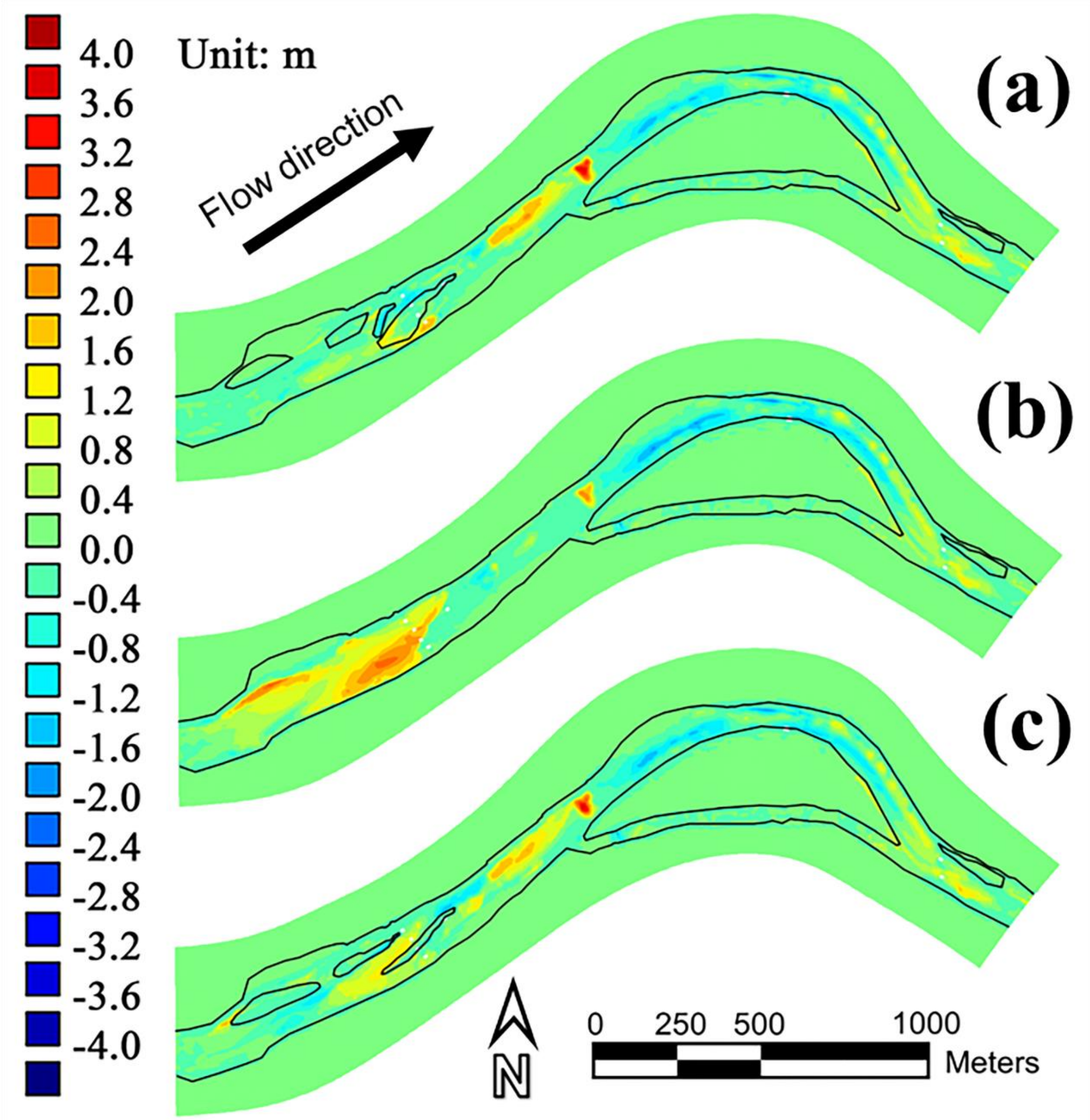

Figure B2. Cumulative deposition and erosion map of different bar management plans after the short-term simulation. (a) do nothing; (b) bar removal; (c) bar relocation.

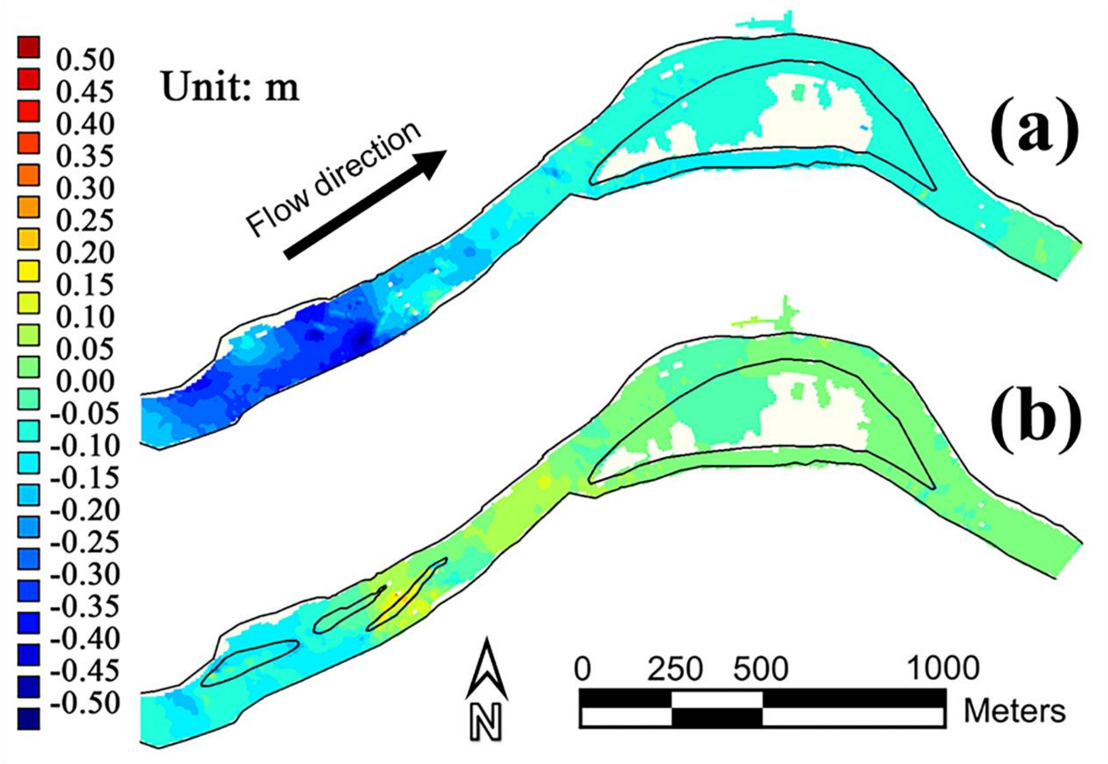

Figure B3. 35-year flood peak level difference (a) between "bar removal" and "do nothing", and (b) between "bar relocation" and "do nothing".

Appendix C

This appendix archives additional information that supports "Chapter 6. TiFA: An Efficient and Robust LSPIV Algorithm Based on Joint Distribution Analysis". It contains:

- The velocity map produced by five image velocimetry algorithms in the Bradano River case;
- The velocity map produced by five image velocimetry algorithms in the Arrow River case;
- The linear relationship between noise threshold, V_{noise} and average surface velocity $\bar{V}$;
- The linear relationship between count threshold, N_c and average surface tracer density, ρ_T.

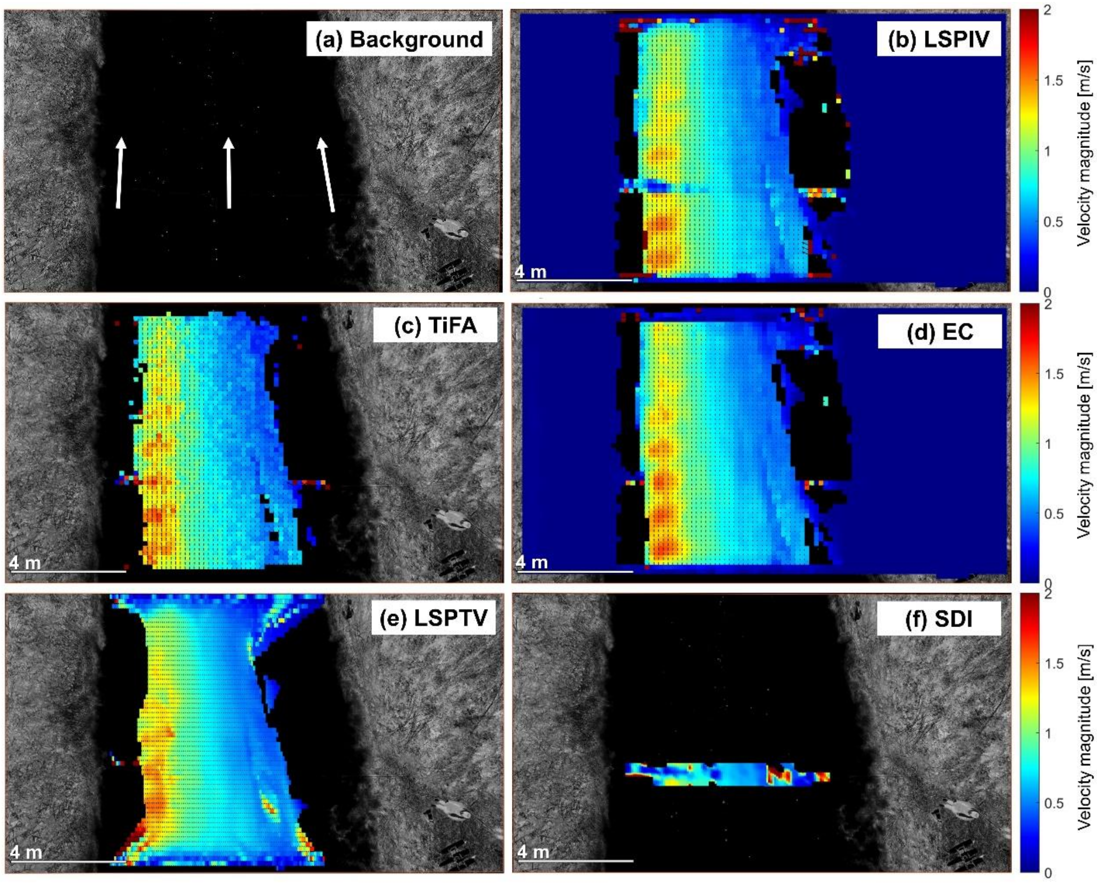

Figure C1. Velocity maps of five image velocimetry algorithms in the Bradano River case. (a) background map; (b) Traditional LSPIV; (c) TiFA; (d) EC; (e) LSPTV; (f) SDI. White arrows mark the flow direction.

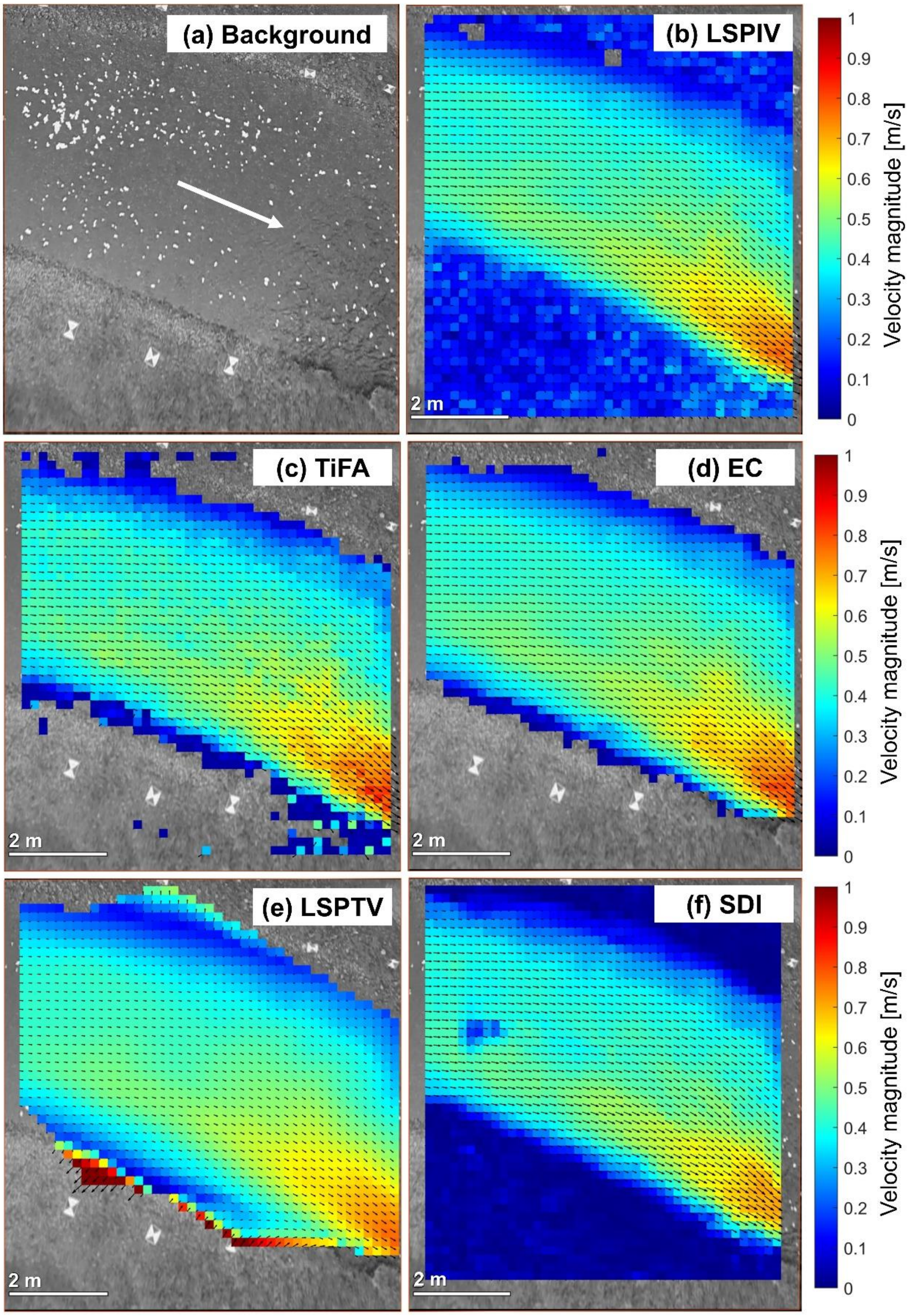

Figure C2. Velocity maps of five image velocimetry algorithms in the Arrow River case. (a) background map; (b) Traditional LSPIV; (c) TiFA; (d) EC; (e) LSPTV; (f) SDI. The white arrow marks the flow direction.

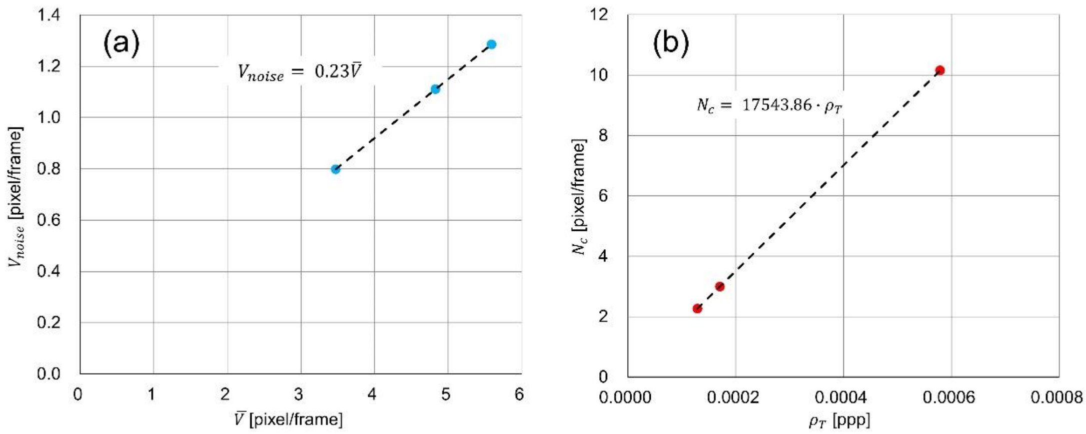

Figure C3. (a) The linear relationship between noise threshold, V_{noise} and average surface velocity $\overline{V_s}$; (b) The linear relationship between count threshold, N_c and average surface tracer density, ρ_T.

Appendix D

This appendix archives additional information that supports “Chapter 7. Inundation Dynamics of an Extreme Urban Confluence Flood: Insights from In-Situ Measurements, Remote Sensing, and Hydrodynamic Modelling”. It contains:

- Model validation results on April 30th, 2019;
- Derivation process of the flow rating curve (i.e. “Q-H” relationship) at a trapezoidal compound channel. The flow rating curve contains a “in-channel phase” and a “compound phase”;
- Exploration on the possibility of the decreasing friction slope assumption at the Ottawa-Gatineau confluence.

D.1. Model validation results on April 30th, 2019

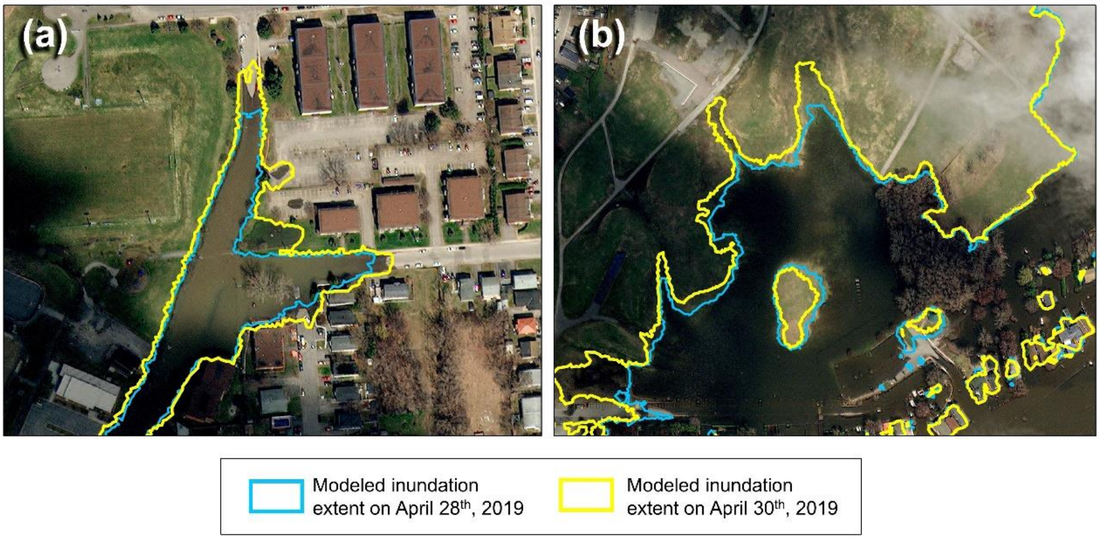

Figure D1. Modeled flood extent on April 30th, 2019 at two places marked by the red polygons in Figure 7.6 (a) & (b). Background satellite imagery was collected on April 30th, 2019.

D.2. Derivation of the flow rating curve at a trapezoidal compound channel

This section provides the derivation of the flow rating curve in the following trapezoidal compound channel (see Figure D2).

B_1 is the bottom base width of the none-compound portion; B_2 is the bottom base width of the compound channel; α is the slope angle of the none-compound portion; h_1 is the channel height of the none-compound portion; β is the slope angle of the compound portion; H is the water surface elevation relative to the cease-to-flow reference level H_0; D is the water depth.

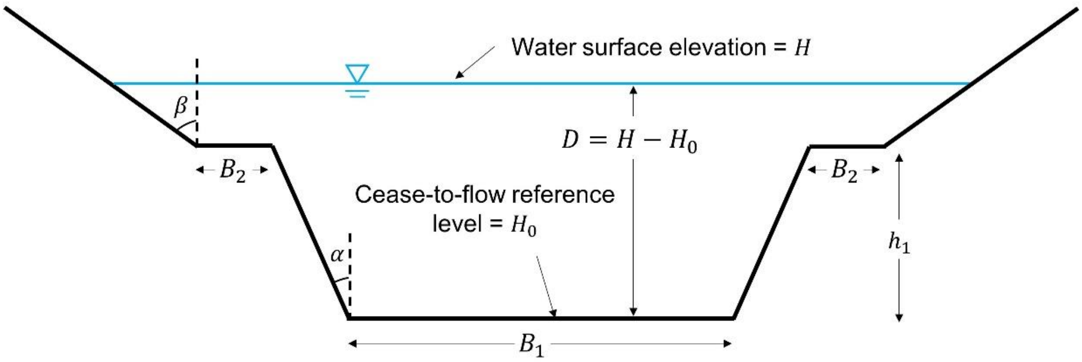

Figure D2. The cross-sectional view of an idealized trapezoidal compound channel.

Based on the Chezy's formula, flow discharge of uniform flow can be formulated as:

$$Q = V \cdot A = C\sqrt{RS} \cdot A = \frac{1}{n} R^{1/6} \cdot \sqrt{RS} \cdot A = \frac{1}{n} \cdot \sqrt{S} \cdot R^{2/3} \cdot A \qquad \text{(D1.1)}$$

where Q is flow discharge, n is Manning roughness, S is friction slope, R is hydraulic radius, A is flow cross-sectional area.

D.2.1. In-channel phase

When $0 < D \leq h_1$, the cross-sectional area is:

$$A = (2D \cdot tan\alpha + B_1 + B_1) \cdot D \cdot \frac{1}{2} = D(B_1 + D \cdot tan\alpha) \qquad \text{(D1.2)}$$

The wetted perimeter is:

$$P = \frac{2D}{cos\alpha} + B_1 \qquad \text{(D1.3)}$$

The hydraulic radius is:

$$R = \frac{A}{P} = \frac{D(B_1 + D \cdot tan\alpha)}{\frac{2D}{cos\alpha} + B_1} = \frac{D \cdot cos\alpha \cdot (B_1 + D \cdot tan\alpha)}{2D + B_1 cos\alpha}$$

$$= \frac{D \cdot cos\alpha \cdot (1 + \frac{D}{B_1} \cdot tan\alpha)}{\frac{2D}{B_1} + cos\alpha} \qquad \text{(D1.4)}$$

With the wide channel approximation (i.e., $D \ll B_1$), Eq. (D1.4) can be approximated as:

$$R \approx \frac{D \cdot cos\alpha \cdot (1 + 0 \cdot tan\alpha)}{0 + cos\alpha} = D \quad \text{(D1.5)}$$

Substitute Eq. (D1.2) and Eq. (D1.5) into Eq. (D1.1), we have:

$$Q = \frac{1}{n} \cdot \sqrt{S} \cdot D^{\frac{2}{3}} \cdot D \cdot (B_1 + D \cdot tan\alpha)$$

$$= \frac{1}{n}\sqrt{S}B_1 \cdot D^{1.67} + \frac{1}{n}\sqrt{S} \cdot D^{2.67} tan\alpha \quad \text{(D1.6)}$$

$$= \frac{1}{n}\sqrt{S} \cdot B_1 \cdot (H - H_0)^{1.67} + \frac{1}{n}\sqrt{S} \cdot tan\alpha \cdot (H - H_0)^{2.67} \cdots 0 \leq H < H_0 \quad \text{(D1.7)}$$

D.2.2. Compound phase

When $D > h_1$, the in-channel cross-sectional area is:

$$A_1 = (2h_1 \cdot tan\alpha + B_1 + B_1) \cdot h_1 \cdot \frac{1}{2} = h_1(B_1 + h_1 \cdot tan\alpha) \quad \text{(D1.8)}$$

The compound cross-sectional area is:

$$A_2 = [4B_2 + 2B_1 + 4h_1 \cdot tan\alpha + 2(D - h_1)tan\beta] \cdot (D - h_1) \cdot \frac{1}{2}$$

$$= [2B_2 + B_1 + 2h_1 \cdot tan\alpha + (D - h_1)tan\beta] \cdot (D - h_1) \quad \text{(D1.9)}$$

The total cross-sectional area is:

$$A = A_1 + A_2 = (B_1h_1 + h_1^2 \cdot \tan\alpha) + [2B_2D - 2B_2h_1 + B_1D - B_1h_1 + 2h_1D \cdot tan\alpha - 2h_1^2 \cdot \tan\alpha + (D - h_1)^2 tan\beta]$$

$$= 2B_2D - 2B_2h_1 + B_1D + 2Dh_1 \cdot tan\alpha - h_1^2 \cdot tan\alpha + (D - h_1)^2 tan\beta \quad \text{(D1.10)}$$

The wetted perimeter is:

$$P = 2B_2 + B_1 + \frac{2h_1}{cos\alpha} + \frac{2(D - h_1)}{cos\beta} \quad \text{(D1.11)}$$

The hydraulic radius is:

$$R = \frac{A}{P} = \frac{2B_2D - 2B_2h_1 + B_1D + 2Dh_1 \cdot tan\alpha - h_1^2 \cdot tan\alpha + (D-h_1)^2 tan\beta}{2B_2 + B_1 + \frac{2h_1}{cos\alpha} + \frac{2(D-h_1)}{cos\beta}} \tag{D1.12}$$

$$= \frac{cos\alpha \cdot cos\beta \cdot [2B_2D - 2B_2h_1 + B_1D + 2Dh_1 \cdot tan\alpha - h_1^2 \cdot tan\alpha + (D-h_1)^2 tan\beta]}{(2B_2 + B_1) \cdot cos\alpha \cdot cos\beta + 2h_1 cos\beta + 2(D-h_1)cos\alpha} \tag{D1.13}$$

$$= \frac{cos\alpha \cdot cos\beta \cdot [(2B_2 + B_1)D - 2B_2h_1 + 2Dh_1 \cdot tan\alpha - h_1^2 \cdot tan\alpha + (D-h_1)^2 tan\beta]}{(2B_2 + B_1) \cdot cos\alpha \cdot cos\beta + 2h_1 cos\beta + 2(D-h_1)cos\alpha} \tag{D1.14}$$

$$= \frac{cos\alpha \cdot cos\beta \cdot [D - \frac{2B_2h_1}{2B_2+B_1} + \frac{2Dh_1 \cdot tan\alpha}{2B_2+B_1} - \frac{h_1^2 \cdot tan\alpha}{2B_2+B_1} + \frac{(D-h_1)^2 tan\beta}{2B_2+B_1}]}{cos\alpha \cdot cos\beta + \frac{2h_1 cos\beta}{2B_2+B_1} + \frac{2(D-h_1)cos\alpha}{2B_2+B_1}} \tag{D1.15}$$

With the wide channel approximation (i.e., $[h_1 \ll 2B_2 + B_1]$ and $[D - h_1 \ll 2B_2 + B_1]$, Eq. (D1.15) can be approximated as:

$$R \approx \frac{cos\alpha \cdot cos\beta \cdot [D - \frac{2B_2h_1}{2B_2+B_1} + \frac{2Dh_1 \cdot tan\alpha}{2B_2+B_1} - \frac{h_1^2 \cdot tan\alpha}{2B_2+B_1} + \frac{(D-h_1)^2 tan\beta}{2B_2+B_1}]}{cos\alpha \cdot cos\beta + 0 + 0} \tag{D1.16}$$

$$= D - \frac{2B_2h_1}{2B_2+B_1} + \frac{2Dh_1 \cdot tan\alpha}{2B_2+B_1} - \frac{h_1^2 \cdot tan\alpha}{2B_2+B_1} + \frac{(D-h_1)^2 tan\beta}{2B_2+B_1} \tag{D1.17}$$

$$= D + \frac{2Dh_1 \cdot tan\alpha + (D-h_1)^2 tan\beta - h_1^2 \cdot tan\alpha - 2B_2h_1}{2B_2+B_1} \tag{D1.18}$$

Substitute Eq. (D1.10) and Eq. (D1.18) into Eq. (D1.1), we have the Q-H relation in a trapezoidal compound channel as:

$$Q = \frac{1}{n} \cdot \sqrt{S} \cdot \left[D + \frac{2Dh_1 \cdot tan\alpha + (D-h_1)^2 tan\beta - h_1^2 \cdot tan\alpha - 2B_2h_1}{2B_2+B_1}\right]^{\frac{2}{3}} \cdot (2B_2D - 2B_2h_1 + B_1D + 2Dh_1 \cdot tan\alpha - h_1^2 \cdot tan\alpha + (D-h_1)^2 tan\beta) \tag{D1.19}$$

D.2. The possibility of a sudden decrease of friction slope

With the standard rating curve function (Eq. D1.19) at a trapezoidal compound channel, we can substitute the known physical parameters at the Ottawa-Gatineau confluence (e.g. roughness, channel width, slope angle, water surface elevation, flow discharge, etc.) into the Eq. (D1.19) to see if a sudden decrease of friction slope around data point "B" can lead to the flow rating curve segmentation. Note that data points "A" – "D" correspond to the "In-channel phase" (Eq. D1.6) while data points "E" and "F" correspond to the "Compound phase" (Eq. D1.19) in this document.

The calculation results are presented in Table S1. River cross-sectional shape and data points are shown in Figure D3. All friction slope data except for data point “D” are assumed values. Friction slope at data point “D” (i.e. 0.0011%) is measured from land-based RTK GNSS. Results show that the modeled total discharge can fit with the observed values quite good, which indicates that a sudden decrease of friction slope (i.e. from 0.0016% to 0.0013%) around data point “B” is theoretically possible.

Table D1. Calculation of the total discharge using the trapezoidal compound channel rating curve.

Data points	Manning's n [s/m$^{1/3}$]	Slope [-]	B_1 [m]	B_2 [m]	H [m]	H_0 [m]	D [m]	h_1 [m]	tan(α)	tan(β)	Q_{pre} [m^3/s]	Q_{obs} [m^3/s]
A	0.050	0.0006%	300	——	41.384	28.290	13.094	——	4	——	1287.0	1287.0
A1	0.041	0.0012%	300	——	42.030	28.290	13.740	——	4	——	2366.0	2366.0
A2	0.036	0.0016%	300	——	42.401	28.290	14.111	——	4	——	3289.0	3289.0
B	0.030	0.0013%	300	——	42.677	28.290	14.387	——	4	——	3644.5	3644.5
C	0.027	0.0012%	300	——	42.989	28.290	14.699	——	4	——	4031.0	4031.0
D	0.023	0.0011%	300	——	43.664	28.290	15.374	——	4	——	4967.2	4967.2
E	0.021	0.0010%	300	10	44.864	28.290	16.574	16	4	160	6753.0	6753
F	0.020	0.0010%	300	10	45.073	28.290	16.783	16	4	160	7134.0	7134

#1 H corresponds to the measured water surface elevation (WSE) data.

#2 Q_{pre} corresponds to the predicted total flow discharge, using Eq.(D1.19).

#3 Q_{obs} corresponds to the observed total flow discharge at gauge stations.

#4 Manning’s roughness at data point “A” is calibrated in the numerical model in the “low flow” run.

#5 Manning’s roughness at data point “B” is calibrated in the numerical model in the “high flow” run.

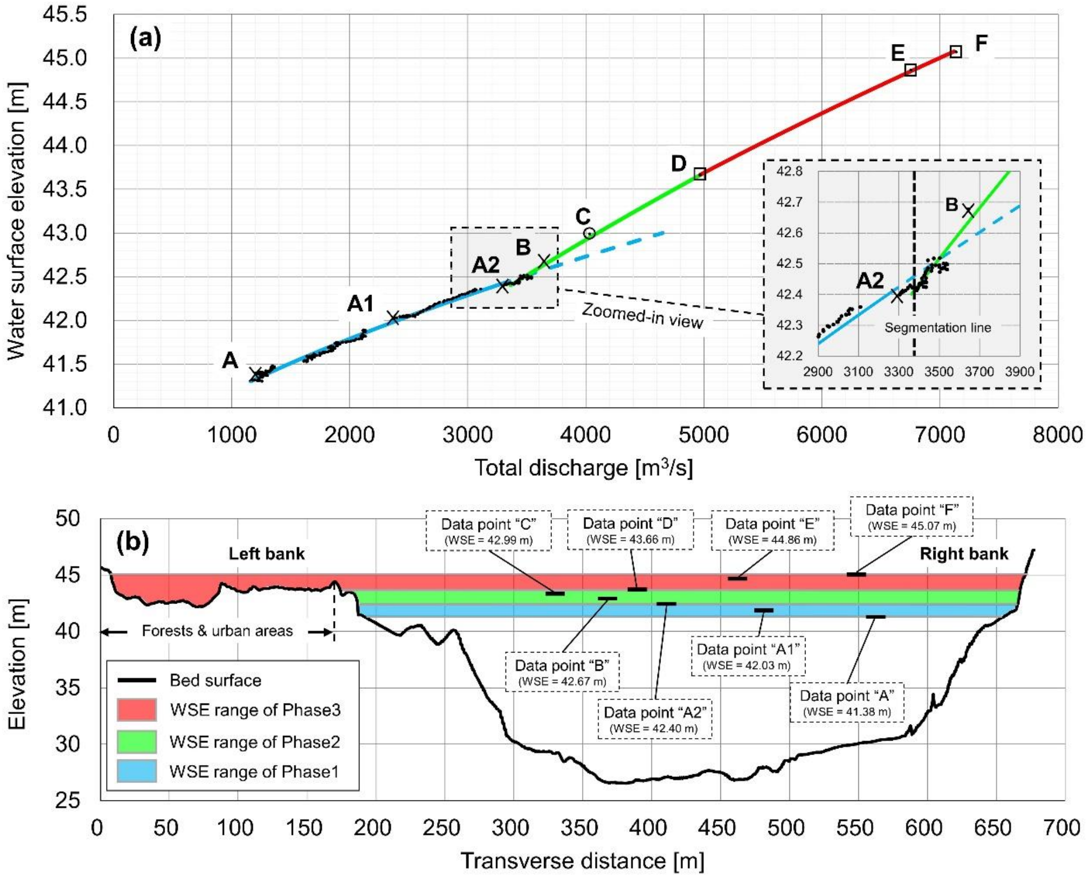

Figure D3. (a) Raw data points and fitted flow rating curve segments at the OG confluence outlet (b) the cross-sectional shape of the confluence outlet and WSE data ranges of different rating curve segments.

References

Ahilan, S., Guan, M., Sleigh, A., Wright, N., & Chang, H. (2016). The influence of floodplain restoration on flow and sediment dynamics in an urban river. *Journal of Flood Risk Management*, 11, S986–S1001. https://doi.org/10.1111/jfr3.12251

Ahmadisharaf, E., Kalyanapu, A. J., & Bates, P. D. (2018). A probabilistic framework for floodplain mapping using hydrological modeling and unsteady hydraulic modeling. *Hydrological Sciences Journal*, 63(12), 1759–1775. https://doi.org/10.1080/02626667.2018.1525615

Ansari, S., Rennie, C. D., Venditti, J. G., Kwoll, E., & Fairweather, K. (2018). Shore-based monitoring of flow dynamics in a steep bedrock canyon river. *E3S Web of Conferences*, 40, 06025–06025. https://doi.org/10.1051/e3sconf/20184006025

Ansari, S., Rennie, C. D., Jamieson, E. C., O. Seidou, & Clark, S. P. (2023). RivQNet: Deep Learning Based River Discharge Estimation Using Close‐Range Water Surface Imagery. *Water Resources Research*, 59(2). https://doi.org/10.1029/2021wr031841

Ashworth, P., Ferguson, R. I., & Powell, D. M. (1992). Bedload transport and sorting in braided channels. In P. Billi, R. D. Hey, C. R. Thorne, & P. Taconni (Eds.), Dynamics of gravel-bed rivers (pp. 497-513). John Wiley and Sons.

Ashworth, P.J. (1996). Mid-Channel bar growth and its relationship to local flow strength and direction. *Earth Surface Processes and Landforms*. 21(2):103 – 123. https://doi.org/10.1002/(SICI)1096-9837(199602)21:2<103::AID-ESP569>3.0.CO;2-O

Aureli, F., Mignosa, P., Prost, F., & Dazzi, S. (2021). Hydrological and Hydraulic Flood Hazard Modeling in Poorly Gauged Catchments: An Analysis in Northern Italy. *Hydrology*, 8(4), 149. https://doi.org/10.3390/hydrology8040149

Baar, A.W., Boechat Albernaz, M., van Dijk, W.M., & Kleinhans, M.G. (2019). Critical dependence of morphodynamic models of fluvial and tidal systems on empirical downslope sediment transport. *Nature Communications*. 10, 4903. https://doi.org/10.1038/s41467-019-12753-x

Bagnold, R. A. (1966). An approach to the sediment transport problem from general physics. U.S. Geological Survey Professional Paper 422-I, pp. v 37, with 15 figs, and 1 table. U.S. Government Printing Office, Washington, D.C., 1966. Price 35 cents. *Geological Magazine*, 104(4), 409-409. https://doi.org/10.1017/S0016756800049074

Bandini, F., Frías, M. C., Liu, J., Simkus, K., Karagkiolidou, S., & Bauer-Gottwein, P. (2022). Challenges with Regard to Unmanned Aerial Systems (UASs) Measurement of River Surface Velocity Using Doppler Radar. *Remote Sensing*, 14(5), 1277. https://doi.org/10.3390/rs14051277

Baranya, S., Olsen, N. R. B., & Józsa, J. (2013). Flow Analysis of a River Confluence with Field Measurements and Rans Model with Nested Grid Approach. *River Research and Applications*, 31(1), 28–41. https://doi.org/10.1002/rra.2718

Bartholdy, J. & Billi, P. (2002) Morphodynamics of a pseudo-meandering gravel bar reach. *Geomorphology*, Volume 42, Issues 3-4, Pages 293-310, ISSN 0169-555X, https://doi.org/10.1016/S0169-555X(01)00092-7

Bates, P. D., & De Roo, A. P. J. (2000). A simple raster-based model for flood inundation simulation. *Journal of Hydrology*, 236(1-2), 54–77. https://doi.org/10.1016/s0022-1694(00)00278-x

Bates, P., Trigg, M., Neal, J., & Dabrowa, A. (2013) LISFLOOD-FP User manual Code release 5.9.6. School of Geographical Sciences, University of Bristol, University Road, Bristol, BS8 1SS, UK.

Baynes, E. R. C., Kincey, M. E., & Warburton, J. (2023). Extreme flood sediment production and export controlled by reach-scale morphology. *Geophysical Research Letters*, 50, e2023GL103042. https://doi.org/10.1029/2023GL103042

Beilicci, Erika & Beilicci, Robert & David, Ioan. (2021). Hydroinformatic Tools for Flood Risk Map Achievement. International Journal of Energy. 15. 27-32. 10.46300/91010.2021.15.5.

Benson, M.A., & Dalrymple, T. (1967). General field and office procedures for indirect discharge measurements: U.S. *Geological Survey Techniques of Water-Resources Investigations*, book 3, chap. A1, 30 p. https://doi.org/10.3133/twri03A1

Beretta, R., Ravazzani, G., Maiorano, C., & Mancini, M. (2018). Simulating the Influence of Buildings on Flood Inundation in Urban Areas. *Geosciences*, 8(2), 77. https://doi.org/10.3390/geosciences8020077

Best, J. L. (1987). Flow dynamics at river channel confluences: Implications for sediment transport and bed morphology. Recent Developments in Fluvial Sedimentology, (SP39), 27–35

Betsholtz, A. & Nordlof, B. (2017). Potentials and Limitations of 1D, 2D and Coupled 1D–2D Flood Modeling in HEC-RAS. Master's Thesis, Lund University, Lund, Sweden. https://www.lunduniversity.lu.se/lup/publication/8904721

Birgand, F., Lellouche, G., & Appelboom, T. W. (2013). Measuring flow in non-ideal conditions for short-term projects: Uncertainties associated with the use of stage-discharge rating curves. *Journal of Hydrology*, 503, 186–195. https://doi.org/10.1016/j.jhydrol.2013.09.007

Biron, P. M., Richer, A., Kirkbride, A. D., Roy, A. G., & Han, S. (2002). Spatial patterns of water surface topography at a river confluence. *Earth Surface Processes and Landforms*, 27(9), 913–928. https://doi.org/10.1002/esp.359

Bisht, D., Chatterjee, C., Kalakoti, S., Upadhyay, P., Sahoo, M. & Panda, A. (2016). Modeling urban floods and drainage using SWMM and MIKE URBAN: a case study. *Natural Hazards*. 84. https://doi.org/10.1007/s11069-016-2455-1

Blöschl, G., Hall, J., Viglione, A., Perdigão, R. A. P., Parajka, J., Merz, B., Lun, D., Arheimer, B., Aronica, G. T., Bilibashi, A., Boháč, M., Bonacci, O., Borga, M., Čanjevac, I., Castellarin, A., Chirico, G. B., Claps, P., Frolova, N., Ganora, D., & Gorbachova, L. (2019). Changing climate both increases and decreases European river floods. *Nature*, 573(7772), 108–111. https://doi.org/10.1038/s41586-019-1495-6

Bradbrook, K. F., Lane, S. N., & Richards, K. S. (2000). Numerical simulation of three-dimensional, time-averaged flow structure at river channel confluences. *Water Resources Research*, 36(9), 2731–2746. https://doi.org/10.1029/2000wr900011

Brevis, W., Niño, Y. & Jirka, G.H. (2011). Integrating cross-correlation and relaxation algorithms for particle tracking velocimetry. *Experimental Fluids*. 50, 135–147. https://doi.org/10.1007/s00348-010-0907-z

Brier, g. W. (1950). Verification of forecasts expressed in terms of probability. *Monthly Weather Review*, 78(1), 1–3. https://doi.org/10.1175/1520-0493(1950)078%3C0001:vofeit%3E2.0.co;2

Brooke, S., Chadwick, A. J., Silvestre, J., Lamb, M. P., Edmonds, D. A., & Ganti, V. (2022). Where rivers jump course. *Science*, 376(6596), 987–990. https://doi.org/10.1126/science.abm1215

Brown, A.V., Lyttle, M.M., & Brown, K.B. (1998). Impacts of gravel mining on gravel bed streams. *Transactions of the American Fisheries Society*. 127: 979-994. https://doi.org/10.1577/1548-8659(1998)127<0979:IOGMOG>2.0.CO;2

Brown, R., & Chanson, H. (2013). Turbulence and Suspended Sediment Measurements in an Urban Environment during the Brisbane River Flood of January 2011. *Journal of Hydraulic Engineering*, 139(2), 244–253. https://doi.org/10.1061/(asce)hy.1943-7900.0000666

Buttle, J. M., Allen, D. M., Caissie, D., Davison, B., Hayashi, M., Peters, D. L., Pomeroy, J. W., Simonovic, S., St-Hilaire, A., & Whitfield, P. H. (2016). Flood processes in Canada: Regional and special aspects. *Canadian Water Resources Journal / Revue Canadienne Des Ressources Hydriques*, 41(1-2), 7–30. https://doi.org/10.1080/07011784.2015.1131629

Cao, J., Cheng, F., Wang, Z., Song, Y., & Xie, S. (2023). A “pulse-stairstep” longitudinal pattern of larval fish assemblages in a channelized floodplain river downstream of a dam: dominant influences of major tributaries with a “confluence refuge concept.” *Hydrobiologia*, 850(18), 3981–3995. https://doi.org/10.1007/s10750-023-05281-9.

Cao, Z., Pender, G., Wallis, S. G., & Carling, P. A. (2004). Computational Dam-Break Hydraulics over Erodible Sediment Bed. *Journal of Hydraulic Engineering*, 130(7), 689–703. https://doi.org/10.1061/(asce)0733-9429(2004)130:7(689)

Cao, Z., Hu, P., & Pender, G. (2011). Multiple Time Scales of Fluvial Processes with Bed Load Sediment and Implications for Mathematical Modeling. *Journal of Hydraulic Engineering*, 137(3), 267–276. https://doi.org/10.1061/(asce)hy.1943-7900.0000296

Castelltort, F. X., Bladé, E., Balasch, J. C., & Ribé, M. (2020). The backwater effect as a tool to assess formative long-term flood regimes. *Quaternary International*, 538, 29–43. https://doi.org/10.1016/j.quaint.2020.01.012

CBC News. (2019a). Timeline: Rising water, rising fears. https://www.cbc.ca/news/canada/ottawa/timeline-2019-flooding-ottawa-gatineau-1.5114254

CBC News. (2019b). Ottawa: Under water, again. https://www.cbc.ca/news/canada/ottawa/ottawa-river-flooding-2019-recap-1.5119980

Chaulagain, S., Stone, M. C., Dombroski, D., Gillihan, T., Chen, L., & Zhang, S. (2022). An investigation into remote sensing techniques and field observations to model hydraulic roughness from riparian vegetation. *River Research and Applications*, 38(10), 1730–1745. https://doi.org/10.1002/rra.4053

Chen, J., Li, Y., & Zhang, S. (2023a). Impact of Different Design Rainfall Pattern Peak Factors on Urban Flooding. *Water*, 15(13), 2468–2468. https://doi.org/10.3390/w15132468

Chen, J., Tian, Y., Zhang, S., Li, Y., & Guo, Z. (2023b). Study of Urban Flooding Response under Superstandard Conditions. *Water*, 15(8), 1492–1492. https://doi.org/10.3390/w15081492

Chow, V.T. (1959), Open-channel hydraulics. New York. McGraw-Hill, 680 p. ISBN 007085906X, 9780070859067

Chow, G. C. (1960). Tests of Equality Between Sets of Coefficients in Two Linear Regressions. *Econometrica*, 28(3), 591. https://doi.org/10.2307/1910133

Christoffersen, L., Bauer-Gottwein, P., Sørensen, L. S., & Nielsen, K. (2023). ICE2WSS; an R package for estimating river water surface slopes from ICESat-2. *Environmental Modeling & Software*. 105789. https://doi.org/10.1016/J.ENVSOFT.2023.105789

Church, M. (1992) Channel morphology and typology. In: Calow P, Petts GE (eds) The rivers handbook, vol 1. Blackwell, Oxford, pp 126–143

Church, M., Rempel, L., & Rice, S. (2000). Morphological and habitat classification of the Lower Fraser River gravel-bed reach. Report prepared for the Fraser Basin Council, November 2000: 77pp.

Church, M., Ham, D., & Weatherly, H. (2001). Gravel management in Lower Fraser River. (Report). Department of Geography, University of British Columbia, Vancouver, B.C., Canada. 110 pp

City of Gatineau (2024). Gatineau at a glance (population, area, etc.). Webpage link: https://www.gatineau.ca/portail/default.aspx?c=en-CA&p=publications_cartes_statistiques_donnees_ouvertes/coup_oeil_gatineau

City of Ottawa (2024). Current population and household estimates. Webpage link: https://ottawa.ca/en/living-ottawa/statistics-and-demographics/current-population-and-household-estimates#section-29b9341b-b349-49d2-98dc-5e384fb00c53

Clark, M. L., Clark, D. B., & Roberts, D. A. (2004). Small-footprint lidar estimation of sub-canopy elevation and tree height in a tropical rain forest landscape. *Remote Sensing of Environment*, 91(1), 68–89. https://doi.org/10.1016/j.rse.2004.02.008

Cohen, S., James, Ashely, T., Lammers, R. W., Fekete, B. M., & Li, H. (2022). Spatial Trends and Drivers of Bedload and Suspended Sediment Fluxes in Global Rivers. *Water Resources Research*, 58(6). https://doi.org/10.1029/2021wr031583

Collins, B.D. & Dunne, T. (1989). Gravel transport, gravel harvesting, and channel-bed degradation in rivers draining the southern Olympic Mountains, Washington, U.S.A. *Environmental Geology and Water Science*. 13: 213-224. https://doi.org/10.1007/BF01665371

Collins, B. & Dunne, T. (1990). Fluvial geomorphology and river gravel mining: a guide for planners, case studies included. California Department of Conservation, Division of Mines and Geology, Special Publication 98: 29pp.

Constantinescu, G., Miyawaki, S., Rhoads, B., Sukhodolov, A., & Kirkil, G. (2011). Structure of turbulent flow at a river confluence with momentum and velocity ratios close to 1: Insight provided by an eddy-resolving numerical simulation. *Water Resources Research*, 47(5). https://doi.org/10.1029/2010wr010018

Correia, L. P., Krishnappan, B. G., & Graf, W. H. (1992). Fully Coupled Unsteady Mobile Boundary Flow Model. *Journal of Hydraulic Engineering*, 118(3), 476–494. https://doi.org/10.1061/(asce)0733-9429(1992)118:3(476)

Costabile, P., Costanzo, C., & Macchione, F. (2017). Performances and limitations of the diffusive approximation of the 2-d shallow water equations for flood simulation in urban and rural areas. *Applied Numerical Mathematics*, 116, 141–156. https://doi.org/10.1016/j.apnum.2016.07.003

Costabile, P., Costanzo, C., De Lorenzo, G., & Macchione, F. (2020). Is local flood hazard assessment in urban areas significantly influenced by the physical complexity of the hydrodynamic inundation model? *Journal of Hydrology*, 580, 124231. https://doi.org/10.1016/j.jhydrol.2019.124231

Croissant, T., Lague, D., & Davy, P. (2019). Channel Widening Downstream of Valley Gorges Influenced by Flood Frequency and Floodplain Roughness. *Journal of Geophysical Research: Earth Surface*, 124(1), 154–174. https://doi.org/10.1029/2018jf004767

Cunge, J.A., Holly, F.M., & Verwey, A. (1980). *Practical Aspects of Computational River Hydraulics*. London: Pitman Publishing Limited, 1980.

Dai, W., Bilal, A., Xie, Q., Ahmad, I., & Joshi, I. (2020). Numerical Modeling for Hydrodynamics and Near-Surface Flow Patterns of a Tidal Confluence. *Journal of Coastal Research*, 36(2), 295–295. https://doi.org/10.2112/jcoastres-d-19-00058.1

Dal Sasso, S. F., Pizarro, A., Samela, C., Mita, L., & Manfreda, S. (2018). Exploring the optimal experimental setup for surface flow velocity measurements using PTV. *Environmental Monitoring and Assessment*, 190(8). https://doi.org/10.1007/s10661-018-6848-3

Dal Sasso, S. F., Pizarro, A., & Manfreda, S. (2020). Metrics for the Quantification of Seeding Characteristics to Enhance Image Velocimetry Performance in Rivers. *Remote Sensing*, 12(11), 1789–1789. https://doi.org/10.3390/rs12111789

Dal Sasso, S.F., A., Pearce, S., Maddock, I., & Manfreda, S. (2021). Increasing LSPIV performances by exploiting the seeding distribution index at different spatial scales. *Journal of Hydrology*, 598, 126438–126438. https://doi.org/10.1016/j.jhydrol.2021.126438

Dasallas, L., Kim, Y., & An, H. (2019). Case Study of HEC-RAS 1D–2D Coupling Simulation: 2002 Baeksan Flood Event in Korea. *Water*. 2019, 11, 2048. https://doi.org/10.3390/w11102048

Dasgupta, A., Renaud Hostache, Raaj Ramsankaran, Schumann, G., Grimaldi, S., Pauwels, N., & Walker, J. P. (2021). On the Impacts of Observation Location, Timing, and Frequency on Flood Extent Assimilation Performance. *Water Resources Research*, 57(2). https://doi.org/10.1029/2020wr028238

Dazzi, S., Shustikova, I., Domeneghetti, A., Castellarin, A., & Vacondio, R. (2021). Comparison of two modeling strategies for 2D large-scale flood simulations. *Environmental Modeling & Software*, 146, 105225. https://doi.org/10.1016/j.envsoft.2021.105225

De Leo, A., Ruffini, A., Postacchini, M., Colombini, M., & Stocchino, A. (2020). The Effects of Hydraulic Jumps Instability on a Natural River Confluence: The Case Study of the Chiaravagna River (Italy). *Water*, 12(7), 2027. https://doi.org/10.3390/w12072027

Deltares. (2020). "Delft3D-FLOW user manual: Simulation of multidimensional hydrodynamic flows and transport phenomena, including sediments." Delft, Netherlands.

Demir, V. & Kisi, O. (2015). Flood Hazard Mapping by Using Geographic Information System and Hydraulic Model: Mert River, Samsun, Turkey. *Advances in Meteorology (Hindawi Publishing Corporation)*. Volume 2016, Article ID 4891015, 9 pages. http://dx.doi.org/10.1155/2016/4891015

Deopa, R., Thakur, D. A., Kumar, S., Mohanty, M. P., & Asha, P. (2024). Discerning the dynamics of urbanization-climate change-flood risk nexus in densely populated urban mega cities: An appraisal of efficient flood management through spatiotemporal and geostatistical rainfall analysis and hydrodynamic Modeling. *Science of the Total Environment*, 952, 175882. https://doi.org/10.1016/j.scitotenv.2024.175882

Detert, M., Johnson, E. D., & Weitbrecht, V. (2017). Proof-of-concept for low-cost and non-contact synoptic airborne river flow measurements. International Journal of Remote Sensing, 38(8-10), 2780–2807. https://doi.org/10.1080/01431161.2017.1294782

Devi, N.N. & Kuiry, S.N. (2024). A Novel Local - Inertial Formulation Representing Subgrid Scale Topographic Effects for Urban Flood Simulation. *Water Resources Research*, 60(5). https://doi.org/10.1029/2023wr035334

DHI. (2019). MIKE FLOOD: Modeling of River Flooding, Step by step training guide. MIKE by DHI.

Dietrich, W. E., Kirchner, J.W., Ikeda, H., & Iseya, F. (1989). Sediment supply and the development of the coarse surface layer in gravel-bedded rivers. *Nature*, 340, 215–217. https://doi.org/10.1038/340215a0

Ding, Y., & Wang, S.S.Y. (2012). Optimal control of flood diversion in watershed using nonlinear optimization. *Advances in Water Resources*, 44, 30–48. https://doi.org/10.1016/j.advwatres.2012.04.004

Duan, J. G., Engel, F. L., & Cadogan, A. (2023). Discharge Estimation Using Video Recordings from Small Unoccupied Aircraft Systems. *Journal of Hydraulic Engineering*, 149(11). https://doi.org/10.1061/jhend8.hyeng-13591

Dysarz, T. (2020). Development of methodology for assessment of long - term morphodynamic impact on flood hazard. *Journal of Flood Risk Management*. https://doi.org/10.1111/jfr3.12654

Eaton, B.C., & Lapointe, M.F. (2001) Effects of large floods on sediment transport and reach morphology in the cobble-bed Sainte Marguerite River. *Geomorphology*, Volume 40, Issues 3–4, 2001, Pages 291-309, ISSN 0169-555X, https://doi.org/10.1016/S0169-555X(01)00056-3.

Edwards, M., Theunissen, R., Allen, C. B., & Poole, D. J. (2020). On the feasibility of selective spatial correlation to accelerate convergence of PIV image analysis based on confidence statistics. *Experiments in Fluids*, 61(10). https://doi.org/10.1007/s00348-020-03050-1

Exner, F. M. (1925), U¨ ber die Wechselwirkung zwischen Wasser und Geschiebe in Flu¨ssen (in German), Sitz. Acad. Wiss. Wien Math. Naturwiss. Abt. 2a, 134, 165-

203.

Farooq, M., Shafique, M., & Khattak, M. S. (2019). Flood hazard assessment and mapping of River Swat using HEC-RAS 2D model and high-resolution 12-m TanDEM-X DEM (WorldDEM). *Natural Hazards*, 97(2), 477–492. https://doi.org/10.1007/s11069-019-03638-9

Fernández, R., & Garcia, M. H. (2017). Input-variable sensitivity assessment for sediment transport relations. Water Resources Research, 53(9), 8105–8119. https://doi.org/10.1002/2016wr020249

Fleit, G., & Baranya, S. (2022). LSPIV analysis of ship-induced wave wash. *Experiments in Fluids*, 63(10). https://doi.org/10.1007/s00348-022-03508-4

Fujita, I., Muste, M., & Kruger, A. (1997). Large-scale particle image velocimetry for flow analysis in hydraulic engineering applications. *Journal of Hydraulic Research*, 36(3), 397–414. https://doi.org/10.1080/00221689809498626

Fujita, I., Watanabe, H., & Ryota Tsubaki. (2007). Development of a non‐intrusive and efficient flow monitoring technique: The space‐time image velocimetry (STIV). *International Journal of River Basin Management*, 5(2), 105–114. https://doi.org/10.1080/15715124.2007.9635310

Gaeuman, D., Andrews, E. D., Krause, A., & Smith, W. (2009). Predicting fractional bed load transport rates: Application of the Wilcock-Crowe equations to a regulated gravel bed river, *Water Resources Research*, 45, W06409, https://doi.org/10.1029/2008WR007320

Geertsema, T. J., Teuling, A. J., Uijlenhoet, R., Torfs, P. J. J. F., & Hoitink, A. J. F. (2018). Anatomy of simultaneous flood peaks at a lowland confluence. *Hydrology and Earth System Sciences*, 22(10), 5599–5613. https://doi.org/10.5194/hess-22-5599-2018

Gharahjeh, S., & Aydin, I. (2016). Application of video imagery techniques for low cost measurement of water surface velocity in open channels. *Flow Measurement and Instrumentation*, 51, 79–94. https://doi.org/10.1016/j.flowmeasinst.2016.09.001

Ghinassi, M., Moody, J., & Martin, D. (2018). Influence of extreme and annual floods on point-bar sedimentation: Inferences from Powder River, Montana, USA. *GSA Bulletin*. 131 (1-2): 71–83. https://doi.org/10.1130/B31990.1.

Gilles, D. and Moore, M. (2010) Review of Hydrau-lic Flood Modeling Software Used in Belgium, the Netherlands, and the United Kingdom. - References - Scientific Research Publishing. (2018). Scirp.org. https://www.scirp.org/reference/referencespapers?referenceid=2369534

Gleason, C. J., & Wang, J. (2015). Theoretical basis for at‐many‐stations hydraulic geometry. *Geophysical Research Letters*, 42(17), 7107–7114.

https://doi.org/10.1002/2015gl064935

Golder Associates Ltd. (2011). Bow and Elbow River updated hydraulic model project: survey data collection and DEM creation. Report prepared for The City of Calgary and Alberta Environment and Water.

Golder Associates (2015). Hydraulic Model and Flood Inundation Mapping Update. Prepared for the City of Calgary.

Government of Alberta (2014). June 2013 Southern Alberta Floods, One Year Report. Available at: https://www.alberta.ca/AlbertaCode/images/Flood-Recovery-One-Year-Report.pdf

Guan, M., Wright, N. G., & Sleigh, P. A. (2014). 2D Process-Based Morphodynamic Model for Flooding by Noncohesive Dyke Breach. *Journal of Hydraulic Engineering*, 140(7). https://doi.org/10.1061/(asce)hy.1943-7900.0000861

Guan, M., Carrivick, J. L., Wright, N. G., Sleigh, P. A., & Staines, K. E. H. (2016). Quantifying the combined effects of multiple extreme floods on river channel geometry and on flood hazards. *Journal of Hydrology*, 538, 256–268. https://doi.org/10.1016/j.jhydrol.2016.04.004

Guan, M., Wright, N. G., & Sleigh, P. A. (2015a). Multiple effects of sediment transport and geomorphic processes within flood events: Modeling and understanding. *International Journal of Sediment Research*, 30, 371-381. https://doi.org/10.1016/j.ijsrc.2014.12.001

Guan, M., Wright, N. G., Sleigh, P. A., & Carrivick, J.L. (2015b). Assessment of hydro-morphodynamic Modeling and geomorphological impacts of a sediment-charged jökulhlaup, at Sólheimajökull, Iceland. *Journal of Hydrology*, 530, 336-349. https://doi.org/10.1016/j.jhydrol.2015.09.062

Gudmundsson, L., Boulange, J., Do, H. X., Gosling, S. N., Grillakis, M. G., Koutroulis, A. G., Leonard, M., Liu, J., Müller Schmied, H., Papadimitriou, L., Pokhrel, Y., Seneviratne, S. I., Satoh, Y., Thiery, W., Westra, S., Zhang, X., & Zhao, F. (2021). Globally observed trends in mean and extreme river flow attributed to climate change. *Science*, 371(6534), 1159–1162. https://doi.org/10.1126/science.aba3996

Guillén, N. F., Patalano, A., García, C. M., & Bertoni, J. C. (2017). Use of LSPIV in assessing urban flash flood vulnerability. *Natural Hazards*, 87(1), 383–394. https://doi.org/10.1007/s11069-017-2768-8

Hacine-Gharbi, A., & Ravier, P. (2021). On the optimal number estimation of selected features using joint histogram based mutual information for speech emotion recognition. *Journal of King Saud University - Computer and Information Sciences*, 33(9), 1074–1083. https://doi.org/10.1016/j.jksuci.2019.07.008

Hagstrom, C.A., Leckie, D.A., & Smith, M.G. (2018). Point bar sedimentation and erosion produced by an extreme flood in a sand and gravel-bed meandering river.

Sedimentary Geology, Volume 377, Pages 1-16, ISSN 0037-0738, https://doi.org/10.1016/j.sedgeo.2018.09.003.

Haque, A., Holsen, T. M., & Baki, M. (2024). Distribution and risk assessment of microplastic pollution in a rural river system near a wastewater treatment plant, hydro-dam, and river confluence. *Scientific Reports*, 14(1). https://doi.org/10.1038/s41598-024-56730-x

Hamidifar, H., Nones, M., & Rowinski, P. M. (2024). Flood modeling and fluvial dynamics: A scoping review on the role of sediment transport. *Earth-Science Reviews*, 253, 104775–104775. https://doi.org/10.1016/j.earscirev.2024.104775

Hammond, M. J., Chen, A. S., Djordjević, S., Butler, D., & Mark, O. (2013). Urban flood impact assessment: A state-of-the-art review. Urban Water Journal, 12(1), 14–29. https://doi.org/10.1080/1573062x.2013.857421

Han, K., Sun, J., Lin, B., Huang, Z. & Shi, X. (2023) Large-scale Modeling of highly braided and laterally confined reach of a sand-bed river. *Earth Surface Processes and Landforms*, 48(8), 1557–1572. Available from: https://doi.org/10.1002/esp.5568

Hasan, O., Smrkulj, N., Miko, S., Dea Brunović, Nikolina Ilijanić, & Martina Šparica Miko. (2023). Integrated Reconstruction of Late Quaternary Geomorphology and Sediment Dynamics of Prokljan Lake and Krka River Estuary, Croatia. *Remote Sensing*, 15(10), 2588–2588. https://doi.org/10.3390/rs15102588

Hauer, C. & Habersack, H. (2009). Morphodynamics of a 1000-year flood in the Kamp River, Austria, and impacts on floodplain morphology. *Earth Surface Process and Landforms*, 34: 654-682. https://doi.org/10.1002/esp.1763

He, Z., Jia, L., Jia, Y., & He, J. (2020). Effects of flood events on sediment transport and deposition in the waterways of Lingding Bay, Pearl River Delta, China. *Ocean & Coastal Management*, Volume 185, 105062, ISSN 0964-5691, https://doi.org/10.1016/j.ocecoaman.2019.105062.

Herrera Gómez, V., Ramírez Franco, L., Ravazzani, G., Passoni, G., & Mancini, M. (2024). Modeling arboreal vegetation-induced friction and its influence on river flooding using a two-dimensional model. *Environmental Fluid Mechanics*, 24(3), 387–411. https://doi.org/10.1007/s10652-024-09991-z

Hidayat, H., Vermeulen, B., Sassi, M. G., & HoitinkHoitink, P. A. J. F. A. J. F. (2011). Discharge estimation in a backwater affected meandering river. *Hydrology and Earth System Sciences*, 15(8), 2717–2728. https://doi.org/10.5194/hess-15-2717-2011

Hirabayashi, Y., Mahendran, R., Koirala, S., Konoshima, L., Yamazaki, D., Watanabe, S., Kim, H., & Kanae, S. (2013). Global flood risk under climate change. *Nature Climate Change*, 3(9), 816–821. https://doi.org/10.1038/nclimate1911

Hirano, M. (1971). River-bed degradation with armoring. *Proceedings of the Japan*

Society of Civil Engineers. 195, 55–65, [in Japanese]. https://doi.org/10.2208/jscej1969.1971.195_55

Hooke, J.M. (2016). Morphological impacts of flow events of varying magnitude on ephemeral channels in a semiarid region, *Geomorphology*, Volume 252, 2016, Pages 128-143, ISSN 0169-555X, https://doi.org/10.1016/j.geomorph.2015.07.014.

Hooke, J.M. & Yorke, L. (2011), Channel bar dynamics on multi-decadal timescales in an active meandering river. *Earth Surface Processes and Landforms*, 36: 1910-1928. https://doi.org/10.1002/esp.2214

Horváth, Z., Buttinger-Kreuzhuber, A., Konev, A., Cornel, D., Komma, J., Blöschl, G., Noelle, S., & Waser, J. (2020). Comparison of Fast Shallow-Water Schemes on Real-World Floods. *Journal of Hydraulic Engineering*, 146(1), 05019005. https://doi.org/10.1061/(asce)hy.1943-7900.0001657

Hou, J., Yang, L., Wang, X., Chai, J., Zhang, Z., Li, X., Shao, J., Du, Y., & Bai, G. (2022). Adaptive large-scale particle image velocimetry method for physical model experiments of flood propagation with complex flow patterns. *Measurement*, 198, 111309–111309. https://doi.org/10.1016/j.measurement.2022.111309

Hrafnkelsson, B., Sigurdarson, H., Rögnvaldsson, S., Örn Jansson, A., Vias, R.D., & Gardarsson, S. M. (2021). Generalization of the power-law rating curve using hydrodynamic theory and Bayesian hierarchical Modelling. *Environmetrics*, 33(2). https://doi.org/10.1002/env.2711

Hu, P., Lei, Y., Deng, S., Cao, Z., Liu, H., & He, Z. (2020). Role of bar-channel interactions in a dominant branch shift: The Taipingkou waterway, Yangtze River, China. *River Research and Applications*, 37(3), 494 – 508. https://doi.org/10.1002/rra.3761

Huizinga, R.J., & Heimann, D.C., (2018), Hydrographic surveys of rivers and lakes using a multibeam echosounder mapping system: U.S. Geological Survey Fact Sheet 2018–3021, 6 p., https://doi.org/10.3133/fs20183021.

Ikeda, S. & Nishimura, T. (1986) Flow and bed profile in meandering sand silt rivers. *Journal of Hydraulic Engineering*. 112, 562–579. https://doi.org/10.1061/(ASCE)0733-9429(1986)112:7(562)

Insurance Bureau of Canada (2017). Spring Flooding in Ontario and Quebec Caused More Than $223 Million in Insured Damage; *Insurance Bureau of Canada*. Available online: https://www.insurance-canada.ca/2017/09/01/ibc-spring-flooding-insured-damage/

Iwasaki, T., Shimizu, Y., & Kimura, I. (2016). Numerical simulation of bar and bank erosion in a vegetated floodplain: A case study in the Otofuke River. *Advances in*

Water Resources, 93, 118–134. https://doi.org/10.1016/j.advwatres.2015.02.001

Jakob, M., Holm, K., Lazarte, E., & Church, M. (2014). A flood risk assessment for the City of Chilliwack on the Fraser River, British Columbia, Canada. *International Journal of River Basin Management*, 13(3), 263–270. https://doi.org/10.1080/15715124.2014.903259

Javernick, L., Redolfi, M., & Bertoldi, W. (2018). Evaluation of a numerical model's ability to predict bed load transport observed in braided river experiments. *Advances in Water Resources*. 115, 207–218. https://doi.org/10.1016/j.advwatres.2018.03.012

Jeon, Y.J., Chatellier, L., & David, L. (2014). Fluid trajectory evaluation based on an ensemble-averaged cross-correlation in time-resolved PIV. *Experiments in Fluids*, 55(7). https://doi.org/10.1007/s00348-014-1766-9

Jiao, Z., Zhang, Z., & Wu, L. (2024). SAR-based dynamic information retrieving of the Beijing-Tianjin-Hebei flood-inundation happened in July 2023, North China. *Geomatics Natural Hazards and Risk*, 15(1). https://doi.org/10.1080/19475705.2024.2366361

Jolley, M. J., Russell, A. J., Quinn, P. F., & Perks, M. T. (2021). Considerations When Applying Large-Scale PIV and PTV for Determining River Flow Velocity. *Frontiers in Water*, 3. https://doi.org/10.3389/frwa.2021.709269

Julien, P.Y. & Anthony, D.J. (2002) Bed load motion and grain sorting in a meandering stream. *Journal of Hydraulic Research*, 40:2, 125-133, https://doi.org/10.1080/00221680209499855.

Jung, Y., & Merwade, V. (2012). Uncertainty Quantification in Flood Inundation Mapping Using Generalized Likelihood Uncertainty Estimate and Sensitivity Analysis. *Journal of Hydrologic Engineering*, 17(4), 507–520. https://doi.org/10.1061/(asce)he.1943-5584.0000476

Jyoti, J.S., Medeiros, H., Sebo, S., & McDonald, W. (2023). River velocity measurements using optical flow algorithm and unoccupied aerial vehicles: A case study. *Flow Measurement and Instrumentation*, 91, 102341–102341. https://doi.org/10.1016/j.flowmeasinst.2023.102341

Kang, H., Kim, Y., An, H., Byun, J., & Noh, J. (2024). Estimation of river discharge using Monte Carlo simulations and a 1D hydraulic model based on artificial multi-segmented rating curves at the confluence of two rivers. *Environmental Research Communications*. https://doi.org/10.1088/2515-7620/ad277c

Kantoush, S. A., Schleiss, A. J., Sumi, T., & Murasaki, M. (2011). LSPIV implementation for environmental flow in various laboratory and field cases.

Journal of Hydro-Environment Research, 5(4), 263–276. https://doi.org/10.1016/j.jher.2011.07.002

Kasvi, E., Alho, P., Lotsari, E., Wang, Y., Kukko, A., Hyyppä, H., & Hyyppä, J. (2015). Two-dimensional and three-dimensional computational models in hydrodynamic and morphodynamic reconstructions of a river bend: sensitivity and functionality. *Hydrological Processes*, 29(6), 1604-1629. https://doi.org/10.1002/hyp.10277

Kavousizadeh, A., & Ahmadi, A. (2018). High-performance approach for estimating stage-discharge curves in the open channels. *Journal of Hydrology*, 565, 197–213. https://doi.org/10.1016/j.jhydrol.2018.08.002

Keulegan, G.H. (1938) Laws of Turbulent Flow in Open Channels. Journal of Research of the National Bureau of Standards, 21, 707-741. https://doi.org/10.6028/jres.021.039

Khan, S. I., Hong, Y., Wang, J., Yilmaz, K. K., Gourley, J. J., Adler, R. F., Brakenridge, G. R., Policelli, F., Habib, S., & Irwin, D. (2011). Satellite Remote Sensing and Hydrologic Modeling for Flood Inundation Mapping in Lake Victoria Basin: Implications for Hydrologic Prediction in Ungauged Basins. *IEEE Transactions on Geoscience and Remote Sensing*, 49(1), 85–95. https://doi.org/10.1109/tgrs.2010.2057513

Khosronejad, A., Kang, S., Borazjani, I., & Sotiropoulos, F. (2011). Curvilinear immersed boundary method for simulating coupled flow and bed morphodynamic interactions due to sediment transport phenomena. *Advances in Water Resources*, 34(7), 829–843. https://doi.org/10.1016/j.advwatres.2011.02.017

Khosronejad, A., Le, T., DeWall, P., Bartelt, N., Woldeamlak, S., Yang, X., & Sotiropoulos, F. (2016) High-fidelity numerical modeling of the Upper Mississippi River under extreme flood condition. *Advances in Water Resources*, Volume 98, Pages 97-113, ISSN 0309-1708, https://doi.org/10.1016/j.advwatres.2016.10.018.

Kiage, L. M., Walker, N. D., Balasubramanian, S., Babin, A., & Barras, J. (2005). Applications of Radarsat-1 synthetic aperture radar imagery to assess hurricane-related flooding of coastal Louisiana. *International Journal of Remote Sensing*, 26(24), 5359–5380. https://doi.org/10.1080/01431160500442438

Kim, B.-H., Sanders, B. F., Famiglietti, J. S., & Guinot, V. (2015). Urban flood modeling with porous shallow-water equations: A case study of model errors in the presence of anisotropic porosity. *Journal of Hydrology*, 523, 680–692. https://doi.org/10.1016/j.jhydrol.2015.01.059

Kim, Y.-G., Kim, P., Jo, M.-B., Oh, S.-N., & Paek, C.-H. (2021). A Study on the One-Dimensional Flood Numerical Analysis Method in Open Channels of Cascade

Barrage Network. *Journal of Testing and Evaluation*, 49(1), 20180959. https://doi.org/10.1520/jte20180959

Kirchmeier-Young, M. C., Wan, H., & Zhang, X. (2021). Anthropogenic Contribution to the Rainfall Associated with the 2019 Ottawa River Flood. *Bulletin of the American Meteorological Society*, 102(1), S33–S38. https://doi.org/10.1175/bams-d-20-0191.1

Klemas, V. (2015). Remote Sensing of Floods and Flood-Prone Areas: An Overview. *Journal of Coastal Research*. 1 July 2015; 31 (4): 1005–1013. doi: https://doi.org/10.2112/JCOASTRES-D-14-00160.1

Klohn Crippen Berger (2016). Calgary Rivers Morphology and Fish Habitat Study: Geological Review of the Bow and Elbow Rivers. Prepared for the City of Calgary.

Klösch, M., Blamauer, B., & Habersack, H. (2015), Intra-event scale bar–bank interactions and their role in channel widening. *Earth Surface Processes and Landforms*, 40, 1506–1523. https://doi.org/10.1002/esp.3732

Koch, F. G. & Flokstra, C. (1980). Bed level computations for curved alluvial channels. In Proceedings of the XIXth congress of the International Association for Hydraulic Research, 2-7 Feb. 1981, New Delhi, India, vol. 2, pages 357–364.

Kondolf, G. M. (1994). Geomorphic and environmental effects of instream gravel mining. *Landscape and Urban Planning*. 28:225–243. https://doi.org/10.1016/0169-2046(94)90010-8

Kondolf, G.M., (1997). Hungry water: effects of dams and gravel mining on river channels. *Environmental Management*. 21, 533–551. https://doi.org/10.1007/s002679900048

Kondolf, G.M., & Wolman, M.G. (1993). The sizes of salmonid spawning gravels. Water Resources Research. 29:2275–2285. https://doi.org/10.1029/93WR00402

Kori, E. & Mathada, H. (2012). An assessment of environmental impacts of sand and gravel mining in Nzhelele Valley, Limpopo Province, South Africa. Proceedings, 3rd International Proceedings of Chemical, Biological, and Environmental Engineering; 137–141.

Kumar, S., Prashanth Reddy Hanmaiahgari, Chowdary, V. M., & Pu, J. H. (2024). Geomorphological characteristics of Gandak river between Sahibganj and confluence with Ganga river during 1989–2022. *Environmental Earth Sciences*, 83(17). https://doi.org/10.1007/s12665-024-11812-x

Lai, R., Li, J., Wang, P., Guo, Y., Xu, L., Zhang, X., Wang, M., & Zhang, X. (2024). Cumulative sedimentation hazard map of urban areas subject to hyperconcentrated flash flood: A case study of Suide County in the Wuding River basin, China. *Journal of Flood Risk Management*. https://doi.org/10.1111/jfr3.12996

Lawal, M. A., & Omosanya, K. O. (2023). Multidecadal changes in planform morphology of the confluence of River Niger and River Benue, West Africa. *Journal of Hydrology*. 623, 129764–129764. https://doi.org/10.1016/j.jhydrol.2023.129764

Le Coz, J., Hauet, A., Pierrefeu, G., Dramais, G., & Camenen, B. (2010). Performance of image-based velocimetry (LSPIV) applied to flash-flood discharge measurements in Mediterranean rivers. *Journal of Hydrology*, 394(1-2), 42–52. https://doi.org/10.1016/j.jhydrol.2010.05.049

LeFavour, G., & Alsdorf, D. (2005). Water slope and discharge in the Amazon River estimated using the shuttle radar topography mission digital elevation model. *Geophysical Research Letters*, 32(17). https://doi.org/10.1029/2005gl023836

Legleiter, C. J., & Kinzel, P. J. (2021). Surface Flow Velocities From Space: Particle Image Velocimetry of Satellite Video of a Large, Sediment-Laden River. *Frontiers in Water*, 3. https://doi.org/10.3389/frwa.2021.652213

Leitão, J. P., Peña-Haro, S., Lüthi, B., Scheidegger, A., & Moy de Vitry, M. (2018). Urban overland runoff velocity measurement with consumer-grade surveillance cameras and surface structure image velocimetry. *Journal of Hydrology*, 565, 791–804. https://doi.org/10.1016/j.jhydrol.2018.09.001

Leopold, L. B. (1992), Sediment size that determines channel geometry. Dynamics of Gravel-Bed Rivers, edited by P. Billi et al., pp. 297–311, Wiley, Chichester, U. K.

Lesser, G. R., Roelvink, J. A., Van Kester, J. A. T. M., & Stelling, G. S. (2004). Development and validation of a three-dimensional morphological model. *Coastal Engineering*, 51(8), 883-915. https://doi.org/10.1016/j.coastaleng.2004.07.014

Lewis, Q. W., & Rhoads, B. L. (2015). Resolving two-dimensional flow structure in rivers using large‐scale particle image velocimetry: An example from a stream confluence. *Water Resources Research*, 51(10), 7977 – 7994. https://doi.org/10.1002/2015wr017783

Lewis, Q. W., & Rhoads, B. L. (2018). LSPIV Measurements of Two‐Dimensional Flow Structure in Streams Using Small Unmanned Aerial Systems: 2. Hydrodynamic Mapping at River Confluences. *Water Resources Research*, 54(10), 7981 – 7999. https://doi.org/10.1029/2018wr022551

Li, L., & Yan, H. (2022). A robust filtering algorithm based on the estimation of tracer visibility and stability for large scale particle image velocimetry. *Flow Measurement and Instrumentation*, 102204. https://doi.org/10.1016/j.flowmeasinst.2022.102204

Li, M., Zheng, Z., Niu, C., Quan, L., Liu, C., Li, X., Shi, C., Li, D., Zhao, L., Han, S., & Hu, C. (2024). Prediction of water level at Huayuankou station based on rating curve. *Scientific Reports*, 14(1). https://doi.org/10.1038/s41598-024-71510-3

Li, S., & Duffy, C. J. (2011). Fully coupled approach to modeling shallow water flow, sediment transport, and bed evolution in rivers. *Water Resources Research,* 47(3). https://doi.org/10.1029/2010wr009751

Li, S.S., Millar, R.G., & Islam, S. (2008). Modeling gravel transport and morphology for the Fraser River Gravel Reach, British Columbia, *Geomorphology*, Volume 95, Issues 3–4, 2008, Pages 206-222, ISSN 0169-555X, https://doi.org/10.1016/j.geomorph.2007.06.010.

Li, W., Xu, B., & Wen, J. (2016). Scenario-based community flood risk assessment: a case study of Taining county town, Fujian province, China. *Natural Hazards*, 82(1), 193–208. https://doi.org/10.1007/s11069-016-2187-2

Li, Z., Wang, Z., Pan, B., Zhu, H., & Li, W. (2014). The development mechanism of gravel bars in rivers. *Quaternary International*, Volume 336, 2014, Pages 73-79, ISSN 1040-6182, https://doi.org/10.1016/j.quaint.2013.12.039.

Lim, N. J., & Brandt, S. A. (2019). Are Feature Agreement Statistics Alone Sufficient to Validate Modelled Flood Extent Quality? A Study on Three Swedish Rivers Using Different Digital Elevation Model Resolutions. *Mathematical Problems in Engineering*, 2019, 1–16. https://doi.org/10.1155/2019/9816098

Lin, J., Kantoush, S. A., Almamari, M. M., & Sumi, T. (2024). Image-based measurements of surface flow velocity, turbulence, and depth distribution during sediment replenishment implementation in the Naka River, Japan. *Flow Measurement and Instrumentation*, 102626–102626. https://doi.org/10.1016/j.flowmeasinst.2024.102626

Lindroth, E. M., Rhoads, B. L., Castillo, C. R., Czuba, J. A., Güneralp, İ., & Edmonds, D. (2020). Spatial Variability in Bankfull Stage and Bank Elevations of Lowland Meandering Rivers: Relation to Rating Curves and Channel Planform Characteristics. *Water Resources Research*, 56(8). https://doi.org/10.1029/2020wr027477

Liu, J., Bauer‐Gottwein, P., Monica Coppo Frias, Aske Folkmann Musaeus, Christoffersen, L., & Jiang, L. (2023). Stage-Slope-Discharge Relationships Upstream of River Confluences Revealed by Satellite Altimetry. *Geophysical Research Letters*, 50(23). https://doi.org/10.1029/2023gl106394

Liu, T.H., Wang, Y.K., Wang, X.K., Duan, H.F., & Yan., X.F. (2020). Morphological environment survey and hydrodynamic Modelling of a large bifurcation-confluence complex in Yangtze River, China. *Science of the Total Environment*, 737, 139705–139705. https://doi.org/10.1016/j.scitotenv.2020.139705

Liu, W.C., Lu, C.H., & Huang, W.C. (2021). Large-Scale Particle Image Velocimetry to Measure Streamflow from Videos Recorded from Unmanned Aerial Vehicle and Fixed Imaging System. *Remote Sensing*, 13(14), 2661–2661. https://doi.org/10.3390/rs13142661

Ljubičić, R., Silvano, & Budo Zindović. (2024). SSIMS-Flow: Image velocimetry workbench for open-channel flow rate estimation. *Environmental Modeling & Software*, 173, 105938–105938. https://doi.org/10.1016/j.envsoft.2023.105938

Lotsari, E. S., Calle, M., Benito, G., Kukko, A., Kaartinen, H., Hyyppä, J., Hyyppä, H., & Alho, P. (2018). Topographical change caused by moderate and small floods in a gravel bed ephemeral river – a depth-averaged morphodynamic simulation approach. *Earth Surface Dynamics*, 6(1), 163–185. https://doi.org/10.5194/esurf-6-163-2018

Lu, M., Wan, B., Zhang, X., Yu, Z., Peng, Z., Fu, X., Xu, P., & Yao, Q. (2024). Impacts of River Network Connectivity on Flood Signatures and Severity Regulated by Flood Control Projects. *Water*, 16(17), 2390–2390. https://doi.org/10.3390/w16172390

Luchi, R., Bolla Pittaluga, M., & Seminara, G. (2012). Spatial width oscillations in meandering rivers at equilibrium, *Water Resources Research*, 48, W05551, https://doi.org/10.1029/2011WR011117

Luchi, R., Zolezzi, G. and Tubino, M. (2010), Modeling mid-channel bars in meandering channels. *Earth Surface Processes and Landforms*, 35: 902-917. https://doi.org/10.1002/esp.1947

Luu, C., Von Meding, J., & Kanjanabootra, S. (2017). Assessing flood hazard using flood marks and analytic hierarchy process approach: a case study for the 2013 flood event in Quang Nam, Vietnam. *Natural Hazards*, 90(3), 1031–1050. https://doi.org/10.1007/s11069-017-3083-0

Magilligan, F.J., Buraas, E. M., & Renshaw, C.E. (2015) The efficacy of stream power and flow duration on geomorphic responses to catastrophic flooding, *Geomorphology*, Volume 228, Pages 175-188, ISSN 0169-555X, https://doi.org/10.1016/j.geomorph.2014.08.016.

Mahdizadeh, H., & Sharifi, S. (2020). Coupled and splitting bedload sediment transport models based on a modified flux-wave approach. *International Journal of Sediment Research*. https://doi.org/10.1016/j.ijsrc.2020.05.001

Marangoz, H.O. & Anilan., T. (2021). Two-dimensional modeling of flood wave propagation in residential areas after a dam break with application of diffusive and dynamic wave approaches. *Natural Hazards*, 110(1), 429–449. https://doi.org/10.1007/s11069-021-04953-w

Masafu, C., & Williams, R. (2024). Satellite Video Remote Sensing for Flood Model Validation. *Water Resources Research*, 60(1). https://doi.org/10.1029/2023wr034545

Mat Salleh, M.Z. & Ariffin, J. (2013). Flow and Sediment Matrix in Mid-Channel Bar Formation. International Journal of Scientific & Engineering Research. 4. 1757-1764

McLean, D. G., Church, M., & Tassone, B. (1999). Sediment transport along lower

Fraser River: 1. Measurements and hydraulic computations. *Water Resources Research*, 35(8), 2533-2548. https://doi.org/10.1029/1999WR900101.

Meinhart, C. D., Wereley, S. T., & Santiago, J. G. (2000). A PIV Algorithm for Estimating Time-Averaged Velocity Fields. *Journal of Fluids Engineering*, 122(2), 285–289. https://doi.org/10.1115/1.483256

Meyer-Peter, E., & Müller, R. (1948). Formulas for bed load transport. In Proceedings of the 2nd Congress IAHR, Stockholm, vol. 2, pages 39–64.

Miller, A.C., King, R.H., Glover, J.E., & Army engineer waterways experiment station Vicksburg MS environmental lab. (1983) Design of a Gravel Bar Habitat for the Tombigbee River Near Columbus, Mississippi. Defense Technical Information Center. 64 pages.

Mool, P., Popescu, I., Giri, S., Omer, A., Sloff, K., Kitamura, Y., & Solomatine, D. (2017). Delft3D morphological Modeling of sediment management in daily peaking run-of-the-river hydropower (PROR) reservoirs in Nepal. 85th Annual Meeting of International Commission on Large Dams. July 3-7, 2017. Prague, Czech Republic.

Moerman, E. (2011). Long-term morphological Modeling of the mouth of the Columbia River. Doctoral dissertation, Delft University, Netherlands.

Mustafa, A., & Szydłowski, M. (2021). Application of different building representation techniques in HEC-RAS 2-D for urban flood modeling using the Toce River experimental case. *PeerJ*, 9, e11667. https://doi.org/10.7717/peerj.11667

Muste, M., Kim, D., & Kim, K. (2022). A flood-crest forecast prototype for river floods using only in-stream measurements. *Communications Earth & Environment*, 3(1). https://doi.org/10.1038/s43247-022-00402-z

Muste, M., Xiong, Z., Sch€one, J., & Li, Z. (2004). Validation and extension of image velocimetry capabilities for flow diagnostics in hydraulic modeling. *Journal of Hydraulic Engineering*, 130(3), 175–185. https://doi.org/10.1061/(ASCE)0733-9429(2004)130:3(175)

Naghavi, M., Mohammadi, M., & Ghorban Mahtabi. (2022). An experimental evaluation of the blocks in floodplain on hydraulic characteristics of flow in a meandering compound channel. *Journal of Hydrology*, 612, 127976–127976. https://doi.org/10.1016/j.jhydrol.2022.127976

Nash, J. E. & Sutcliffe, J. V. (1970). River flow forecasting through conceptual models part I — A discussion of principles. *Journal of Hydrology*. 10 (3): 282–290. https://doi.org/10.1016/0022-1694(70)90255-6

Naulet, R., Lang, M., Ouarda, T. B. M. J., Coeur, D., Bobée, B., Recking, A., & Moussay, D. (2005). Flood frequency analysis on the Ardèche river using French documentary sources from the last two centuries. *Journal of Hydrology*, 313(1-2), 58–78. https://doi.org/10.1016/j.jhydrol.2005.02.011

Naves, J., Anta, J., Puertas, J., Regueiro-Picallo, M., & Suárez, J. (2019). Using a 2D shallow water model to assess Large-Scale Particle Image Velocimetry (LSPIV) and Structure from Motion (SfM) techniques in a street-scale urban drainage physical model. *Journal of Hydrology*, 575, 54–65. https://doi.org/10.1016/j.jhydrol.2019.05.003

Neal, J. C., Bates, P. D., Fewtrell, T. J., Hunter, N. M., Wilson, M. D., & Horritt, M. S. (2009). Distributed whole city water level measurements from the Carlisle 2005 urban flood event and comparison with hydraulic model simulations. *Journal of Hydrology*, 368(1-4), 42–55. https://doi.org/10.1016/j.jhydrol.2009.01.026

Neal, J., Villanueva, I., Wright, N., Willis, T., Fewtrell, T., & Bates, P. (2011). How much physical complexity is needed to model flood inundation? *Hydrological Processes*, 26(15), 2264–2282. https://doi.org/10.1002/hyp.8339

Ngo, H.Q., Bomers, A., Augustijn, D.C.M., Ranasinghe, R., Filatova, T., van, Herget, J., & Suzanne J.M.H. Hulscher. (2023). Reconstruction of the 1374 Rhine river flood event around Cologne region using 1D-2D coupled hydraulic modeling approach. *Journal of Hydrology*, 617, 129039–129039. https://doi.org/10.1016/j.jhydrol.2022.129039

Nguyen, T. T., Nakatsugawa, M., Yamada, T. J., & Hoshino, T. (2021). Flood Inundation Assessment in the Low-Lying River Basin Considering Extreme Rainfall Impacts and Topographic Vulnerability. *Water*, 13(7), 896. https://doi.org/10.3390/w13070896

Northwest Hydraulic Consultants Ltd. (1986). River Regime Study - Bow and Elbow Rivers at Calgary, Alberta. Prepared for the City of Calgary.

Núñez-González, F., Rovira, A., & Ibàez, C. (2018) Bed load transport and incipient motion below a large gravel bed river bend. *Advances in Water Resources*, 120 (2018) 83–97. http://dx.doi.org/10.1016/j.advwatres.2017.07.026

Orrú, C., Blom, A., & Uijttewaal, W. S. J. (2016). Armor breakup and reformation in a degradational laboratory experiment. *Earth Surface Dynamics*, 4(2), 461–470. https://doi.org/10.5194/esurf-4-461-2016

Ottawa RIVERKEEPER (2024). Map Gallery. Webpage link: https://ottawariverkeeper.ca/map-gallery/

Ottawa River Regulation Planning Board. (2017). Summary of the 2017 Spring Flood. https://ottawariver.ca/wp-content/uploads/2019/02/2017-Spring-Flood-Summary.pdf

Ottawa River Regulation Planning Board. (2024). Website pape : https://ottawariver.ca/

Pan, F., Wang, C., & Xi, X. (2016). Constructing river stage-discharge rating curves using remotely sensed river cross-sectional inundation areas and river bathymetry. *Journal of Hydrology*, 540, 670–687.

https://doi.org/10.1016/j.jhydrol.2016.06.024

Pandey, A. K., & Mohapatra, P. K. (2022). Three-Dimensional Numerical Simulation of the Flood-Wave Propagation at a Combining Open-Channel Junction. *Journal of Irrigation and Drainage Engineering*, 148(11). https://doi.org/10.1061/(asce)ir.1943-4774.0001713

Pariartha, I.P.G.S., Aggarwal, S., Rallapalli, S., Egodawatta, P., McGree, J., & Goonetilleke, A. (2023). Compounding effects of urbanization, climate change and sea-level rise on monetary projections of flood damage. *Journal of Hydrology*, 129535–129535. https://doi.org/10.1016/j.jhydrol.2023.129535

Park, I., & Jain, S. C. (1986). River - Bed Profiles with Imposed Sediment Load. *Journal of Hydraulic Engineering*, 112(4), 267 – 280. https://doi.org/10.1061/(asce)0733-9429(1986)112:4(267)

Park, I., & Jain, S. C. (1987). Numerical Simulation of Degradation of Alluvial Channel Beds. *Journal of Hydraulic Engineering*, 113(7), 845–859. https://doi.org/10.1061/(asce)0733-9429(1987)113:7(845)

Parker, G., & Klingeman. P. C. (1982). On why gravel bed streams are paved. *Water Resources Research*. 18, 1409– 1423. https://doi.org/10.1029/WR018i005p01409

Parker, G., Klingeman, P.C., & McLean, D.G. (1982). Bedload and size distribution in paved gravel-bed streams. *Journal of the Hydraulics Division*. 108 (4), 544–571. https://doi.org/10.1061/JYCEAJ.0005854

Parker, G., Klingeman, P. C., & McLean, D. G. (1983). Bedload and size distribution in paved gravel-bed streams. Journal of Hydraulic Engineering, 109(5), 793-794. https://doi.org/10.1061/(ASCE)0733-9429(1983)109:5(793)

Parker, G., Shimizu, Y., Wilkerson, G. V., Eke, E. C., Abad, J. D., Lauer, J. W., Paola, C., Dietrich, W. E., & Voller, V. R. (2010). A new framework for modeling the migration of meandering rivers. Earth Surface Processes and Landforms, 36(1), 70–86. https://doi.org/10.1002/esp.2113

Parsapour-Moghaddam, P., Brennan, C. P., Rennie, C. D., Elvidge, C. K., & Cooke, S. J. (2019a). Impacts of channel morphodynamics on fish habitat utilization. *Environmental management*, 64(3), 272-286. https://doi.org/10.1007/s00267-019-01197-0

Parsapour-Moghaddam, P., & Rennie, C. D. (2017). Hydrostatic versus nonhydrostatic hydrodynamic Modeling of secondary flow in a tortuously meandering river:

Application of Delft3D. River research and applications, 33(9), 1400-1410. https://doi.org/10.1002/rra.3214

Parsapour-Moghaddam, P., & Rennie, C. D. (2018). Calibration of a 3D Hydrodynamic Meandering River Model Using Fully Spatially Distributed 3D ADCP Velocity Data. *Journal of Hydraulic Engineering*, 144(4). https://doi.org/10.1061/(asce)hy.1943-7900.0001424

Parsapour-moghaddam, P., Rennie, C. D., & Slaney, J. (2018). Hydrodynamic Simulation of an Irregularly Meandering Gravel-Bed River: Comparison of MIKE 21 FM and Delft3D Flow models. *E3S Web of Conferences*, 40, 02004. https://doi.org/10.1051/e3sconf/20184002004

Parsapour-Moghaddam, P., Rennie, C.D., Slaney, J. (2019b) Morphodynamic modeling to evaluate flood mitigation strategies, *38th IAHR World Congress*, Panama City, Panama, Sep 1-6, https://doi.org/10.3850/38WC092019-1083

Pauley, G. B., Thomas, G. L., Marino, D. A., & Weigand, D. C. (1989). Evaluation of the effects of gravel bar scalping on juvenile salmonids in the Puyallup River drainage. University of Washington Cooperative Fishery Research Unit Report. University of Washington, Seattle.

Patalano, A., García, C. M., & Rodríguez, A. (2017). Rectification of Image Velocity Results (RIVeR): A simple and user-friendly toolbox for large scale water surface Particle Image Velocimetry (PIV) and Particle Tracking Velocimetry (PTV). *Computers & Geosciences*, 109, 323–330. https://doi.org/10.1016/j.cageo.2017.07.009

Patalano, A. (2024). PTVlab (Particle Tracking Velocimetry - lab) (https://www.mathworks.com/matlabcentral/fileexchange/41235-ptvlab-particle-tracking-velocimetry-lab), MATLAB Central File Exchange. Retrieved August 17, 2024.

Pavelsky, T. M. (2014). Using width-based rating curves from spatially discontinuous satellite imagery to monitor river discharge. *Hydrological Processes*, 28 (6), 3035–3040. https://doi.org/10.1002/hyp.10157

Pearce, S., Ljubičić, R., Peña‐Haro, S., Perks, M., Tauro, F., Pizarro, A., Silvano, Dariia Strelnikova, Grimaldi, S., Maddock, I., Paulus, G., Jasna Plavšić, Dušan Prodanović, & Manfreda, S. (2020). An Evaluation of Image Velocimetry Techniques under Low Flow Conditions and High Seeding Densities Using Unmanned Aerial Systems. *Remote Sensing*, 12(2), 232–232. https://doi.org/10.3390/rs12020232

Pekárová, P., Halmová, D., Mitková, V., Miklánek, P., Pekár, J. & Škoda,P. (2013).Historic flood marks and flood frequency analysis of the Danube River at

Bratislava, Slovakia. *Journal of Hydrology and Hydromechanics*,61(4) 326-333. https://doi.org/10.2478/johh-2013-0041

Perks, M. T. (2020). KLT-IV v1.0: image velocimetry software for use with fixed and mobile platforms. *Geoscientific Model Development*, 13(12), 6111–6130. https://doi.org/10.5194/gmd-13-6111-2020

Perks, M. T., Dal Sasso, S. F., Hauet, A., Jamieson, E., Le Coz, J., Pearce, S., Peña-Haro, S., Pizarro, A., Strelnikova, D., Tauro, F., Bomhof, J., Grimaldi, S., Goulet, A., Hortobágyi, B., Jodeau, M., Käfer, S., Ljubičić, R., Maddock, I., Mayr, P., & Paulus, G. (2020). Towards harmonisation of image velocimetry techniques for river surface velocity observations. *Earth System Science Data*, 12(3), 1545–1559. https://doi.org/10.5194/essd-12-1545-2020

Petersen-Øverleir, A., & Reitan, T. (2005). Objective segmentation in compound rating curves. *Journal of Hydrology*, 311(1-4), 188–201. https://doi.org/10.1016/j.jhydrol.2005.01.016

Petit, F., Poinsart, D., & Bravard, J.-P. (1996). Channel incision, gravel mining and bedload transport in the Rhone River upstream of Lyon, France ("canal de Miribel"). *Catena*. 26: 209-226. https://doi.org/10.1016/0341-8162(95)00047-X

Phillips, J. V. & Tadayon, S. (2006) Selection of Manning's Roughness Coefficient for Natural and Constructed Vegetated and Non-Vegetated Channels, and Vegetation Maintenance Plan Guidelines for Vegetated Channels in Central Arizona. Scientific Investigations Report. 2006-5108. https://doi.org/10.3133/sir20065108

Pizarro, A., Dal Sasso, S. F., Perks, M. T., & Manfreda, S. (2020a). Identifying the optimal spatial distribution of tracers for optical sensing of stream surface flow. *Hydrology and Earth System Sciences*, 24(11), 5173–5185. https://doi.org/10.5194/hess-24-5173-2020

Pizarro, A., Silvano, & Manfreda, S. (2020b). Refining image - velocimetry performances for streamflow monitoring: Seeding metrics to errors minimization. *Hydrological Processes*, 34(25), 5167 - 5175. https://doi.org/10.1002/hyp.13919

Pomeroy, J.W., Stewart, R.E., & Whitfield, P.H., (2016). The 2013 flood event in the South Saskatchewan and Elk River basins: Causes, assessment and damages. *Canadian Water Resources Journal*. 41, 105–117. https://doi.org/10.1080/07011784.2015.1089190

Qian, Y., Chakraborty, T. C., Li, J., Li, D., He, C., Sarangi, C., Chen, F., Yang, X., & Leung, L. R. (2022). Urbanization Impact on Regional Climate and Extreme Weather: Current Understanding, Uncertainties, and Future Research Directions. *Advances in Atmospheric Sciences*, 39(6), 819–860. https://doi.org/10.1007/s00376-021-1371-9

Qiu, J., Liu, B., Yu, X., & Yang, Z. (2021). Combining a segmentation procedure and the BaRatin stationary model to estimate nonstationary rating curves and the associated uncertainties. *Journal of Hydrology*, 597, 126168–126168. https://doi.org/10.1016/j.jhydrol.2021.126168

Raffel, M., Willert, C., Scarano, F., Kähler, C. J., Wereley, S., & Jürgen Kompenhans. (2018). *Particle Image Velocimetry*. https://doi.org/10.1007/978-3-319-68852-7

Rahimzadeh, O., Bahremand, A., Noura, N., & Mukolwe, M. (2019). Evaluating flood extent mapping of two hydraulic models, 1D HEC‐RAS and 2D LISFLOOD‐FP in comparison with aerial imagery observations in Gorgan flood plain, Iran. *Natural Resource Modeling*, 32(4). https://doi.org/10.1111/nrm.12214

Ramirez, M. T., & M. A. Allison (2013), Suspension of bed material over sand bars in the Lower Mississippi River and its implications for Mississippi delta environmental restoration. *Journal of Geophysical Research: Earth Surface*, 118, https://doi.org/10.1002/jgrf.20075

Ravichandran, S.; Reddy, V.M.; Ray, L.K. (2024). Change and coincidence risk analysis of floods in the Mahanadi River Basin, India. *Journal of Water and Climate Change*. https://doi.org/10.2166/wcc.2024.729

Reisenbüchler, M., Bui, M.D., Skublics, D. & Rutschmann, P. (2019). An integrated approach for investigating the correlation between floods and river morphology: A case study of the Saalach River, Germany. *Science of The Total Environment*, Volume 647, 2019, Pages 814-826, ISSN 0048-9697, https://doi.org/10.1016/j.scitotenv.2018.08.018

Rempel, L.L., Healey, K., & Lewis, F.J.A. (2012). Lower Fraser River juvenile fish habitat suitability criteria. Canadian Technical Report of Fisheries and Aquatic Sciences. 2991: ix + 73 p.

Rennie, C. D., & Church, M. (2010). Mapping spatial distributions and uncertainty of water and sediment flux in a large gravel bed river reach using an acoustic Doppler current profiler. *Journal of Geophysical Research: Earth Surface*, 115, F03035, https://doi.org/10.1029/2009JF001556

Rennie, C. D., & Millar, R. G. (2004). Measurement of the spatial distribution of fluvial bedload transport velocity in both sand and gravel. *Earth Surface Processes and Landforms*, 29(10), 1173–1193. https://doi.org/10.1002/esp.1074

Righini, M., Surian, N., Wohl, E., Marchi, L., Comiti, F., Amponsah, W., & Borga, M. (2017). Geomorphic response to an extreme flood in two Mediterranean rivers (northeastern Sardinia, Italy): Analysis of controlling factors. *Geomorphology*, 290, 184–199. https://doi.org/10.1016/j.geomorph.2017.04.014

Riley, J. D., Rhoads, B. L., Parsons, D. R., & Johnson, K. K. (2014). Influence of junction angle on three-dimensional flow structure and bed morphology at confluent meander bends during different hydrological conditions. *Earth Surface Processes and Landforms*, 40(2), 252–271. https://doi.org/10.1002/esp.3624

Roelvink, J. A. & Walstra, D.J.R. (2004). Keeping it simple by using complex models. In Proceedings of the 6th International Conference on Hydro-Science and Engineering. *Advances in Hydro-Science and Engineering*, vol. VI, page p. 12. Brisbane, Australia.

Rood, S.B., Kaluthota, S., Philipsen, L.J., Slaney, J., Jones, E., Chasmer, L., & Hopkinson, C. (2019) Camo-maps: An efficient method to assess and project riparian vegetation colonization after a major river flood. *Ecological Engineering*, Volume 141, 2019, 105610, ISSN 0925-8574, https://doi.org/10.1016/j.ecoleng.2019.105610.

Ruiz-Bellet, J.L., Castelltort, X., J. Carles Balasch, & Tuset., J. (2016). Uncertainty of the peak flow reconstruction of the 1907 flood in the Ebro River in Xerta (NE Iberian Peninsula). *Journal of Hydrology*, 545, 339–354. https://doi.org/10.1016/j.jhydrol.2016.12.041

Sahoo, B., Perumal, M., Moramarco, T., & Barbetta, S. (2014). Rating Curve Development at Ungauged River Sites using Variable Parameter Muskingum Discharge Routing Method. *Water Resources Management*, 28(11), 3783–3800. https://doi.org/10.1007/s11269-014-0709-9

Samarage, C. R., Carberry, J., Hourigan, K., & Fouras, A. (2011). Optimisation of temporal averaging processes in PIV. *Experiments in Fluids*, 52(3), 617–631. https://doi.org/10.1007/s00348-011-1080-8

Santiago, J. G., Wereley, S. T., Meinhart, C. D., Beebe, D. J., & Adrian, R. J. (1998). A particle image velocimetry system for microfluidics. *Experiments in Fluids*, 25(4), 316–319. https://doi.org/10.1007/s003480050235

Sanyal, J. & Lu, X.X. (2004). Application of Remote Sensing in Flood Management with Special Reference to Monsoon Asia: A Review. *Natural Hazards*. 33, 283–301 (2004). https://doi.org/10.1023/B:NHAZ.0000037035.65105.95

Scamardo, J., Nelson, P. A., Nichols, M., & Wohl, E. (2022). Modeling the relative morphodynamic influence of vegetation and large wood in a dryland ephemeral stream, Arizona, USA. *Geomorphology*, 417, 108444. https://doi.org/10.1016/j.geomorph.2022.108444

Scherer, D., Schwatke, C., Dettmering, D., & Seitz, F. (2022). ICESat-2 based river surface slope and its impact on water level time series from satellite altimetry. *Water Resources Research*, 58(11). https://doi.org/10.1029/2022WR032842

Schlaffer, S., Matgen, P., Hollaus, M. & Wagner, W. (2015). Flood detection from multi-temporal SAR data using harmonic analysis and change detection, *International Journal of Applied Earth Observation and Geoinformation*, Volume 38, 2015, Pages 15-24, ISSN 0303-2434. https://doi.org/10.1016/j.jag.2014.12.001

Schuurman, F., Marra, W. A., & Kleinhans, M. G. (2013). Physics-based modeling of large braided sand-bed rivers: Bar pattern formation, dynamics, and sensitivity. *Journal of Geophysical Research: Earth Surface*, 118(4), 2509-2527. https://doi.org/10.1002/2013JF002896

Schweitzer, S. A., & Cowen, E. A. (2021). Instantaneous River‐Wide Water Surface Velocity Field Measurements at Centimeter Scales Using Infrared Quantitative Image Velocimetry. *Water Resources Research*, 57(8). https://doi.org/10.1029/2020wr029279

Sear, D.A., & Archer, D. (1998). Effects of gravel extraction on stability of gravel-bed rivers: The Wooler Water, Northumberland, UK. In: Klingeman, P.C., Beschta, R.L., Komar, P.D., Bradley, J.B. (Eds.), Gravel-bed Rivers in the Environment. Water Resources Publication, Highlands Ranch, CO, pp. 415–432.

Shaker, A., Yan W.Y., Wong, M.S., El-Ashmawy, N., & Alhaddad, B.I. (2008). Flood hazard assessment using panchromatic satellite imagery. The International Archives of the Photogrammetry, Remote Sensing and Spatial Information Sciences. Vol. XXXVII. Part B7. Beijing 2008

Shen, X., Gao, W., Cao, L., Li, S., Cai, H., Li, R., & Hodges, B. R. (2023). Characteristics of water free-surface with different momentum ratio at 45° confluence. *Journal of Hydrology*, 623, 129787–129787. https://doi.org/10.1016/j.jhydrol.2023.129787

Shi, L., Sun, J., Lin, B., Liu, Z., & Zuo, X. (2022). Hydro-Thermodynamic Processes at a Large Confluence Under Reservoir Regulation. *Water Resources Research*, 58(12). https://doi.org/10.1029/2022wr033315

Siemes, R.W.A., Duong, T.M., Borsje, B. W., & Hulscher S.J.M.H. (2024). Climate Change Can Intensify the Effects of Local Interventions: A Morphological Modeling Study of a Highly Engineered Estuary. *Journal of Geophysical Research Earth Surface*, 129(7). https://doi.org/10.1029/2023jf007595

Simpson, G., & Castelltort, S. (2006). Coupled model of surface water flow, sediment transport and morphological evolution. *Computers & Geosciences*, 32(10), 1600–1614. https://doi.org/10.1016/j.cageo.2006.02.020

Slaney, J., Rood, S., Dick, W., & Rennie, C. (2019). The city of Calgary's river morphology risk mitigation program. Proceedings of the 38th IAHR World Congress, Panama. 4202-4210. https://doi.org/10.3850/38WC092019-1423.

Soares-Frazão, S., Lhomme, J., Guinot, V., & Zech, Y. (2008). Two-dimensional shallow-water model with porosity for urban flood modeling. *Journal of Hydraulic Research*, 46(1), 45–64. https://doi.org/10.1080/00221686.2008.9521842

Soulsby, R. (1997). Dynamics of Marine Sands, a Manual for Practical Applications.

Thomas Telford, London, United Kingdom.

Sreekumar, U., Nistor, I., Rennie, C., & Abdolmajid Mohammadian. (2024). Numerical Modeling of Downstream Morphological Evolution during Mount Polley Tailings Dam Failure. *Journal of Hydraulic Engineering*, 150(1). https://doi.org/10.1061/jhend8.hyeng-13497

Staines, K. E. H., & Carrivick, J. L. (2015). Geomorphological impact and morphodynamic effects on flow conveyance of the 1999 jökulhlaup at sólheimajökull, Iceland. *Earth Surface Processes and Landforms*, 40(10), 1401–1416. https://doi.org/10.1002/esp.3750

Straatsma, M. W., & Baptist, M. J. (2008). Floodplain roughness parameterization using airborne laser scanning and spectral remote sensing. *Remote Sensing of Environment*, 112(3), 1062–1080. https://doi.org/10.1016/j.rse.2007.07.012

Strelnikova, D., Paulus, G., Käfer, S., Anders, K.-H., Mayr, P., Mader, H., Scherling, U., & Schneeberger, R. (2020). Drone-Based Optical Measurements of Heterogeneous Surface Velocity Fields around Fish Passages at Hydropower Dams. *Remote Sensing*, 12(3), 384–384. https://doi.org/10.3390/rs12030384

Sukhodolov, A. N., Krick, J., Sukhodolova, T. A., Cheng, Z., Rhoads, B. L., & Constantinescu, G. S. (2017). Turbulent flow structure at a discordant river confluence: Asymmetric jet dynamics with implications for channel morphology. Journal of Geophysical Research: *Earth Surface*, 122(6), 1278–1293. https://doi.org/10.1002/2016jf004126

Sukhodolov, A. N., & Sukhodolova, T. A. (2019). Dynamics of Flow at Concordant Gravel Bed River Confluences: Effects of Junction Angle and Momentum Flux Ratio. *Journal of Geophysical Research Earth Surface*, 124(2), 588–615. https://doi.org/10.1029/2018jf004648

Surf Anywhere. (2020). Initial design report for the Calgary River Wave Park at Calgary, Alberta. SA-2018-009-R1. Prepared for the City of Calgary. Access through: https://albertariversurfing.com/surfyyc

Surian, N. (1999). Channel changes due to river regulation: the case of the Piave River, Italy. *Earth Surface Processes and Landforms*. 24: 1135-1151. https://doi.org/10.1002/(SICI)1096-9837(199911)24:12<1135::AID-ESP40>3.0.CO;2-F

Sutherland, J., Peet, A. H., & Soulsby, R. L. (2004). Evaluating the performance of morphological models. *Coastal Engineering*, 51(8-9), 917–939. https://doi.org/10.1016/j.coastaleng.2004.07.015

Taherkhani, M., Vitousek, S., Barnard, P. L., Frazer, N., Anderson, T. R., & Fletcher, C. H. (2020). Sea-level rise exponentially increases coastal flood frequency. *Scientific Reports*, 10(1). https://doi.org/10.1038/s41598-020-62188-4

Tang, H., Chen, K., Yuan, S., Xu, L., Qiu, J., Lin, Q., & Gualtieri, C. (2024). Effects of tributary inflows on unsteady flow hysteresis and hydrodynamics in the mainstream. *Hydrology Research*. https://doi.org/10.2166/nh.2024.018

Tarpanelli, A., Barbetta, S., Brocca, L., & Moramarco, T. (2013). River Discharge Estimation by Using Altimetry Data and Simplified Flood Routing Modeling. *Remote Sensing*, 5(9), 4145–4162. https://doi.org/10.3390/rs5094145

Tauro, F., Piscopia, R., & Grimaldi, S. (2017). Streamflow observations from cameras: large-scale particle image velocimetry or particle tracking velocimetry? *Water Resources Research*, 53, 10,374–10,394. https://doi.org/10.1002/2017WR020848

Tauro, F., Petroselli, A., & Grimaldi, S. (2018a). Optical sensing for stream flow observations: A review. *Journal of Agricultural Engineering*, 49(4), 199–206. https://doi.org/10.4081/jae.2018.836

Tauro, F., Tosi, F., Stefano Mattoccia, Toth, E., R. Piscopia, & Grimaldi, S. (2018b). Optical Tracking Velocimetry (OTV): Leveraging Optical Flow and Trajectory-Based Filtering for Surface Streamflow Observations. *Remote Sensing*, 10(12), 2010–2010. https://doi.org/10.3390/rs10122010

Thapa, S., Sinclair, H. D., Creed, M. J., Mudd, S. M., Attal, M., Borthwick, L., Ghimire, B. N., & C. Scott Watson. (2023). The impact of sediment flux and calibre on flood risk in the Kathmandu Valley, Nepal. *Earth Surface Processes and Landforms*, 49(2), 706–727. https://doi.org/10.1002/esp.5731

Theunissen, R., & Edwards, M. (2018). A general approach to evaluate the ensemble cross-correlation response for PIV using Kernel density estimation. *Experiments in Fluids*, 59(11). https://doi.org/10.1007/s00348-018-2627-8

Thieken, A. H., Kienzler, S., Kreibich, H., Kuhlicke, C., Kunz, M., Mühr, B., Müller, M., Otto, A., Petrow, T., Pisi, S., & Schröter, K. (2016). Review of the flood risk management system in Germany after the major flood in 2013. *Ecology and Society*, 21(2). https://doi.org/10.5751/es-08547-210251

Thielicke, W., & Sonntag, R. (2021). Particle Image Velocimetry for MATLAB: Accuracy and enhanced algorithms in PIVlab. Journal of Open Research Software, 9(1), 12. Ubiquity Press, Ltd. Retrieved from https://doi.org/10.5334%2Fjors.334

Thielicke, W. (2022) Pulse-length induced motion blur in PIV particle images: To be avoided at any cost?. Proceedings of the Fachtagung Experimentelle Strömungsmechanik 2022, 6.–8. September 2022, Ilmenau, Germany, ISBN 978-3-9816764-8-8, https://www.gala-ev.org/images/Beitraege/Beitraege2022/pdf/04.pdf

Tu, T., Carr, K.J., Ercan, A., Trinh, T., Kavvas, M.L. & Nosacka, J. (2017) Assessment of the effects of multiple extreme floods on flow and transport processes under competing flood protection and environmental management strategies. *Science of*

The Total Environment, Volumes 607–608, 2017, Pages 613-622, ISSN 0048-9697, https://doi.org/10.1016/j.scitotenv.2017.06.271

Uthra Sreekumar, Nistor, I., Rennie, C., & Abdolmajid Mohammadian. (2024). Numerical Modeling of Downstream Morphological Evolution during Mount Polley Tailings Dam Failure. *Journal of Hydraulic Engineering*, 150(1). https://doi.org/10.1061/jhend8.hyeng-13497

Van Emelen, S., Soares-Frazão, S., Riahi-Nezhad, C. K., Hanif Chaudhry, M., Imran, J., & Zech, Y. (2012). Simulations of the New Orleans 17th Street Canal breach flood. *Journal of Hydraulic Research*, 50(1), 70–81. https://doi.org/10.1080/00221686.2011.642578

Van Rijn, L. C. (1993). Principles of Sediment Transport in Rivers, Estuaries and Coastal Seas. Aqua Publications, The Netherlands.

Van Rijn, L. C. (2007). Unified View of Sediment Transport by Currents and Waves. I: Initiation of Motion, Bed Roughness, and Bed-Load Transport. Journal of Hydraulic Engineering, 133(6), 649–667. https://doi.org/10.1061/(asce)0733-9429(2007)133:6(649)

Vázquez-Tarrío, D., Ruiz-Villanueva, V., Garrote, J., Benito, G., Calle, M., Lucía, A., & Díez-Herrero, A. (2023). Effects of sediment transport on flood hazards: Lessons learned and remaining challenges. *Geomorphology*, 108976. https://doi.org/10.1016/j.geomorph.2023.108976

Veiga, V.B., Hassan, Q.K., & He, J. (2015) Development of Flow Forecasting Models in the Bow River at Calgary, Alberta, Canada. *Water*, 7, 99-115. https://doi.org/10.3390/w7010099

Velickovic, M., Zech, Y., & Soares-Frazão, S. (2016). Steady-flow experiments in urban areas and anisotropic porosity model. *Journal of Hydraulic Research*, 55(1), 85–100. https://doi.org/10.1080/00221686.2016.1238013

Vericat, D., Batalla, R. J., & Garcia, C. (2006). Breakup and reestablishment of the armour layer in a large gravel-bed river below dams: The lower Ebro. *Geomorphology*, 76(1-2), 122–136. https://doi.org/10.1016/j.geomorph.2005.10.005

Vestby, J., Schutte, S., Tollefsen, A. F., & Buhaug, H. (2024). Societal determinants of flood-induced displacement. *Proceedings of the National Academy of Sciences of the United States of America*, 121(3), e2206188120. https://doi.org/10.1073/pnas.2206188120

Viparelli, E., Sequeiros, O.E., Cantelli, A., Wilcock, P.R., & Parker, G. (2010). River morphodynamics with creation/consumption of grain size stratigraphy 2: numerical model, *Journal of Hydraulic Research*, 48:6, 727-741, https://doi.org/10.1080/00221686.2010.526759

Wang, J., Dai, Z., Fagherazzi, S., Zhang, X., & Liu, X. (2022) Hydro-morphodynamics triggered by extreme riverine floods in a mega fluvial-tidal delta. *Science of The Total Environment*, Volume 809, 152076, ISSN 0048-9697, https://doi.org/10.1016/j.scitotenv.2021.152076.

Wang, J., Liu, X., Ouyang, X., Zhang, G., & Zhang, Y. (2024a). A method of applying deep learning based optical flow algorithm to river flow discharge measurement. *Measurement Science & Technology*, 35(6), 065303–065303. https://doi.org/10.1088/1361-6501/ad3183

Wang, X., Cheng, K., Luo, M., Xu, Z., & Yan, X. (2024b). Numerical assessment of hydro‐morphodynamics affected by altered upstream discharge in the Dujiangyan reach of the Min River, China. *Hydrological Processes*, 38(3). https://doi.org/10.1002/hyp.15113

Wang, Z., He, W., Lan, J., Zhu, C., Lei, J., & Liu, X. (2024c). Ship Trajectory Classification Prediction at Waterway Confluences: An Improved KNN Approach. *Journal of Marine Science and Engineering*, 12(7), 1070–1070. https://doi.org/10.3390/jmse12071070.

Wang, Z., Li, H., & Cai, X. (2018) Remotely Sensed Analysis of Channel Bar Morphodynamics in the Middle Yangtze River in Response to a Major Monsoon Flood in 2002. *Remote Sensing*. 2018, 10, 1165. https://doi.org/10.3390/rs10081165.

Water Survey of Canada. (2024) Real-Time Hydrometric Data. Access through: https://wateroffice.ec.gc.ca/search/real_time_e.html

Westerweel, J., Geelhoed, P. F., & Lindken, R. (2004). Single-pixel resolution ensemble correlation for micro-PIV applications. *Experiments in Fluids*. 37(3), 375–384. https://doi.org/10.1007/s00348-004-0826-y

Williams, R.D., Brasington, J., Hicks, M., Measures, R., Rennie, C.D, & Vericat, D (2013). Hydraulic validation of two-dimensional simulations of braided river flow with spatially continuous aDcp data, *Water Resources Research*, 49:5183–5205, https://doi.org/10.1002/wrcr.20391

Williams, R. D., Rennie, C. D., Brasington, J., Hicks, D. M., & Vericat, D. (2015). Linking the spatial distribution of bed load transport to morphological change during high-flow events in a shallow braided river. *Journal of Geophysical Research: Earth Surface*, 120(3), 604–622. https://doi.org/10.1002/2014jf003346

Williams, R. D., Measures, R., Hicks, D. M., & Brasington, J. (2016). Assessment of a numerical model to reproduce event-scale erosion and deposition distributions in a braided river. *Water Resources Research*, 52(8), 6621–6642. https://doi.org/10.1002/2015wr018491

Wintenberger, C. L., Rodrigues, S., Claude, N., Jugé, P., Bréhéret, J.-G., & Villar, M.

(2015). Dynamics of nonmigrating mid-channel bar and superimposed dunes in a sandy-gravelly river (Loire River, France). *Geomorphology*, 248, 185–204. https://doi.org/10.1016/j.geomorph.2015.07.032

Wishart, D., Warburton, J., & Bracken, L. (2008). Gravel extraction and planform change in a wandering gravel-bed river: The River Wear, Northern England. *Geomorphology*., 94 (1-2). pp. 131-152. http://dx.doi.org/10.1016/j.geomorph.2007.05.003

Wolman, M.G. & Miller, J.P. (1960). Magnitude and frequency of forces in geomorphic processes. *Journal of Geology*. 68, 54–74. https://doi.org/10.1086/626637.

Wong, J. S., Freer, J. E., Bates, P. D., Sear, D. A., & Stephens, E. M. (2014). Sensitivity of a hydraulic model to channel erosion uncertainty during extreme flooding. *Hydrological Processes*, 29(2), 261–279. https://doi.org/10.1002/hyp.10148

World Meteorological Organization (2010). Manual on stream gauging. Volume II -.Computation of Discharge WMO-No., 1044.

World Urbanization Prospects, the 2011 Revision | Latest Major Publications - United Nations Department of Economic and Social Affairs. (2011). Un.org. https://www.un.org/en/development/desa/publications/world-urbanization-prospects-the-2011-revision.html

Worni, R., Stoffel, M., Huggel, C., Volz, C., Casteller, A., & Luckman, B. (2012). Analysis and dynamic modeling of a moraine failure and glacier lake outburst flood at Ventisquero Negro, Patagonian Andes (Argentina). *Journal of Hydrology*, 444-445. https://doi.org/10.1016/j.jhydrol.2012.04.013.

Worni, R., Huggel, C., Clague, J.J., Schaub, Y., & Stoffel, M. (2014). Coupling glacial lake impact, dam breach, and flood processes: A modeling perspective. *Geomorphology*, 224, 161-176. https://doi.org/10.1016/j.geomorph.2014.06.031

Wu, C., Ullah, M.S., Lu, J., & Bhattacharya, J.P. (2016), Formation of point bars through rising and falling flood stages: Evidence from bar morphology, sediment transport and bed shear stress. *Sedimentology*, 63: 1458-1473. https://doi.org/10.1111/sed.12269.

Wu, G., Wang, K., Liang, B., Wu, X., Wang, H., Li, H., & Shi, B. (2023). Modeling the Morphological Responses of the Yellow River Delta to the Water‐Sediment Regulation Scheme: The Role of Impulsive River Floods and Density‐Driven Flows. *Water Resources Research*, 59(7). https://doi.org/10.1029/2022wr033003

Xie, Q., Yang, J., Lundström, S., & Dai, W. (2018). Understanding Morphodynamic Changes of a Tidal River Confluence through Field Measurements and Numerical Modeling. *Water*, 10(10), 1424. https://doi.org/10.3390/w10101424

Xu, L., & Gao, L. (2024). A hybrid surrogate model for real-time coastal urban flood prediction: An application to Macao. *Journal of Hydrology*, 642, 131863–131863. https://doi.org/10.1016/j.jhydrol.2024.131863

Xu, L., Yuan, S., Tang, H., Qiu, J., Xiao, Y., Whittaker, C., & Gualtieri, C. (2022). Mixing Dynamics at the Large Confluence Between the Yangtze River and Poyang Lake. *Water Resources Research*, 58(11). https://doi.org/10.1029/2022wr032195

Yan, G., Yuan, S., Tang, H., Xu, D., Liu, M., Whittaker, C., & Gualtieri, C. (2024). Hydrodynamic Response of Channel Flow Confluence to the Tributary Floodplain Topography. *Water Resources Research,* 60(8). https://doi.org/10.1029/2023wr036244

Yan, K., Di Baldassarre, G., Solomatine, D. P., & Schumann, G. J.-P. (2015). A review of low-cost space-borne data for flood modeling: topography, flood extent and water level. *Hydrological Processes,* 29(15), 3368–3387. https://doi.org/10.1002/hyp.10449

Yang, Q., Wang, X., Sun, Y., Duan, W., & Xie, S. (2022). Numerical Investigation on a Flash Flood Disaster in Streams with Confluence and Bifurcation. *Water*, 14(10), 1646. https://doi.org/10.3390/w14101646

Yanites, B. J. (2018). The dynamics of channel slope, width, and sediment in actively eroding bedrock river systems. *Journal of Geophysical Research: Earth Surface*, 123, 1504–1527. https://doi.org/10.1029/2017JF004405

Yonesi H.A., Omid M.H., & Ayyoubzadeh S.A. (2013). The Hydraulics of Flow in Non-Prismatic Compound Channels. *Journal of Civil Engineering and Urbanism*, 3(6): 342-356.

Yu, K., Kim, S., & Kim, D. (2015). Correlation analysis of spatio-temporal images for estimating two-dimensional flow velocity field in a rotating flow condition. *Journal of Hydrology*, 529(Part 3), 1810–1822. https://doi.org/10.1016/j.jhydrol.2015.08.005

Yu, Q., Rennie, C. D., Slaney, J. M., & Parsapour-Moghaddam, P. (2022). Impact evaluation of instream bar management using morphodynamic modeling. *Journal of Environmental Management*, 318, 115564. https://doi.org/10.1016/j.jenvman.2022.115564

Yu, Q., Yuan, S., & Rennie, C. D. (2020). Experiments on the morphodynamics of open channel confluences: Implications for the accumulation of contaminated sediments. *Journal of Geophysical Research: Earth Surface*, 125, e2019JF005438. https://doi.org/10.1029/2019JF005438

Yuan, S., Tang, H., Xiao, Y., Qiu, X., Zhang, H., & Yu, D. (2016). Turbulent flow structure at a 90-degree open channel confluence: Accounting for the distortion of the shear layer. *Journal of Hydro-environment Research*. 12, 130–147. https://doi.org/10.1016/j.jher.2016.05.006

Yuan, S., Tang, H., Xiao, Y., Xia, Y., Melching, C. S., & Li, Z. (2019). Phosphorus contamination of the surface sediment at a river confluence. *Journal of Hydrology*, 573, 568–580. https://doi.org/10.1016/j.jhydrol.2019.02.036.

Yuan, S., Tang, H., Li, K., Xu, L., Xiao, Y., Gualtieri, C., Rennie, C. D., & Melville, B. W. (2021). Hydrodynamics, Sediment Transport and Morphological Features at the Confluence Between the Yangtze River and the Poyang Lake. *Water Resources Research*. 57(3). https://doi.org/10.1029/2020wr028284

Yuill, B. T., Gaweesh, A., Allison, M. A., & Meselhe, E. A. (2016) Morphodynamic evolution of a lower Mississippi River channel bar after sand mining. *Earth Surface Processes and Landforms*, 41: 526– 542. https://doi.org/10.1002/esp.3846.

Zeng, Q., Shi, L., Wen, L., Chen, J., Duo, H., & Lei, G. (2015) Gravel Bars Can Be Critical for Biodiversity Conservation: A Case Study on Scaly-Sided Merganser in South China. *PLoS One*. 10(5): e0127387. https://doi.org/10.1371/journal.pone.0127387

Zhang, R., Liu, D., Xiong, L., Chen, J., Chen, H., Yin, J., & Wang, J. (2024). An agent-based modeling method to determine the number of flash flood warnings for improving the warning response levels. *Journal of Hydrology*, 640, 131709–131709. https://doi.org/10.1016/j.jhydrol.2024.131709

Zhang, Y., & Crawford, P. (2020). Automated Extraction of Visible Floodwater in Dense Urban Areas from RGB Aerial Photos. *Remote Sensing*. 12(14):2198. https://doi.org/10.3390/rs12142198

Zhang, T., Feng, M., & Chen, K. (2020). Hydrodynamic characteristics and channel morphodynamics at a large asymmetrical confluence with a high sediment-load main channel. *Geomorphology*, 356, 107066. https://doi.org/10.1016/j.geomorph.2020.107066

Zhang H, Qi Z, Li X, Chen Y, Wang X, & He Y. (2021) An Urban Flooding Index for Unsupervised Inundated Urban Area Detection Using Sentinel-1 Polarimetric SAR Images. *Remote Sensing*. 2021; 13(22):4511. https://doi.org/10.3390/rs13224511

Zhou, R., Zheng, H., Liu, Y., Xie, G., & Wan, W. (2022). Flood impacts on urban road connectivity in southern China. *Scientific Reports*, 12(1). https://doi.org/10.1038/s41598-022-20882-5